

1 LEVERAGING MULTI-MESSENGER ASTROPHYSICS FOR DARK MATTER SEARCHES

By

Daniel Nicholas Salazar-Gallegos

A DISSERTATION

Submitted to
Michigan State University
in partial fulfillment of the requirements
for the degree of

Physics—Doctor of Philosophy
Computational Mathematics in Science and Engineering—Dual Major

Today

ABSTRACT

3 I did Dark Matter with HAWC and IceCube. I also used Graph Neural Networks

⁴ Copyright by

⁵ DANIEL NICHOLAS SALAZAR-GALLEGOS

⁶ Today

ACKNOWLEDGMENTS

8 I love my friends. Thanks to everyone that helped me figure this out. Amazing thanks to the people
9 at LANL who supported me. Eames, etc Dinner Parties Jenny and her child Kaydince Kirsten, Pat,
10 Andrea Family. You're so far but so critical to my formation. Unconditional love. Roommate

TABLE OF CONTENTS

12	LIST OF TABLES	vii
13	LIST OF FIGURES	ix
14	LIST OF ABBREVIATIONS	xix
15	CHAPTER 1 INTRODUCTION	1
16	CHAPTER 2 DARK MATTER IN THE COSMOS	2
17	2.1 Introduction	2
18	2.2 Dark Matter Basics	3
19	2.3 Evidence for Dark Matter	4
20	2.4 Searching for Dark Matter: Particle DM	11
21	2.5 Sources for Indirect Dark Matter Searches	16
22	2.6 Multi-Messenger Dark Matter	18
23	CHAPTER 3 HIGH ALTITUDE WATER CHERENKOV (HAWC) OBSERVATORY	21
24	3.1 The Detector	21
25	3.2 Events Reconstruction and Data Acquisition	21
26	3.3 Remote Monitoring	21
27	CHAPTER 4 ICECUBE NEUTRINO OBSERVATORY	22
28	4.1 The Detector	22
29	4.2 Events Reconstruction and Data Acquisition	22
30	4.3 Northern Test Site	22
31	CHAPTER 5 GLORY DUCK: MULTI-WAVELENGTH SEARCH FOR DARK MATTER ANNIHILATION TOWARDS DWARF SPHEROIDAL GALAXIES	23
32	5.1 Introduction	23
33	5.2 Dataset and Background	25
34	5.3 Analysis	27
35	5.4 Likelihood Methods	31
36	5.5 HAWC Results	38
37	5.6 Glory Duck Combined Results	40
38	5.7 HAWC Systematics	45
39	5.8 J -factor distributions	47
40	5.9 Discussion and Conclusions	53
43	CHAPTER 6 MULTITHREADING HAWC ANALYSES FOR DARK MATTER SEARCHES	57
44	6.1 Introduction	57
45	6.2 Dataset and Background	57
46	6.3 Analysis	59

48	6.4 Likelihood Methods	63
49	6.5 Computational Methods: Multithreading	63
50	6.6 Analysis Results	69
51	6.7 Systematics	74
52	6.8 Conclusion and Discussion	74
53	CHAPTER 7 HEAVY DARK MATTER ANNIHILATION SEARCH WITH ICE-CUBE'S NORTH SKY TRACK DATA	76
55	7.1 Introduction	76
56	7.2 Dataset and Background	77
57	7.3 Analysis	78
58	7.4 Likelihood Methods	87
59	7.5 Background Simulation	87
60	7.6 Signal Recovery	105
61	7.7 Systematics	108
62	7.8 Conclusions	109
63	CHAPTER 8 NU DUCK	114
64	APPENDIX A MULTI-EXPERIMENT SUPPLEMENTARY FIGURES	115
65	APPENDIX B MULTITHREADING DARK MATTER ANALYSES SUPPLEMENTARY MATERIAL	116
66	B.1 Remaining Spectral Models	116
67	B.2 <code>mpu_analysis.py</code>	117
68	B.3 Comparison with Glory Duck	126
70	APPENDIX C ICECUBE HEAVY DARK MATTER ANALYSIS SUPPLEMENTARY MATERIAL	129
71	C.1 Docker Image for Oscillating Neutrino Spectra	129
72	C.2 Spline Fitting Statuses	132
73	C.3 Neutrino Composite Spectra	133
74	C.4 Segue 1 And Ursa Major II Signal Recovery	134
75	C.5 n_s Sensitivities	140
77	BIBLIOGRAPHY	142

LIST OF TABLES

79	Table 5.1	Summary of the relevant properties of the dSphs used in the present work. Column 1 lists the dSphs. Columns 2 and 3 present their heliocentric distance and galactic coordinates, respectively. Columns 4 and 5 report the J -factors of each source given from the \mathcal{GS} and \mathcal{B} independent studies and their estimated $\pm 1\sigma$ uncertainties. The values $\log_{10} J$ (\mathcal{GS} set) [45] correspond to the mean J -factor values for a source extension truncated at the outermost observed star. The values $\log_{10} J$ (\mathcal{B} set) [49] are provided for a source extension at the tidal radius of each dSph. Bolded sources are within HAWC's field of view and provided to the Glory Duck analysis.	32
88	Table 5.2	Summary of dSph observations by each experiment used in this work. A ‘-’ indicates the experiment did not observe the dSph for this study. For Fermi-LAT, the exposure at 1 GeV is given. For HAWC, $ \Delta\theta $ is the absolute difference between the source declination and HAWC latitude. HAWC is more sensitive to sources with smaller $ \Delta\theta $. For IACTs, we show the zenith angle range, the total exposure, the energy range, the angular radius θ of the signal or ON region, the ratio of exposures between the background-control (OFF) and signal (ON) regions (τ), and the significance of gamma-ray excess in standard deviations, σ .	33
97	Table 6.1	Summary of the relevant properties of the dSphs used in the present work. Column 1 lists the dSphs. Columns 2 and 3 present their heliocentric distance and galactic coordinates, respectively. Column 4 reports the J -factors of each source given from the \mathcal{LS} studies and estimated $\pm 1\sigma$ uncertainties. The values $\log_{10} J$ (\mathcal{LS} set) [66] correspond to the mean J -factor values for a source extension truncated at 0.5° .	63
103	Table 6.2	Timing summaries for analyses for serial and multithreaded processes. M tasks is the number of functional-parallel tasks ran for the computation. $T_{p,c}$ is a single run time in hours:minutes:seconds for runs utilizing p nodes and c threads. Runs are run interactively on the same computer to maximize consistency. Empty entries are indicated with ‘-’. (·) entries are estimated entries extrapolated from data earlier in the column.	67
109	Table 6.3	Speed up summaries for analyses for serial and multithreaded processes. M tasks is the number of functional-parallel tasks ran for the computation. $S_{p,c}$ is a single speedup comparison for runs utilizing p nodes and c threads. [·] are the estimated speedups calculated from Tab. 6.2, Eq. (6.7), and Eq. (6.4). Empty entries are indicated with ‘-’.	69

114	Table 7.1 Spline err tolerances used for input in particle physics component to Eq. (7.1).	
115	Column 1 is the DM annihilation channel being fit. Columns 2, 3, and 4	
116	are the tolerances for "GOOD" (pass), "OK" requires inspection, and "FAIL"	
117	(tune and refit) respectively. Column 5 has the X ranges over which the error	
118	is evaluated. MAX/MIN [·,·] takes the maximum or minimum of the two	
119	enclosed values.	84
120	Proof I know how to include	

LIST OF FIGURES

122	Figure 2.1	Rotation curve fit to NGC 6503 from [7]. Dashed line is the contribution 123 from visible matter. Dotted curves are from gas. Dash-dot curves are from 124 dark matter (DM). Solid line is the composite contribution from all matter 125 and DM sources. Data are indicated with bold dots with error bars. Data 126 agree strongly with a matter + DM composite prediction.	5
127	Figure 2.2	Light from distant galaxy is bent in unique ways depending on the distribution 128 of mass between the galaxy and Earth. Yellow dashed lines indicate where 129 the light would have gone if the matter were not present [8].	7
130	Figure 2.3	(left) Optical image of galactic cluster 1E0657-558. (right) X-ray image of the 131 cluster with redder meaning hotter and higher baryon density. (both) Green 132 contours are reconstruction of gravity contours from weak lensing. White 133 rings are the best fit mass maxima at 68.3%, 95.5%, and 99.7% confidence. 134 The matter maxima of the clusters are clearly separated from x-ray maxima. [9]	8
135	Figure 2.4	Plank CMB sky. Sky map features small variations in temperature in primor- 136 dial light. These anisotropies are used to make inferences about the universe's 137 energy budget and developmental history. [10]	9
138	Figure 2.5	Observed Cosmic Microwave Background power spectrum as a function of 139 multipole moment from Plank [10]. Blue line is best fit model from Λ CDM . 140 Red points and lines are data and error, respectively.	10
141	Figure 2.6	Predicted power spectra of CMB for different $\Omega_m h^2$ values for fixed baryon 142 density from [11]. (left) Low $\Omega_m h^2$ increases the prominence of first and 143 second peaks. (middle) $\Omega_m h^2$ is most similar to the observed power spectrum. 144 The second and third peaks are similar in height. (right) $\Omega_m h^2$ is large which 145 suppresses the first peak and raises the prominence of the third peak.	10
146	Figure 2.7	The Standard Model (SM) of particle physics. Figure taken from http://www.quantumdiaries.org/2014/03/14/the-standard-model-a-beautiful-but-flawed-theory/	12
149	Figure 2.8	Simplified Feynman diagram demonstrating with different ways DM can 150 interact with SM particles. The 'X's refer to the DM particles whereas the 151 SM refer to fundamental particles in the SM. The large circle in the center 152 indicates the vertex of interaction and is purposely left vague. The colored 153 arrows refer to different directions of time as well as their respective labels. 154 The arrows indicate the initial and final state of the DM -SM interaction in time.	13

155	Figure 2.9 A single jet event in ATLAS detector from 2017 [16]. Jet momentum was 156 observed to be 1.9 TeV. Missing transverse momentum was observed to be 157 1.9 TeV compared to the initial transverse momentum of the event was 0. 158 Implied MET is traced by a red dashed line in event display.	14
159	Figure 2.10 More detailed pseudo-Feynman diagram of particle cascade from dark matter 160 annihilation into 2 quarks. The quarks hadronize and down to stable particles 161 like γ or the anti-proton (p^-). Diagram pulled from ICRC 2021 presentation 162 on DM annihilation search [17].	15
163	Figure 2.11 Dark Matter (DM) decay spectrum for $b\bar{b}$ initial state and γ final state. Redder 164 spectra are for larger DM masses. Bluer spectra are light DM masses. x is a 165 unitless factor defined as the ratio of the mass of DM, m_χ , and the final state 166 particle energy E_γ . Figure from [19].	17
167	Figure 2.12 Different dark matter density profiles compared. Some models produce ex- 168 ceptionally large densities at small r [20].	18
169	Figure 2.13 The Milky Way Galaxy in photons (γ) and neutrinos (ν) [22]. The Galactic 170 center is at $l=0^\circ$ and is the brightest region in all panels. (top) An Optical 171 color image of the Milky Way galaxy seen from Earth. Clouds of gas and dust 172 obscure some light from stars. (2nd down) Integrated flux of γ -rays observed 173 by the Fermi-LAT telescope [23]. (middle) Expected neutrino emission 174 that corresponds with Fermi-LAT observations. (2nd up) Expected neutrino 175 emission profile after considering detector systematics of IceCube. (bottom) 176 Observed neutrino emission from region of the galactic plane. Substantial 177 neutrino emission was detected.	19
178	Figure 2.14 Dark Matter annihilation spectra for different final state particle and standard 179 model annihilation channels [24]. Photons (red), e^\pm (green), \bar{p} (blue), ν (black).	20
180	Figure 5.1 Sensitivities of five gamma-ray experiments compared to percentages of the 181 Crab nebula's emission and dark matter annihilation. Solid lines present 182 estimated sensitivities to power law spectra [FACT CHECK THIS] for each 183 experiment. Green lines are Fermi-LAT sensitivities where lighter green is 184 the sensitivity to the galactic center and dark green is its sensitivity to higher 185 declinations. Orange, red, and purple solid lines represent the MAGIC, HESS, 186 and VERITAS 50 hour sensitivities respectively. The maroon and brown lines 187 are the HAWC 1 year and 5 year sensitivities. Across four decades of gamma- 188 ray energy, these experiments have similar sensitivities on the order 10^{-12} 189 $\text{erg cm}^{-2}\text{s}^{-1}$. The dotted lines are estimated dark matter fluxes assuming 190 $m_\chi = 5 \text{ TeV}$ DM annihilating to bottom quarks (red), tau leptons (blue), 191 and W bosons (green). Faded gray lines outline percentage flux of the Crab 192 nebula. Figure is an augmented version of [25]	24

193	Figure 5.2	Effect of Electroweak (EW) corrections on expected DM annihilation spectrum for $\chi\chi \rightarrow W^-W^+$. Solid lines are spectral models that consider EW corrections. Dash-dot lines are spectral models without EW corrections. Red lines are models for $M_\chi = 1$ TeV. Blue lines represent models for $M_\chi = 100$ TeV. All models are sourced from the PPPC4DMID [44].	28
198	Figure 5.3	$\frac{dJ}{d\Omega}$ maps for Segue1 (top) and Coma Berenices (bottom). Origin is centered on the specific dwarf spheroidal galaxies (dSph). X and Y axes are the angular separation from the center of the dwarf. Profile is truncated at the scale radius. Plots of the remaining 11 dSph HAWC studied are linked in Fig. A.1.	30
202	Figure 5.4	Illustration of the combination technique showing a comparison between $-2 \ln \lambda$ provided by four instruments (colored lines) from the observation of the same dSph without any J nuisance and their sum, <i>i.e.</i> the resulting combined likelihood (thin black line). According to the test statistics of Equation (5.7), the intersection of the likelihood profiles with the line $-2 \ln \lambda = 2.71$ indicates the 95% C.L. upper limit on $\langle \sigma v \rangle$. The combined likelihood (thin black line) shows a smaller value of upper limit on $\langle \sigma v \rangle$ than those derived by individual instruments. We also show how the uncertainties on the J factor effects the combined likelihood and degrade the upper limit on $\langle \sigma v \rangle$ (thick black line). All likelihood profiles are normalized so that the global minimum $\widehat{\langle \sigma v \rangle}$ is 0. We note that each profile depends on the observational conditions in which a target object was observed. The sensitivity of a given instrument can be degraded and the upper limits less constraining if the observations are performed in non-optimal conditions such as a high zenith angle or a short exposure time.	36
217	Figure 5.5	39
218	Figure 5.6	HAWC TS values for best fit $\langle \sigma v \rangle$ versus m_χ for seven SM annihilation channels with J factors from \mathcal{GS} . The solid black line shows the combined best fit TS values. The colored, dashed lines are the TS values for each of the 13 sources HAWC studied.	40
222	Figure 5.7	HAWC Brazil bands at 95% confidence level on $\langle \sigma v \rangle$ versus DM mass for seven annihilation channels with J -factors from \mathcal{GS} [55]. The solid line represents the combined limit from 13 dSphs. The dashed line is the expected limit. The green band is the 68% containment. The yellow band is the 95% containment.	41

227	Figure 5.8	Upper limits at 95% confidence level on $\langle \sigma v \rangle$ in function of the DM mass for 228 eight annihilation channels, using the set of J factors from Ref. [55] (\mathcal{GS} set 229 in Table 5.1). The black solid line represents the observed combined limit, 230 the black dashed line is the median of the null hypothesis corresponding 231 to the expected limit, while the green and yellow bands show the 68% and 232 95% containment bands. Combined upper limits for each individual detector 233 are also indicated as solid, colored lines. The value of the thermal relic 234 cross-section in function of the DM mass is given as the red dotted-dashed 235 line [56].	42
236	Figure 5.9	Same as Fig. 5.8, using the set of J factors from Ref. [49, 57] (\mathcal{B} set in Table 5.1).	43
237	Figure 5.10	Comparisons of the combined limits at 95% confidence level for each of the 238 eight annihilation channels when using the J factors from Ref. [55] (\mathcal{GS} set in 239 Table 5.1), plain lines, and the J factor from Ref. [49, 57] (\mathcal{B} set in Table 5.1), 240 dashed lines. The cross-section given by the thermal relic is also indicated [56].	45
241	Figure 5.11	Comparisons of the combined limits at 95% confidence level for a point source 242 analysis and extended source using [55] \mathcal{GS} J-factor distributions and PPPC 243 [44] annihilation spectra. Shown are the limits for Segue1 which will have 244 the most significant impact on the combined limit. 6 of the 7 DM annihilation 245 channels are shown. Solid lines are extended source studies. Dashed lines 246 are point source studies. Overall, the extended source analysis improves the 247 limit by a factor of 2.	47
248	Figure 5.12	Same as Fig. 5.11 on Coma Berenices. This dSph also contributes signifi- 249 cantly to the limit. The limits are identical in this case.	48
250	Figure 5.13	Comparison of combined limits when correcting for HAWC's pointing sys- 251 tematic. All DM annihilation channels are shown. The solid black line is the 252 ratio between published limit to the declination corrected limit. The blue solid 253 line or "Combined_og" represented the limits computed for Glory Duck. The 254 solid orange line or "Combined_ad" represented the limits computed after 255 correcting for the pointing systematic.	49
256	Figure 5.14	Differential map of dJ/Ω from model built in Section 5.8.1 and profiles 257 provided directly from authors. (Top) Differential from Segue1. (bottom) 258 Differential from Coma Berenices. Note that their scales are not the same. 259 Segue1 shows the deepest discrepancies which is congruent with its large 260 uncertainties. Both models show anuli where unique models become apparent.	50

261	Figure 5.15 HAWC limits for Coma Berenices (top) and Segue1 (bottom) for two different 262 map sets. Blue lines are limits calculated on maps with poor model repre- 263 sentation. Orange lines are limits calculated on spatial profiles provided by 264 the authors of [45]. Black line is the ratio of the poor spatial model limits to 265 the corrected spatial models. The left y-axis measures $\langle \sigma v \rangle$ for the blue and 266 orange lines. The right y-axis measures the ratio and is unitless.	51
267	Figure 5.16 Comparisons between the J -factors versus the angular radius for the com- 268 putation of J factors from Ref. [55] (\mathcal{GS} set in Table 5.1) in blue and for 269 the computation from Ref. [49, 57] (\mathcal{B} set in Tab. 5.1) in orange. The solid 270 lines represent the central value of the J -factors while the shaded regions 271 correspond to the 1σ standard deviation.	53
272	Figure 5.17 Comparisons between the J -factors versus the angular radius for the computa- 273 tion of J factors from Ref. [55] (\mathcal{GS} set in Tab. 5.1) in blue and for the 274 computation from Ref. [49, 57] (\mathcal{B} set in Tab. 5.1) in orange. The solid 275 lines represent the central value of the J -factors while the shaded regions 276 correspond to the 1σ standard deviation.	54
277	Figure 6.1 Spectral hypotheses from PPPC [44] and HDM [65] for DM annihilation: 278 $\chi\chi \rightarrow W^-W^+$. Solid lines are spectral models with EW corrections from the 279 PPPC. Dash-dot lines are spectral models from HDM. Red lines are models 280 for $M_\chi = 1$ TeV. Blue lines represent models for $M_\chi = 100$ TeV.	59
281	Figure 6.2 Photon spectra for $\chi\chi \rightarrow \gamma\gamma$ (left) and $\chi\chi \rightarrow ZZ$ (right) after Gaussian 282 convolution of line features. Both spectra have δ -features at photon energies 283 equal to the DM mass. Bluer lines are annihilation spectra with lower DM 284 mass. Redder lines are spectra from larger DM mass. All spectral models are 285 sourced from the Heavy Dark Matter models [65]. Axes are drawn roughly 286 according to the energy sensitivity of HAWC.	60
287	Figure 6.3 $\frac{dJ}{d\Omega}$ maps for Coma Berenices, Draco, Segue1, and Sextans. Columns are 288 divided for the $\pm 1\sigma$ uncertainties in $dJ/d\Omega$ around the mean value from \mathcal{LS} 289 [66]. Origin is centered on the specific dwarf spheroidal galaxies (dSph). θ 290 and ϕ axes are the angular separation from the center of the dwarf. Profiles 291 are truncated at 1° and flattened beyond.	62
292	Figure 6.4 Infographic on how jobs and DM computation was organized in Section 5.3. 293 Jobs were built for each permutation of CHANS and SOURCES shown by the 294 left block in the figure. Each job, which took on the order 2 hrs to compute, 295 had the following work flow: 1. Import HAWC analysis software, 2 min to 296 run. 2. Load HAWC count maps, 5 min to run. 3. Load HAWC energy and 297 spatial resolutions, 4 min. 5. Load DM spatial source templates and spectral 298 models, less than 1 s. 6. Perform likelihood fit on data and model, about 8 299 min per DM mass. 7. Write results to file, less than 1s.	64

300	Figure 6.5	Graphic of Gustafson parallel coding pattern. f_s is the fraction of a program, in time, spent on serial computation. f_p is the fraction of computing time that is parallelizable. T_p is the total time for a parallel program to run. T_1 is the total time for a parallel program to run if only 1 processor is allocated. P_N is the N -th processor where it's row is the computation the processor performs. The Gustafson pattern is most similar to what is implemented for this analysis. Figure is pulled from [68].	65
307	Figure 6.6	Task chart for one multithreaded job developed for this project. Green blocks indicate a shared resource across the threads AND computation performed serially. Red blocks indicate functional parallel processing within each thread. 3 threads are represented here, yet many more can be employed during the full analysis. Jobs are defined by the SOURCE as these require unique maps to be loaded into the likelihood estimator. The m_χ , CHAN, and $\langle\sigma v\rangle$ variables are entered into the thread pool and allocated as evenly as possible across the threads.	67
315	Figure 6.7	HAWC upper limits at 95% confidence level on $\langle\sigma v\rangle$ versus m_χ for $\chi\chi \rightarrow b\bar{b}, t\bar{t}, u\bar{u}, d\bar{d}, s\bar{s}, c\bar{c}, gg, W^+W^-$, and hh . Limits are with \mathcal{LS} J-factors [66]. The solid line represents the observed combined limit. Dashed lines represent limits from individual dSphs.	70
319	Figure 6.8	HAWC upper limits at 95% confidence level on $\langle\sigma v\rangle$ versus m_χ for $\chi\chi \rightarrow \nu_e\bar{\nu}_e, \nu_\mu\bar{\nu}_\mu, \nu_\tau\bar{\nu}_\tau, e\bar{e}, \mu\bar{\mu}, \tau\bar{\tau}, \gamma\gamma$ and ZZ . Limits use \mathcal{LS} J-factors [66]. The solid line represents the observed combined limit. Dashed lines represent limits from individual dSphs.	71
323	Figure 6.9	HAWC TS values for best fit $\langle\sigma v\rangle$ versus m_χ for SM annihilation channels: $\chi\chi \rightarrow b\bar{b}, t\bar{t}, u\bar{u}, d\bar{d}, s\bar{s}, c\bar{c}, gg, W^+W^-$, and hh . Limits use \mathcal{LS} J-factors. The solid black line shows the combined best fit TS values. The colored, dashed lines are the TS values from each dSph.	72
327	Figure 6.10	HAWC TS values for best fit $\langle\sigma v\rangle$ versus m_χ for SM annihilation channels: $\chi\chi \rightarrow \nu_e\bar{\nu}_e, \nu_\mu\bar{\nu}_\mu, \nu_\tau\bar{\nu}_\tau, e\bar{e}, \mu\bar{\mu}, \tau\bar{\tau}, \gamma\gamma$ and ZZ . Limits use \mathcal{LS} J-factors. The solid black line shows the combined best fit TS values. The colored, dashed lines are the TS values from each dSph.	73
331	Figure 6.11	Comparison of HAWC limits from this analysis to Glory Duck (Fig. 5.5) for 3 dSphs and 3 DM annihilation channels: $b\bar{b}, \tau\bar{\tau}$, and $e\bar{e}$. Each sector shows the 95% confidence limit from Glory Duck (blue line) and this analysis (orange line) in the top plot. The lower plot features the ratio in log scale of Glory Duck to this analysis in a red solid line. Horizontal dashed lines are for ratios of 1.0 (black) and $\sqrt{2}$ (blue). Ratios larger than 1.0 are for limits smaller, or stricter, than Glory Duck. Ratios larger than $\sqrt{2}$ indicates limits are stricter than a simple doubling of the Glory Duck data.	75

339	Figure 7.1	Neutrino spectra at production (left panels) and after oscillation at Earth 340 (right panels). Blue, orange, and green lines are the ν_e , ν_μ , and ν_τ spectra 341 respectively. Top panels show the spectra in $\frac{dN}{dE}$. Lower panels plot the flavor 342 ratio to $\nu_e + \nu_\mu + \nu_\tau$. SM annihilation channels $b\bar{b}$, $\tau\bar{\tau}$, and $\nu_\mu\bar{\nu}_\mu$ are shown 343 for $M_\chi = 1$ PeV, TeV, and EeV.	80
344	Figure 7.2	Signal recovery for 100 TeV DM annihilation into $\nu_\mu\bar{\nu}_\mu$ for a source at Dec 345 = 16.06° . n_{inj} is the number of injected signal events in simulation. n_s is 346 the number of reconstructed signal events from the simulation. Although 347 the uncertainties are small and tight, the reconstructed n_s are systematically 348 underestimated.	81
349	Figure 7.3	Left panel shows the two kernels overlaying the original spectrum from 350 χ arony after propagation to Earth [71]. The vertical red line indicates where 351 the original neutrino line is maximized. Blue line is the output from χ aroy. 352 Green line is the spectrum after convolution with a flat kernel. Orange line 353 is the spectrum after Gaussian convolution. Right panel shows the signal 354 recovery of the spectral model using the Gaussian kernel with parameters 355 enumerated above.	82
356	Figure 7.4	Example spline that failed the fit. Failed splined are corrected on a case by 357 case basis unless the SM channel has a systematic problem fitting the splines. 358 In this case, I made a bookkeeping error and loaded the incorrect spectral model	84
359	Figure 7.5	Summary of input spectral models that were smoothed with Gaussian kernel. 360 Spectral models are for $\chi\chi \rightarrow e\bar{e}$, $\mu\bar{\mu}\tau\bar{\tau}$, $\nu_e\bar{\nu}_e$, $\nu_\mu\bar{\nu}_\mu$, and $\nu_\tau\bar{\nu}_\tau$. These spectra 361 are the composite ($\nu_\mu + \nu_\tau$) of neutrino flavors. Every spectral model used for 362 this analysis is featured as a colored solid line. Bluer lines are for lower DM 363 mass spectral models. DM masses range from 681 GeV to 100 PeV. HDM 364 [65], χ aroy [71], and Photospline [75] are used to generate these spectra. 365 Energy (x-axis) was chosen to roughly represent the energy sensitivity of NST. .	85
366	Figure 7.6	Test statistic (TS) distributions for Segue 1 and $\chi\chi \rightarrow b\bar{b}$. Each subplot, 367 except the final, is the TS distribution for a specific DM mass listed in the 368 subplot. Orange dashed lines are the traces for a χ^2 distribution with 1 degree 369 of freedom. $\epsilon[\cdot]$ is the fraction of trials smaller than the bracketed value. The 370 final subplot plots the all DM spectral models, similar to Fig. 7.5, used as 371 input for the TS distributions.	88
372	Figure 7.7	Same as Fig. 7.6 for Segue 1 $\chi\chi \rightarrow \tau\bar{\tau}$	89
373	Figure 7.8	Same as Fig. 7.6 for Segue 1 $\chi\chi \rightarrow \nu_\mu\bar{\nu}_\mu$	90
374	Figure 7.9	Same as Fig. 7.6 for Ursa Major II 1 $\chi\chi \rightarrow b\bar{b}$	91
375	Figure 7.10	Same as Fig. 7.6 for Ursa Major II 1 $\chi\chi \rightarrow \tau\bar{\tau}$	92

376	Figure 7.11 Same as Fig. 7.6 for Ursa Major II 1 $\chi\chi \rightarrow \nu_\mu\bar{\nu}_\mu$	93
377	Figure 7.12 Same as Fig. 7.6 for 15, \mathcal{GS} J -factor, stacked sources and $\chi\chi \rightarrow b\bar{b}$	94
378	Figure 7.13 Same as Fig. 7.6 for 15, \mathcal{GS} J -factor, stacked sources and $\chi\chi \rightarrow t\bar{t}$	95
379	Figure 7.14 Same as Fig. 7.6 for 15, \mathcal{GS} J -factor, stacked sources and $\chi\chi \rightarrow u\bar{u}$	96
380	Figure 7.15 Same as Fig. 7.6 for 15, \mathcal{GS} J -factor, stacked sources and $\chi\chi \rightarrow d\bar{d}$	97
381	Figure 7.16 Same as Fig. 7.6 for 15, \mathcal{GS} J -factor, stacked sources and $\chi\chi \rightarrow e\bar{e}$	98
382	Figure 7.17 Same as Fig. 7.6 for 15, \mathcal{GS} J -factor, stacked sources and $\chi\chi \rightarrow \mu\bar{\mu}$	99
383	Figure 7.18 Same as Fig. 7.6 for 15, \mathcal{GS} J -factor, stacked sources and $\chi\chi \rightarrow \tau\bar{\tau}$	100
384	Figure 7.19 Same as Fig. 7.6 for 15, \mathcal{GS} J -factor, stacked sources and $\chi\chi \rightarrow W^+W^-$	101
385	Figure 7.20 Same as Fig. 7.6 for 15, \mathcal{GS} J -factor, stacked sources and $\chi\chi \rightarrow ZZ$	102
386	Figure 7.21 Same as Fig. 7.6 for 15, \mathcal{GS} J -factor, stacked sources and $\chi\chi \rightarrow \nu_e\bar{\nu}_e$	103
387	Figure 7.22 Same as Fig. 7.6 for 15, \mathcal{GS} J -factor, stacked sources and $\chi\chi \rightarrow \nu_\mu\bar{\nu}_\mu$	104
388	Figure 7.23 Signal Recovery study for an analysis with 15 stacked sources using the \mathcal{GS} 389 J -factors [45]. Each panel block represents 14 studies for DM mass ranging 390 between 1 TeV and 20 PeV and one annihilation channel. Panel block is for 391 $\nu_\mu\bar{\nu}_\mu$. Each panel block features every spectral model used as input in the 392 bottom-right subpanel. The remaining panels show n_{inj} as the number of 393 signal events injected into background simulation. Whereas, n_s is the number 394 of signal events recovered from analyzing the injected simulation. Blue line 395 represents the median values of 100 simulations. Light blue bands show the 396 1σ statistical uncertainty around the median.	106
397	Figure 7.24 Same as Fig. 7.23 but for $\chi\chi \rightarrow t\bar{t}$ (top) and $b\bar{b}$ (bottom).	107
398	Figure 7.25 IceCube North Sky Track Sensitivities. Each panel shows sensitivity curves 399 for a specific DM annihilation channel. Sensitivities are for the velocity- 400 weighted cross-section $\langle\sigma v\rangle$ versus m_χ . Dotted, colored lines are sensitivities 401 for individual sources. Solid white lines are for the combined sensitivity of 402 all 15 \mathcal{GS} sources used in this study.	111
403	Figure 7.26 Same as Fig. 7.25 for three additional DM annihilation channels.	112

404	Figure 7.27 Panel A: Neutrino's from the Northern sky and incident on the IceCube 405 detector will travel through the Earth. How much of the Earth these neutrinos 406 travels is a function of zenith from the vertical axis. Panel B: SM precision of 407 neutrino transmission probabilities for neutrinos arriving at $90^\circ - 180^\circ$ zenith 408 and with 100 GeV to 100 PeV energies. High-energy neutrinos traverseing 409 the whole Earth are completely absorbed, whereas low-energy neutrinos pass 410 through unimpeded. Neutrinos coming from above the horizon will arrive 411 unimpeded for all neutrino energies. Figure pulled from [76].	113
412	Figure 7.28 $\langle\sigma v\rangle$ sensitivities for 5 imaginary sources with $\log_{10} J = 19.42 \log_{10}(\text{GeV}^2\text{cm}^{-5})$. 413 Each imaginary source shares a declination with a source in Tab. 5.1	113
414	Figure A.1 Sister figure to Figure 5.3. Sources in the first row from left to right: Bootes 415 I, Canes Venatici I, II. In second row: Draco, Hercules, Leo I. In the first row: 416 Leo II, Leo IV, Sextans. In the final row: Ursa Major I, Ursa Major II.	115
417	Figure B.1 Sister figure to Figure 6.2 for remaining SM primary annihilation channels 418 studied for this thesis. These did not require any post generation smoothing 419 and so are directly pulled from [65] with a binning scheme most helpful for a 420 HAWC analysis.	116
421	Figure B.2 Comparison of HAWC limits from this analysis to Glory Duck (Fig. 5.5) for 422 Coma Berenices and 7 DM annihilation channels.	126
423	Figure B.3 Same as Fig. B.2 but for Segue 1.	127
424	Figure B.4 Same as Fig. B.2 but for Sextans.	128
425	Figure C.1 Current status of spline tables according to contraints defined by Tab. 7.1. 426 Green splines are splines that passed under the GOOD tolerance. Yellow 427 are splines that are OK. Red are splines that FAIL. All yellow splines were 428 inspected individually before running the analysis. Splines were made for the 429 μ (PID 14; top panel) flavor and τ (PID 16; bottom panel) neutrino flavors.	132
430	Figure C.2 Sister figure to Fig. 7.5 for annihilation channels that did not require kernel 431 smoothing. These spectra are the composite ($\nu_\mu + \nu_\tau$) of neutrino flavors. 432 Every spectral model used for this analysis is featured as a colored solid line. 433 Bluer lines are for lower DM mass spectral models. DM masses range from 434 681 GeV to 100 PeV.	133
435	Figure C.3 Same as Fig. 7.23 but for Segue 1 and $\chi\chi \rightarrow b\bar{b}$	134
436	Figure C.4 Same as Fig. 7.23 but for Segue 1 and $\chi\chi \rightarrow t\bar{t}$	135
437	Figure C.5 Same as Fig. 7.23 but for Segue 1 and $\chi\chi \rightarrow \nu_\mu\bar{\nu}_\mu$	136

438	Figure C.6 Same as Fig. 7.23 but for Ursa Major II and $\chi\chi \rightarrow b\bar{b}$.	137
439	Figure C.7 Same as Fig. 7.23 but for Ursa Major II and $\chi\chi \rightarrow t\bar{t}$.	138
440	Figure C.8 Same as Fig. 7.23 but for Ursa Major II and $\chi\chi \rightarrow \nu_\mu\bar{\nu}_\mu$.	139
441	Figure C.9 IceCube North Sky Track Sensitivities for $n_s/\langle N \rangle$. n_s values are the counts fed into Eq. (7.8) to produce Fig. 7.25 and Fig. 7.26.	140
443	Figure C.10 Same as Fig. C.9 for three additional DM annihilation channels.	141

LIST OF ABBREVIATIONS

- 445 **MSU** Michigan State University
446 **LANL** Los Alamos National Laboratory
447 **DM** Dark Matter
448 **SM** Standard Model
449 **HAWC** High Altitude Water Cherenkov Observatory
450 **dSph** Dwarf Spheroidal Galaxy

451

CHAPTER 1

INTRODUCTION

452 Is the text not rendering right? Ah ok it knows im basically drafting the doc still

CHAPTER 2

453

DARK MATTER IN THE COSMOS

454 **2.1 Introduction**

455 The dark matter problem can be summarized in part by the following thought experiment.

456 Let us say you are the teacher for an elementary school classroom. You take them on a field
457 trip to your local science museum and among the exhibits is one for mass and weight. The exhibit
458 has a gigantic scale, and you come up with a fun problem for your class.

459 You ask your class, "What is the total weight of the classroom? Give your best estimation to
460 me in 30 minutes, and then we'll check your guess on the scale. If your guess is within 10% of the
461 right answer, we will stop for ice cream on the way back."

462 The students are ecstatic to hear this, and they get to work. The solution is some variation of
463 the following strategy. The students should give each other their weight or best guess if they do
464 not know. Then, all they must do is add each student's weight and get a grand total for the class.

465 The measurement on the giant scale should show the true weight of the class. When comparing
466 the measured weight to your estimation, multiply the measurement by 1.0 ± 0.1 to get the $\pm 10\%$
467 tolerances for your estimation.

468 Two of your students, Sandra and Mario, return to you with a solution.

469 They say, "We weren't sure of everyone's weight. We used 65 lbs. for the people we didn't
470 know and added everyone who does know. There are 30 of us, and we got 2,000 lbs.! That's a ton!"

471 You estimated 1,900 lbs. assuming the average weight of a student in your class was 60 lbs.
472 So, you are pleased with Sandra's and Mario's answer. You instruct your students to all gather on
473 the giant scale and read off the weight together. To all your surprise, the scale reads *10,000 lbs.*!
474 10,000 is significantly more than a 10% error from 2,000. In fact, it is approximately 5 times more
475 massive than either your or your students' estimates. You think to yourself and conclude there
476 must be something wrong with the scale. You ask an employee to check the scale and verify it is
477 well calibrated. They confirm that the scale is in working order. You weigh a couple of students
478 individually to assess that the scale is well calibrated. Sandra weighs 59 lbs., and Mario weighs

479 62 lbs., typical weights for their age. You then weigh each student individually and see that their
480 weights individually do not deviate greatly from 60 lbs. So, where does all the extra weight come
481 from?

482 This thought experiment serves as an analogy to the Dark Matter problem. The important
483 substitution to make however is to replace the students with stars and the classroom with a galaxy,
484 say the Milky Way. Individually the mass of stars is well measured and defined with the Sun as our
485 nearest test case. However, when we set out to measure the mass of a collection of stars as large as
486 galaxies, our well-motivated estimation is wildly incorrect. There simply is no way to account for
487 this discrepancy except without some unseen, or dark, contribution to mass and matter in galaxies.
488 I set out in my thesis to narrow the possibilities of what this Dark Matter could be.

489 This chapter is organized like the following... **TODO: Text should look like ... Chapter x has**
490 **blah blah blah.**

491 2.2 Dark Matter Basics

492 Presently, a more compelling theory of cosmology that includes Dark Matter (DM) in order
493 to explain a variety of observations is Λ Cold Dark Matter, or Λ CDM. I present the evidence
494 supporting Λ CDM in Section 2.3 yet discuss the conclusions of the Λ CDM model here. According
495 to Λ CDM fit to observations on the Cosmic Microwave Background (CMB), DM is 26.8% of the
496 universe's current energy budget. Baryonic matter, stuff like atoms, gas, and stars, contributes to
497 4.9% of the universe's current energy budget [1, 2, 3].

498 DM is dark; it does not interact readily with light at any wavelength. DM also does not interact
499 noticeably with the other standard model forces (Strong and Weak) at a rate that is readily observed
500 [3]. DM is cold, which is to say that the average velocity of DM is below relativistic speeds [1].
501 'Hot' DM would not likely manifest the dense structures we observe like galaxies, and instead
502 would produce much more diffuse galaxies than what is observed [3, 1]. DM is old; it played a
503 critical role in the formation of the universe and the structures within it [1, 2].

504 Observations of DM have so far been only gravitational. The parameter space available to what
505 DM could be therefore is extremely broad. The broad DM parameter space is iteratively tested in

506 DM searches by supposing a hypothesis that has not yet been ruled out and performing observations
507 to test them. When the observations yield a null result, the parameter space is constrained further.
508 I present some approaches for DM searches in Section 2.4.

509 **2.3 Evidence for Dark Matter**

510 Dark Matter (DM) has been a looming problem in physics for almost 100 years. Anomalies
511 have been observed by astrophysicists in galactic dynamics as early as 1933 when Fritz Zwicky
512 noticed unusually large velocity dispersion in the Coma cluster. Zwicky's measurement was the
513 first recorded to use the Virial theorem to measure the mass fraction of visible and invisible matter
514 in celestial bodies [4]. From Zwicky in [5], "*If this would be confirmed, we would get the surprising*
515 *result that dark matter is present in much greater amount than luminous matter.*" Zwicky's and
516 others' observation did not instigate a crisis in astrophysics because the measurements did not
517 entirely conflict with their understanding of galaxies [4]. In 1978, Rubin, Ford, and Norbert
518 measured rotation curves for ten spiral galaxies [6]. Rubin et al.'s 1978 publication presented a
519 major challenge to the conventional understanding of galaxies that could no longer be dismissed by
520 measurement uncertainties. Evidence has been mounting ever since for this exotic form of matter.
521 The following subsections provide three compelling pieces of evidence in support of the existence
522 of DM.

523 **2.3.1 First Clues: Stellar Velocities**

524 Zwicky, and later Rubin, measured the stellar velocities of various galaxies to estimate their
525 virial mass. The Virial Theorem upon which these observations are interpreted is written as

$$2T + V = 0. \quad (2.1)$$

526 Where T is the kinetic energy and V is the potential energy in a self-gravitating system. The
527 classical Newton's law of gravity from stars and gas was used for gravitational potential modeled in
528 the observed galaxies:

$$V = -\frac{1}{2} \sum_i \sum_{j \neq i} \frac{m_i m_j}{r_{ij}}. \quad (2.2)$$

529 Zwicky et al. measured just the velocities of stars apparent in optical wavelengths [5]. Rubin et al.
 530 added by measuring the velocity of the hydrogen gas via the 21 cm emission line of Hydrogen [6].
 531 The velocities of the stars and gas are used to infer the total mass of galaxies and galaxy clusters
 532 via Equation (2.1). An inferred mass is obtained from the luminosity of the selected sources. The
 533 two inferences are compared to each other as a luminosity to mass ratio which typically yielded [1]

$$\frac{M}{L} \sim 400 \frac{M_{\odot}}{L_{\odot}} \quad (2.3)$$

534 M_{\odot} and L_{\odot} referring to stellar mass and stellar luminosity, respectively. These ratios clearly indicate
 535 a discrepancy in apparent light and mass from stars and gas and their velocities.

536 Rubin et al. [6] demonstrated that the discrepancy was unlikely to be an underestimation of
 537 the mass of the stars and gas. The inferred "dark" mass was up to 5 times more than the luminous
 538 mass. This dark mass also needed to extend well beyond the extent of the luminous matter.

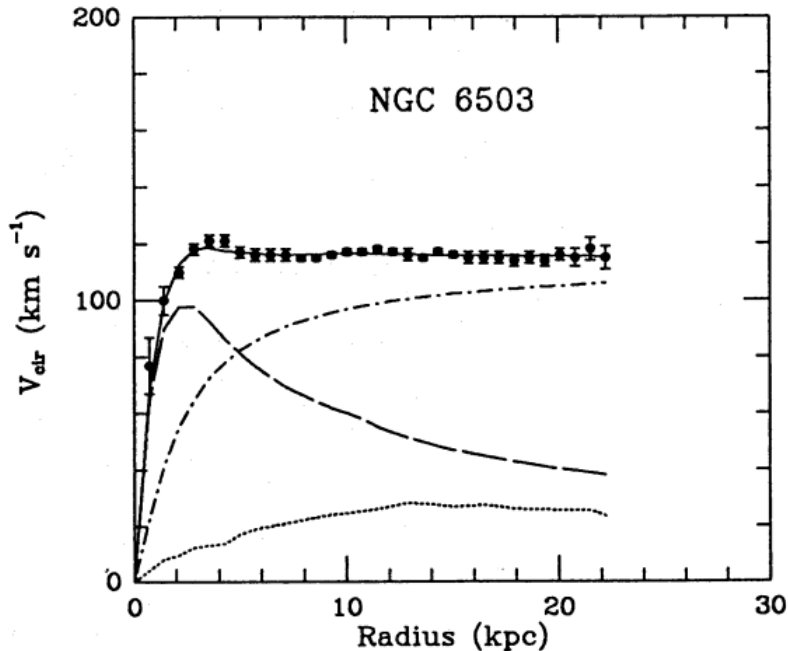


Figure 2.1 Rotation curve fit to NGC 6503 from [7]. Dashed line is the contribution from visible matter. Dotted curves are from gas. Dash-dot curves are from dark matter (DM). Solid line is the composite contribution from all matter and DM sources. Data are indicated with bold dots with error bars. Data agree strongly with a matter + DM composite prediction.

539 Figure 2.1 features one of many rotation curves plotted from the stellar velocities within galaxies.

540 The measured rotation curves mostly feature a flattening of velocities at higher radius which is not
541 expected if the gravity was only coming from gas and luminous matter. The extension of the
542 flat velocity region also indicates that the DM is distributed far from the center of the galaxy.
543 Modern velocity measurements include significantly larger objects, galactic clusters, and smaller
544 objects, dwarf galaxies. Yet, measurements along this regime are leveraging the Virial theorem
545 with Newtonian potential energies. We know Newtonian gravity is not a comprehensive description
546 of gravity. New observational techniques have been developed since 1978, and those are discussed
547 in the following sections.

548 **2.3.2 Evidence for Dark Matter: Gravitational Lensing**

549 Modern evidence for dark matter comes from new avenues beyond stellar velocities. Grav-
550 itational lensing from DM is a new channel from general relativity. General relativity predicts
551 aberrations in light caused by massive objects. In recent decades we have been able to measure the
552 lensing effects from compact objects and DM halos. Figure 2.2 shows how different massive ob-
553 jects change the final image of a faraway galaxy resulting from gravitational lensing. Gravitational
554 lensing developed our understanding of dark matter in two important ways.

555 Gravitational lensing provides additional compelling evidence for DM. The observation of two
556 merging galactic clusters in 2006, shown in Figure 2.3, provided a compelling argument for DM
557 outside the Standard Model. These clusters merged recently in astrophysical time scales. Galaxies
558 and star cluster have mostly passed by each other as the likelihood of their collision is low. Therefore,
559 these massive objects will mostly track the highest mass, dark and/or baryonic, density. Yet, the
560 intergalactic gas is responsible for the majority of the baryonic mass in the systems [4]. These gas
561 bodies will not phase through and will heat up as they collide together. The hot gas is located via
562 x-ray emission from the cluster. Two observations of the clusters were performed independently of
563 each other.

564 The first was the lensing of light around the galaxies due to their gravitational influences.
565 When celestial bodies are large enough, the gravity they exert bends space and time itself. The
566 warped space-time lenses light and will deflect in an analogous way to how glass lenses will bend

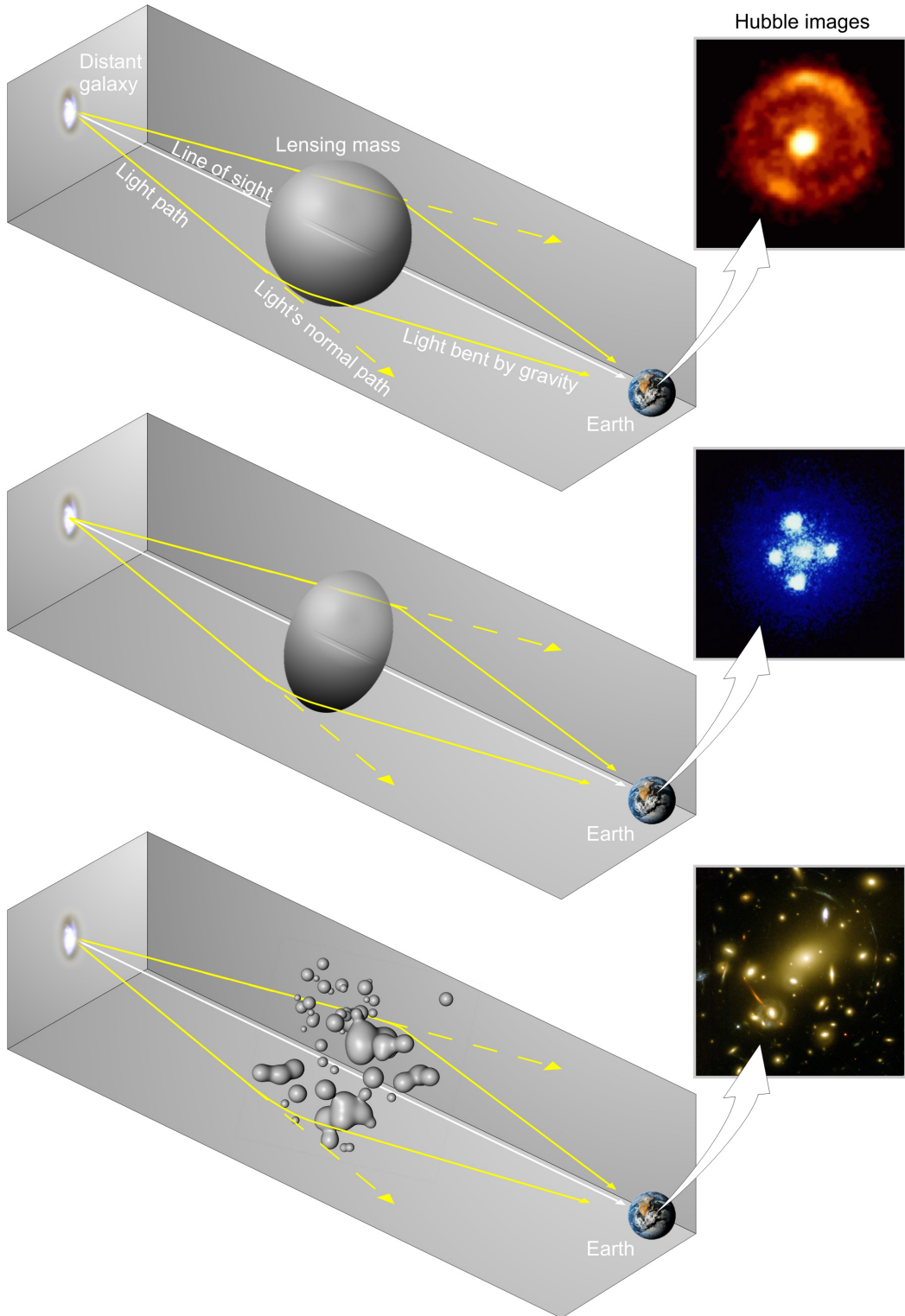


Figure 2.2 Light from distant galaxy is bent in unique ways depending on the distribution of mass between the galaxy and Earth. Yellow dashed lines indicate where the light would have gone if the matter were not present [8].

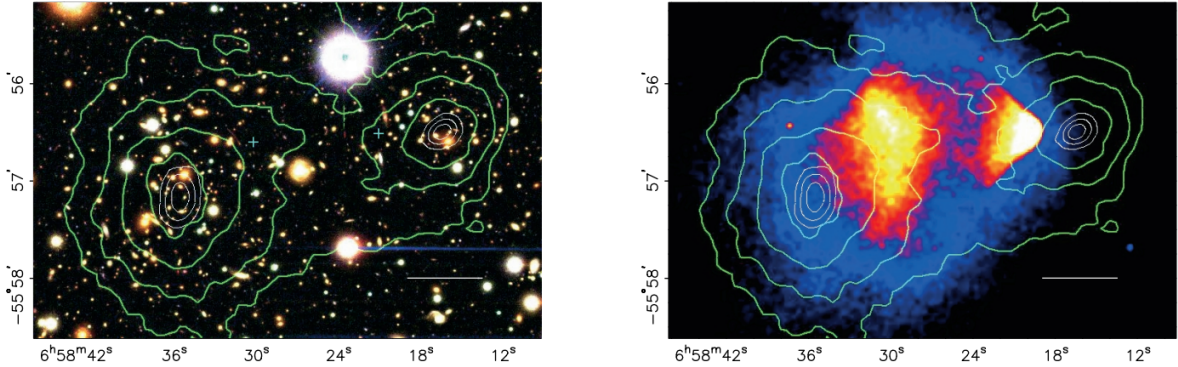


Figure 2.3 (left) Optical image of galactic cluster 1E0657-558. (right) X-ray image of the cluster with redder meaning hotter and higher baryon density. (both) Green contours are reconstruction of gravity contours from weak lensing. White rings are the best fit mass maxima at 68.3%, 95.5%, and 99.7% confidence. The matter maxima of the clusters are clearly separated from x-ray maxima. [9]

567 light, see Figure 2.2. With a sufficient understanding of light sources behind a massive object, we
 568 can reconstruct the contours of the gravitational lenses. The gradient of the contours shown in
 569 Figure 2.3 then indicates how dense the matter is and where it is.

570 The x-ray emission can then be observed from the clusters. Since these galaxies are mostly gas
 571 and are merging, then the gas should be getting hotter. If they are merging, the x-ray emissions
 572 should be the strongest where the gas is mostly moving through each other. Hence, X-ray emission
 573 maps out where the gas is in the merging galaxy cluster.

574 The lensing and x-ray observations were done on the Bullet cluster featured on Figure 2.3.
 575 The x-ray emissions do not align with the gravitational contours from lensing. The incongruence
 576 in mass density and baryon density suggests that there is a lot of matter somewhere that does
 577 not interact with light. Moreover, this dark matter cannot be baryonic [9]. The Bullet Cluster
 578 measurement did not really tell us what DM is exactly, but it did give the clue that DM also does
 579 not interact with itself very strongly. If DM did interact strongly with itself, then it would have been
 580 more aligned with the x-ray emission [9]. There have been follow-up studies of galaxy clusters with
 581 similar results. The Bullet Cluster and others like it provide a persuasive case against something
 582 possibly amiss in our gravitational theories.

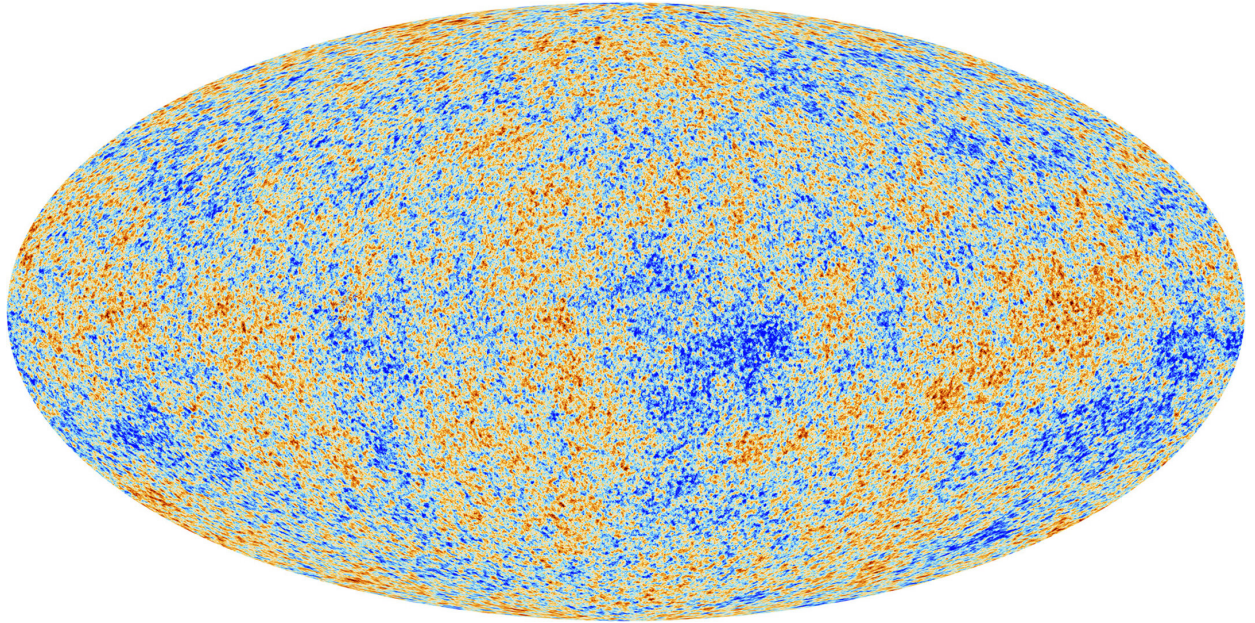


Figure 2.4 Plank CMB sky. Sky map features small variations in temperature in primordial light. These anisotropies are used to make inferences about the universe's energy budget and developmental history. [10]

583 **2.3.3 Evidence for Dark Matter: Cosmic Microwave Background**

584 The Cosmic Microwave Background (CMB) is the primordial light from the early universe
585 when Hydrogen atoms formed from the free electron and proton soup in the early universe. The
586 CMB is the earliest light we can observe; released when the universe was about 380,000 years old.
587 Then we look at how the simulated universes look like compared to what we see. Figure 2.4 is the
588 most recent CMB image from the Plank satellite after subtracting the average value and masking the
589 galactic plane [10]. Redder regions indicate a slightly hotter region in the CMB, and blue indicates
590 colder. The intensity variations are on the order of 1 in 1000 with respect to the average value.

591 The Cosmic Microwave Background shows that the universe had DM in it from an incredibly
592 early stage. To measure the DM, Dark Energy, and matter fractions of the universe from the CMB,
593 the image is analyzed into a power spectrum, which shows the amplitude of the fluctuations as
594 a function of spherical multipole moments. Λ CDM provides the best fit to the power spectra of
595 the CMB as shown in Figure 2.5. The CMB power spectrum is quite sensitive to the fraction
596 of each energy contribution in the early universe. Low l modes are dominated by variations
597 in gravitational potential. Intermediate l emerge from oscillations in photon-baryon fluid from

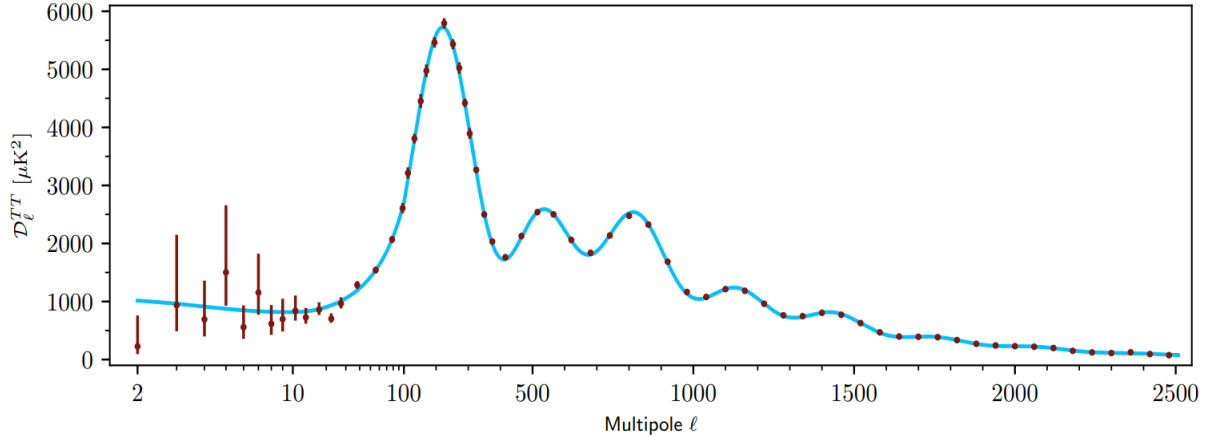


Figure 2.5 Observed Cosmic Microwave Background power spectrum as a function of multipole moment from Plank [10]. Blue line is best fit model from Λ CDM. Red points and lines are data and error, respectively.

598 competing baryon pressures and gravity. High l is a damped region from the diffusion of photons
 599 during electron-proton recombination. [1]

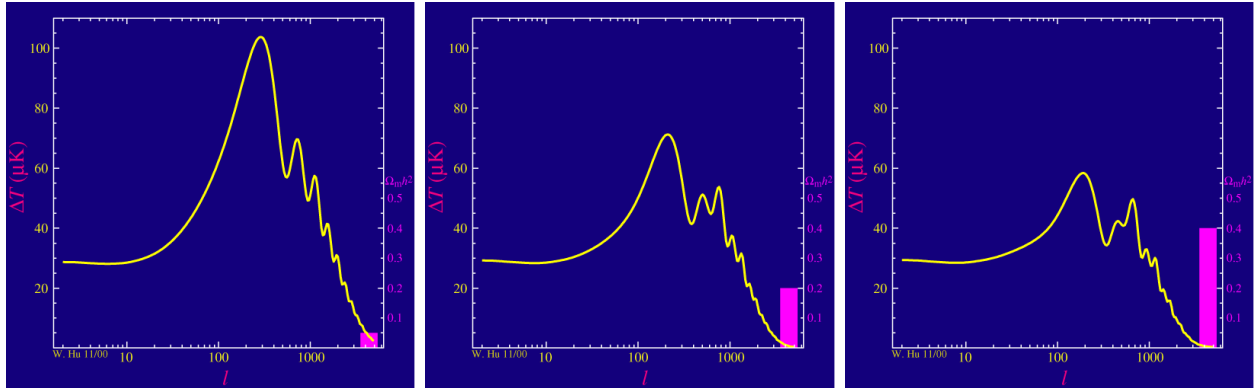


Figure 2.6 Predicted power spectra of CMB for different $\Omega_m h^2$ values for fixed baryon density from [11]. (left) Low $\Omega_m h^2$ increases the prominence of first and second peaks. (middle) $\Omega_m h^2$ is most similar to the observed power spectrum. The second and third peaks are similar in height. (right) $\Omega_m h^2$ is large which suppresses the first peak and raises the prominence of the third peak.

600 The harmonics would look quite different for a universe with less DM. Figure 2.6 demonstrates
 601 the effect $\Omega_m h^2$ has on the expected power spectrum for fixed baryon matter density. [11] Sweeping
 602 $\Omega_m h^2$ in this way clearly shows the effect dark matter has on the CMB power spectrum. The
 603 observations fit well with the Λ CDM model, and the derived fractions are as follows. The matter
 604 fraction: $\Omega_m = 0.3153$; and the baryon fraction: $\Omega_b = 0.04936$ [10]. Plank's observations also
 605 provide a measure of the Hubble constant, H_0 . H_0 especially has seen a growing tension in the

606 past decade that continues to deepened with observations from instruments like the James Webb
607 Telescope [12, 13]. As Hubble tensions deepen, we may find that perhaps Λ **CDM**, despite its
608 successes, is missing some critical physics.

609 Overall, the Newtonian motion of stars in galaxies, weak lensing from galactic clusters, and
610 power spectra from primordial light form a compelling body of research in favor of dark matter.
611 It takes another leap of theory and experimentation to make observations of DM that are non-
612 gravitational in nature. In Section 2.3, the evidence for DM implies strongly that the DM is matter
613 and not a lost parameter in the gravitational fields between massive objects. Finally, if we take one
614 axiom: that this matter has quantum behavior, such as being described by some Bohr wavelength
615 and abiding by some fermion or boson statistics; then we arrive at particle dark matter. One particle
616 DM hypothesis is the Weakly Interacting Massive Particle (WIMP). This DM candidate theory is
617 discussed further in the next section and is the focus of this thesis.

618 **2.4 Searching for Dark Matter: Particle DM**

619 Section 2.4 shows the Standard Model of particle physics and is currently the most accurate
620 model for the dynamics of fundamental particles like electrons and photons. The current status
621 of the SM does not have a viable DM candidate. When looking at the standard model, we can
622 immediately exclude any charged particle because charged particles interact strongly with light.
623 Specifically, this will rule out the following charged, fundamental particles: $e, \mu, \tau, W, u, d, s, c, t, b$
624 and their corresponding antiparticles. Recalling from Section 2.2 that DM must be long-lived and
625 stable over the age of the universe which excludes all SM particles with decay half-lives at or shorter
626 than the age of the universe. The lifetime constraint additionally eliminates the Z and H bosons.
627 Finally, the candidate DM needs to be somewhat massive. Recall from Section 2.2 that DM is cold
628 or not relativistic through the universe. This eliminates the remaining SM particles: $\nu_{e,\mu,\tau}, g, \gamma$ as
629 DM candidates. Because there are no DM candidates within the SM, the DM problem strongly
630 hints to physics beyond the SM (BSM).

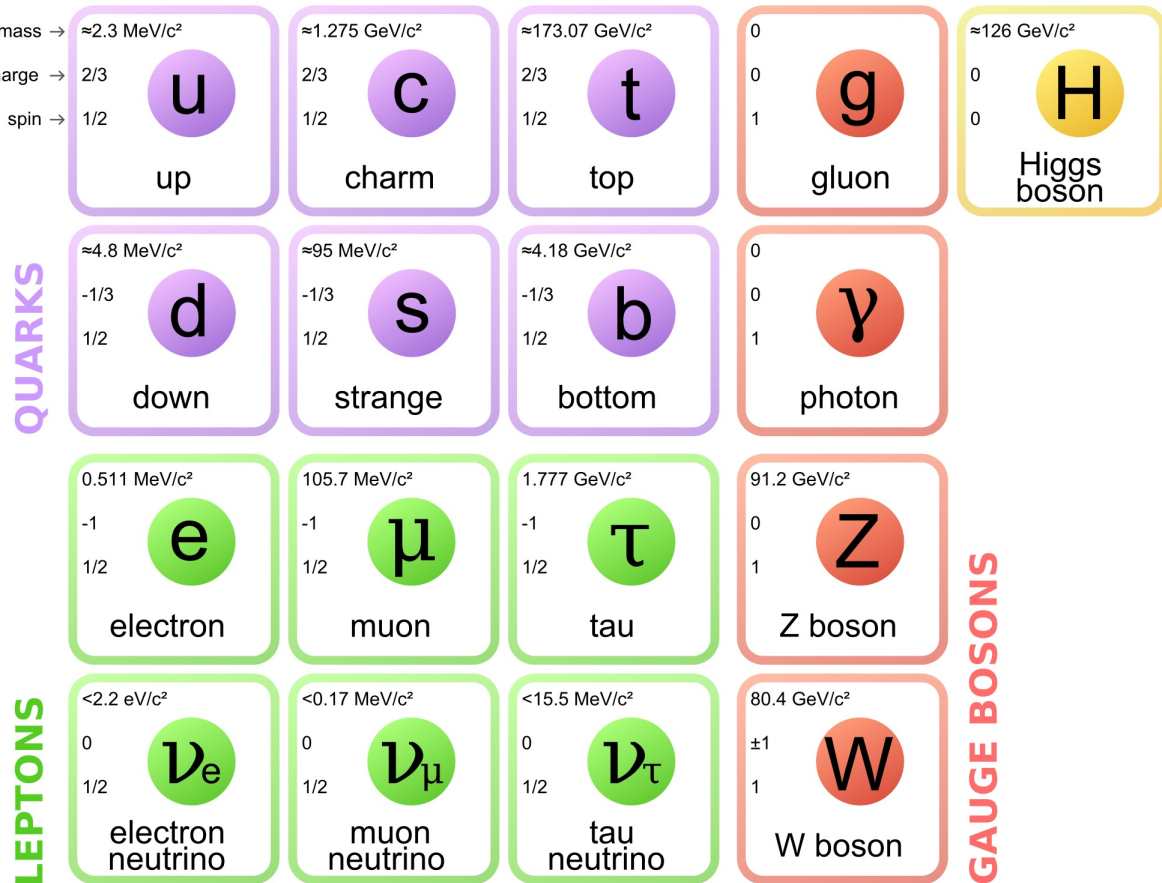


Figure 2.7 The Standard Model (SM) of particle physics. Figure taken from <http://www.quantumdiaries.org/2014/03/14/the-standard-model-a-beautiful-but-flawed-theory/>

631 2.4.1 Shake it, Break it, Make it

632 When considering DM that couples in some way with the SM, the interactions are roughly
 633 demonstrated by interaction demonstrated in Figure 2.8. The figure is a simplified Feynman
 634 diagram where the arrow of time represents the interaction modes of: **Shake it, Break it, Make it.**
 635 **Shake it** refers to the direct detection of dark matter. Direct detection interactions start with
 636 a free DM particle and an SM particle. The DM and SM interact via elastic or inelastic collision
 637 and recoil away from each other. The DM remains in the dark sector and imparts some momentum
 638 onto the SM particle. The hope is that the momentum imparted onto the SM particle is sufficiently
 639 high enough to pick up with extremely sensitive instruments. Because we cannot create the DM in
 640 the lab, a direct detection experiment must wait until DM is incident on the detector. Most direct
 641 detection experiments are therefore placed in low-background environments with inert detection

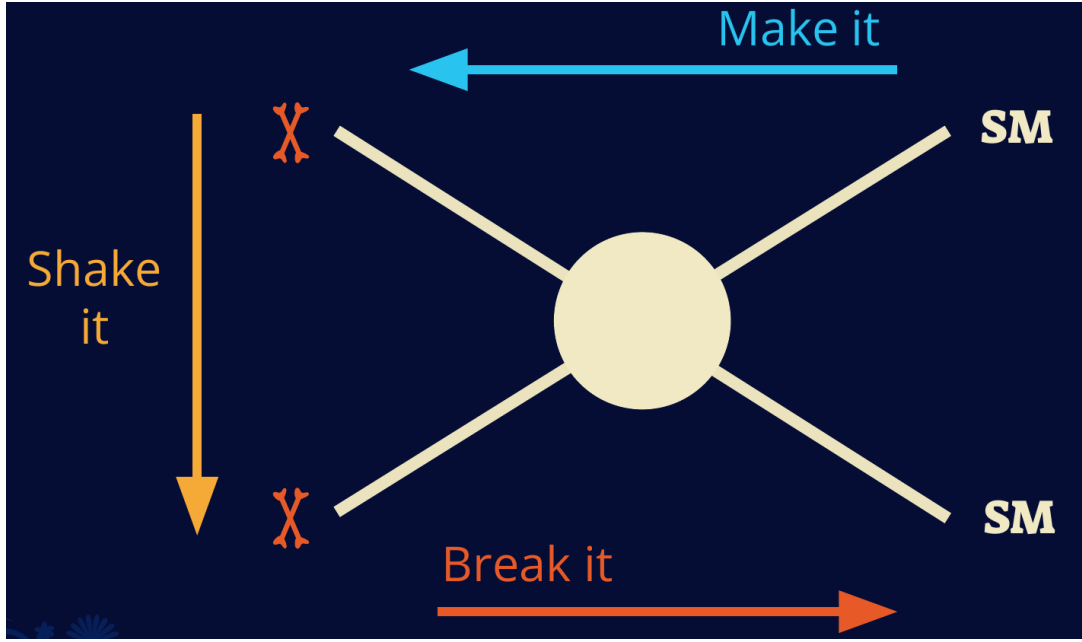


Figure 2.8 Simplified Feynman diagram demonstrating different ways DM can interact with SM particles. The 'X's refer to the DM particles whereas the SM refer to fundamental particles in the SM. The large circle in the center indicates the vertex of interaction and is purposely left vague. The colored arrows refer to different directions of time as well as their respective labels. The arrows indicate the initial and final state of the DM -SM interaction in time.

642 media like the noble gas Xenon. [14]

643 **Make it** refers to the production of DM from SM initial states. The experiment starts with
 644 particles in the SM. These SM particles are accelerated to incredibly high energies and then collide
 645 with each other. In the confluence of energy, DM hopefully emerges as a byproduct of the SM
 646 annihilation. Often it is the collider experiments that are energetic enough to hypothetically produce
 647 DM. These experiments include the world-wide collaborations ATLAS and CMS at CERN where
 648 proton collide together at extreme energies. The DM searches, however, are complex. DM likely
 649 does not interact with the detectors and lives long enough to escape the detection apparatus of
 650 CERN's colliders. This means any DM production experiment searches for an excess of events
 651 with missing momentum or energy in the events. An example event with missing transverse
 652 momentum is shown in Figure 2.9. The missing momentum with no particle tracks implies a
 653 neutral particle carried the energy out of the detector. However, there are other neutral particles
 654 in the SM, like neutrons or neutrinos, so any analysis has to account for SM signatures of missing

655 momentum. [15]

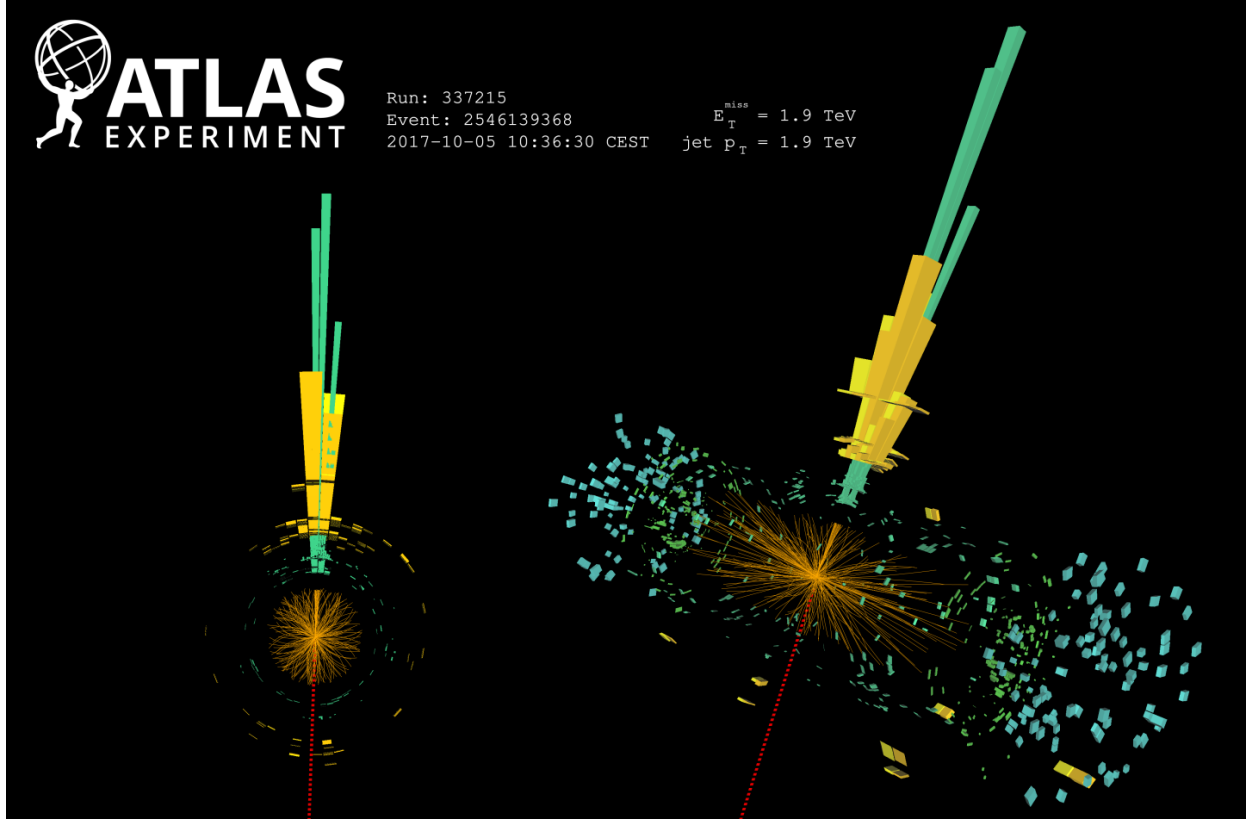


Figure 2.9 A single jet event in ATLAS detector from 2017 [16]. Jet momentum was observed to be 1.9 TeV. Missing transverse momentum was observed to be 1.9 TeV compared to the initial transverse momentum of the event was 0. Implied MET is traced by a red dashed line in event display.

656 2.4.2 Break it: Standard Model Signatures of Dark Matter through Indirect Searches

657 **Break it** refers to the creation of SM particles from the dark sector, and it is the primary focus
658 of this thesis. The interaction begins with DM or in the dark sector. The hypothesis is that this
659 DM will either annihilate with itself or decay and produce an SM byproduct. This method is
660 often referred to as the Indirect Detection of DM because we have no lab to directly control or
661 manipulate the DM. Therefore, most indirect DM searches are performed using observations of
662 known DM densities among the astrophysical sources. The strength is that we have the whole of the
663 universe and its 13.6-billion-year lifespan to use as a detector and particle accelerator. Additionally,
664 locations of dark matter are well cataloged since it was astrophysical observations that presented

665 the problem of DM in the first place.

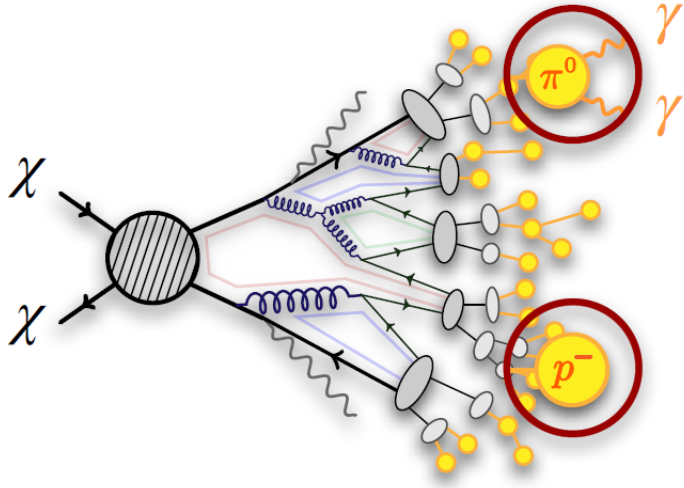


Figure 2.10 More detailed pseudo-Feynman diagram of particle cascade from dark matter annihilation into 2 quarks. The quarks hadronize and down to stable particles like γ or the anti-proton (p^-). Diagram pulled from ICRC 2021 presentation on DM annihilation search [17].

666 However, anything can happen in the universe. There are many difficult to deconvolve back-
667 grounds when searching for DM. One prominent example is the galactic center. We know the
668 galactic center has a large DM content because of stellar kinematics in our Milky Way and DM halo
669 simulations. Yet, any signal from the galactic center is challenging to parse apart from the extreme
670 environment of our supermassive black hole, unresolved sources, and diffuse emission from the
671 interstellar medium [18]. Despite the challenges, any DM model that yields evidence in the other
672 two observation methods, **Shake it or Make it** must be corroborated with indirect observations of
673 the known DM sources. Without corroborating evidence, DM observation in the lab is hard-pressed
674 to demonstrate that it is the model contributing to the DM seen at the universal scale.

675 In the case of WIMP DM, signals are described in terms of primary SM particles produced
676 from DM decay or annihilation. The SM initial state particles are then simulated down to stable
677 final states such as the γ , ν , p , or e which can traverse galactic lengths to reach Earth.

678 Figure 2.10 shows the quagmire of SM particles that emerges from SM initial states that are not
679 stable [17]. There are many SM particles with varying energies that can be produced in such an

680 interaction. For any arbitrary DM source and stable SM particle, the SM flux from DM annihilating
 681 to a neutral particle in the SM, ϕ , from a region in the sky is described by the following.

$$\frac{d\Phi_\phi}{dE_\phi} = \frac{\langle\sigma v\rangle}{8\pi m_\chi^2} \frac{dN_\phi}{dE_\phi} \times \int_{\text{source}} d\Omega \int_{l.o.s} \rho_\chi^2 dl(r, \theta') \quad (2.4)$$

682 In Equation (7.1), $\langle\sigma v\rangle$ is the velocity-weighted annihilation cross-section of DM to the SM. m_χ
 683 refers to the mass of DM, noted with Greek letter χ . $\frac{dN_\phi}{dE_\phi}$ is the N particle flux weighted by the
 684 particle energy. An example is provided in Figure 2.11 for the γ final state. The integrated terms
 685 are performed over the solid angle, $d\Omega$, and line of sight, l.o.s. ρ is the density of DM for a
 686 location (r, θ') in the sky. The terms left of the ' \times ' are often referred to as the particle physics
 687 component. The terms on the right are referred to as the astrophysical component. For decaying
 688 DM, the equation changes to...

$$\frac{d\Phi_\phi}{dE_\phi} = \frac{1}{4\pi\tau m_\chi} \frac{dN_\phi}{dE_\phi} \times \int_{\text{source}} d\Omega \int_{l.o.s} \rho_\chi dl(r, \theta') \quad (2.5)$$

689 In Equation (2.5), τ is the decay lifetime of the DM. Just as in Equation (7.1), the left and right
 690 terms are the particle physics and the astrophysical components respectively. The integrated
 691 astrophysical component of Equation (7.1) is often called the J-Factor. Whereas the integrated
 692 astrophysical component of Equation (2.5) is often called the D-Factor.

693 Exact DM $\text{DM} \rightarrow \text{SM SM}$ branching ratios are not known, so it is usually assumed to go 100%
 694 into an SM particle/anti-particle. Additionally, when a DM annihilation or decay produces one of
 695 the neutral, long-lived SM particles (ν or γ), the particle is traced back to a DM source. For DM
 696 above GeV energies, there are very few SM processes that can produce particles with such a high
 697 energy. Seeing such a signal would almost certainly be an indication of the presence of dark matter.
 698 Fortunately, the universe provides us with the largest volume and lifetime ever for a particle physics
 699 experiment.

700 2.5 Sources for Indirect Dark Matter Searches

701 The first detection of DM relied on optical observations. Since then, we have developed new
 702 techniques to find DM dense regions. As described in Section 2.3.1, many DM dense regions were
 703 through observing galactic rotation curves. Our Milky Way galaxy is among DM dense regions

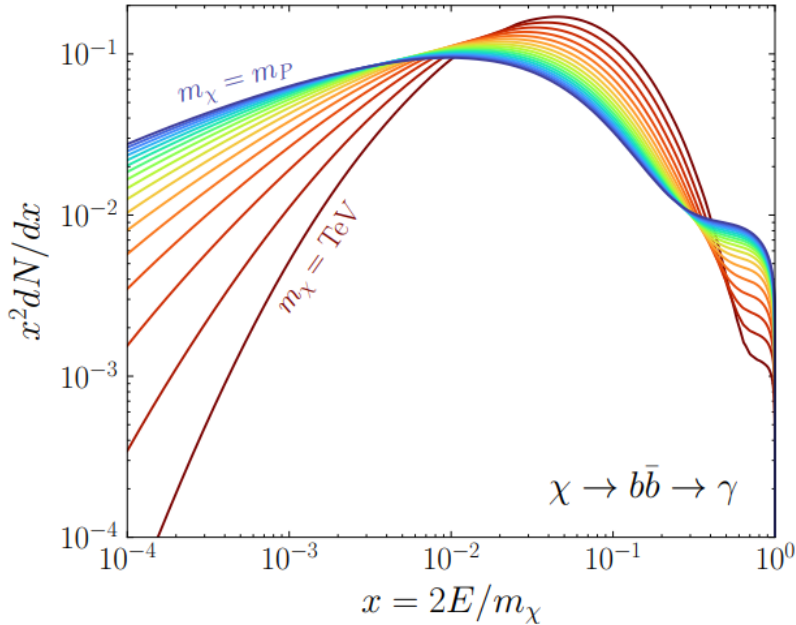


Figure 2.11 Dark Matter (DM) decay spectrum for $b\bar{b}$ initial state and γ final state. Redder spectra are for larger DM masses. Bluer spectra are light DM masses. x is a unitless factor defined as the ratio of the mass of DM, m_χ , and the final state particle energy E_γ . Figure from [19].

discovered, and it is the largest nearby DM dense region to look at. Additionally, the DM halo surrounding the Milky Way is clumpy [18]. There are regions in the DM halo of the Milky Way that have more DM than others that have captured gas over time. These sub-halos were dense enough to collapse gas and form stars. These apparent sub galaxies are known as dwarf spheroidal galaxies and are the main sources studied in this thesis. Each source type comes with different trade-offs. Galactic Center studies will be very sensitive to the assumed distribution of DM. The central DM density can vary substantially as demonstrated in Figure 2.12. At distances close to the center of the galaxy, or small r , the differences in DM densities can be 3-4 orders of magnitude. Searches toward the galactic center will therefore be quite sensitive to the assumed DM distribution.

Searches toward Dwarf Spheroidal Galaxies (dSph's) suffer from uncertainties in the DM density less than the galactic center studies. This is mostly from their diminutive size being smaller than the angular resolution of most γ -ray observatories [18]. The DM content dSph's are typically determined with the Virial theorem, Equation (2.1), and are usually majority DM [18] in mass. DSph's tend to be ideal sources to look at for DM searches. Their environments are quiet with little

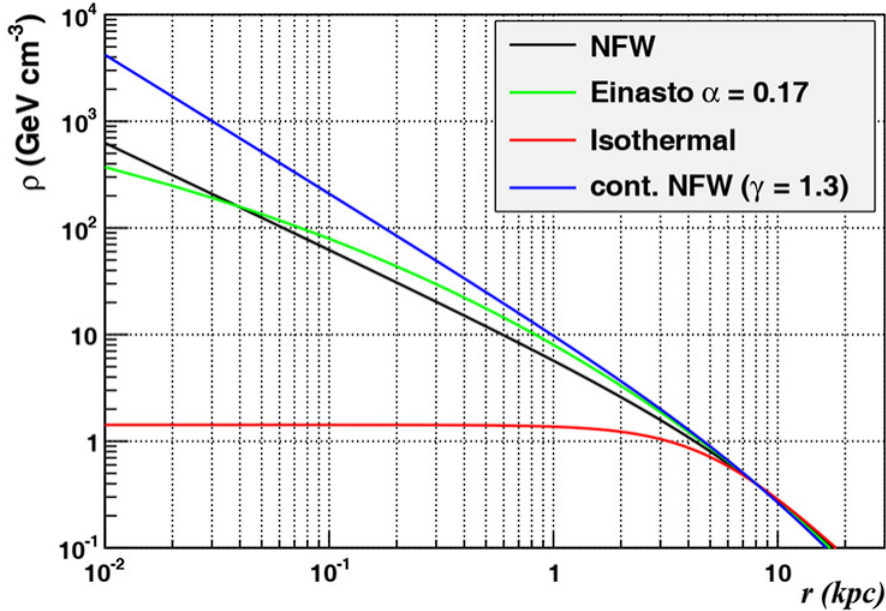


Figure 2.12 Different dark matter density profiles compared. Some models produce exceptionally large densities at small r [20].

718 astrophysical background. Unlike the galactic center, the most active components of dSph's are the
 719 stars within them versus a violent accretion disc around a black hole. All this together means that
 720 dSph's are among the best sources to look at for indirect DM searches. dSph's are the targets of
 721 focus for this thesis.

722 2.6 Multi-Messenger Dark Matter

723 Astrophysics entered a new phase in the past few decades that leverages our increasing sensitivity
 724 to SM channels and general relativity (GR). Up until the 21st century, astrophysical observations
 725 were performed with photons (γ) only. Astrophysics with this 'messenger' is fairly mature now.
 726 Novel observations of the universe have since only adjusted the sensitivity of the wavelength of
 727 light that is observed except at MeV energies. Gems like the CMB [10], and more have ultimately
 728 been observations of different wavelengths of light. Multi-messenger astrophysics proposes using
 729 other SM particles such the p^{+-} , or ν or gravitation waves predicted by general relativity.

730 The experiment LIGO had a revolutionary discovery in 2016 with the first detection of a binary
 731 black hole merger [21]. This opened the collective imagination to observing the universe through
 732 gravitational waves. There has also been a surge of interest in the neutrino (ν) sector. IceCube

733 demonstrated that we are sensitive to neutrinos in regions that correlate with significant photon
 734 emission like the galactic plane [22]. Neutrinos, like gravitational waves and light, travel mostly
 735 unimpeded from their source to our observatories. This makes pointing to the originating source
 736 of these messengers much easier than it is for cosmic rays which are deflected from their source by
 737 magnetic fields.

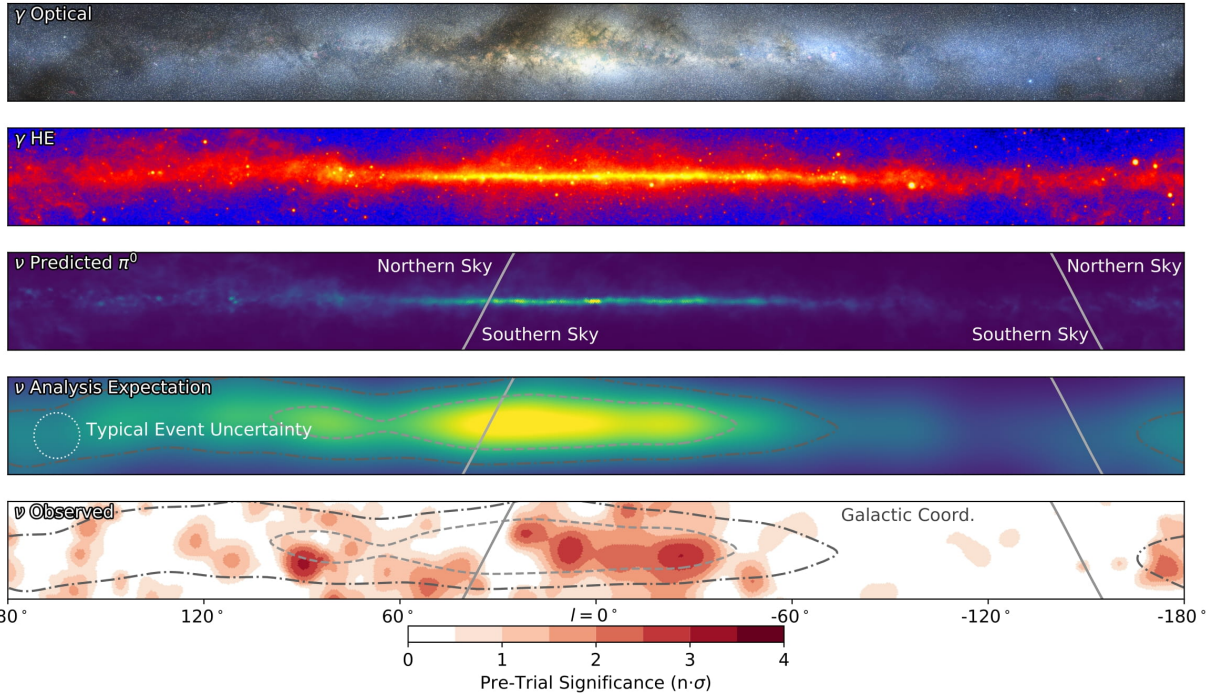


Figure 2.13 The Milky Way Galaxy in photons (γ) and neutrinos (ν) [22]. The Galactic center is at $l=0^\circ$ and is the brightest region in all panels. (top) An Optical color image of the Milky Way galaxy seen from Earth. Clouds of gas and dust obscure some light from stars. (2nd down) Integrated flux of γ -rays observed by the Fermi-LAT telescope [23]. (middle) Expected neutrino emission that corresponds with Fermi-LAT observations. (2nd up) Expected neutrino emission profile after considering detector systematics of IceCube. (bottom) Observed neutrino emission from region of the galactic plane. Substantial neutrino emission was detected.

738 The IceCube collaboration recently published a groundbreaking result of the Milky Way in
 739 neutrinos. The recent result from IceCube, shown in Figure 2.13, proves that we can make
 740 observations under different messenger regimes. The top two panels show the appearance of the
 741 galactic plane to different wavelengths of light. Some sources are more apparent in some panels,
 742 while others are not. This new channel is powerful because neutrinos are readily able to penetrate
 743 through gas and dust in the Milky Way. This new image also refines our understanding of how high

744 energy particles are produced. For example, the fit to IceCube data prefers neutrino production
 745 from the decay of π^0 [22].

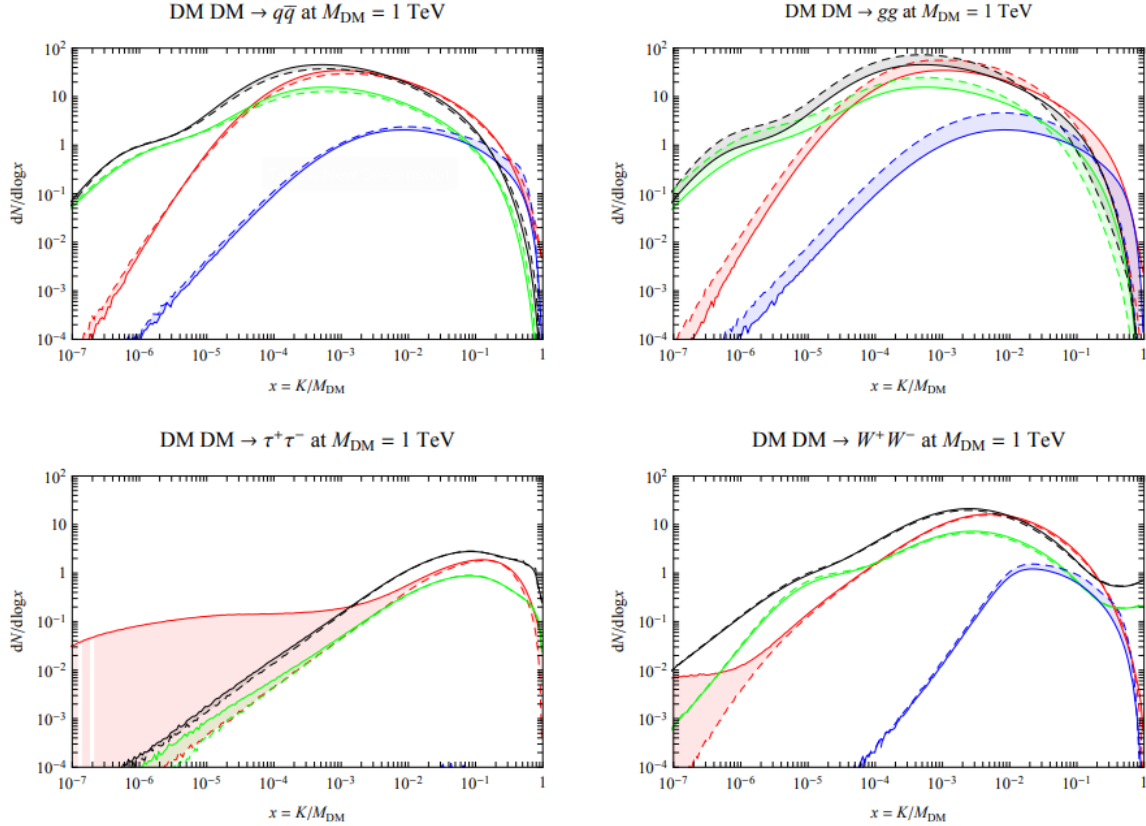


Figure 2.14 Dark Matter annihilation spectra for different final state particle and standard model annihilation channels [24]. Photons (red), e^\pm (green), \bar{p} (blue), ν (black).

746 Exposing our observations to more cosmic messengers greatly increases our sensitivity to
 747 rare processes. In the case of DM, Figure 2.14, there are many SM particles produced in DM
 748 annihilation. Among the final state fluxes are gammas and neutrinos. Charged particles are also
 749 produced however they would not likely make it to Earth since they will be deflected by magnetic
 750 fields between the source and Earth. This means observatories that can see the neutral messengers
 751 are especially good for DM searches and for combining data for a multi-messenger DM search.

CHAPTER 3

752

HIGH ALTITUDE WATER CHERENKOV (HAWC) OBSERVATORY

753 **3.1 The Detector**

754 **3.2 Events Reconstruction and Data Acquisition**

755 **3.2.1 G/H Discrimination**

756 **3.2.2 Angle**

757 **3.2.3 Energy**

758 **3.3 Remote Monitoring**

759 **3.3.1 ATHENA Database**

760 **3.3.2 HOMER**

761

CHAPTER 4

ICECUBE NEUTRINO OBSERVATORY

762 **4.1 The Detector**

763 **4.2 Events Reconstruction and Data Acquisition**

764 **4.2.1 Angle**

765 **4.2.2 Energy**

766 **4.3 Northern Test Site**

767 **4.3.1 PIgeon remote dark rate testing**

768 **4.3.2 Bulkhead Construction**

CHAPTER 5

GLORY DUCK: MULTI-WAVELENGTH SEARCH FOR DARK MATTER ANNIHILATION TOWARDS DWARF SPHEROIDAL GALAXIES

5.1 Introduction

The field of astrophysics now has several instruments and observatories sensitive to high energy gamma-rays. The energy sensitivity for the modern gamma-ray program spans many orders of magnitude. Figure 5.1 demonstrates these comparable sensitivities across energies for the five experiments: Fermi-LAT, HAWC, HESS, MAGIC, and VERITAS.

Each of the five experiments featured in Figure 5.1 have independently searched for DM annihilation from dwarf spheroidal galaxies (dSph) and set limits on annihilation cross-section of WIMPs. Intriguingly, there are regions of substantial overlap in their energy sensitivities. This clearly motivates an analysis that combines data from these five. Each experiment has unique gamma-ray detection methods and their weaknesses and strengths can be leveraged with each other. The HAWC gamma-ray observatory is extensively introduced in chapter 3, so it is not introduced here. A brief description of the remaining experiments are in the following paragraphs.

The Large Area Telescope (LAT) is a pair conversion telescope mounted on the NASA Fermi satellite in orbit \sim 550 km above the Earth [26]. LAT's field of view covers about 20% of the whole sky, and it sweeps the whole sky approximately every 3 hours. LAT's gamma-ray energy sensitivity ranges from 20 MeV up to 1 TeV. Previous DM searches towards dSphs using Fermi-LAT are published in [27] and [28].

The High Energy Spectroscopic System (HESS), Major Atmospheric Gamma Imaging Cherenkov (MAGIC), and Very Energetic Radiation Imaging Telescope Array System (VERITAS) are arrays of Imaging Atmospheric Cherenkov Telescopes (IACT). These telescopes observe the Cherenkov light emitted from gamma-ray showers in the Earth's atmosphere. The field of view for these telescopes is no larger than 5° with energy sensitivities ranging from 30 GeV up to 100 TeV [29, 30, 31]. IACTs are able to make precise observations in selected regions of the sky, however can only be operated in ideal dark conditions. HESS's observations of the dwarves

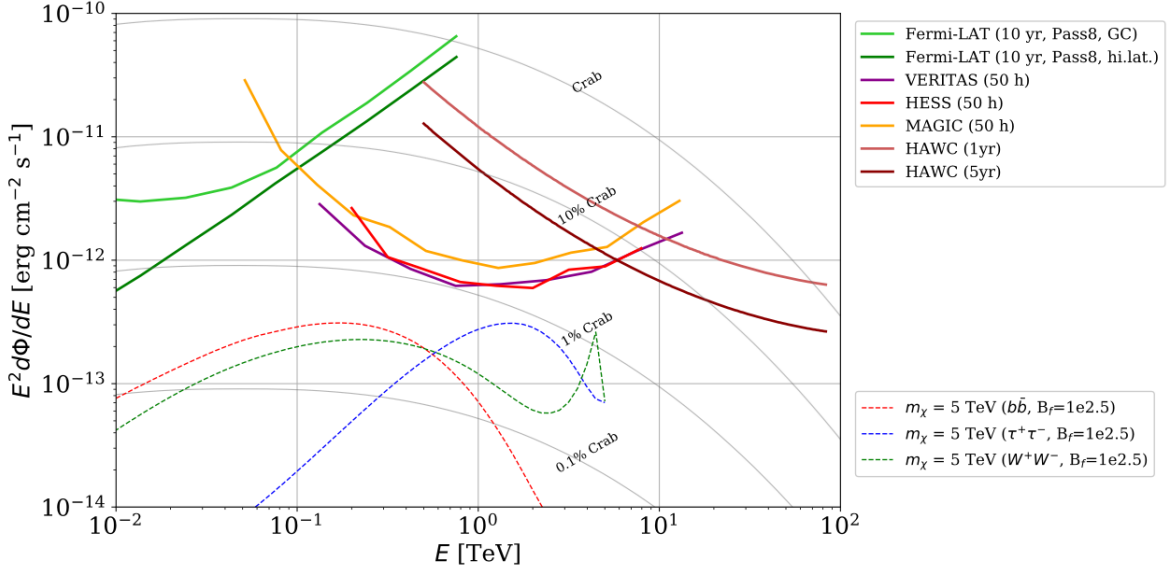


Figure 5.1 Sensitivities of five gamma-ray experiments compared to percentages of the Crab nebula's emission and dark matter annihilation. Solid lines present estimated sensitivities to power law spectra [FACT CHECK THIS] for each experiment. Green lines are Fermi-LAT sensitivities where lighter green is the sensitivity to the galactic center and dark green is its sensitivity to higher declinations. Orange, red, and purple solid lines represent the MAGIC, HESS, and VERITAS 50 hour sensitivities respectively. The maroon and brown lines are the HAWC 1 year and 5 year sensitivities. Across four decades of gamma-ray energy, these experiments have similar sensitivities on the order 10^{-12} erg $\text{cm}^{-2}\text{s}^{-1}$. The dotted lines are estimated dark matter fluxes assuming $m_\chi = 5$ TeV DM annihilating to bottom quarks (red), tau leptons (blue), and W bosons (green). Faded gray lines outline percentage flux of the Crab nebula. Figure is an augmented version of [25]

795 Sculptor and Carina were between January 2008 and December 2009. HESS's observations of
 796 Coma Berenices were taken from 2010 to 2013, and Fornax was observed in 2010 [32, 33, 34].
 797 MAGIC provided deep observations of Segue1 between 2011 and 2013 [35]. MAGIC also provides
 798 data for three additional dwarves: Coma Berenices, Draco, and Ursa Major II where observations
 799 were made in: January - June 2019 [36], March - September 2018 [36], and 2014 - 2016 [37]
 800 respectively. VERITAS provided data for Boötes I, Draco, Segue 1, and Ursa Minor from 2009 to
 801 2016 [38].

802 This chapter presents the Glory Duck analysis, the name given for the search for dark matter
 803 annihilation from dSph by combining data from the five gamma-ray observatories: Fermi-LAT,
 804 HAWC, HESS, MAGIC, and VERITAS. Specifically, the methods in analysis and modeling are
 805 presented for the HAWC gamma-ray observatory. This work will be published in the Journal of

806 Cosmology and Astroparticle Physics and presented at the International Cosmic Ray Conference
807 in 2019, 2021, and 2023 [39, 40, 41] and others.

808 **5.2 Dataset and Background**

809 This section enumerates the data analysis and background estimation methods used for HAWC's
810 study of dSphs. Section 5.2.1 and Section 5.2.2 are most useful for fellow HAWC collaborators
811 looking to replicate the Glory Duck analysis.

812 **5.2.1 Itemized HAWC files**

813 These files are only available withing HAWC's internal documentation and collaborators. They
814 are not meant for public access, and are presented here so that HAWC collaborators can reproduce
815 results accurately.

- 816 • Detector Response: `response_aerie_svn_27754_systematics_best_mc_test_noBr`
817 `oadpulse\10pctlogchargesmearing_0.63qe_25kHzNoise_run5481_curvature`
818 `0_index3.root`
- 819 • Data Map: `maps-20180119/liff/maptree_1024.root`
- 820 • Spectral Dictionary: `DM_CirrelliSpectrum_dict_gammas.npy`
- 821 • Analysis wiki: https://private.hawc-observatory.org/wiki/index.php/Glory_Duck_Multi-Experiment_Dark_Matter_Search

823 **5.2.2 Software Tools and Development**

824 This analysis was performed using HAL and 3ML [42, 43] in Python version 2. I built software
825 to implement the *A Poor Particle Physicist Cookbook for Dark Matter Indirect Detection* (PPPC)
826 [44] DM spectral model and dSphs spatial model from [45] for HAWC analysis. A NumPy version
827 of this dictionary was made for both Py2 and Py3. The code base for creating this dictionary is
828 linked on my GitLab sandbox:

- 829 • Py2: [Dictionary Generator \(Deprecated\)](#)

- 830 • Py3: [PPPC2Dict](#)

831 The analysis was performed using the f_{hit} framework as used and described in the HAWC Crab
832 paper [42]. The Python2 NumPy dictionary file for gamma-ray final states is `dmCirSpecDict.npy`.
833 The corresponding Python3 file is `DM_CirrelliSpectrum_dict_gammas.npy`. These files can
834 also be used for decay channels and the PPPC describes how [44]. All other software used for data
835 analysis, DM profile generation, and job submission to SLURM are also kept in my sandbox for
836 [the Glory Duck](#) project.

837 **5.2.3 Data Set and Background Description**

838 The HAWC data maps used for this analysis contain 1017 days of data between runs 2104
839 (2014-11-26) and 7476 (2017-12-20). They were generated from pass 4.0 reconstruction. The
840 analysis is performed using the f_{hit} energy binning scheme with bins (1-9) similar to what was done
841 for the Crab and previous HAWC dSph analysis [42, 46]. Bin 0 was excluded as it has substantial
842 hadronic contamination and poor angular resolution.

843 This analysis was done on dSphs because of their large DM mass content relative to baryonic
844 mass. We consider the following to estimate the background to this study.

- 845 • The dSphs' angular extent are small relative to HAWC's spatial resolution, so the analysis is
846 not sensitive to large or small scale anisotropies.
- 847 • The dSphs used in this analysis are off the galactic plane and therefore not contaminated by
848 diffuse emission from the galaxy.
- 849 • The dSphs are baryonically faint relative to their expected dark matter content and are not
850 expected to contain high energy gamma-ray sources.

851 Therefor we make no additional assumptions on the background from our sources and use
852 HAWC's standard direct integration method for background estimation [42]. The largest background
853 under this consideration is from an isotropic flux of cosmic rays. The contamination of this hadronic
854 flux is worse at lower energies where HAWC's gamma/hadron discrimination worse. It is possible

855 for gamma rays from DM annihilation to scatter in transit to HAWC via Inverse Compton Scattering
856 (ICS). This was investigated and its impact on the flux is negligible. Supporting information on
857 this is in Section 5.7.1

858 **5.3 Analysis**

859 The expected differential photon flux from DM-DM annihilation to standard model particles,
860 $d\Phi_\gamma/dE_\gamma$, over solid angle, Ω , is described by the familiar equation.

$$\frac{d\Phi_\gamma}{dE_\gamma} = \frac{\langle\sigma v\rangle}{8\pi m_\chi^2} \frac{dN_\gamma}{dE_\gamma} \times \int_{\text{source}} d\Omega \int_{l.o.s} dl \rho_\chi^2 J(r, \theta') \quad (5.1)$$

861 Where $\langle\sigma v\rangle$ is the velocity weighted annihilation cross-section. $\frac{dN}{dE}$ is the expected differential
862 number of photons produced at each energy per annihilation. m_χ is the rest mass of the supposed
863 DM particle. ρ_χ is the DM density. J is the astrophysical J-factor and is defined as

$$J = \int d\Omega \int_{l.o.s} dl \rho_\chi^2(r, \theta') \quad (5.2)$$

864 l is the distance to the source from Earth. r is the radial distance from the center of the source. θ' is
865 the half angle defining a cone containing the DM source. How each component is synthesized and
866 considered for HAWC's analysis is presented in the following sections. Section 5.3.1 presents the
867 particle physics model for DM annihilation. Section 5.3.2 presents the spatial distributions built
868 for each dSph.

869 **5.3.1 $\frac{dN_\gamma}{dE_\gamma}$ - Particle Physics Component**

870 For these spectra, we import the PPPC with Electroweak (EW) corrections [44]. Public versions
871 of the imported tables are provided by the [authors online](#). The spectrum is implemented as a model
872 script in astromodels for 3ML. The EW corrections were previously not considered for HAWC and
873 are significant for DM annihilating to EW coupled SM particles such as all leptons, and the γ ,
874 Z , and W bosons [46]. Figure 5.2 demonstrates the significance of EW corrections for W boson
875 annihilation. Across EW SM channels, the gamma-ray spectra become harder than spectra without
876 EW corrections. Tables from the PPPC were reformatted into Python NumPy dictionaries for
877 collaboration-wide use. A class in astromodels was developed to include the EW correction from
878 the PPPC and is aptly named `PPPCSpectra` within `DM_models.py`.

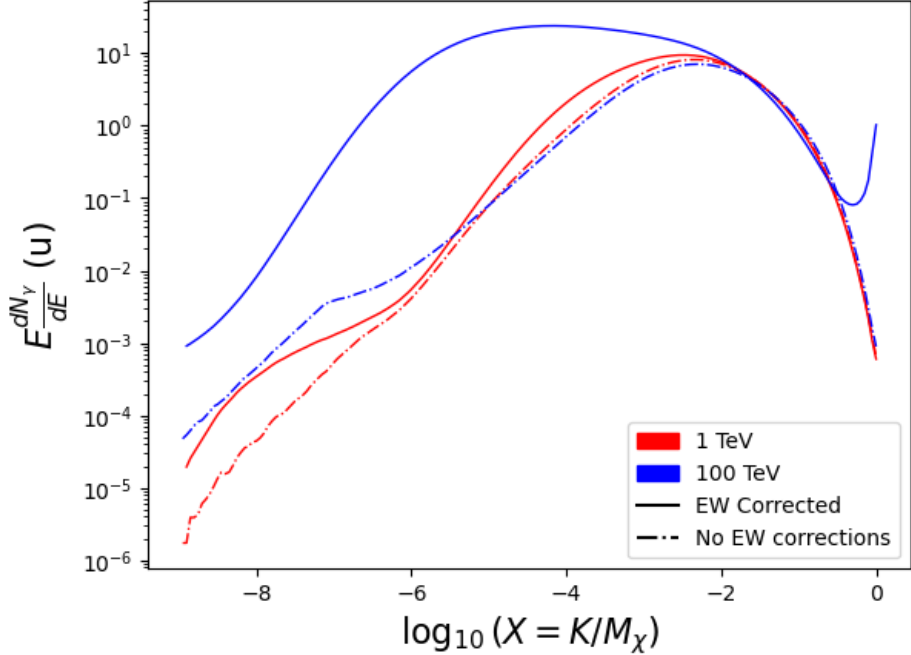


Figure 5.2 Effect of Electroweak (EW) corrections on expected DM annihilation spectrum for $\chi\chi \rightarrow W^-W^+$. Solid lines are spectral models that consider EW corrections. Dash-dot lines are spectral models without EW corrections. Red lines are models for $M_\chi = 1$ TeV. Blue lines represent models for $M_\chi = 100$ TeV. All models are sourced from the PPPC4DMID [44].

879 5.3.2 J- Astrophysical Component

880 The J-factor profiles for each source are imported from Geringer-Sameth (referred to with \mathcal{GS})
 881 [45]. \mathcal{GS} fits the Zhao DM profile to the dSphs which has a DM density described as [47]

$$\rho(r) = \frac{\rho_0}{(r/R_s)^\gamma (1 + (r/R_s)^\alpha)^{(\beta-\gamma)}}. \quad (5.3)$$

882 R_s is the scale radius and free parameter in the model. γ is the logarithmic slope in the region
 883 $r \ll R_s$. β is the logarithmic slope in the region $r \gg R_s$. α is known as the sharpness of transition
 884 where $r \approx R_s$. The classic Navarro-Frenk-White [48] (NFW) can be retrieved from Zhao by fixing
 885 $(\alpha, \beta, \gamma) = (1, 3, 1)$.

886 \mathcal{GS} best fits were pulled from the publication as $J(\theta)$, where θ is the angular separation from
 887 the center of the source. HAWC requires maps in terms of $\frac{dJ}{d\Omega}$, so the conversion from the maps
 888 was done in the following way...

889 First, convert the angular distances to solid angles

$$\Omega = 2 \cdot \pi(1 - \cos(\theta)) \quad (5.4)$$

890 which reduces with a small angle approximation to $\pi\theta^2$. Next, the central difference for both the
891 ΔJ and $\Delta\Omega$ value were calculated from the discretized $J(\theta)$ with the central difference stencil:

$$\Delta\phi_i = \phi_{i+1} - \phi_{i-1} \quad (5.5)$$

892 Where ϕ is either Ω or J . These were done separately in case the grid spacing in θ was not uniform.
893 Finally, these lists are divided so that we are left with an approximation of the $dJ/d\Omega$ profile that
894 is a function of θ . Admittedly, this is an approximation method for the map which introduces small
895 errors compared to the true profile estimate. This was checked as a systematic against the author's
896 profiling of the spatial distribution and is documented in Section 5.8.1.

897 With $\frac{dJ}{d\Omega}(\theta)$, a map is generated, first by filling in the north-east quadrant of the map. This
898 quadrant is then reflected twice, vertically then horizontally, to fill the full map. Maps are then
899 normalized by dividing the discrete 2D integral of the map. The 2D integral was a simple height
900 of bins, Newton's integral:

$$p^2 \cdot \sum_{i,j=0}^{N,M} \frac{dJ}{d\Omega}(\theta_{i,j}, \phi_{i,j}) \quad (5.6)$$

901 These maps are HEALpix maps with NSIDE 16384 and saved in the .fits format. The hyper fine
902 resolution was selected to better preserve the total expected counts after integrating Eq. (7.1) with
903 the detector response.

904 Another DM spatial distribution model from Bonnivard (\mathcal{B}) [49] was used for the Glory Duck
905 study. However, to save computational time, limits from \mathcal{GS} were scaled to \mathcal{B} instead of each
906 experiment performing a full study a second time. How these models compare is demonstrated
907 for each dSph in Figure 5.16 and Figure 5.17 Plots of these maps are provided for each source
908 in chapter A Examples of the two most impactful dSphs derived from \mathcal{GS} , Segue1 and Coma
909 Berenices are featured in Figure 5.3

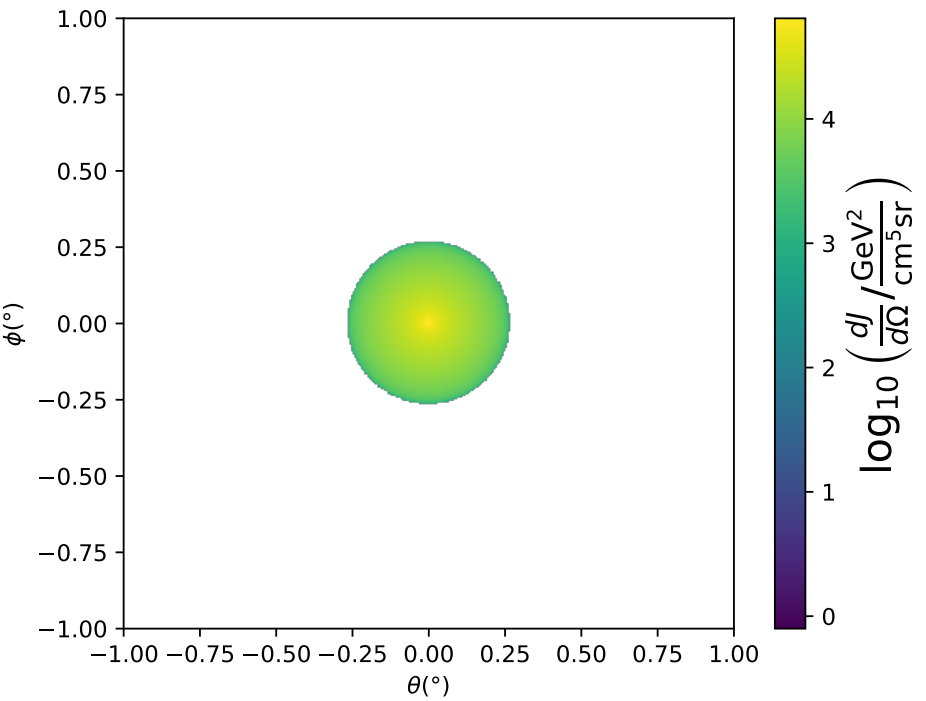
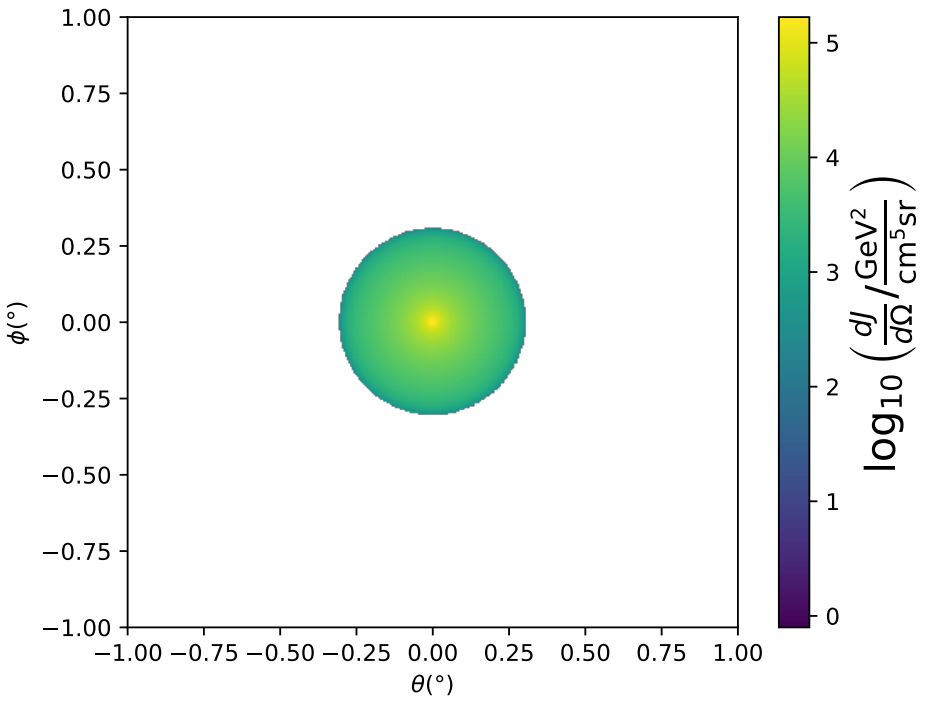


Figure 5.3 $\frac{dJ}{d\Omega}$ maps for Segue1 (top) and Coma Berenices (bottom). Origin is centered on the specific dwarf spheroidal galaxies (dSph). X and Y axes are the angular separation from the center of the dwarf. Profile is truncated at the scale radius. Plots of the remaining 11 dSph HAWC studied are linked in Fig. A.1.

910 **5.3.3 Source Selection and Annihilation Channels**

911 We use many of the dSphs presented in HAWC’s previous dSph DM search [46]. HAWC’s
912 sources for Glory Duck include Boötes I, Coma Berenices, Canes Venatici I + II, Draco, Hercules,
913 Leo I, II, + IV, Segue 1, Sextans, and Ursa Major I + II. A full description of all sources used
914 in Glory Duck is found in Table 5.1. Triangulum II was excluded from the Glory Duck analysis
915 because of large uncertainties in its J factor. Ursa Minor was excluded from HAWC’s contribution
916 to the combination because the source extension model extended Ursa Minor beyond HAWC’s field
917 of view. Ursa Minor was not expected to contribute significantly to the combined limit, so work
918 was not invested in a solution to include Ursa Minor.

919 This analysis improves on the previous HAWC dSph paper [46] in the following ways. Pre-
920 viously, the dSphs were treated and implemented as point sources. For this analysis, dSphs are
921 modeled and treated as extended source. The impact of this change with respect to the upper limit
922 is source dependent and is explored in Section 5.7.2. Previously, the particle physics model used for
923 gamma-ray spectra from DM annihilation did not have EW corrections where the PPPC includes
924 them. Finally, the gamma-ray ray dataset is much larger. The study performed here analyzes over
925 1000 days of data compared to 507.

926 The SM annihilation channels probed for the Glory Duck combination include $b\bar{b}$, $e\bar{e}$, $\mu\bar{\mu}$, $\tau\bar{\tau}$,
927 $t\bar{t}$, W^+W^- , and ZZ . A summary of all sources, with a description of each experiments’ sensitivity
928 to the source, is provided in Table 5.2.

929 **5.4 Likelihood Methods**

930 **5.4.1 HAWC Likelihood**

931 For every analysis bin in energy, f_{hit} bins (1-9), and location, we can expect N signal events and
932 B background events. The expected number of excess signal events from dark matter annihilation,
933 S , is estimated by convolving Equation (7.1) with HAWC’s energy response and pixel point spread
934 functions. I then compute the test statistic (TS) with the log-likelihood ratio test,

$$TS_{max} = -2 \ln \left(\frac{\mathcal{L}_0}{\mathcal{L}^{max}} \right) \quad (5.7)$$

Table 5.1 Summary of the relevant properties of the dSphs used in the present work. Column 1 lists the dSphs. Columns 2 and 3 present their heliocentric distance and galactic coordinates, respectively. Columns 4 and 5 report the J -factors of each source given from the \mathcal{GS} and \mathcal{B} independent studies and their estimated $\pm 1\sigma$ uncertainties. The values $\log_{10} J$ (\mathcal{GS} set) [45] correspond to the mean J -factor values for a source extension truncated at the outermost observed star. The values $\log_{10} J$ (\mathcal{B} set) [49] are provided for a source extension at the tidal radius of each dSph. **Bolded sources are within HAWC's field of view and provided to the Glory Duck analysis.**

Name	Distance (kpc)	l, b ($^{\circ}$)	$\log_{10} J$ (\mathcal{GS} set) $\log_{10}(\text{GeV}^2\text{cm}^{-5}\text{sr})$	$\log_{10} J$ (\mathcal{B} set) $\log_{10}(\text{GeV}^2\text{cm}^{-5}\text{sr})$
Boötes I	66	358.08, 69.62	$18.24^{+0.40}_{-0.37}$	$18.85^{+1.10}_{-0.61}$
Canes Venatici I	218	74.31, 79.82	$17.44^{+0.37}_{-0.28}$	$17.63^{+0.50}_{-0.20}$
Canes Venatici II	160	113.58, 82.70	$17.65^{+0.45}_{-0.43}$	$18.67^{+1.54}_{-0.97}$
Carina	105	260.11, -22.22	$17.92^{+0.19}_{-0.11}$	$18.02^{+0.36}_{-0.15}$
Coma Berenices	44	241.89, 83.61	$19.02^{+0.37}_{-0.41}$	$20.13^{+1.56}_{-1.08}$
Draco	76	86.37, 34.72	$19.05^{+0.22}_{-0.21}$	$19.42^{+0.92}_{-0.47}$
Fornax	147	237.10, -65.65	$17.84^{+0.11}_{-0.06}$	$17.85^{+0.11}_{-0.08}$
Hercules	132	28.73, 36.87	$16.86^{+0.74}_{-0.68}$	$17.70^{+1.08}_{-0.73}$
Leo I	254	225.99, 49.11	$17.84^{+0.20}_{-0.16}$	$17.93^{+0.65}_{-0.25}$
Leo II	233	220.17, 67.23	$17.97^{+0.20}_{-0.18}$	$18.11^{+0.71}_{-0.25}$
Leo IV	154	265.44, 56.51	$16.32^{+1.06}_{-1.70}$	$16.36^{+1.44}_{-1.65}$
Leo V	178	261.86, 58.54	$16.37^{+0.94}_{-0.87}$	$16.30^{+1.33}_{-1.16}$
Leo T	417	214.85, 43.66	$17.11^{+0.44}_{-0.39}$	$17.67^{+1.01}_{-0.56}$
Sculptor	86	287.53, -83.16	$18.57^{+0.07}_{-0.05}$	$18.63^{+0.14}_{-0.08}$
Segue I	23	220.48, 50.43	$19.36^{+0.32}_{-0.35}$	$17.52^{+2.54}_{-2.65}$
Segue II	35	149.43, -38.14	$16.21^{+1.06}_{-0.98}$	$19.50^{+1.82}_{-1.48}$
Sextans	86	243.50, 42.27	$17.92^{+0.35}_{-0.29}$	$18.04^{+0.50}_{-0.28}$
Ursa Major I	97	159.43, 54.41	$17.87^{+0.56}_{-0.33}$	$18.84^{+0.97}_{-0.43}$
Ursa Major II	32	152.46, 37.44	$19.42^{+0.44}_{-0.42}$	$20.60^{+1.46}_{-0.95}$
Ursa Minor	76	104.97, 44.80	$18.95^{+0.26}_{-0.18}$	$19.08^{+0.21}_{-0.13}$

Table 5.2 Summary of dSph observations by each experiment used in this work. A ‘-’ indicates the experiment did not observe the dSph for this study. For Fermi-LAT, the exposure at 1 GeV is given. For HAWC, $|\Delta\theta|$ is the absolute difference between the source declination and HAWC latitude. HAWC is more sensitive to sources with smaller $|\Delta\theta|$. For IACTs, we show the zenith angle range, the total exposure, the energy range, the angular radius θ of the signal or ON region, the ratio of exposures between the background-control (OFF) and signal (ON) regions (τ), and the significance of gamma-ray excess in standard deviations, σ .

Source name	Fermi-LAT	HAWC	H.E.S.S, MAGIC, VERITAS						
	Exposure (10^{11} s m 2)	$ \Delta\theta $ ($^\circ$)	IACT	Zenith ($^\circ$)	Exposure (h)	Energy range (GeV)	θ ($^\circ$)	τ	S (σ)
Boötes I	2.6	4.5	VERITAS	15 – 30	14.0	100–41000	0.10	8.6	-1.0
Canes Venatici I	2.9	14.6	–	–	–	–	–	–	–
Canes Venatici II	2.9	15.3	–	–	–	–	–	–	–
Carina	3.1	–	H.E.S.S.	27 – 46	23.7	310 – 70000	0.10	18.0	-0.3
Coma Berenices	2.7	4.9	H.E.S.S.	47 – 49	11.4	550 – 70000	0.10	14.4	-0.4
			MAGIC	5 – 37	49.5	60 – 10000	0.17	1.0	–
			MAGIC	29 – 45	52.1	70 – 10000	0.22	1.0	–
Draco	3.8	38.1	VERITAS	25 – 40	49.8	120 – 70000	0.10	9.0	-1.0
Fornax	2.7	–	H.E.S.S.	11 – 25	6.8	230 – 70000	0.10	45.5	-1.5
Hercules	2.8	6.3	–	–	–	–	–	–	–
Leo I	2.5	6.7	–	–	–	–	–	–	–
Leo II	2.6	3.1	–	–	–	–	–	–	–
Leo IV	2.4	19.5	–	–	–	–	–	–	–
Leo V	2.4	–	–	–	–	–	–	–	–
Leo T	2.6	–	–	–	–	–	–	–	–
Sculptor	2.7	–	H.E.S.S.	10 – 46	11.8	200 – 70000	0.10	19.8	-2.2
Segue I	2.5	2.9	MAGIC	13 – 37	158.0	60 – 10000	0.12	1.0	-0.5
			VERITAS	15 – 35	92.0	80 – 50000	0.10	7.6	0.7
Segue II	2.7	–	–	–	–	–	–	–	–
Sextans	2.4	20.6	–	–	–	–	–	–	–
Ursa Major I	3.4	32.9	–	–	–	–	–	–	–
Ursa Major II	4.0	44.1	MAGIC	35 – 45	94.8	120 – 10000	0.30	1.0	-2.1
Ursa Minor	4.1	–	VERITAS	35 – 45	60.4	160 – 93000	0.10	8.4	-0.1

935 where \mathcal{L}_0 is the null hypothesis, or no DM emission, likelihood. \mathcal{L}^{\max} is the best fit signal
 936 hypothesis where $\langle\sigma v\rangle$ maximizes the likelihood. We calculate the likelihood of each source and
 938 model, assuming events are Poisson distributed, with

$$\mathcal{L} = \prod_i \frac{(B_i + S_i)^{N_i} e^{-(B_i + S_i)}}{N_i!} \quad (5.8)$$

939 where S_i is the sum of expected number of signal counts. B_i is the number of background counts
 940 observed. N_i is the total number of counts.

941 I also calculate an upper limit on $\langle\sigma v\rangle$ by calculating the 95% confidence level (CL). For the
 942 CL, we define a parameter, TS_{95} , as

$$TS_{95} \equiv \sum_{\text{bins}} \left[2N \ln \left(1 + \frac{\epsilon S_{\text{ref}}}{B} \right) - 2\epsilon S_{\text{ref}} \right] \quad (5.9)$$

943 where the expected signal counts from a dSph is scaled by ϵ . S_{ref} is the expected number of excess
 944 counts in a bin from DM emission from a dSph with a corresponding annihilation cross-section,
 945 $\langle\sigma v\rangle$. We scan ϵ such that

$$2.71 = TS_{\max} - TS_{95} \quad (5.10)$$

946 HAWC's exclusive results are provided in Section 5.5.

947 5.4.2 Glory Duck Joint Likelihood

948 The joint likelihood for the 5-experiment combination was done similarly as Section 5.4.1. We
 949 calculate upper limits on $\langle\sigma v\rangle$ from the TS, Eq. (5.7), and define the likelihood ratio more generally

$$\lambda(\langle\sigma v\rangle | \mathcal{D}_{\text{dSphs}}) = \frac{\mathcal{L}(\langle\sigma v\rangle; \hat{\nu} | \mathcal{D}_{\text{dSphs}})}{\mathcal{L}(\widehat{\langle\sigma v\rangle}; \hat{\nu} | \mathcal{D}_{\text{dSphs}})} \quad (5.11)$$

950 $\mathcal{D}_{\text{dSphs}}$ is the totality of observations across experiments and dSphs. ν are the nuisance parameters
 951 which are the J factors in this study. $\widehat{\langle\sigma v\rangle}$ and $\hat{\nu}$ are the respective estimate that maximize \mathcal{L}
 952 globally. Finally, $\hat{\nu}$ is the set of nuisance parameters that maximize \mathcal{L} for a fixed value of $\langle\sigma v\rangle$.

953 The *complete* joint likelihood, \mathcal{L} that encompasses all observations from all instruments and
 954 dSphs can be factorized into *partial* functions for each dSph l (with $\mathcal{L}_{\text{dSph},l}$) and its J factor (\mathcal{J}_l):

$$\mathcal{L}(\langle\sigma v\rangle; \nu | \mathcal{D}_{\text{dSphs}}) = \prod_{l=1}^{N_{\text{dSphs}}} \mathcal{L}_{\text{dSph},l}(\langle\sigma v\rangle; J_l, \nu_l | \mathcal{D}_l) \times \mathcal{J}_l(J_l | J_{l,\text{obs}}, \sigma_{\log J_l}). \quad (5.12)$$

955 For this study, $N_{\text{dSphs}} = 20$ is the number of dSphs studied. \mathcal{D}_l are the gamma-ray observations
 956 of dSph, l . ν_l are the nuisance parameters modifying the gamma-ray observations of dSph, l ,
 957 but excludes \mathcal{J}_l . \mathcal{J}_l is the J factor for dSph, l , as defined in Equation (5.2), and it is a nuisance
 958 parameter whose value is unknown. $\log_{10} J_{l,\text{obs}}$ and $\sigma_{\log J_l}$ are obtained by fitting a log-normal
 959 function of $J_{l,\text{obs}}$ to the posterior distribution of J_l [50]. $\log_{10} J_{l,\text{obs}}$ and $\sigma_{\log J_l}$ values are provided
 960 in Table 5.1. The term \mathcal{J}_l constraining J_l is written as:

$$\mathcal{J}_l(J_l | J_{l,\text{obs}}, \sigma_{\log J_l}) = \frac{1}{\ln(10)J_{l,\text{obs}}\sqrt{2\pi}\sigma_{\log J_l}} \exp\left(-\frac{(\log_{10} J_l - \log_{10} J_{l,\text{obs}})^2}{2\sigma_{\log J_l}^2}\right). \quad (5.13)$$

961 Both the \mathcal{GS} and \mathcal{B} , displayed in Table 5.1, sets of J factors are used in this analysis. Equation (5.13)
 962 is also normalized, so it can also be interpreted as a probability density function (PDF) for $J_{l,\text{obs}}$.
 963 From Equation (7.1), we can also see that $\langle\sigma v\rangle$ and J_l are degenerate when computing $\mathcal{L}_{\text{dSph},l}$.
 964 Therefore, as noted in [51], it is sufficient to compute $\mathcal{L}_{\text{dSph},l}$ versus $\langle\sigma v\rangle$ for a fixed value of J_l .
 965 We used $J_{l,\text{obs}}(\mathcal{GS})$ reported in Tab. 5.1, in order to perform the profile of \mathcal{L} with respect to J_l .
 966 The degeneracy implies that for any $J'_l \neq J_{l,\text{obs}}$ (in practice in our case we used $J'_l = J_{l,\text{obs}}(\mathcal{B})$ to
 967 compute results from a different set of J factors):

$$\mathcal{L}_{\text{dSph},l}(\langle\sigma v\rangle; J'_l, \nu_l | \mathcal{D}_l) = \mathcal{L}_{\text{dSph},l}\left(\frac{J'_l}{J_{l,\text{obs}}} \langle\sigma v\rangle; J_{l,\text{obs}}, \nu_l | \mathcal{D}_l\right), \quad (5.14)$$

968 which is a straightforward rescaling operation that reduces the computational needs of the profiling
 969 operation since:

$$\mathcal{L}(\langle\sigma v\rangle; \hat{\nu} | \mathcal{D}_{\text{dSphs}}) = \prod_{l=1}^{N_{\text{dSphs}}} \max_{J_l} \left[\mathcal{L}_{\text{dSph},l}(\langle\sigma v\rangle; J_l, \hat{\nu}_l | \mathcal{D}_l) \times \mathcal{J}_l(J_l | J_{l,\text{obs}}, \sigma_{\log J_l}) \right]. \quad (5.15)$$

970 In addition, Eq. (5.14) enables the combination of data from different gamma-ray instruments and
 971 observed dSphs via tabulated values of $\mathcal{L}_{\text{dSph},l}$, or equivalently of λ from Eq. (5.11) as was done in
 972 this work, versus $\langle\sigma v\rangle$. $\mathcal{L}_{\text{dSph},l}$ is computed for a fixed value of J_l and profiled with respect to all
 973 instrumental nuisance parameters ν_l , these nuisance parameters are discussed in more detail below.
 974 These values are produced by each detector independently and therefore there is no need to share
 975 sensitive low-level information used to produce them, such as event lists. Figure 5.4 illustrates the
 976 multi-instrument combination technique used in this study with a comparison of the upper limit

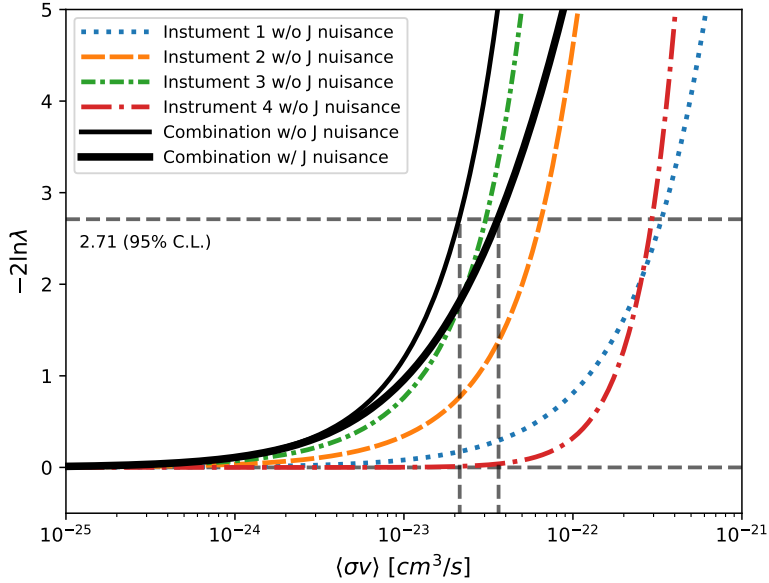


Figure 5.4 Illustration of the combination technique showing a comparison between $-2 \ln \lambda$ provided by four instruments (colored lines) from the observation of the same dSph without any J nuisance and their sum, *i.e.* the resulting combined likelihood (thin black line). According to the test statistics of Equation (5.7), the intersection of the likelihood profiles with the line $-2 \ln \lambda = 2.71$ indicates the 95% C.L. upper limit on $\langle\sigma v\rangle$. The combined likelihood (thin black line) shows a smaller value of upper limit on $\langle\sigma v\rangle$ than those derived by individual instruments. We also show how the uncertainties on the J factor effects the combined likelihood and degrade the upper limit on $\langle\sigma v\rangle$ (thick black line). All likelihood profiles are normalized so that the global minimum $\widehat{\langle\sigma v\rangle}$ is 0. We note that each profile depends on the observational conditions in which a target object was observed. The sensitivity of a given instrument can be degraded and the upper limits less constraining if the observations are performed in non-optimal conditions such as a high zenith angle or a short exposure time.

977 on $\langle\sigma v\rangle$ obtained from the combination of the observations of four experiments towards one dSph
 978 versus the upper limit from individual instruments. It also shows graphically the effect of the
 979 J -factor uncertainty on the combined observations.

980 The *partial* joint likelihood function for gamma-ray observations of each dSph ($\mathcal{L}_{\text{dSph},l}$) is
 981 written as the product of the likelihood terms describing the $N_{\text{exp},l}$ observations performed with
 982 any of our observatories:

$$\mathcal{L}_{\text{dSph},l} (\langle\sigma v\rangle; J_l, \nu_l | \mathcal{D}_l) = \prod_{k=1}^{N_{\text{exp},l}} \mathcal{L}_{lk} (\langle\sigma v\rangle; J_l, \nu_{lk} | \mathcal{D}_{lk}), \quad (5.16)$$

983 where each \mathcal{L}_{lk} term refers to an observation of the l -th dSph with associated k -th instrument

984 responses. $N_{\text{exp},l}$ varies from dSph to dSph and can be inferred from Table 5.2.

985 Each collaboration separately analyzes their data for \mathcal{D}_{lk} corresponding to dSph l and gamma-
986 ray detector k , using as many common assumptions as possible in the analysis. HAWC's treatment
987 was described earlier in Section 5.4.1 whereas the specifics of the remaining experiments is left to
988 the publication. We compute the values for the likelihood functions \mathcal{L}_{lk} (see Eq. (5.16)) for a fixed
989 value of J_l and profile over the rest of the nuisance parameters ν_{lk} . Then, values of λ from Eq. (5.11)
990 are computed as a function of $\langle \sigma v \rangle$, and shared using a common format. Results are computed for
991 seven annihilation channels, W^+W^- , ZZ , $b\bar{b}$, $t\bar{t}$, e^+e^- , $\mu^+\mu^-$, and $\tau^+\tau^-$ over 62 m_χ values between
992 5 GeV and 100 TeV provided in [44]. The $\langle \sigma v \rangle$ range is defined between 10^{-28} and $10^{-18} \text{cm}^3 \cdot \text{s}^{-1}$,
993 with 1001 logarithmically spaced values. The likelihood combination, i.e. Equation (5.12), and
994 profile over the J -factor to compute the profile likelihood ratio λ , Equation (5.11), are carried out
995 with two different public analysis software packages, namely `gLike` [52] and `LklCom` [53], that
996 provide the same results [54].

997 As mentioned previously, each experiment computes the \mathcal{L}_{lk} from Equation (5.11) differently.
998 The remainder of this section highlights the differences in this calculation across the experiments.
999 Four experiments, namely *Fermi*-LAT, H.E.S.S., HAWC and MAGIC, use a binned likelihood to
1000 compute the \mathcal{L}_{lk} . For these experiments, for each observation \mathcal{D}_{lk} of a given dSph l carried out
1001 using a given gamma-ray detector k , the binned likelihood function is:

$$\mathcal{L}_{lk} (\langle \sigma v \rangle; J_l, \nu_{lk} | \mathcal{D}_{lk}) = \prod_{i=1}^{N_E} \prod_{j=1}^{N_P} \left[\mathcal{P}(s_{lk,ij}(\langle \sigma v \rangle, J_l, \nu_{lk}) + b_{lk,ij}(\nu_{lk}) | N_{lk,ij}) \right] \times \mathcal{L}_{lk,\nu} (\nu_{lk} | \mathcal{D}_{\nu_{lk}}) \quad (5.17)$$

1002 where N_E and N_P are the number of considered bins in reconstructed energy and arrival direction,
1003 respectively; \mathcal{P} represents a Poisson PDF for the number of gamma-ray candidate events $N_{lk,ij}$
1004 observed in the i -th bin in energy and j -th bin in arrival direction, when the expected number is
1005 the sum of the expected mean number of signal events s_{ij} (produced by DM annihilation) and of
1006 background events b_{ij} ; $\mathcal{L}_{lk,\nu}$ is the likelihood term for the extra ν_{lk} nuisance parameters that vary
1007 from one instrument k to another. The expected counts for signal events s_{ij} for a given dSph l and

1008 detector k is given by:

$$s_{ij}(\langle\sigma\nu\rangle, J) = \int_{E'_{\min,i}}^{E'_{\max,i}} dE' \int_{P'_{\min,j}}^{P'_{\max,j}} d\Omega' \int_0^\infty dE \int_{\Delta\Omega_{tot}} d\Omega \int_0^{T_{\text{obs}}} dt \frac{d^2\Phi(\langle\sigma\nu\rangle, J)}{dEd\Omega} \text{IRF}(E', P' | E, P, t) \quad (5.18)$$

1009 where E' and E are the reconstructed and true energies, P' and P the reconstructed and true
1010 arrival directions; $E'_{\min,i}$, $P'_{\min,j}$, $E'_{\max,i}$, and $P'_{\max,j}$ are their lower and upper limits of the i -th
1011 energy bin and the j -th arrival direction bin; T_{obs} is the (dead-time corrected) total observation
1012 time; t is the time along the observations; $d^2\Phi/dEd\Omega$ is the DM flux in the source region (see
1013 Equation (7.1)); and $\text{IRF}(E', P' | E, P, t)$ is the IRF, which can be factorized as the product of the
1014 effective collection area of the detector $A_{\text{eff}}(E, P, t)$, the PDFs for the energy estimator $f_E(E' | E, t)$,
1015 and arrival direction $f_P(P' | E, P, t)$ estimators. Note that for Fermi-LAT, HAWC, MAGIC, and
1016 VERITAS the effect of the finite angular resolution is taken into account through the convolution
1017 of $d\Phi/dEd\Omega$ with f_P in Equation (5.18), whereas in the cases of H.E.S.S. f_P is approximated by a
1018 delta function. This approximation has been made in order to maintain compatibility of the result
1019 with what has been previously published. The difference introduced by this approximation is $< 5\%$
1020 for all considered dSphs. A more comprehensive review of the differences between the analyses of
1021 different instruments can be found in [25].

1022 5.5 HAWC Results

1023 13 of the 20 dSphs considered for the Glory Duck analysis are within HAWC's field of view.
1024 These dSph are analyzed for emission from DM annihilation according to the likelihood method
1025 described in Section 5.4. The 13 likelihood profiles are then stacked to synthesize a combined
1026 limit on the dark matter cross-section, $\langle\sigma\nu\rangle$. This combination is done for the 7 SM annihilation
1027 channels used in the Glory Duck analysis. Figure 5.5 shows the combined limit for all annihilation
1028 channels with HAWC only observations. We also perform 300 studies of Poisson trials on the
1029 background. These trials are used to produce HAWC sensitivities with $\pm 1\sigma$ and $\pm 2\sigma$ uncertainty
1030 bands which were shared with the other collaborators for combination. The results on fitting to
1031 HAWC's Poisson trials of the DM hypothesis is shown in Figure 5.7 for all the DM annihilation
1032 channels studied for Glory Duck.

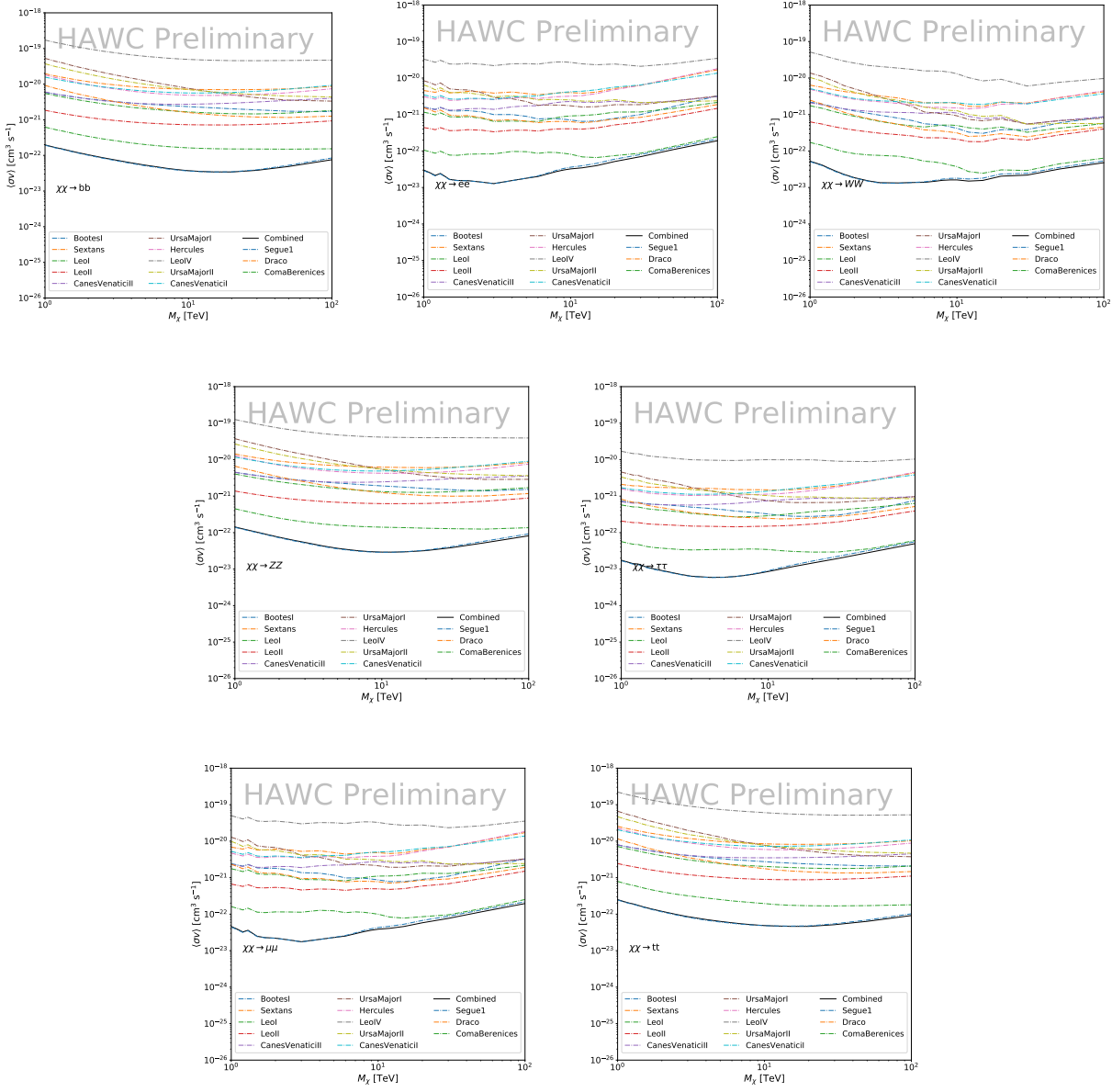


Figure 5.5

1033 No DM was found in HAWC observations. HAWC's limits are dominated by the dSphs Segue1
 1034 and Coma Berenices. The remaining 11 dSphs do not contribute significantly to the limit because
 1035 they are at high zenith and/or have much smaller J factors. Even though some remaining dSphs
 1036 have large J factors, they are towards the edge of HAWC's field of view where HAWC analysis is
 1037 less sensitive.

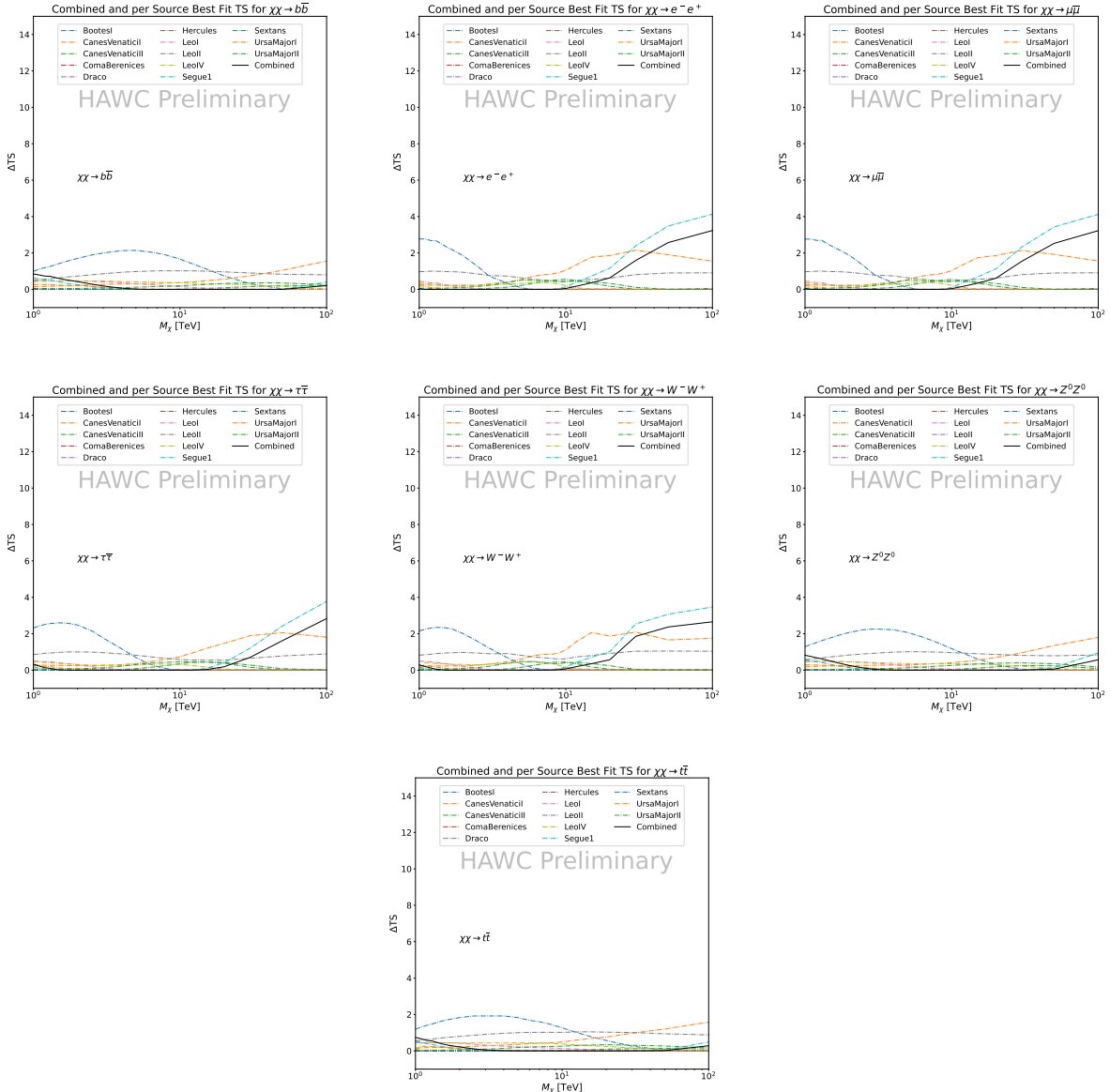


Figure 5.6 HAWC TS values for best fit $\langle\sigma v\rangle$ versus m_χ for seven SM annihilation channels with J factors from \mathcal{GS} . The solid black line shows the combined best fit TS values. The colored, dashed lines are the TS values for each of the 13 sources HAWC studied.

1038 5.6 Glory Duck Combined Results

1039 The crux of this analysis is that HAWC's results are combined with 4 other gamma-ray observa-
 1040 tories: Fermi-LAT, H.E.S.S., MAGIC, and VERITAS. No significant DM emission was observed
 1041 by any of the five instruments. We present the upper limits on $\langle\sigma v\rangle$ assuming seven independent
 1042 DM self annihilation channels, namely W^+W^- , Z^+Z^- , $b\bar{b}$, $t\bar{t}$, e^+e^- , $\mu^+\mu^-$, and $\tau^+\tau^-$. The 68%

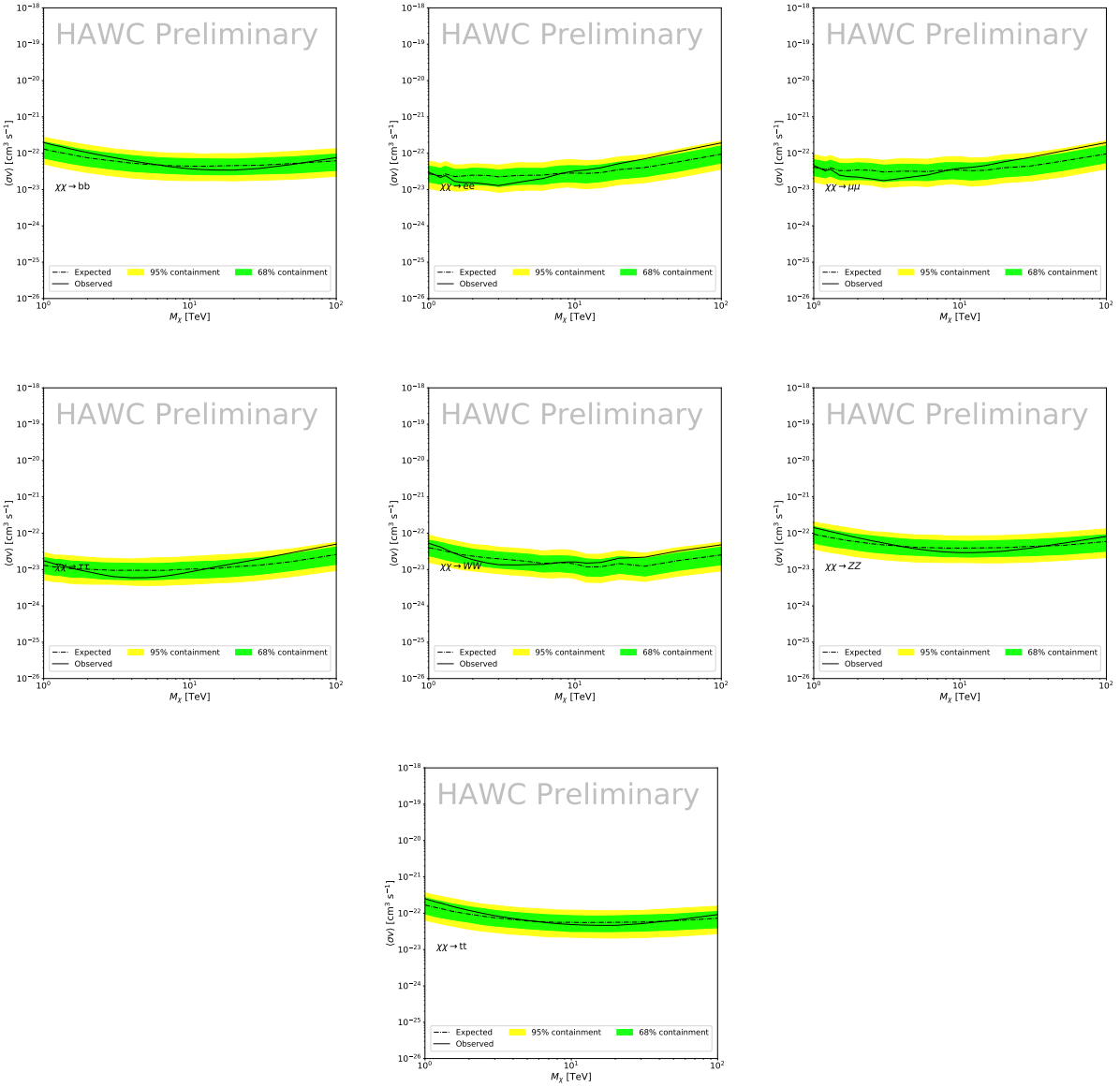


Figure 5.7 HAWC Brazil bands at 95% confidence level on $\langle\sigma v\rangle$ versus DM mass for seven annihilation channels with J -factors from \mathcal{GS} [55]. The solid line represents the combined limit from 13 dSphs. The dashed line is the expected limit. The green band is the 68% containment. The yellow band is the 95% containment.

1043 and 95% containment bands are produced from 300 Poisson realizations of the null hypothesis
 1044 corresponding to each of the combined datasets. These 300 realizations are combined identically
 1045 to dSph observations. The containment bands and the median are extracted from the distribution
 1046 of resulting limits on the null hypothesis. These 300 realizations are obtained either by fast simu-
 1047 lations of the OFF observations, for H.E.S.S., MAGIC, VERITAS, and HAWC, or taken from real

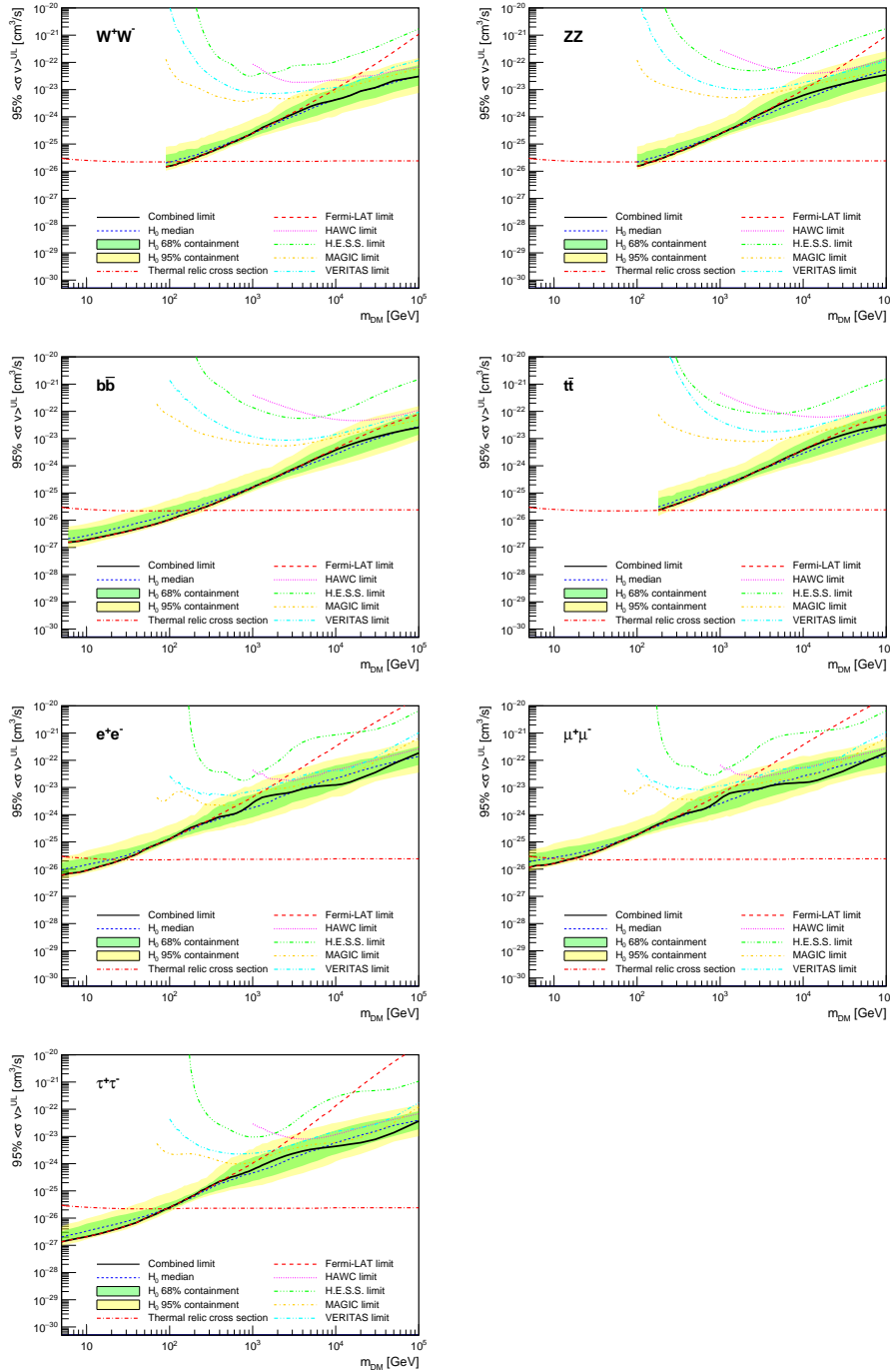


Figure 5.8 Upper limits at 95% confidence level on $\langle\sigma v\rangle$ in function of the DM mass for eight annihilation channels, using the set of J factors from Ref. [55] (\mathcal{GS} set in Table 5.1). The black solid line represents the observed combined limit, the black dashed line is the median of the null hypothesis corresponding to the expected limit, while the green and yellow bands show the 68% and 95% containment bands. Combined upper limits for each individual detector are also indicated as solid, colored lines. The value of the thermal relic cross-section in function of the DM mass is given as the red dotted-dashed line [56].

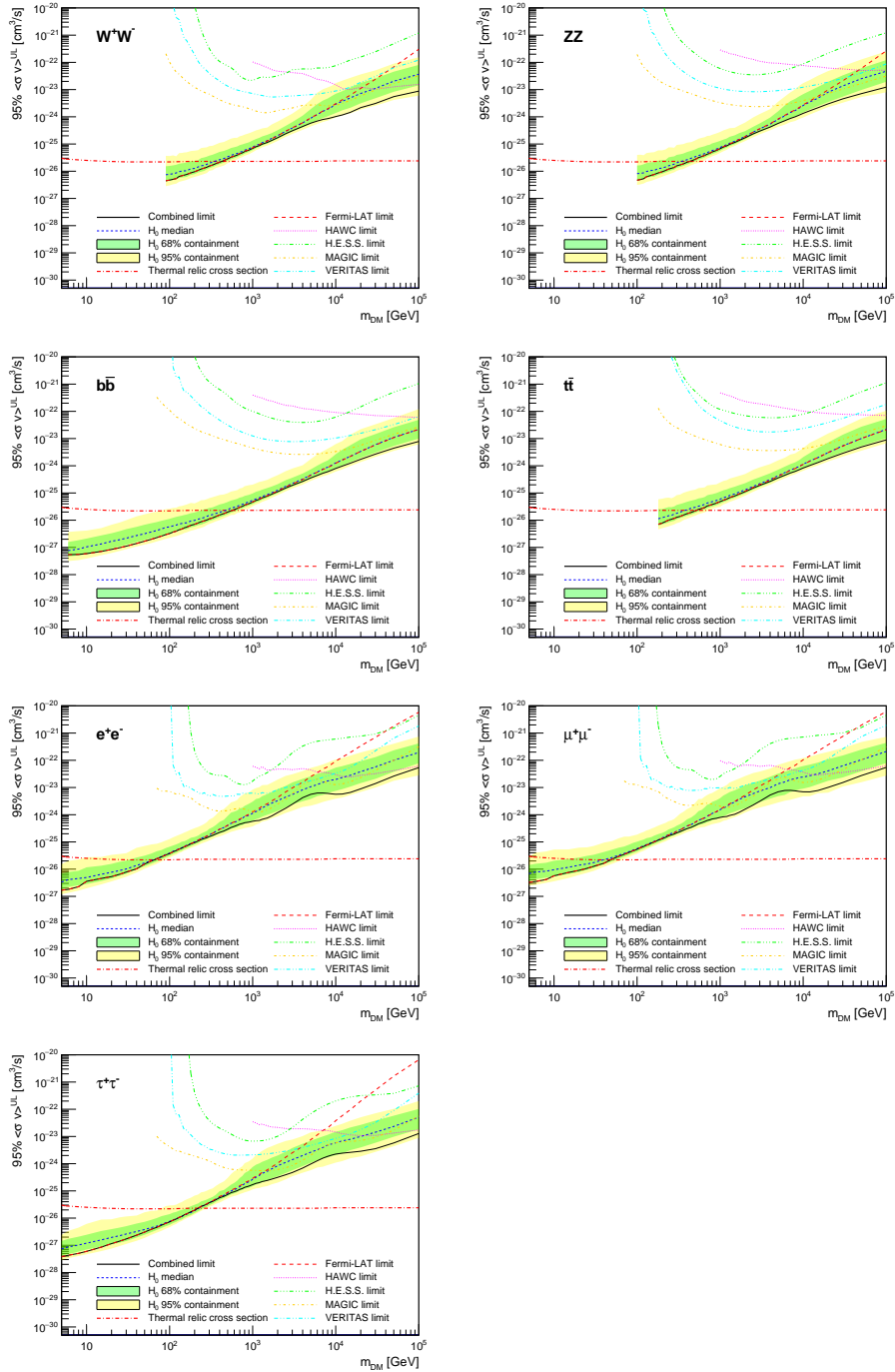


Figure 5.9 Same as Fig. 5.8, using the set of J factors from Ref. [49, 57] (\mathcal{B} set in Table 5.1).

1048 observations of empty fields of view in the case of Fermi-LAT [50, 58, 59].

1049 The obtained limits are shown in Figure 5.8 for the \mathcal{GS} set of J -factors [55] and in Figure 5.9
1050 for the \mathcal{B} set of J -factors [49, 57]. The combined limits are presented with their 68% and 95%
1051 containment bands, and are expected to be close to the median limit when no signal is present.

1052 We observe agreement with the null hypothesis for all channels, within 2σ standard deviations,
1053 between the observed limits and the expectations given by the median limits. Limits obtained from
1054 each detector are also indicated in the figures, where limits for all dSphs observed by the specific
1055 instrument have been combined.

1056 Below ~ 300 GeV, the *Fermi*-LAT dominates the DM limits for all annihilation channels. From
1057 ~ 300 GeV to ~ 2 TeV, *Fermi*-LAT continues to dominate for the hadronic and bosonic DM channels,
1058 yet the IACTs (H.E.S.S., MAGIC, and VERITAS) and *Fermi*-LAT all contribute to the limit for
1059 leptonic DM channels. For DM masses between ~ 2 TeV to ~ 10 TeV, the IACTs dominate leptonic
1060 DM annihilation channels, whereas both the *Fermi*-LAT and the IACTs dominate bosonic and
1061 hadronic DM annihilation channels. From ~ 10 TeV to ~ 100 TeV, both the IACTs and HAWC
1062 contribute significantly to the leptonic DM limit. For hadronic and bosonic DM, the IACTs and
1063 *Fermi*-LAT both contribute strongly.

1064 We notice that the limits computed using the \mathcal{B} set of J -factor are always better compared to the
1065 ones calculated with the \mathcal{GS} set. For the W^+W^- , Z^+Z^- , $b\bar{b}$, and $t\bar{t}$ channels, the ratio between the
1066 limits computed with the two sets of J -factor is varying between a factor of ~ 3 and ~ 5 depending
1067 on the energy, with the largest ratio around 10 TeV. For the channels e^+e^- , $\mu^+\mu^-$, and $\tau^+\tau^-$, the
1068 ratio lies between ~ 2 to ~ 6 , being maximum around 1 TeV. Examining Figure 5.16 and Figure 5.17
1069 in Section 5.8, these differences are explained by the fact that the \mathcal{B} set provides higher J -factors
1070 for the majority of the studied dSphs, with the notable exception of Segue I. The variation on the
1071 ratio of the limits for the two sets is due to different dSph dominating the limits depending on the
1072 energy. One set, \mathcal{B} , pushes the range of which thermal cross-section which can be excluded to
1073 higher mass. This comparison demonstrates the magnitude of systematic uncertainties associated
1074 with the choice of the J -factor calculation. The \mathcal{GS} and \mathcal{B} sets present a difference in the limits for
1075 all channels of about This difference is explained, see Figure 5.16 and Figure 5.17, by the fact that
1076 the \mathcal{B} set provides higher J -factors for all dSph except for Segue I.

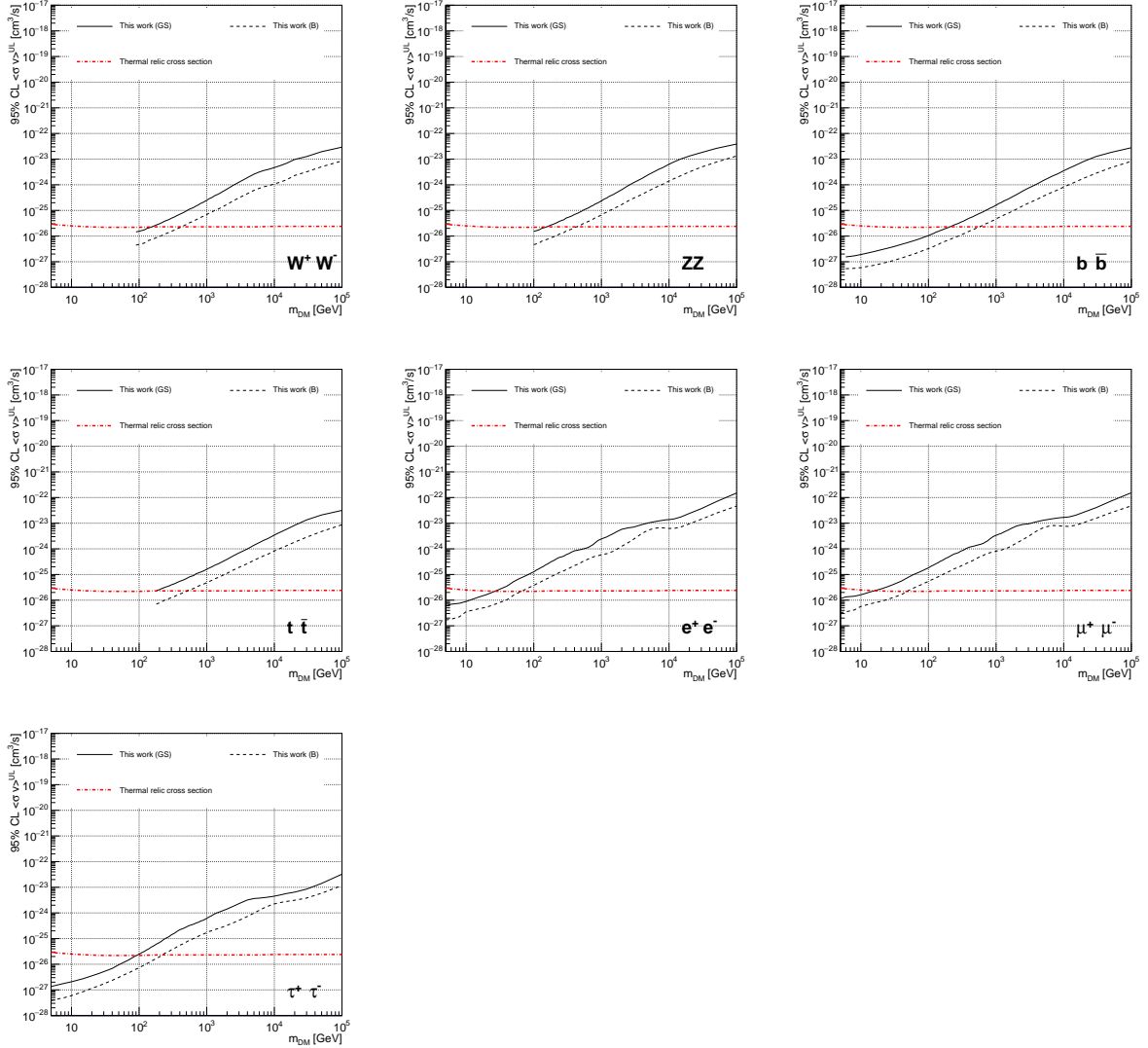


Figure 5.10 Comparisons of the combined limits at 95% confidence level for each of the eight annihilation channels when using the J factors from Ref. [55] (\mathcal{GS} set in Table 5.1), plain lines, and the J factor from Ref. [49, 57] (\mathcal{B} set in Table 5.1), dashed lines. The cross-section given by the thermal relic is also indicated [56].

1077 5.7 HAWC Systematics

1078 5.7.1 Inverse Compton Scattering

1079 The DM-DM annihilation channels produce many high energy electrons regardless of the
 1080 primary annihilation channel. These high energy electrons can produce high energy gamma-rays
 1081 through Inverse Compton Scattering (ICS). If this effect is strong, it would change the morphology
 1082 of the source and increase the total expected gamma-ray counts from any source. The PPPC [44]

1083 provides tools in Mathematica for calculating the impact of ICS for an arbitrary location in the
1084 sky for a specified annihilation channel. We calculated the change in gamma-ray counts for DM
1085 annihilation to primary $e\bar{e}$ for RA and Dec corresponding to Segue1 and Coma Berenices. These
1086 dSphs were chosen because they are the strongest contributors to the limit. $e\bar{e}$ was selected because
1087 it would have the largest number of high energy electrons. The effect was found to be on the order
1088 of 10^{-7} on the gamma-ray spectrum. As a result, this systematic is not considered in our analysis.

1089 **5.7.2 Point Source Versus Extended Source Limits**

1090 The previous DM search toward dSph approximated the dSphs as point sources [46]. In
1091 this analysis, the dSphs are implemented as extended with J-factor distributions following those
1092 produced by [55]. The resolution of the cited map is much finer than HAWC's angular resolution.
1093 The vast majority of the J-factor distribution is represented on the central HAWC pixel of the dSph
1094 spatial map. However, the neighboring 8 pixels are not negligible and contribute to our limit.

1095 Figure 5.11 shows a substantial improvement to the limit for Segue1. Fig. 5.12 however showed
1096 identical limits. These disparities are best explained by the relative difference in their J-Factors.
1097 Both dSphs pass almost overhead the HAWC detector, however Segue1 has the larger J-Factor
1098 between the two. Adjacent pixels to the central pixel will therefore contribute to the limits. This is
1099 the case for other dSph that are closer to the zenith of the HAWC detector.

1100 Comparison plots for all sources and the combined limit can be found in the sandbox for the
1101 Glory Duck project.

1102 **5.7.3 Impact of Pointing Systematic**

1103 During the analysis it was discovered that directional reconstruction of gamma-rays had a
1104 systematic bias at large zenith angles. Slides describing this systematic can be found [here](#). Shown
1105 on the presentation is dependence on the pointing systematic on declination. New spatial profiles
1106 were generated for every dSph and limits were computed for the adjusted declination.

1107 Section 5.7.3 demonstrates the impact of this systematic for all DM annihilation channels
1108 studied by HAWC. The impact is a tiny improvement, yet mostly identical, to the combined limits.

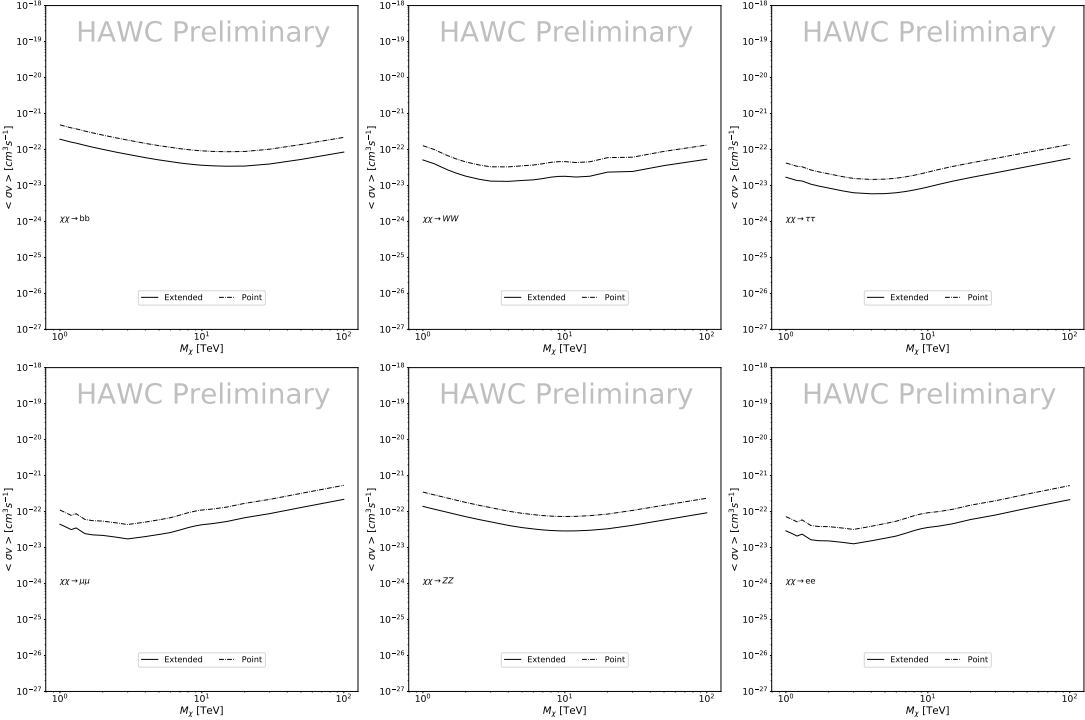


Figure 5.11 Comparisons of the combined limits at 95% confidence level for a point source analysis and extended source using [55] \mathcal{GS} J-factor distributions and PPPC [44] annihilation spectra. Shown are the limits for Segue1 which will have the most significant impact on the combined limit. 6 of the 7 DM annihilation channels are shown. Solid lines are extended source studies. Dashed lines are point source studies. Overall, the extended source analysis improves the limit by a factor of 2.

1109 5.8 J-factor distributions

1110 5.8.1 Numerical integration of \mathcal{GS} maps

1111 It was discovered well after the HAWC analysis was completed that the published tables from
 1112 \mathcal{GS} [45] quoted median J -factors were computed in a non-trivial manner. The assumption myself
 1113 and collaborators had been that the published tables represented the J -factor as a function of θ for
 1114 the best global fit model on a per-source basis. However, this is not the case. Instead, what is
 1115 published are the best fit model for each dwarf that only considers stars up to the angular separation
 1116 θ . Therefore, the model is changing for each value of θ for each dwarf. Yet, the introduced features
 1117 from unique models at each θ are much smaller than the angular resolution of HAWC. It is not
 1118 expected for these effects to impact the limits and TS greatly as a result.

1119 Median J -factor model profiles were provided by the authors. New maps were generated

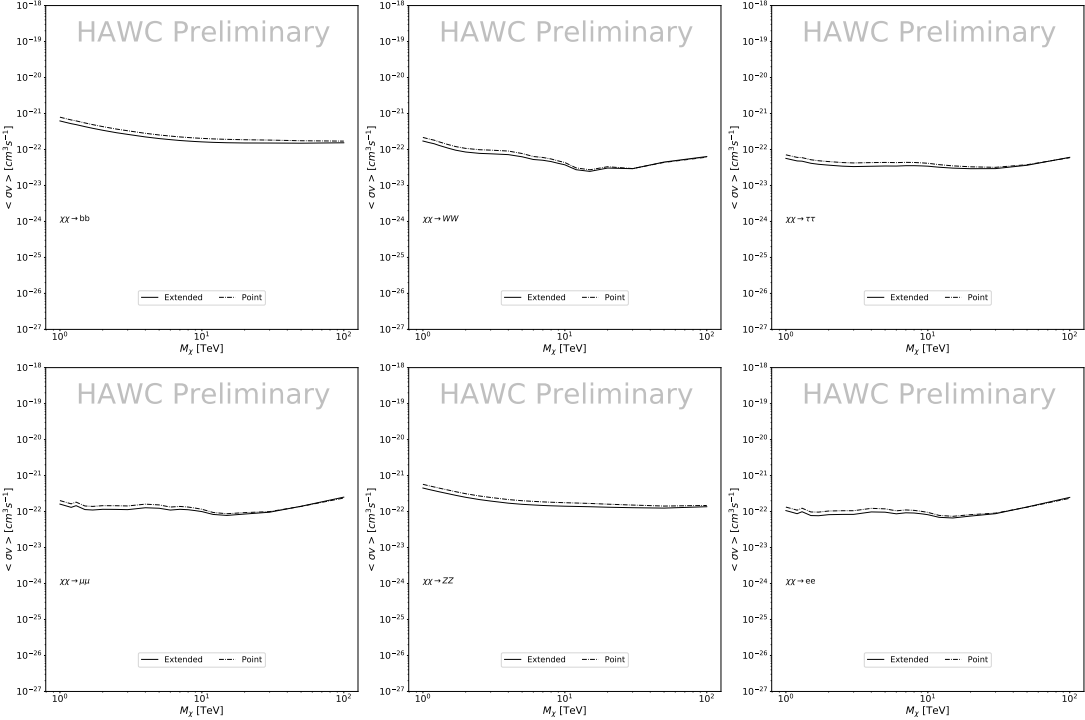


Figure 5.12 Same as Fig. 5.11 on Coma Berenices. This dSph also contributes significantly to the limit. The limits are identical in this case.

and analyzed for Segue1 and Coma Berenices. Figure 5.14 shows the differential between maps generated with the method from Section 5.8.1 and from the authors of [45]. These maps were reanalyzed for all SM DM annihilation channels. Upper limits for these channels are shown in Figure 5.15

From Figure 5.15, we can see that the impact of these model difference was no substantial. The observed impact was a fractional effect which is much smaller than the impact from selecting another DM spatial distribution model as was shown in Figure 5.10.

5.8.2 \mathcal{GS} Versus \mathcal{B} spatial models

We show in this appendix a comparison between the J -factors computed by Geringer-Sameth *et al.* [55] (the \mathcal{GS} set) and the ones computed by Bonnivard *et al.* [49, 57] (the \mathcal{B} set). The \mathcal{GS} J -factors are computed through a Jeans analysis of the kinematic stellar data of the selected dSphs, assuming a dynamic equilibrium and a spherical symmetry for the dSphs. They adopted the generalized DM density distribution, known as Zhao-Hernquist, introduced by [47], carrying

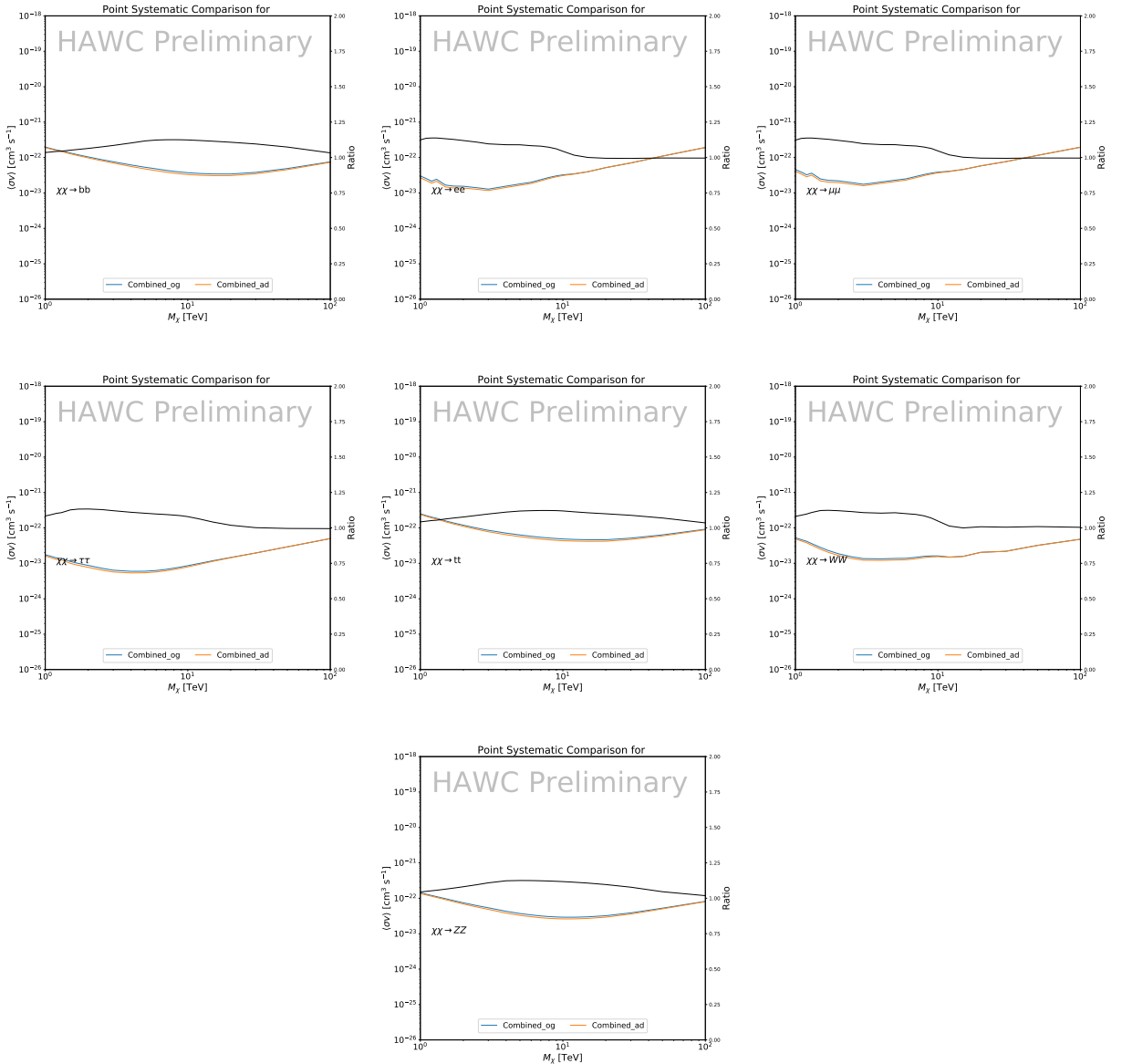


Figure 5.13 Comparison of combined limits when correcting for HAWC's pointing systematic. All DM annihilation channels are shown. The solid black line is the ratio between published limit to the declination corrected limit. The blue solid line or "Combined_og" represented the limits computed for Glory Duck. The solid orange line or "Combined_ad" represented the limits computed after correcting for the pointing systematic.

1133 three additional index parameters to describe the inner and outer slopes, and the break of the
 1134 density profile. Such a profile parametrization allows the reduction of the theoretical bias from
 1135 the choice of a specific radial dependency on the kinematic data. In other words, the increase of
 1136 free parameters with the use of the Zhao-Hernquist profile allows a better description of the mass

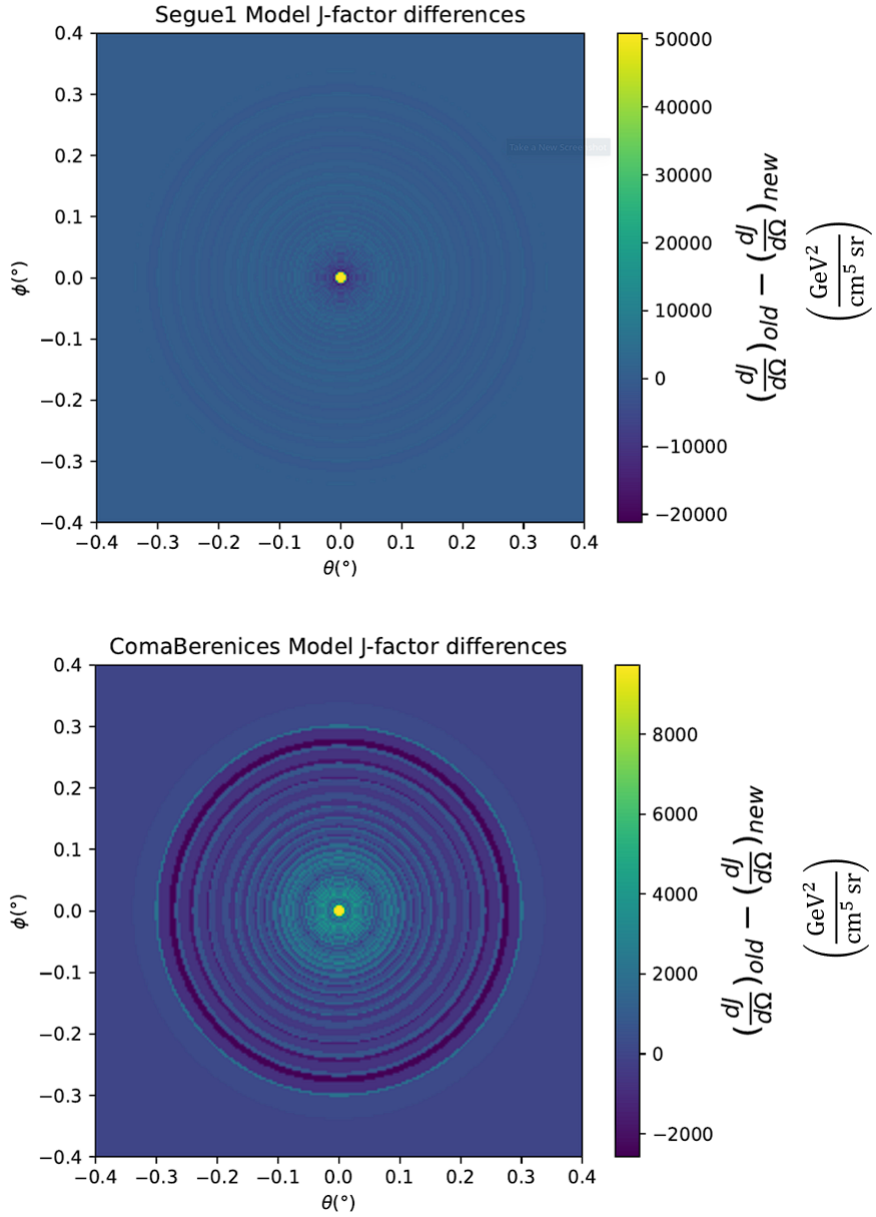


Figure 5.14 Differential map of dJ/Ω from model built in Section 5.8.1 and profiles provided directly from authors. (Top) Differential from Segue1. (bottom) Differential from Coma Berenices. Note that their scales are not the same. Segue1 shows the deepest discrepancies which is congruent with its large uncertainties. Both models show anuli where unique models become apparent.

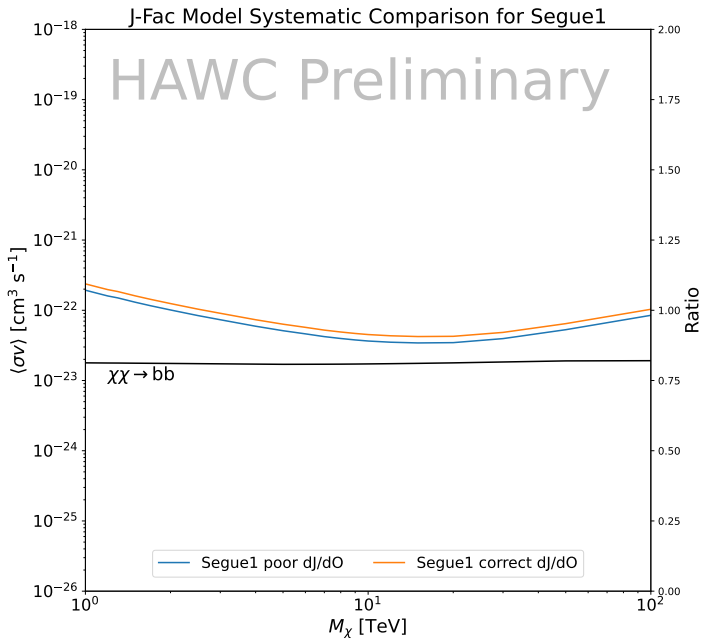
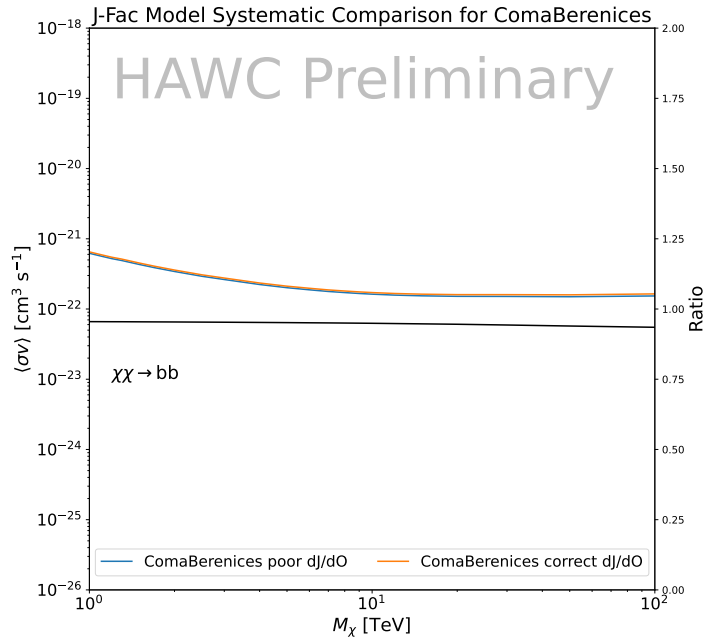


Figure 5.15 HAWC limits for Coma Berenices (top) and Segue1 (bottom) for two different map sets. Blue lines are limits calculated on maps with poor model representation. Orange lines are limits calculated on spatial profiles provided by the authors of [45]. Black line is the ratio of the poor spatial model limits to the corrected spatial models. The left y-axis measures $\langle \sigma v \rangle$ for the blue and orange lines. The right y-axis measures the ratio and is unitless.

1137 density distribution of dark matter.

1138 In addition, a constant velocity anisotropy profile and a Plummer light profile [60] for the stellar
1139 distribution were assumed. The velocity anisotropy profile depends on the radial and tangential
1140 velocity dispersion. However, its determination remains challenging since only the line-of-sight
1141 velocity dispersion can be derived from velocity measurements. Therefore, the parametrization of
1142 the anisotropy profile is obtained from simulated halos (see [61] for more details). They provide the
1143 values of the J -factors of regions extending to various angular radius up to the outermost member
1144 star.

1145 The \mathcal{B} J -factors were computed through a Jeans analysis taking into account the systematic
1146 uncertainties induced by the DM profile parametrization, the radial velocity anisotropy profile, and
1147 the triaxiality of the halo of the dwarf galaxies. They performed a more complete study of the dSph
1148 kinematics and dynamics than \mathcal{GS} for the determination of the J -factor. Conservative values of the
1149 J -factors where obtained using an Einasto DM density profile [62], a realistic anisotropy profile
1150 known as the Baes & Van Hese profile [63] which takes into account that the inner regions can be
1151 significantly non-isotropic, and a Zhao-Hernquist light profile [47].

1152 For both sets, J -factor values are provided for all dSphs as a function of the radius of the
1153 integration region [55, 49, 57]. Table 5.1 shows the heliocentric distance and Galactic coordinates
1154 of the twenty dSphs, together with the two sets of J -factor values integrated up to the outermost
1155 observed star for \mathcal{GS} and the tidal radius for \mathcal{B} . Both J -factor sets were derived through a Jeans
1156 analysis based on the same kinematic data, except for Draco where the measurements of [64] have
1157 been adopted in the computation of the \mathcal{B} value. The computations for producing the \mathcal{GS} and \mathcal{B}
1158 samples differ in the choice of the DM density, velocity anisotropy, and light profiles, for which the
1159 set \mathcal{B} takes into account some sources of systematic uncertainties.

1160 Figure 5.16 and Figure 5.17 show the comparisons for the J -factor versus the angular radius
1161 for each of the 20 dSphs used in this study. The uncertainties provided by the authors are also
1162 indicated in the figures. For the \mathcal{GS} set, the computation stops at the angular radius corresponding
1163 to the outermost observed star, while for the \mathcal{B} set, the computation stops at the angular radius

1164 corresponding to the tidal radius.

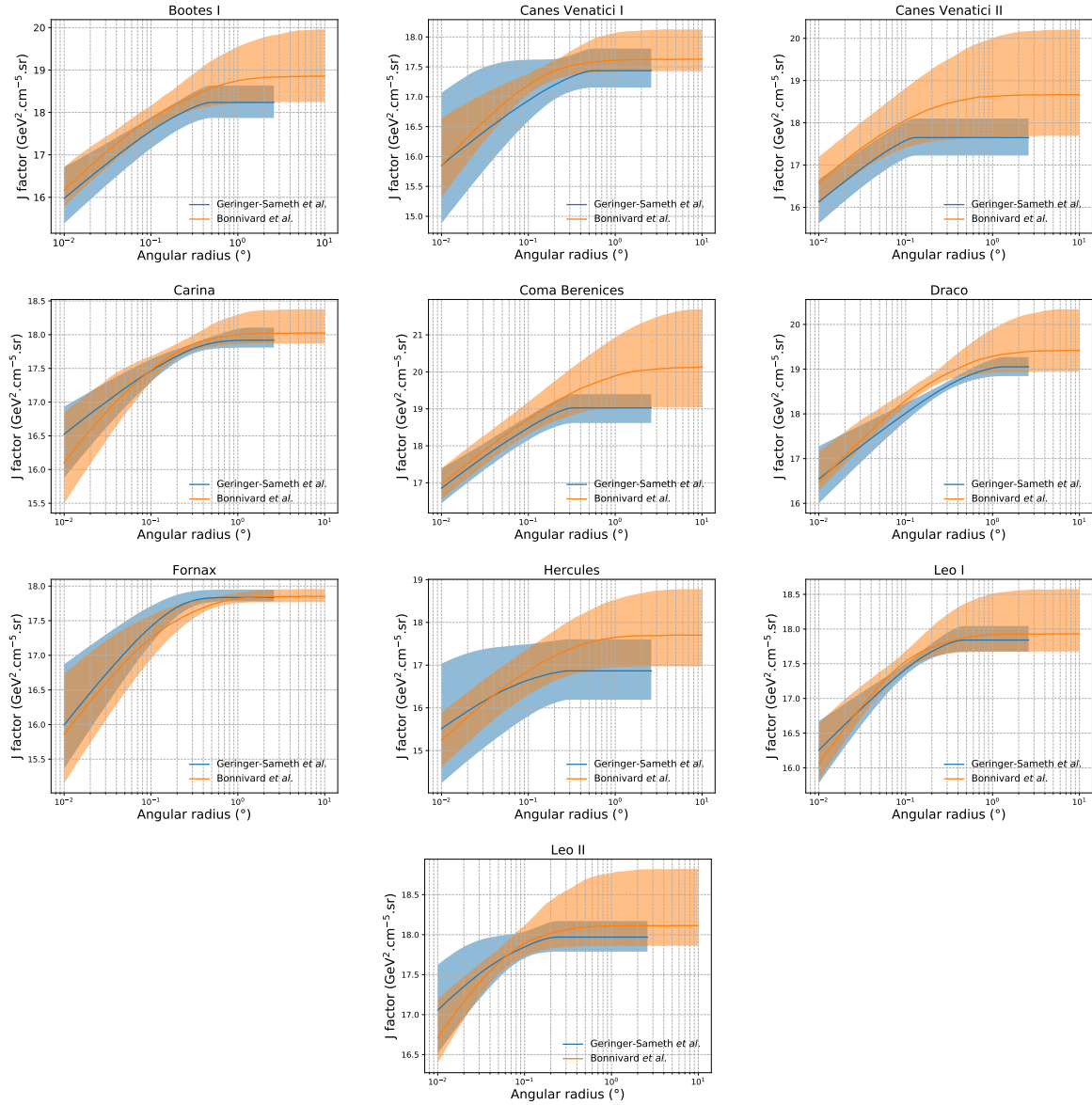


Figure 5.16 Comparisons between the J -factors versus the angular radius for the computation of J factors from Ref. [55] (\mathcal{GS} set in Table 5.1) in blue and for the computation from Ref. [49, 57] (\mathcal{B} set in Tab. 5.1) in orange. The solid lines represent the central value of the J -factors while the shaded regions correspond to the 1σ standard deviation.

1165 5.9 Discussion and Conclusions

1166 In this multi-instrument analysis, we have used observations of 20 dSphs from the gamma-ray
 1167 telescopes Fermi-LAT, H.E.S.S., MAGIC, VERITAS, and HAWC to perform a collective DM
 1168 search annihilation signals. The data were combined across sources and detectors to significantly

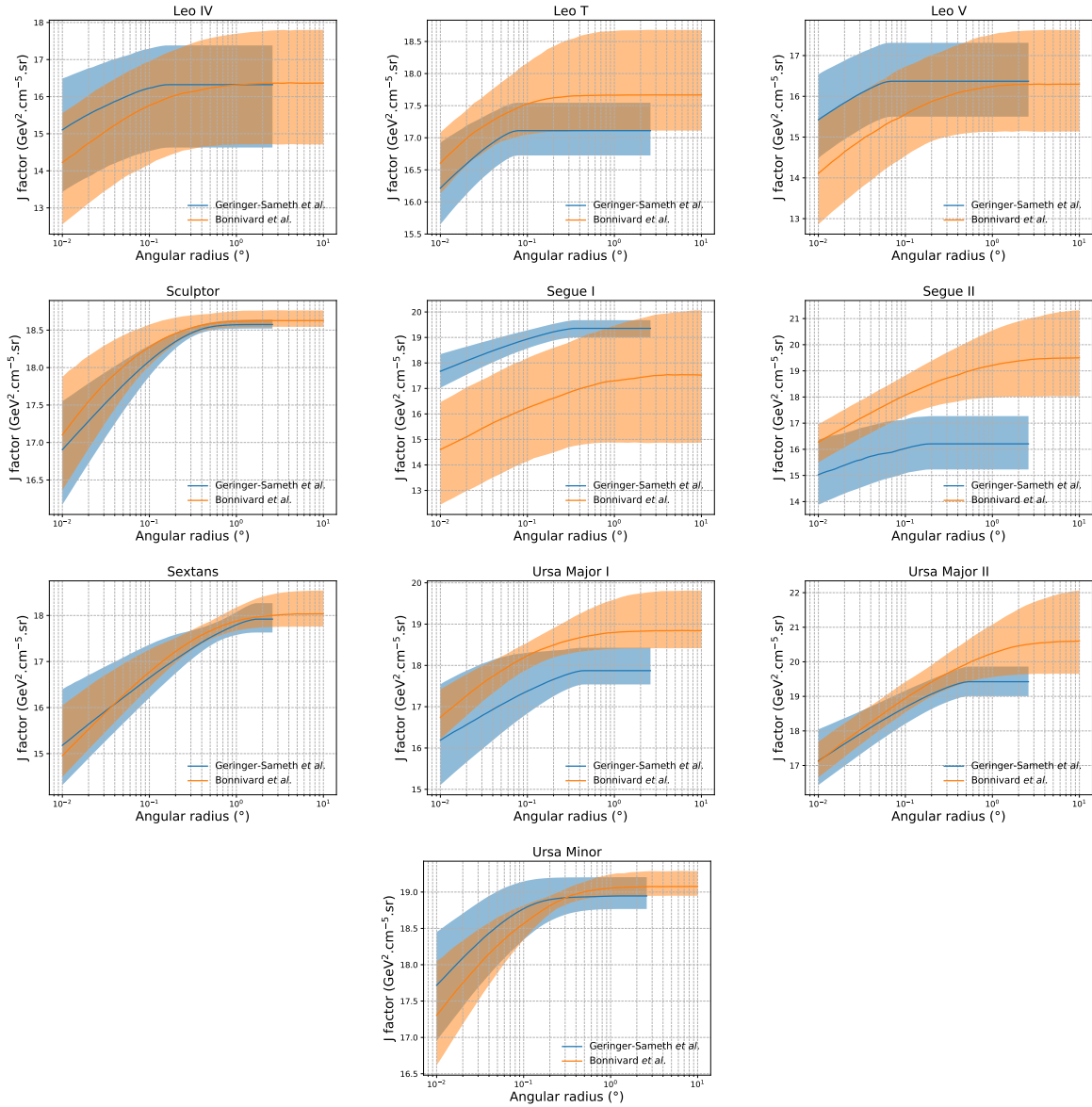


Figure 5.17 Comparisons between the J -factors versus the angular radius for the computation of J factors from Ref. [55] (\mathcal{GS} set in Tab. 5.1) in blue and for the computation from Ref. [49, 57] (\mathcal{B} set in Tab. 5.1) in orange. The solid lines represent the central value of the J -factors while the shaded regions correspond to the 1σ standard deviation.

increase the sensitivity of the search. We have observed no significant deviation from the null, no DM hypothesis, and so present our results in terms of upper limits on the annihilation cross-section for seven potential DM annihilation channels.

Fermi-LAT brings the most stringent constraints for continuum channels below approximately 1 TeV. The remaining detectors dominate at higher energies. Overall, for multi-TeV DM mass,

1174 the combined DM constraints from all five telescopes are 2-3 times stronger than any individual
1175 telescope for multi-TeV DM.

1176 Derived from observations of many dSphs, our results produce robust limits given the DM
1177 content of the dSphs is relatively well constrained. The obtained limits span the largest mass
1178 range of any WIMP DM search. Our combined analysis improves the sensitivity over previously
1179 published results from each detector which produces the most stringent limits on DM annihilation
1180 from dSphs. These results are based on deep exposures of the most promising known dSphs with
1181 the currently most sensitive gamma-ray instruments. Therefore, our results constitute a legacy of
1182 a generation of gamma-ray instruments on WIMP DM searches towards dSphs. Our results will
1183 remain the reference in the field until a new generation of more sensitive gamma-ray instruments
1184 begin operations, or until new dSphs with higher J -factors are discovered.

1185 This analysis serves as a proof of concept for future multi-instrument and multi-messenger
1186 combination analyses. With this collaborative effort, we have managed to sample over four orders
1187 in magnitude in gamma-ray energies with distinct observational techniques. Determining the nature
1188 of DM continues to be an elusive and difficult problem. Larger datasets with diverse measurement
1189 techniques could be essential to tackling the DM problem. A future collaboration using similar
1190 techniques as the ones described in this paper could grow even beyond gamma rays. The models we
1191 used for this study include annihilation channels with neutrinos in the final state. Advanced studies
1192 could aim to merge our results with those from neutrino observatories with large data sets. Efforts
1193 are already underway to add data from the IceCube, ANTARES, and KM3NeT observatories to
1194 these gamma-ray results.

1195 From this work, a selection of the best candidates for observations, according to the latest
1196 knowledge on stellar dynamics and modelling techniques for the derivation of the J -factors on
1197 the potential dSphs targets, is highly desirable at the time that new experiments are starting their
1198 dark matter programs using dSphs. Given the systematic uncertainty inherent to the derivation of
1199 the J -factors, an informed observational strategy would be to select both objects with the highest
1200 J -factors that could lead to DM signal detection, and objects with robust J -factor predictions, i.e.

1201 with kinematic measurements on many bright stars, which would strengthen the DM interpretation
1202 reliability of the observation outcome.

1203 This analysis combines data from multiple telescopes to produce strong constraints on astro-
1204 physical objects. From this perspective, these methods can be applied beyond just DM searches.
1205 Almost every astrophysical study can benefit from multi-telescope, multi-wavelength gamma-ray
1206 studies. We have enabled these telescopes to study the cosmos with greater precision and detail.
1207 Many astrophysical searches can benefit from multi-instrument gamma-ray studies, for which our
1208 analysis lays the foundation.

CHAPTER 6

MULTITHREADING HAWC ANALYSES FOR DARK MATTER SEARCHES

6.1 Introduction

HAWC's current software suite, plugins to 3ML and HAL [54, 42], do not fully utilize computational advancements of recent decades. Said advancements include the proliferation of Graphical Processing Units (GPUs), and multithreading on multicore processors. The analysis described in chapter 5 took up to 3 months of wall time waiting for the full gambit of data analysis and simulation of background to compute. Additionally, with the updated 2D energy binning scheme, f_{hit} and Neural Network (NN), the time needed to compute expected to grow. Although excessive computing time was, in part, from an intense use of a shared computing cluster, it was evident that there was room for improvement. In HAWC's next generation dSph DM search, I decided to develop codes that would utilize the multicore processors on modern high performance computing clusters. The results of this work are featured in this chapter and brought a human timing improvement to computation that scales approximately as $1/N$ where N is the number of threads.

6.2 Dataset and Background

This section enumerates the data and background methods used for HAWC's multithreaded study of dSphs. Section 6.2.1 and Section 6.2.2 are most useful for fellow HAWC collaborators looking to replicate a multithreaded dSph DM search.

6.2.1 Itemized HAWC files

These files are only available withing HAWC's internal documentation and collaborators. They are not meant for public access, and are presented here so that HAWC collaborators can reproduce results accurately.

- Detector Resolution: `refit-Pass5-Final-NN-detRes-zenith-dependent.root`
- Data Map: `Pass5-Final-NN-maptree-ch103-ch1349-zenith-dependent.root`
- Spectral Dictionary: `HDMspectra_dict_gamma.npy`

1233 **6.2.2 Software Tools and Development**

1234 This analysis was performed using HAL and 3ML [42, 43] in Python3. I built software
1235 in collaboration with Michael Martin and Letrell Harris to implement the *Dark Matter Spectra*
1236 *from the Electroweak to the Planck Scale* (HDM) [65] and dSphs spatial model from [66] for
1237 HAWC analysis. A NumPy dictionary of HDM, `HDMspectra_dict_gamma.npy`, was made for
1238 portability within the collaboration. These dictionaries were generated from the [git repository](#) [65].
1239 The analysis was performed using the Neural Network energy estimator for Pass 5.F. A description
1240 of this estimator was provided in chapter 3. [TODO: Define a subsection when it's written](#), and its
1241 key, relevant improvements are an improved energy estimation and improved sensitivities at higher
1242 zenith angles. All other software used for data analysis, DM profile generation, and job submission
1243 to SLURM are also kept in my sandbox in the [Dark Matter HAWC](#) project. The above repository
1244 also incorporates the model inputs used previously in Glory Duck, described in chapter 5, so Glory
1245 Duck remains compatible with modern software.

1246 **6.2.3 Data Set and Background Description**

1247 The HAWC data maps used for this analysis contain 2565 days of data between runs 2104 and
1248 7476. They were generated from pass 5.f reconstruction. The analysis is performed using the NN
1249 energy estimator with bin list:

1250 `B1C0Ea, B1C0Eb, B1C0Ec, B1C0Ed, B1C0Ee, B2C0Ea, B2C0Eb, B2C0Ec, B2C0Ed, B2C0Ee,`
1251 `B3C0Ea, B3C0Eb, B3C0Ec, B3C0Ed, B3C0Ee, B3C0Ef, B4C0Eb, B4C0Ec, B4C0Ed, B4C0Ee,`
1252 `B4C0Ef, B5C0Ec, B5C0Ed, B5C0Ee, B5C0Ef, B5C0Eg, B6C0Ed, B6C0Ee, B6C0Ef, B6C0Eg,`
1253 `B6C0Eh, B7C0Ee, B7C0Ef, B7C0Eg, B7C0Eh, B7C0Ei, B8C0Ee, B8C0Ef, B8C0Eg, B8C0Eh,`
1254 `B8C0Ei, B8C0Ej, B9C0Ef, B9C0Eg, B9C0Eh, B9C0Ei, B9C0Ej, B10C0Eg, B10C0Eh,`
1255 `B10C0Ei, B10C0Ej, B10C0Ek, B10C0El`

1256 Bin 0 was excluded as it has substantial hadronic contamination and poor angular resolution.

1257 Background considerations and source selection was identical to Section 5.2.3, and no additional
1258 arguments are provided here. Many of the HAWC systematics explored in Section 5.7 also apply

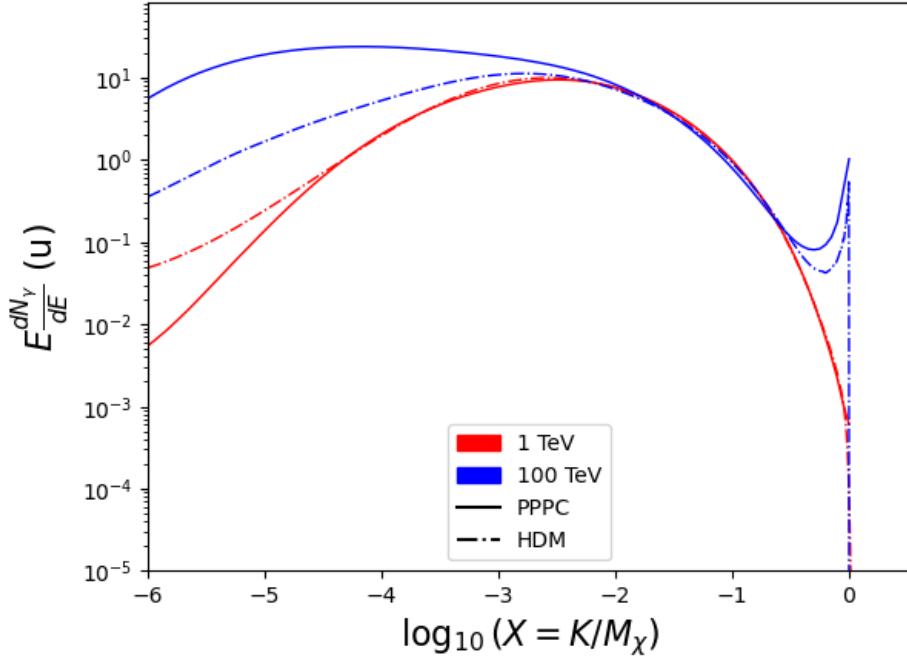


Figure 6.1 Spectral hypotheses from PPPC [44] and HDM [65] for DM annihilation: $\chi\chi \rightarrow W^-W^+$. Solid lines are spectral models with EW corrections from the PPPC. Dash-dot lines are spectral models from HDM. Red lines are models for $M_\chi = 1$ TeV. Blue lines represent models for $M_\chi = 100$ TeV.

1259 for this DM search and are not added upon here.

1260 6.3 Analysis

1261 The analysis and its systematics are almost identical to Section 5.3. Importantly, we use the
 1262 same [TODO: fix this ref](#) Equation (7.1) and Equation (5.2) for estimating the gamma-ray flux at
 1263 HAWC from our sources.

1264 6.3.1 $\frac{dN_\gamma}{dE_\gamma}$ - Particle Physics Component

1265 For these spectra, we import HDM with Electroweak (EW) corrections and additional correc-
 1266 tions for neutrinos above the EW scale [65]. The spectra are implemented as a model script in
 1267 astromodels for 3ML. A comprehensive description of EW corrections and neutrino considerations
 1268 are provided later in Sec. 8.

1269 Figure 6.1 demonstrates the impact of changes implemented in HDM on DM annihilation to W
 1270 bosons. A class in astromodels was developed to include HDM and is aptly named `HDMspectra`
 1271 within `DM_models.py`. The SM DM annihilation channels studied here are $\chi\chi \rightarrow$:

1272 e^+e^- , $\mu^+\mu^-$, $\tau^+\tau^-$, $b\bar{b}$, $t\bar{t}$, gg , W^+W^- , ZZ , $c\bar{c}$, $u\bar{u}$, $d\bar{d}$, $s\bar{s}$, $\nu_e\bar{\nu}_e$, $\nu_\mu\bar{\nu}_\mu$, $\nu_\tau\bar{\nu}_\tau$, $\gamma\gamma$, hh .

1273 For $\gamma\gamma$ and ZZ , a substantial fraction of the signal photons are expected to have $E_\gamma = m_\chi$ [65].
 1274 This introduces δ -function that is much narrower than the energy resolution of the HAWC detector.
 1275 To ensure that this feature is not lost in the likelihood fits, the 'line' feature is convolved with a
 1276 Gaussian kernel with a 1σ width of $0.05 \cdot m_\chi$ and total kernel window of $\pm 4\sigma$. This differs from
 1277 HAWC's previous line study where 30% of HAWC's energy resolution was used for the kernel [67].
 1278 The NN energy estimator's strength compared to f_{hit} at low gamma-ray energy enables narrower
 1279 kernels [65]. $\chi\chi \rightarrow \gamma\gamma$ and ZZ spectral hypotheses are shown in Figure 6.2. We did not explore
 1280 how well we reconstruct injected signal events for various kernels widths. This is a systematic
 1281 that should be tested before publication to journal. Spectral models for the remaining annihilation
 1282 channels are plotted for each m_χ in Figure B.1.

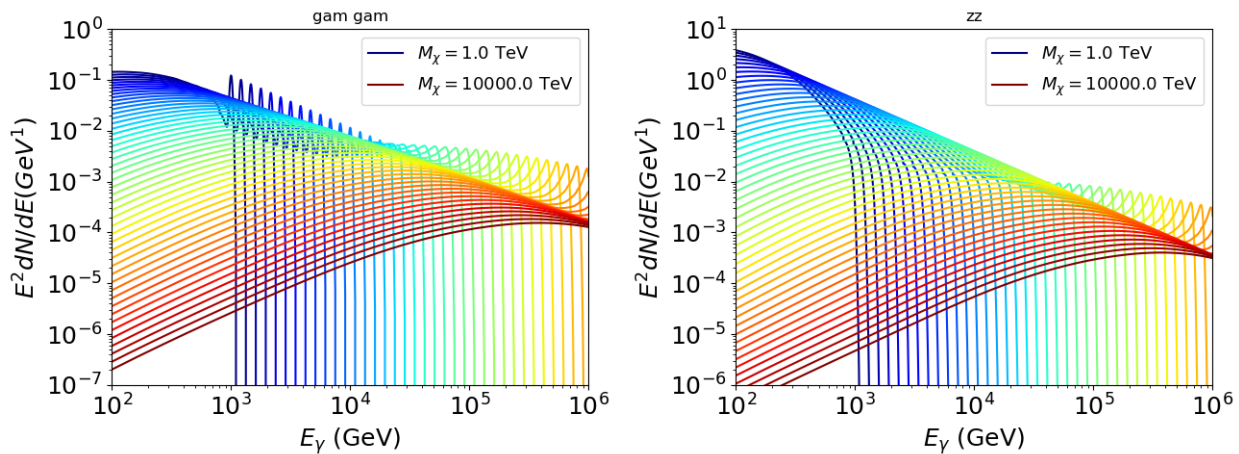


Figure 6.2 Photon spectra for $\chi\chi \rightarrow \gamma\gamma$ (left) and $\chi\chi \rightarrow ZZ$ (right) after Gaussian convolution of line features. Both spectra have δ -features at photon energies equal to the DM mass. Bluer lines are annihilation spectra with lower DM mass. Redder lines are spectra from larger DM mass. All spectral models are sourced from the Heavy Dark Matter models [65]. Axes are drawn roughly according to the energy sensitivity of HAWC.

1283 **6.3.2 J Astrophysical Components**

1284 The J-factor profiles for each source are imported from Louis Strigari et al. (referred to with
 1285 \mathcal{LS}) [66]. The \mathcal{LS} catalog fits a Navarro–Frenk–White (NFW) [48] spatial DM distributions to

1286 the dSphs which has a DM density of

$$\rho(r) = \frac{\rho_0}{\frac{r}{R_s} \left(1 + \frac{r}{R_s}\right)^2}. \quad (6.1)$$

1287 ρ_0 and the scale radius, R_s are free parameters fit for each dSph. r is the distance from the center
1288 of the dSph.

1289 Profiles in $\frac{dJ}{d\Omega}(\theta)$ up to an angular separation $\theta = 0.5^\circ$ were provided directly from the authors.
1290 Map generation from these profiles were almost identical to Section 5.3.2 except that a higher order
1291 trapezoidal integral was used for the normalization of the square, uniformly-spaced map:

$$p^2 \cdot \sum_{i=0}^N \sum_{j=0}^M w_{i,j} \frac{dJ}{d\Omega}(\theta_{i,j}, \phi_{i,j}) \quad (6.2)$$

1292 p is the angular side of one pixel in the map. $w_{i,j}$ is a weight assigned the following ways:

1293 $w_{i,j} = 1$ if $(\theta_{i,j}, \phi_{i,j})$ is fully within the region of integration

1294 $w_{i,j} = 1/2$ if $(\theta_{i,j}, \phi_{i,j})$ is on an edge of the region of integration

1295 $w_{i,j} = 1/4$ if $(\theta_{i,j}, \phi_{i,j})$ is on a corner of the region of integration

1296 Figure 6.3 shows the median and $\pm 1\sigma$ maps used as input for this DM annihilation study.

1297 6.3.3 Source Selection and Annihilation Channels

1298 HAWC's sources for this multithreaded analysis include Coma Berenices, Draco, Segue 1, and
1299 Sextans. \mathcal{LS} observed up to 43 sources in its publication, however only 4 of the best fit profiles
1300 were provided at the time this thesis was written. A full description of each source used in this
1301 analysis is found in Table 6.1.

1302 This analysis improves on chapter 5 in the following ways. Previously, the particle physics
1303 model used for gamma-ray spectra from DM annihilation was from the PPPC [44] which missed
1304 important considerations relevant for the neutrino sector. HDM is used to account for this shortfall
1305 [65]. HDM also models DM to the Planck scale which permits HAWC to probe PeV scale DM. For
1306 this study, we sample DM masses: 1 TeV - 10 PeV with 6 mass bins per decade in DM mass. In

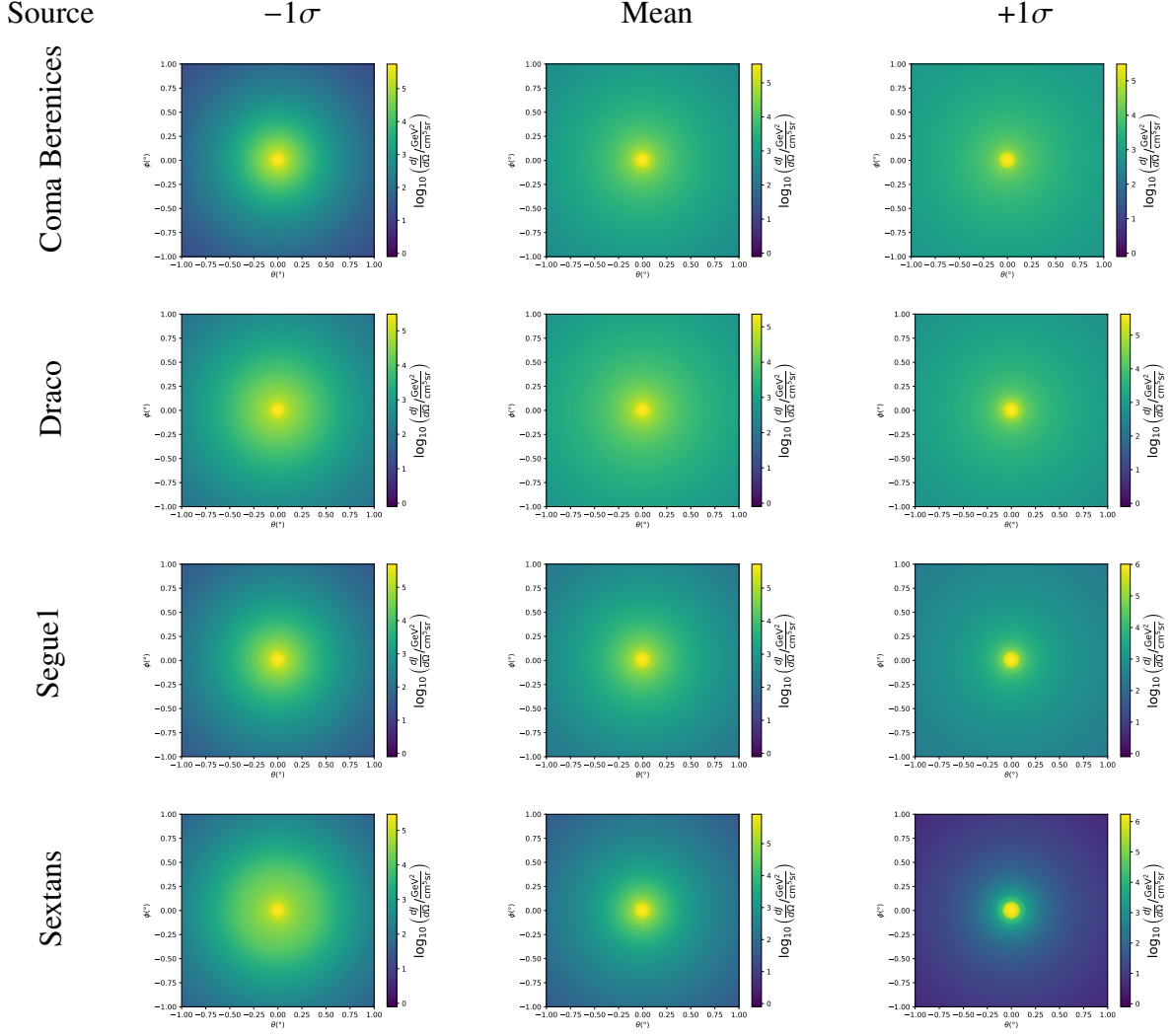


Figure 6.3 $\frac{dJ}{d\Omega}$ maps for Coma Berenices, Draco, Segue1, and Sextans. Columns are divided for the $\pm 1\sigma$ uncertainties in $dJ/d\Omega$ around the mean value from \mathcal{LS} [66]. Origin is centered on the specific dwarf spheroidal galaxies (dSph). θ and ϕ axes are the angular separation from the center of the dwarf. Profiles are truncated at 1° and flattened beyond.

1307 the case of line spectra ($\chi\chi \rightarrow \gamma\gamma$, or ZZ), we double the mass binning to 12 DM mass bins per
 1308 decade in DM mass.

1309 \mathcal{LS} provides 25 sources within HAWC's field of view. Additionally, NFW [48] DM distributions
 1310 have fewer parameters than Zhao [47], so \mathcal{LS} fits ultra-faint dwarves which expands the number of
 1311 sources. However, all sources were not provided by the authors in time for the completion of this
 1312 dissertation. Finally, the gamma-ray ray dataset is much larger. The study performed here analyzes
 1313 2565 days of data compared to 1017 days analyzed in chapter 5.

1314 **6.4 Likelihood Methods**

1315 These are identical to Section 5.4.1 and no additional changes are made to the likelihood. Bins
 1316 in this analysis are expanded to include HAWC’s NN energy estimator.

1317 **6.5 Computational Methods: Multithreading**

1318 Previously, as in Section 5.3, the likelihood was minimized for one model at a time. One model
 1319 in this case representing a DM annihilation channel (CHAN), DM mass (m_χ), and dSph ((SOURCE)).
 1320 In an effort to conserve human and CPU time, jobs submitted for high performance computing
 1321 contained a list of m_χ to iterate over for likelihood fitting. Jobs were then trivially parallelized
 1322 for each permutation of the two lists: CHANS and SOURCES. The lists for CHANS and SOURCES are
 1323 found in Section 6.3.1 and Table 6.1, respectively. Initially, 11 m_χ were serially sampled for one
 1324 job defined by a [CHAN, SOURCE] tuple. Computing the likelihoods would take between 1.5 to 2 hrs,
 1325 stochastically, for a job. We expect to compute likelihoods for data and 300 Poisson background
 1326 trials. The estimated CPU time based on the above for all CHAN (N = 17) and SOURCE (M = 25)
 1327 was estimated to 127,925 jobs. In total, 1,407,175 likelihood fits and profiles would be computed
 1328 for the 11 mass bins we wished to study. The estimated CPU time ranged between 8k CPU days
 1329 to 10k CPU days. Human time is more challenging to estimate as job allocation is stochastic and
 1330 highly dependent on what other users are submitting. Yet, it is unlikely that all jobs would run
 1331 simultaneously. Therefore, we can expect human time to be about as long as was seen in chapter 5

Name	Distance (kpc)	l, b ($^\circ$)	$\log_{10} J$ (\mathcal{LS} set) $\log_{10}(\text{GeV}^2\text{cm}^{-5}\text{sr})$
Coma Berenices	44	241.89, 83.61	$19.00^{+0.36}_{-0.35}$
Draco	76	86.37, 34.72	$18.83^{+0.12}_{-0.12}$
Segue I	23	220.48, 50.43	$19.12^{+0.49}_{-0.58}$
Sextans	86	243.50, 42.27	$17.73^{+0.13}_{-0.12}$

Table 6.1 Summary of the relevant properties of the dSphs used in the present work. Column 1 lists the dSphs. Columns 2 and 3 present their heliocentric distance and galactic coordinates, respectively. Column 4 reports the J -factors of each source given from the \mathcal{LS} studies and estimated $\pm 1\sigma$ uncertainties. The values $\log_{10} J$ (\mathcal{LS} set) [66] correspond to the mean J -factor values for a source extension truncated at 0.5° .

1332 which was on the order of months to fully compute on a smaller analysis. A visual aid to describe
 1333 how jobs were organized is provided in Figure 6.4.

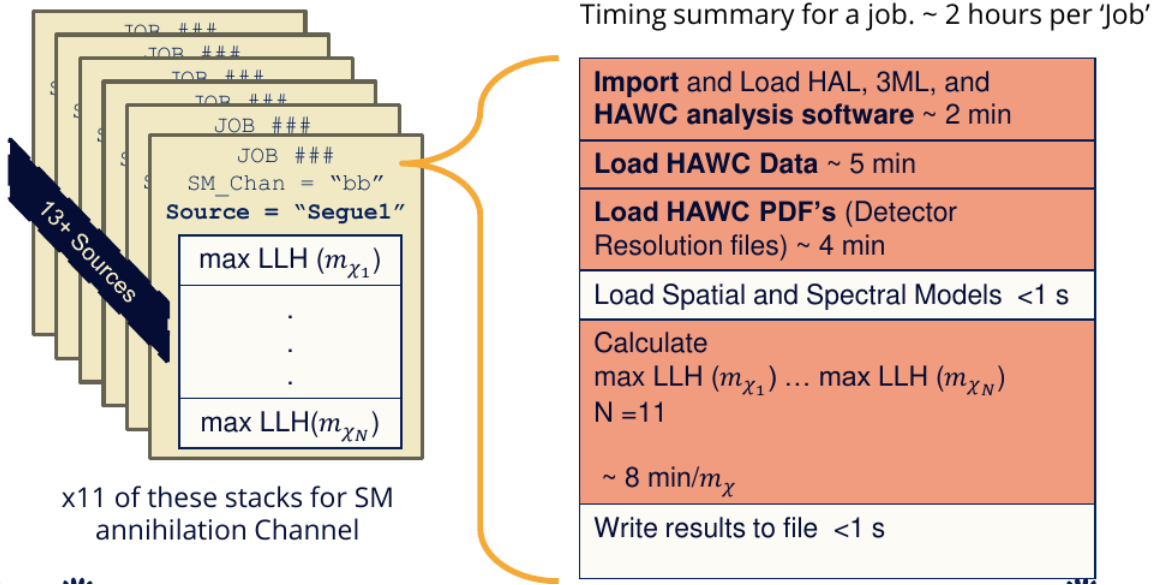


Figure 6.4 Infographic on how jobs and DM computation was organized in Section 5.3. Jobs were built for each permutation of CHANS and SOURCES shown by the left block in the figure. Each job, which took on the order 2 hrs to compute, had the following work flow: 1. Import HAWC analysis software, 2 min to run. 2. Load HAWC count maps, 5 min to run. 3. Load HAWC energy and spatial resolutions, 4 min. 5. Load DM spatial source templates and spectral models, less than 1 s. 6. Perform likelihood fit on data and model, about 8 min per DM mass. 7. Write results to file, less than 1s.

1334 The computational needs for this next generation DM analysis are extreme and is unlike other
 1335 analyses performed on HAWC. It became clear that there was a lot to gain from optimizing how
 1336 the likelihoods are computed. This section discusses how multi-threading was applied to solve and
 1337 reduce HAWC's computing of likelihoods for large parameter spaces like in DM searches.

1338 6.5.1 Relevant Foundational Information

1339 The profiling of the likelihood for HAWC is done via gradient descent where the normalization
 1340 of Equation (7.1) (linearly correlated with $\langle \sigma v \rangle$) is rescaled in the descent. Additionally, we sample
 1341 the likelihood space for a defined list of $\langle \sigma v \rangle$'s described in Section 5.4.2. The time to compute
 1342 these values is not predictable or consistent because many variables can change across the full
 1343 model-space. Comprehensively, these variables are:

1344 • m_χ : DM rest mass
 1345 • CHAN : DM annihilation channel in SM.
 1346 • SOURCE : dSph. Involves a spatial template AND coordinate in HAWC data.
 1347 • $\langle\sigma v\rangle$: Effectively the flux normalization and free parameter in the likelihood fit.
 1348 Therefore, we develop an asynchronous, functional-parallel coding pattern. Asynchronous meaning
 1349 the instructions within a function are independent and permitted to be out of sync with sibling
 1350 computations. Functional-parallel meaning that instructions are the subject of parallelization
 1351 rather than threading the likelihood computation. This is close to trivial parallelization seen in
 1352 Figure 6.4 except that we seek to consolidate the loading stages (software, data, and detector
 1353 resolution loading). Multiple asynchronous threads are expected to reduce total serial processing
 1354 time and total overhead across the entire project in addition to saving human time.

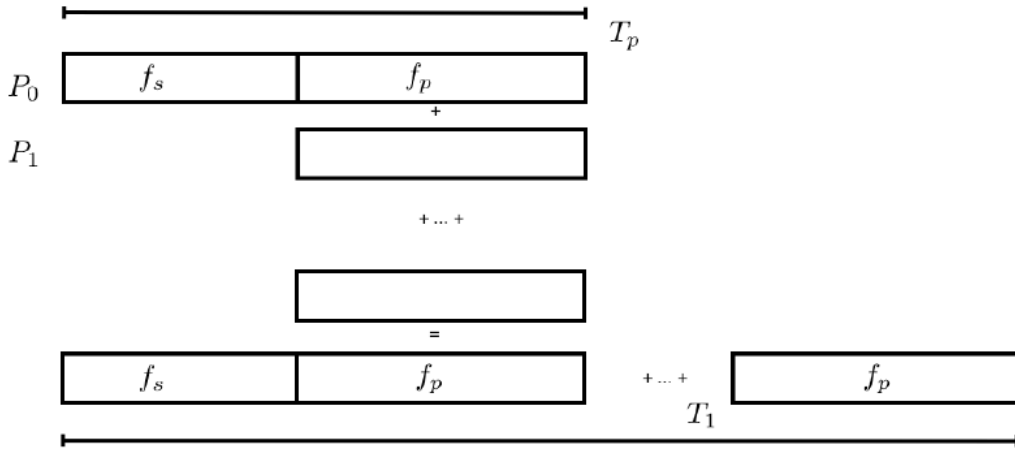


Figure 6.5 Graphic of Gustafson parallel coding pattern. f_s is the fraction of a program, in time, spent on serial computation. f_p is the fraction of computing time that is parallelizable. T_p is the total time for a parallel program to run. T_1 is the total time for a parallel program to run if only 1 processor is allocated. P_N is the N -th processor where it's row is the computation the processor performs. The Gustafson pattern is most similar to what is implemented for this analysis. Figure is pulled from [68].

1355 We need a way to measure and compare the expected speedup and efficiency gain for this
 1356 asynchronous coding pattern. I pull inspiration for timing measurement from [68] and use *Amdahl's*

1357 law with hybrid programming. Hybrid programming meaning that the computation is a mix of
 1358 distributed and shared memory programming. If we assume the code is fully parallelizable over p
 1359 processors and c threads, the ideal speedup is simply pc , and ideal run-time is $T_1/(pc)$. T_1 is the
 1360 total time for a parallel program to run if only 1 processor is allocated. However, the coding pattern
 1361 contains some amount of unavoidable serial computation, as shown in Figure 6.5. In our case, the
 1362 run time, $T_{p,c}$, is estimated to be

$$T_{p,c} = \frac{T_1}{pc} (1 + F_s(c - 1)). \quad (6.3)$$

1363 F_s is the fraction of CPU time dedicated to serial computation. The expected speedup, $S_{p,c}$, is

$$S_{p,c} \equiv \frac{T_1}{T_{p,c}} = \frac{pc}{1 + F_s(c - 1)}. \quad (6.4)$$

1364 From Equation (6.4), we can see that the speed-up scales with p/F_s . We are free to minimize F_s
 1365 asymptotically by enlarging the total models that are submitted to the thread pool, thereby shrinking
 1366 the CPU fraction dedicated to serial operation. We are also free to define exactly how many threads
 1367 and processors we utilize, yet eventually hit a hard cap at the hardware available on our computing
 1368 cluster. HAWC uses Intel Xeon™processors with 48 cores and 96 threads. We see that a successful
 1369 code will scale well as the expected speedup is inversely correlated with F_s . As the total number
 1370 of models sampled grows, the speedup will also.

1371 6.5.2 Implementation

1372 The multithreaded code was written in Python3 and is documented in the `dark_matter_hawc`
 1373 [repository](#) within the script named `mpu_analysis.py`. A version of the script as of April 25
 1374 **TODO: make sure to update on this date** is also provided in Section B.2. It has many dependencies
 1375 including the HAWC analysis software. Figure 6.6 displays the workflow of a job with 3 threads.
 1376 Within a job, SOURCE is kept fixed and CHANS remains 17 elements long. More m_χ are sampled
 1377 from 11 bins up to 49 (for $\gamma\gamma$ and ZZ) and 25 (for remaining CHANS) which amounts to 12 or 6
 1378 mass bins per decade. m_χ and CHANS are permuted into a 473 element list which is split evenly
 1379 across N threads where N is [2, 8, 16]. For each m_χ -CHAN tuple, 1001 $\langle\sigma v\rangle$ values are sampled in

Timing summary for a multi-threaded job.

Import and Load HAL, 3ML, and HAWC analysis software ~ 2 min		
Load HAWC Data ~ 5 min		
Load HAWC PDF's (Detector Resolution files) ~ 4 min		
Load Spatial Model < 1s		
Load Spectra Models <1 s	Load Spectra Models <1 s	Load Spectra Models <1 s
Calculate max LLH (Chan_0, m_{χ_1}) ... max LLH (Chan_?, m_{χ_N}) N = TOTAL/N_THREADS ~ 8 min/Spec_model	Calculate max LLH (Chan_?, m_{χ_1}) ... max LLH (Chan_?, m_{χ_N}) N = TOTAL/N_THREADS ~ 8 min/Spec_model	Calculate max LLH (Chan_?, m_{χ_1}) ... max LLH (Chan_?, m_{χ_N}) N = TOTAL/N_THREADS ~ 8 min/Spec_model
Write results to file <1 s	Write results to file <1 s	Write results to file <1 s
Join Threads and terminate < 1s		

Figure 6.6 Task chart for one multithreaded job developed for this project. Green blocks indicate a shared resource across the threads AND computation performed serially. Red blocks indicate functional parallel processing within each thread. 3 threads are represented here, yet many more can be employed during the full analysis. Jobs are defined by the SOURCE as these require unique maps to be loaded into the likelihood estimator. The m_{χ} , CHAN, and $\langle \sigma v \rangle$ variables are entered into the thread pool and allocated as evenly as possible across the threads.

- 1380 the likelihood, and the value of $\langle \sigma v \rangle$ that maximizes the likelihood is found. Although rare, fits
 1381 that failed are handled on a case by case basis.

1382 6.5.3 Performance

M Tasks	$T_{p,c}$ (hr:min:s)			
	$T_{1,1}$	$T_{1,2}$	$T_{1,8}$	$T_{1,16}$
50	1:40:37.5	0:52:43.7	0:19:13.8	0:13:44.0
74	2:22:30.0	1:15:00.6	0:25:21.3	0:15:49.8
100	(3:07:51.9)	1:40:10.5	0:30:44.4	0:20:01.4
200	(6:02:20.6)	-	1:00:32.0	0:30:35.0
473	(13:58:40.3)	-	2:01:41.4	1:07:53.2

Table 6.2 Timing summaries for analyses for serial and multithreaded processes. M tasks is the number of functional-parallel tasks ran for the computation. $T_{p,c}$ is a single run time in hours:minutes:seconds for runs utilizing p nodes and c threads. Runs are run interactively on the same computer to maximize consistency. Empty entries are indicated with '-'. (·) entries are estimated entries extrapolated from data earlier in the column.

- 1383 We see a significant reduction to wall time needed for our dSph analyses to run. Table 6.2

1384 shows the timing summaries for analyses of different sizes and thread counts. Additionally, the
 1385 efficiency gained when consolidating the serial loading of data is also apparent in our ability to
 1386 study many more tasks in about the same amount of wall time as a smaller serial computation. Trials
 1387 represented in the table were run on an AMD Opteron® processor 6344 with 48 cores, 2 threads per
 1388 core; 2.6 GHz clock. This is not the same architecture used for analysis on the HAWC computing
 1389 cluster however they are similar enough that results shown here are reasonably representative of
 1390 computing on the HAWC computing cluster. I use Tab. 6.2 for the inferences and conclusions in
 1391 the following paragraphs.

1392 First, we want to find T_s , the time of serial computation. From Fig. 6.5, the timing for our
 1393 coding pattern can be written as

$$T_s + Mt_p = T_{1,1}^M. \quad (6.5)$$

1394 M is the number of functional-parallel tasks (represented as column 1 of Tab. 6.2), and t_p is the
 1395 average time to complete a single parallel task. $T_{1,1}^M$ is the total time for a parallel program to run if
 1396 only 1 processor is allocated for M parallel task. With two runs of different M (M_1 and M_2), we
 1397 can use a system of equations to compute

$$T_s = 803.1\text{s} \text{ and } t_p = 104.6\text{s} \quad (6.6)$$

1398 Now, we have specific estimation for the fraction of serial computing time, F_s :

$$F_s = \frac{803.1}{803.1 + 104.6 \cdot M}. \quad (6.7)$$

1399 The maximum M for this study is 473 which evaluates to: $F_s = 0.016$ or 1.6% of computing time.
 1400 Table 6.3 shows the resulting speedups.

1401 We see a speedup that generally exceeds expectations from Eq. (6.4) for real trail runs. We also
 1402 see that there are diminishing returns as the number of threads increases. For small jobs with large c ,
 1403 both the expected and observed speedup are significantly smaller than c . One thing not considered
 1404 in Eq. (6.4) is the time incurred via communication latency. Communication latency increases
 1405 with the number of threads and contributes to diminishing returns. Additionally, these values are

M Tasks	F_s	$S_{1,2}$	$S_{1,8}$	$S_{1,16}$
50	1.33 E-1	1.90 [1.76]	5.23 [4.14]	6.35 [5.34]
74	9.40 E-2	1.90 [1.83]	5.62 [4.82]	9.00 [6.64]
100	7.13 E-2	1.88 [1.87]	6.11 [5.34]	9.38 [7.73]
200	3.70 E-2	- [1.93]	5.98 [6.36]	11.85 [10.29]
473	1.60 E-2	- [1.97]	6.89 [7.20]	12.35 [12.91]

Table 6.3 Speed up summaries for analyses for serial and multithreaded processes. M tasks is the number of functional-parallel tasks ran for the computation. $S_{p,c}$ is a single speedup comparison for runs utilizing p nodes and c threads. [·] are the estimated speedups calculated from Tab. 6.2, Eq. (6.7), and Eq. (6.4). Empty entries are indicated with '-'.

1406 for single runs and do not consider the stochastic variation expected in a shared high performance
 1407 computing resource. Therefor, these results are not strictly conclusive, yet demonstrate the merits
 1408 of multi-threading. We see very clearly that there is a lot to gain, and this new coding pattern will
 1409 expand HAWC's analysis capabilities.

1410 6.6 Analysis Results

1411 3 of the 43 $\mathcal{L}\mathcal{S}$ dSphs considered for the multithreaded analysis. These dSph are analyzed
 1412 for emission from DM annihilation according to the likelihood method described in Section 5.4.
 1413 The three likelihood profiles are then stacked to synthesize a combined limit on the dark matter
 1414 annihilation cross-section, $\langle\sigma v\rangle$. This combination is done each of the 17 SM annihilation channels.
 1415 Figure 6.7 and Fig. 6.8 show the combined limits for all annihilation channels with HAWC's
 1416 observations. Test statistics of the best fit $\langle\sigma v\rangle$ values for each m_χ and CHAN are shown in Fig. 6.9
 1417 and Fig. 6.10. We also compare these limits to HAWC's Glory Duck limits shown in Section 5.5.
 1418 The comparison to Glory Duck are featured in Fig. 6.11 for all the DM annihilation channels studied
 1419 for Glory Duck. A full comparison is provided in the appendix in Fig. B.2, Fig. B.3, and Fig. B.4.
 1420 Here, we show updated limits for $\chi\chi \rightarrow b\bar{b}, e\bar{e}, \mu\bar{\mu}, \tau\bar{\tau}, t\bar{t}, W^+W^-$, $\gamma\gamma$ and ZZ . For the first time
 1421 ever, we show limits for $\chi\chi \rightarrow c\bar{c}, s\bar{s}, u\bar{u}, d\bar{d}, \nu_e\bar{\nu}_e, \nu_\mu\bar{\nu}_\mu, \nu_\tau\bar{\nu}_\tau, gg$, and hh .

1422 No DM was found in HAWC observations. The largest excess found in HAWC data was for DM
 1423 annihilating to W -bosons or $\nu_e\bar{\nu}_e$ for $m_\chi = 10$ TeV at significance 2.11σ and 2.14σ respectively.
 1424 HAWC's limits and excesses are dominated by Segue1. Coma Berenices shows excesses at higher
 1425 DM mass, yet no similar excesses were observed in Segue1 or Sextans. Sextans did not contribute

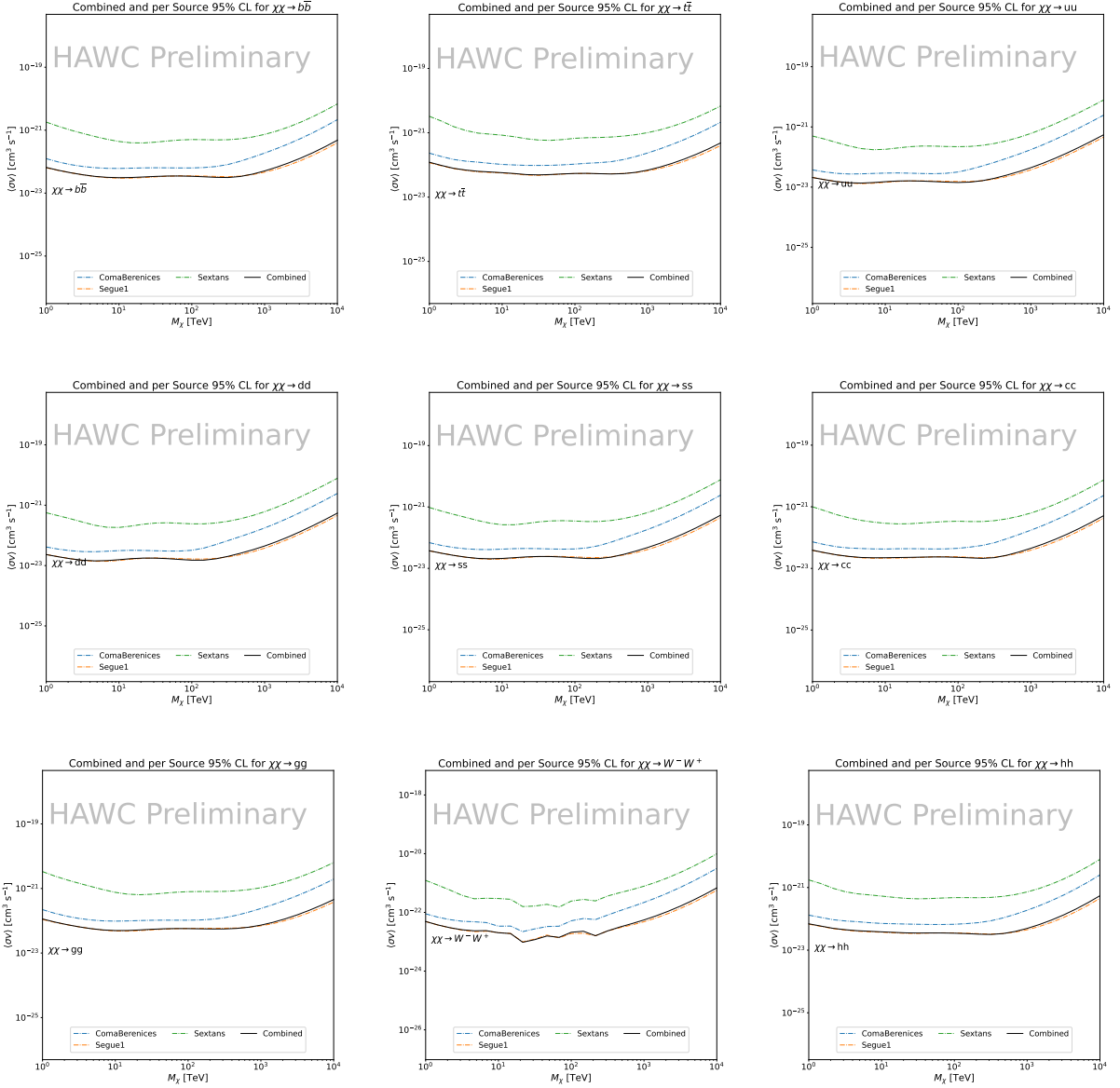


Figure 6.7 HAWC upper limits at 95% confidence level on $\langle\sigma v\rangle$ versus m_χ for $\chi\chi \rightarrow b\bar{b}$, $t\bar{t}$, $u\bar{u}$, $d\bar{d}$, $s\bar{s}$, $c\bar{c}$, gg , W^+W^- , and hh . Limits are with $\mathcal{L}\mathcal{S}$ J -factors [66]. The solid line represents the observed combined limit. Dashed lines represent limits from individual dSphs.

significantly to signal excesses or the combined limit as it is at high zenith. Draco was not included as the PDF of some of our analysis bins were wider than what is reasonable for a point source analysis. Draco is at a high zenith for HAWC, so the effort required to include it was not justified by the benefits.

We did not generate background trials in time of writing this thesis. These are not shown and

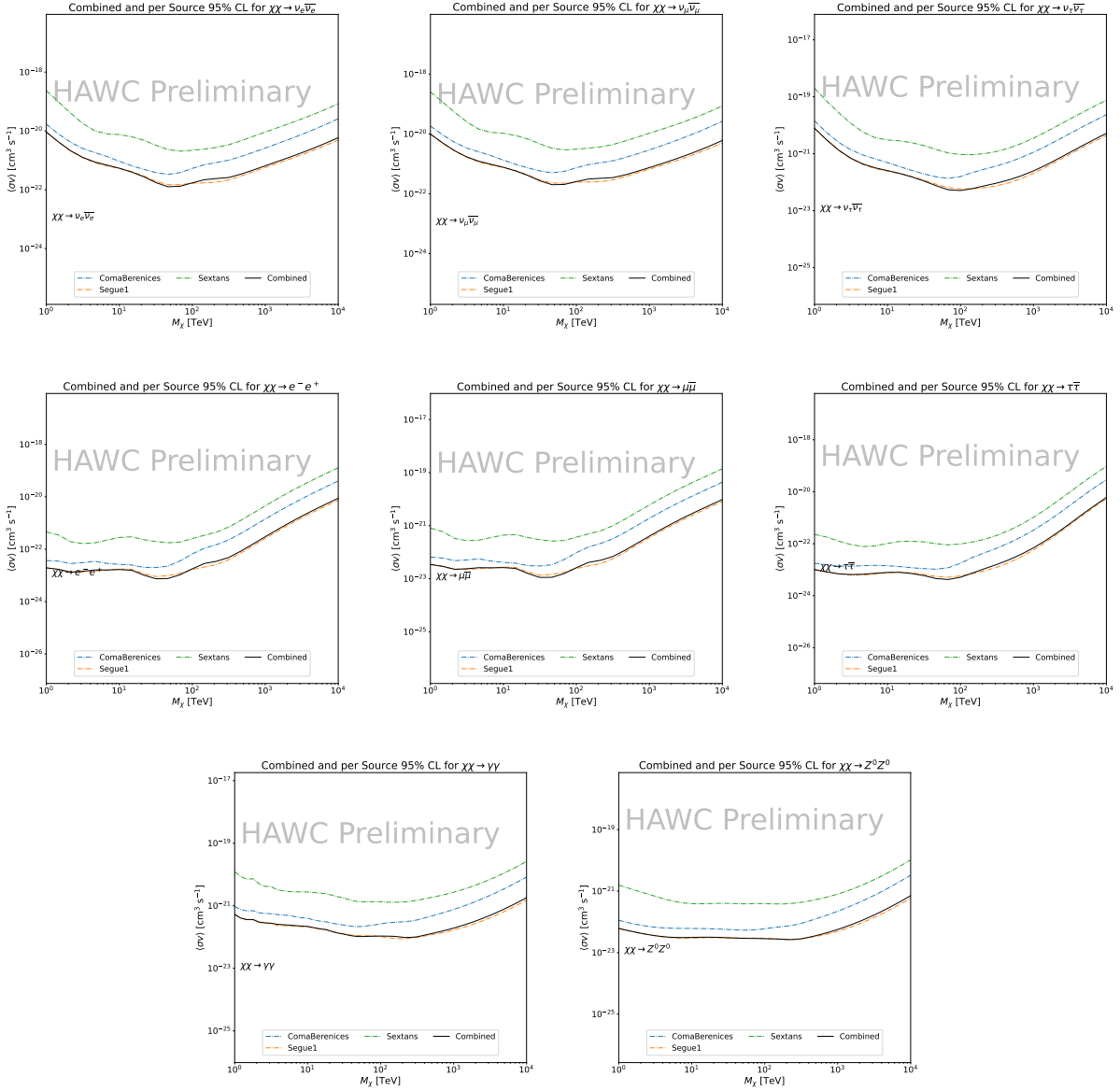


Figure 6.8 HAWC upper limits at 95% confidence level on $\langle\sigma v\rangle$ versus m_χ for $\chi\chi \rightarrow \nu_e \bar{\nu}_e$, $\nu_\mu \bar{\nu}_\mu$, $\nu_\tau \bar{\nu}_\tau$, $e \bar{e}$, $\mu \bar{\mu}$, $\tau \bar{\tau}$, $\gamma\gamma$ and ZZ . Limits use $\mathcal{L}S$ J -factors [66]. The solid line represents the observed combined limit. Dashed lines represent limits from individual dSphs.

1431 are an immediate next step for this analysis before publication.

1432 When comparing these results to Section 5.5, we see an overall decrease to the confidence limit
 1433 therefore improvement to HAWC's expected sensitivity. This improvement is generally stronger
 1434 than a doubling of data, or a factor $\sqrt{2}$ decrease. The comparison is somewhat complex and
 1435 dependent on the dSph and SM annihilation channel. Figure 6.11 shows the comparisons of limits

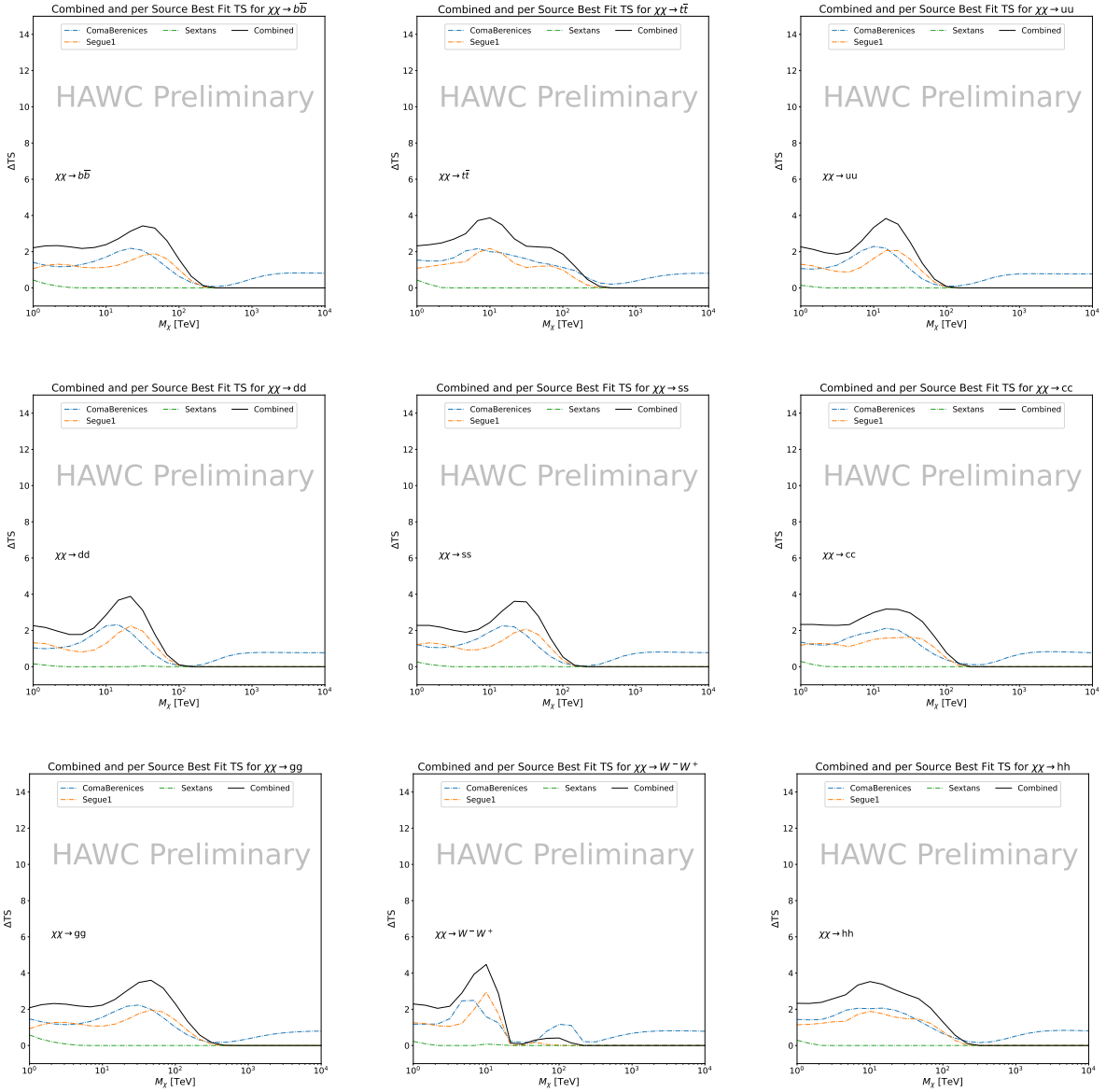


Figure 6.9 HAWC TS values for best fit $\langle\sigma v\rangle$ versus m_χ for SM annihilation channels: $\chi\chi \rightarrow b\bar{b}$, $t\bar{t}$, $u\bar{u}$, $d\bar{d}$, $s\bar{s}$, $c\bar{c}$, gg , W^-W^+ , and hh . Limits use \mathcal{LS} J -factors. The solid black line shows the combined best fit TS values. The colored, dashed lines are the TS values from each dSph.

1436 calculated for this analysis and Glory Duck (Section 5.5). Segue 1 and Coma Berenices are low
 1437 zenith where improvements to HAWC's analysis come only from energy estimation. Differences
 1438 between these two are dominantly from their differences in J -factor, half-light radii of the dSphs,
 1439 and the particle physics inputs. Substantial gains in HAWC's analysis methods (pass 5.F) were
 1440 made at high zenith which is important for sources like Sextans. The HDM particle physics model

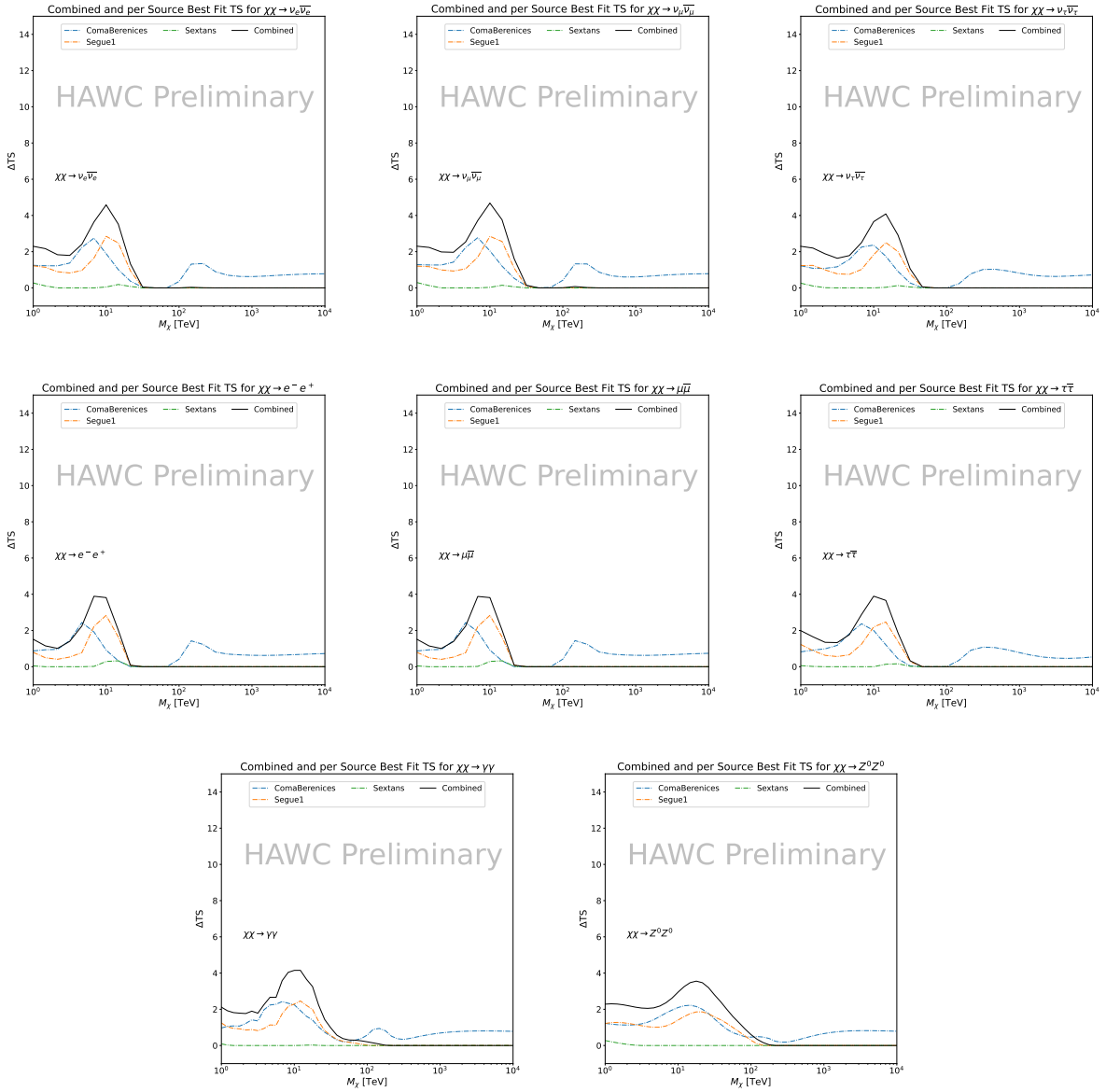


Figure 6.10 HAWC TS values for best fit $\langle\sigma v\rangle$ versus m_χ for SM annihilation channels: $\chi\chi \rightarrow \nu_e \bar{\nu}_e$, $\nu_\mu \bar{\nu}_\mu$, $\nu_\tau \bar{\nu}_\tau$, $e^- e^+$, $\mu \bar{\mu}$, $\tau \bar{\tau}$, $\gamma\gamma$ and ZZ . Limits use \mathcal{LS} J -factors. The solid black line shows the combined best fit TS values. The colored, dashed lines are the TS values from each dSph.

1441 produces almost identical spectra to the PPPC for $\chi\chi \rightarrow e^- e^+$. This channel can be used to
 1442 compare limits between dSph spatial models. Overhead sources see minimal improvement to the
 1443 limits, while high zenith sources see an order of magnitude improvement for all DM masses. Softer
 1444 SM annihilation channels see broad improvements to the limit compared to harder channels.

1445 **6.7 Systematics**

1446 Systematics to this analysis are identical to what was performed earlier in Glory Duck, Sec-
1447 tion 5.7. We are also sensitive to the choice in spatial template, and this was explored in Section 5.7.2
1448 and Section 5.8.2.

1449 **6.8 Conclusion and Discussion**

1450 In this multithreaded analysis, we have used observations of 3 dSphs from HAWC to perform
1451 a collective DM annihilation search towards dSphs. The data were combined across sources
1452 to significantly increase the sensitivity of the search. Advanced computational techniques were
1453 deployed to accelerate wall-time spent analyzing by an order of magnitude. We have observed
1454 no significant deviation from the null, no DM hypothesis, and so present our results in terms of
1455 upper limits on the velocity-weighted cross-section, $\langle\sigma v\rangle$, for seventeen potential DM annihilation
1456 channels across four decades of DM mass.

1457 This analysis serves as a proof of concept for multithreaded HAWC analyses with large parameter
1458 spaces. Larger datasets with fast techniques will be essential to tackling the DM problem. The
1459 models we used for this study include annihilation channels with neutrinos in the final state.
1460 Advanced studies could aim to merge our results with those from neutrino observatories with large
1461 data sets.

1462 A full HAWC analysis will include systematic studies of the J -factor distributions. Additionally,
1463 because of the timing reduction, the study can be doubled in size to include DM decay. We have not
1464 yet received the remaining spatial profiles to the \mathcal{LS} catalog, and limits can be quickly computed
1465 once these are received. Finally, statistical studies with Poisson variation of HAWC's background
1466 are essential to a comprehensive understanding of our observed excesses.

Segue1

Coma Berenices

Sextans

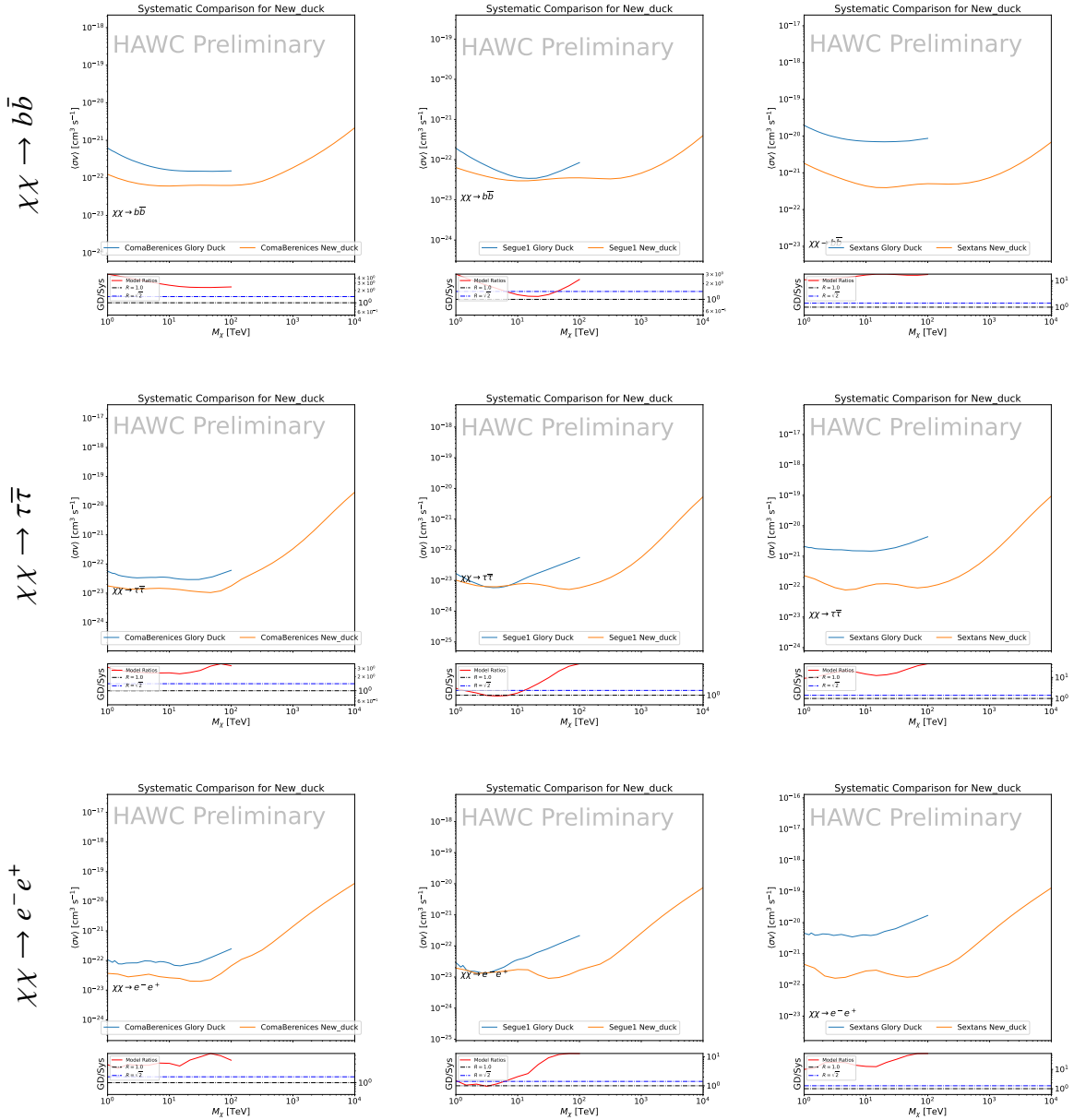


Figure 6.11 Comparison of HAWC limits from this analysis to Glory Duck (Fig. 5.5) for 3 dSphs and 3 DM annihilation channels: $b\bar{b}$, $\tau\bar{\tau}$, and e^-e^+ . Each sector shows the 95% confidence limit from Glory Duck (blue line) and this analysis (orange line) in the top plot. The lower plot features the ratio in log scale of Glory Duck to this analysis in a red solid line. Horizontal dashed lines are for ratios of 1.0 (black) and $\sqrt{2}$ (blue). Ratios larger than 1.0 are for limits smaller, or stricter, than Glory Duck. Ratios larger than $\sqrt{2}$ indicates limits are stricter than a simple doubling of the Glory Duck data.

CHAPTER 7

1467 HEAVY DARK MATTER ANNIHILATION SEARCH WITH ICECUBE'S NORTH SKY 1468 TRACK DATA

1469 7.1 Introduction

1470 Neutrinos are another astrophysical messenger than can travel long distances without significant
1471 attenuation or deflection. Uniquely, they interact less readily than photons especially above PeV
1472 energies. Neutrinos thereofre provide another window through which we can perform dark matter
1473 searches. Neutrinos come in three flavors which triples the multiplicity of the particles we are
1474 searching for.

1475 The previous Icecube DM annihilation analysis towards dwarf galaxies was performed in 2013
1476 [69]. This is in spite of the potentially crucial sensitivity afforded from neutrino spectral lines [70].
1477 A lot has changed in IceCube since its previous DM annihilation search such as, additional strings,
1478 more sophisticated analysis methods, and more accurate theory modeling. It has come time for
1479 IceCube to make a DM dSph contribution.

1480 As I have shown previously in Sec. 5 and Sec. 6, we can build a fast and robust analysis
1481 that shares tools with the field. The hope being that IceCube can eventually combine data with
1482 gamma-ray observatories.

1483 IceCube is sensitive to annihilating DM to the DM ranges above 1 TeV and can produce
1484 competitive results relative to gamma-ray observatories in spectral models that produce sharp
1485 neutrino features. The goal of this analysis is to perform a DM annihilation search using the
1486 Northern Sky Tracks datasets. The search will only be towards dwarf spheroidal galaxies (dSph)
1487 for the strengths mentioned in Section 5.3.3. These sources are treated as point sources for IceCube
1488 with little loss to sensitivity or model dependence on how the DM is distributed. DM masses from
1489 500 GeV to 100 PeV are considered for this analysis. Several DM annihilation channels available
1490 from the HDMspectra are studied in this analysis. This chapter presents the analysis work for IC3
1491 for DM searches toward dSphs.

1492 **7.2 Dataset and Background**

1493 This section enumerates the data and background methods used for IceCube's study of dSphs.

1494 Section 7.2.1 and Section 7.2.2 are most useful for fellow IceCube collaborators looking to replicate

1495 this analysis.

1496 **7.2.1 Itemized IceCube files**

1497 These files are only available withing IceCube's internal documentation and collaborators. They

1498 are not meant for public access, and are presented here so that IceCube collaborators can reproduce

1499 results accurately.

- 1500 • Software Environment: CVMFS Py3-v4.1.1

- 1501 • Data Sample: Northern Tracks NY86v5p1

- 1502 • Analysis Software: csky ([nu_dark_matter](#))

1503 • Analysis wiki: https://wiki.icecube.wisc.edu/index.php/Dark_Matter_Annihilation_Search_towards_dwarf_spheroidals_with_NST_and_DNN_Cascades

- 1505 • Project repository

1506 **7.2.2 Software Tools and Development**

1507 This analysis was performed inside IceCube's CVMFS (3.4.1.1) software environment using

1508 csky for likelihood calculations. Csky at first did not come with dark matter spectral models

1509 nor could accomodate custom flux models. We developed these capacities for single source and

1510 stacked source studies for this analysis. The analysis code is held in a separate repository from

1511 csky. The [nu_dark_matter branch of csky](#) manages the input of custom dark matter spectra and

1512 accompanied DM astrophysical source then calculates likelihoods with a selected data sample. The

1513 [IceCube Dark Matter dSph repository](#) manages the generation of spectral models for neutrinos,

1514 physics parameter extraction from n_{sig} , J -factor per source inputs, and bookkeeping for the large

1515 parameter space. The project repository required a secondary software environment for neutrino

1516 oscillations. How to launch and run those calculations are documented in the project repository
1517 and the Docker image is additionally saved in Section C.1

1518 7.2.3 Data Set and Background Description

1519 For this analysis, I use the Northern Sky Tracks (NST) Sample (Version V005-P01). The sample
1520 contains up-going track-like events, usually from ν_μ and ν_τ with a superior angular resolution
1521 compared to the cascade dataset. This sample covers 10.4 years of data (IC86_2011-2021). The
1522 accepted neutrino energy range used for the analysis is unique from most other IceCube searches
1523 because DM spectra are hard with large contributions close to $E_\nu = m_\chi$. Therefore the sampled
1524 energy range is $1 < \log(E_\nu/\text{GeV}) < 9.51$ with step size 0.125.

1525 The strength of a dwarf analysis is that there is no additional background consideration beyond
1526 nominal, baseline background estimations (see Section 5.2.3). For NST, the nominal contribu-
1527 tion comes from atmospheric neutrinos and isotropic astrophysical neutrinos. We estimate the
1528 background by scrambling NST data along Right Ascension.

1529 7.3 Analysis

1530 The expected differential neutrino flux from DM-DM annihilation to standard model particles,
1531 $d\Phi_\nu/dE_\nu$, over solid angle, Ω is described by the familiar equation.

$$\frac{d\Phi_\nu}{dE_\nu} = \frac{\langle\sigma v\rangle}{8\pi m_\chi^2} \frac{dN_\nu}{dE_\nu} \times \int_{\text{source}} d\Omega \int_{l.o.s} \rho_\chi^2 dl(r, \theta') \quad (7.1)$$

1532 This is identical to past examples, Eq. (7.1) except that there are 3 neutrino flavors, so there are a
1533 corresponding 3 flux equations. Section 5.3 has a complete description of each term in Eq. (7.1).
1534 Additionally, neutrinos oscillate between flavors which needs to be considered for the expected
1535 neutrino flux at Earth. Section 7.3.1 presents the particle physics model and processing for DM
1536 annihilation. Section 7.3.2 presents the spatial distributions built for each dSph.

1537 7.3.1 $\frac{dN_\nu}{dE_\nu}$ - Particle Physics Component

1538 Neutrino spectra from heavy dark matter annihilation were generated using HDMSSpectra [65]
1539 and χ arrov [71]. HDMSSpectra has tables for the decay and annihilation of heavy dark matter
1540 for different dark matter masses and SM primary annihilation channels. The simulation includes

1541 electroweak radiative corrections and higher order loop corrections with quarks. This publication
1542 also pushes the simulated DM mass to the Plank scale (1 EeV), however this study will not explore
1543 that high.

1544 An important feature in the spectra is that neutrino line channels will be accompanied with
1545 a low energy tail [65]. Thus the earth will not fully attenuate a heavy DM line-like signal from
1546 high declination sources where the neutrino flux must first traverse through the Earth. The DM
1547 annihilation channels that feature lines include all leptonic channels. ($\nu_{e,\mu,\tau}$, e , μ , and τ) We use the
1548 `Xarov` software to propagate and oscillate the neutrinos from the source to Earth. Because these
1549 sources are quite large in absolute terms, and also far (order 10 kpc or more), the resulting flavor
1550 spectra are the averages of the transition probabilities [71]:

$$P(\nu_\alpha \rightarrow \nu_\beta) \approx \begin{bmatrix} 0.55 & 0.18 & 0.27 \\ 0.18 & 0.44 & 0.38 \\ 0.27 & 0.38 & 0.35 \end{bmatrix} \quad (7.2)$$

1551 Examples of the spectra before and after propagation are shown in Fig. 7.1.

1552 When calculating the expected contribution to n_s , only ν_μ , ν_τ are considered as NST's effective
1553 area to ν_e is negligible [72]. Therefore the expected composite neutrino spectrum is sum of the two
1554 flavors: $\nu_\mu + \nu_\tau$. The spectral tables are then converted to splines to condense information, enable
1555 random sampling of the spectra, and reduce computing times. The spectral splines are finally
1556 implemented as a DM class in csky.

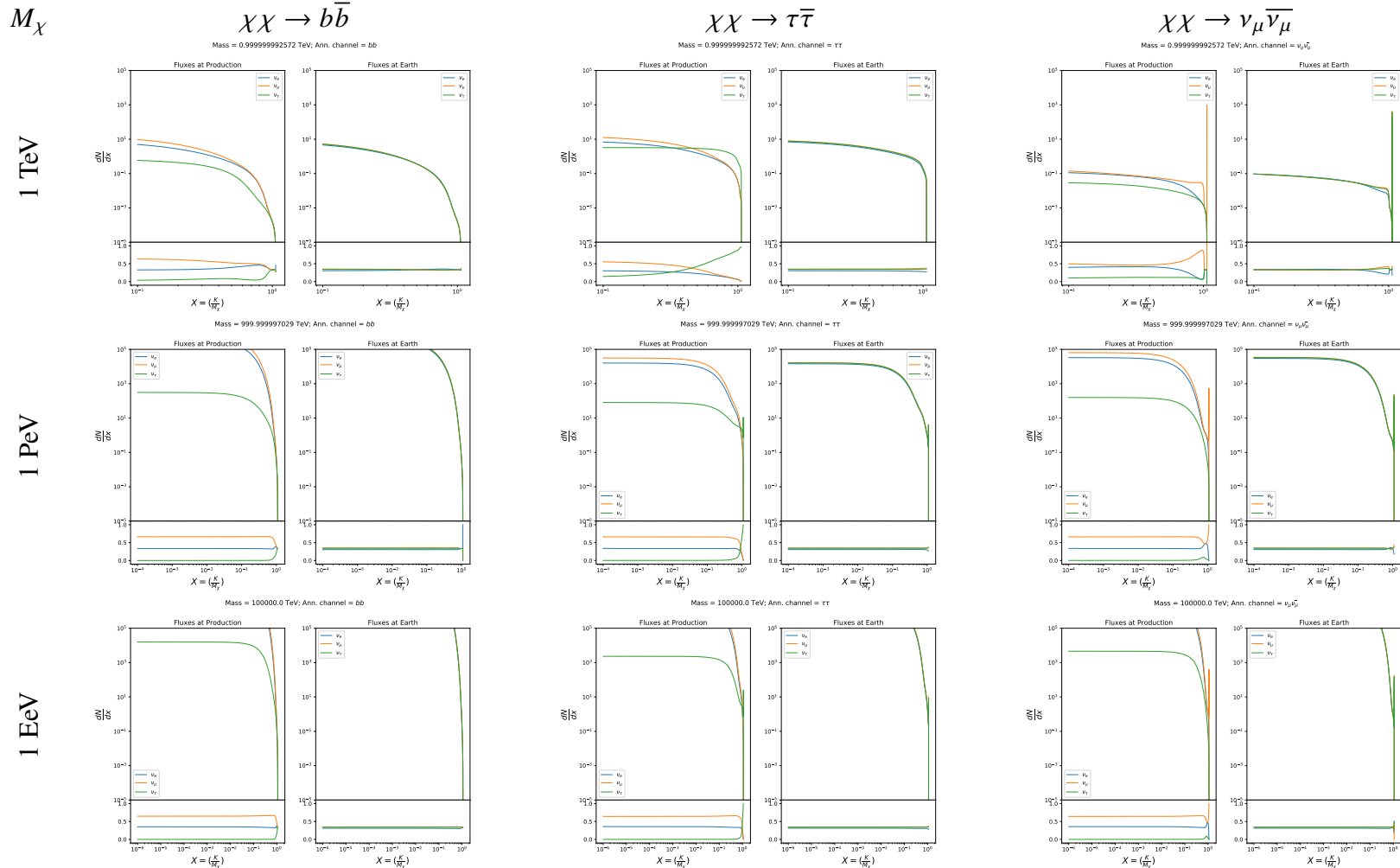


Figure 7.1 Neutrino spectra at production (left panels) and after oscillation at Earth (right panels). Blue, orange, and green lines are the ν_e , ν_μ , and ν_τ spectra respectively. Top panels show the spectra in $\frac{dN}{dE}$. Lower panels plot the flavor ratio to $\nu_e + \nu_\mu + \nu_\tau$. SM annihilation channels $b\bar{b}$, $\tau\bar{\tau}$, and $\nu_\mu\bar{\nu}_\mu$ are shown for $M_\chi = 1 \text{ PeV}$, TeV , and EeV .

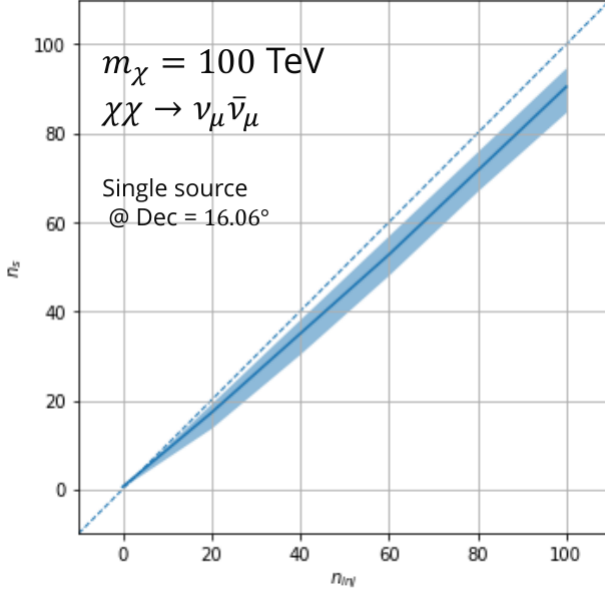


Figure 7.2 Signal recovery for 100 TeV DM annihilation into $\nu_\mu \bar{\nu}_\mu$ for a source at Dec = 16.06°. n_{inj} is the number of injected signal events in simulation. n_s is the number of reconstructed signal events from the simulation. Although the uncertainties are small and tight, the reconstructed n_s are systematically underestimated.

1557 7.3.1.1 Treatment of Neutrino Line Features

1558 All DM annihilation channels into leptons $\chi\chi \rightarrow [\nu_{e,\mu,\tau}, e, \mu, \tau]$ develop a prominent and
 1559 narrow spectral line feature. For all neutrino flavors, this line is visible and prominent in all m_χ
 1560 studied in this analysis. For charged leptons, the feature only really shows up at the larger DM mass
 1561 models and varies between the flavors. Examples for lines in the annihilation spectra with neutrinos
 1562 or charged leptons primary annihilation products are provided in Fig. 7.1.

1563 The neutrino line feature is so narrow relative the sampled energy range that the random
 1564 sampling of the spectra and likelihood fitting rarely capture the line in computation. As a result,
 1565 often the best fit to simulation of background will always floor to TS = 0 and the signal recovery
 1566 systematically underestimates the signal (see Fig. 7.2).

1567 To remedy this, a similar approach to the IceCube's decay analysis [73]. Two smoothing
 1568 kernels were tested (Gaussian, uniform) to widen the line feature. The widths were tuned such that
 1569 the signal recovery approached unity for DM mass 100 TeV to 1 PeV for a source at Segue 1's
 1570 declination, 16.06°. Near horizon was chosen in order to isolate loss in signal recovery from too
 1571 narrow a line versus from Earth's attenuation of very high energy neutrinos. The convolution also

needed to as close as possible preserve the integrated counts of neutrinos. The optimized kernel window for all lines is summarized as:

- Guassian kernel with 2σ width = $3.5E-3 \cdot m_\chi$

- Minimum energy included in convolution = $\text{MIN}[0.995 \cdot m_\chi, E(\nu_{\text{line}}) - 4\sigma]$

- Maximum energy included in convolution = $\text{MAX}[1.005 \cdot m_\chi, E(\nu_{\text{line}}) + 4\sigma]$

where $E(\nu_{\text{line}})$ is the neutrino energy where the neutrino line is at the maximum.

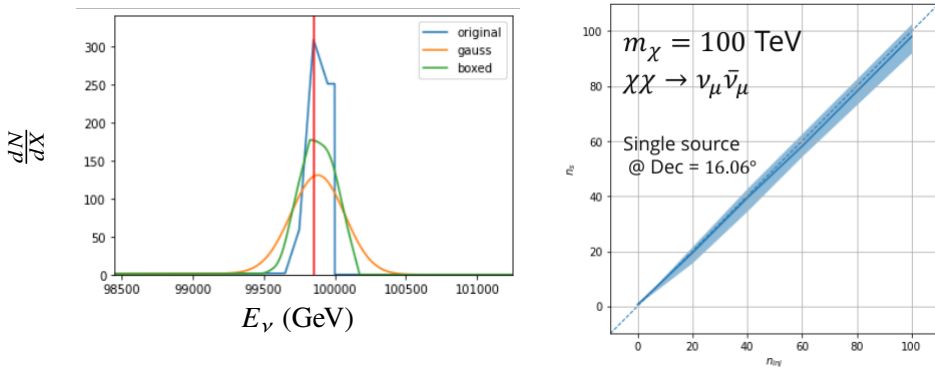


Figure 7.3 Left panel shows the two kernels overlaying the original spectrum from χaronv after propagation to Earth [71]. The vertical red line indicates where the original neutrino line is maximized. Blue line is the output from χaronv . Green line is the spectrum after convolution with a flat kernel. Orange line is the spectrum after Gaussian convolution. Right panel shows the signal recovery of the spectral model using the Gaussian kernel with parameters enumerated above.

These parameters broadly improved the signal recovery of the line spectra. An example is in Fig. 7.3. Signal recovery studies for are expanded upon in Section 7.6.

7.3.1.2 Spline Fitting

In an effort to reduce computational work, memory burden, and align with point source methods used for NGC1068 [74], spectral splines were created and adopted for estimating the neutrino flux for the different spectral models. Software was written to generate, book keep, and calculate values on the splines.

When using splines, one has to be careful of the goodness to fit. The spline software used here, Photospline [75], uses the penalized spline technique. Through the penlized technique, poor fits

1587 are penalized according to the accuracy of the nominal value, and the smoothness of the first and
 1588 second derivatives. The B-spline construction however does not penalize on the integral of the fit
 1589 distribution which is critical in low signal studies, such as DM searches. There are additional caveats
 1590 when testing the goodness to fit to the MC generated above for all DM annihilation channels.

- 1591 • The splines must be Log10(*) in Energy and dN/dE to account for the exponential nature of
 1592 the flux.
- 1593 • The fidelity of the fit matters more at $E_\nu \approx m_\chi$ where the model uncertainties are minimal
 1594 and physical considerations (like the cut-off) are most important.
- 1595 • The fidelity of the fit matters less at low E_ν as the model uncertainties are large AND
 1596 IceCube's sensitivity diminishes significantly below 500 GeV.
- 1597 • Total integrated counts should be well preserved.

1598 The resulting cost function was built to evaluate the goodness of spline fits to account for the above
 1599 considerations.

$$e_i = x_i \cdot \left(\frac{dN_i}{dE_i} - 10^{\hat{e}_i} \right) \quad (7.3)$$

1600 Where \hat{e}_i is the spline estimator's value for x_i . $x_i = E_{\nu_i}/m_\chi$. $\frac{dN_i}{dE_i}$ is the flux value from MC. I then
 1601 take the RMS of the error distribution and the resulting value, err, is used to evaluate the fidelity of
 1602 the spectral spline.

$$\text{err} = \sqrt{\frac{1}{x_{\max} - x_{\min}} \int_{x_{\min}}^{x_{\max}} e^2 dx} \quad (7.4)$$

1603 Each SM channel had unique tolerances for 'err'. Channels with very hard cut-offs had looser
 1604 tolerance for err because a significant error would be generated from single counts over/underes-
 1605 timated at the cut-off. Soft channels do not share this issue, so the tolerance is much stricter. All
 1606 annihilation channels from HDM are modeled well below IceCube's NST sensitivity. We do not
 1607 think it is necessary to evaluate the spline fits below 100 GeV [72] and use this value as the default
 1608 lower cut-off. Yet, HDM's model uncertainties at $E_\nu < 10^{-6} \cdot m_\chi$ span an order of magnitude
 1609 [65]. We also choose not to evaluate the splines below this critical value if it is within IceCube's

$\chi\chi \rightarrow$	GOOD	OK	FAIL	Limits of err calc [X_{min}, X_{max}]
$Z^0 Z^0, W^+ W^-$	1.0E-3	1.0E-3, 1.0E-2	1.0E-2	MAX[100GeV/ m_χ , 10^{-6}], 1.0
$t\bar{t}, hh$	1.0E-5	1.0E-5, 1.0E-4	1.0E-4	MAX[100GeV/ m_χ , 10^{-6}], 1.0
$b\bar{b}, d\bar{d}, u\bar{u}$	9.0E-7	9.0E-7, 9.0E-6	9.0E-6	MAX[100GeV/ m_χ , 10^{-6}], 1.0
$\nu\bar{\nu}_{e,\mu,\tau}$	1.0E-3	1.0E-3, 1.0E-2	1.0E-2	MAX[100GeV/ m_χ , 10^{-6}], MIN[0.995, ($E_n(\nu_{line}) - 4\sigma$)/ M_χ]
$e\bar{e}, \mu\bar{\mu}, \tau\bar{\tau}$	1.0E-3	1.0E-3, 1.0E-2	1.0E-2	MAX[100GeV/ m_χ , 10^{-6}], MIN[0.995, ($E_n(\nu_{line}) - 4\sigma$)/ M_χ]

Table 7.1 Spline err tolerances used for input in particle physics component to Eq. (7.1). Column 1 is the DM annihilation channel being fit. Columns 2, 3, and 4 are the tolerances for "GOOD" (pass), "OK" requires inspection, and "FAIL" (tune and refit) respectively. Column 5 has the X ranges over which the error is evaluated. MAX/MIN [·, ·] takes the maximum or minimum of the two enclosed values.

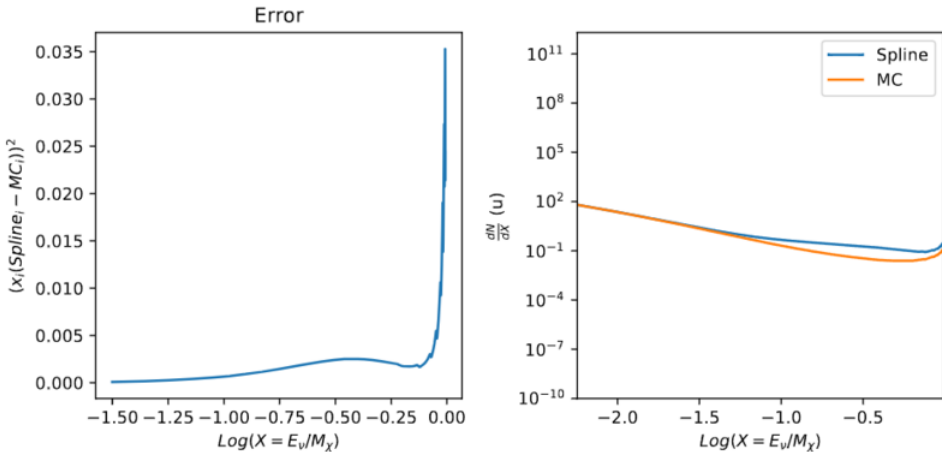


Figure 7.4 Example spline that failed the fit. Failed splined are corrected on a case by case basis unless the SM channel has a systematic problem fitting the splines. In this case, I made a bookkeeping error and loaded the incorrect spectral model

1610 sensitivity. Finally, the smoothing of the spectral lines in leptonic annihilation channels are ignored
 1611 for evaluating the fit. We used the lower limit of the kernel mask as the upper limit of evaluation.
 1612 Table 7.1 summarizes the tolerances for the DM annihilation channels used for this analysis.

1613 The errors are then plotted in two ways. First, FAIL and OK are directly plotted with e_i as a
 1614 function of x, and the full spline and MC. An example of a single failure is provided in Fig. 7.4
 1615 Second, a summary plot of all the splines is plotted and colors coded. Figure C.1 are the spline
 1616 summaries as of writing this thesis. The goal broadly is to eliminate all red and inspect yellow
 1617 statuses.

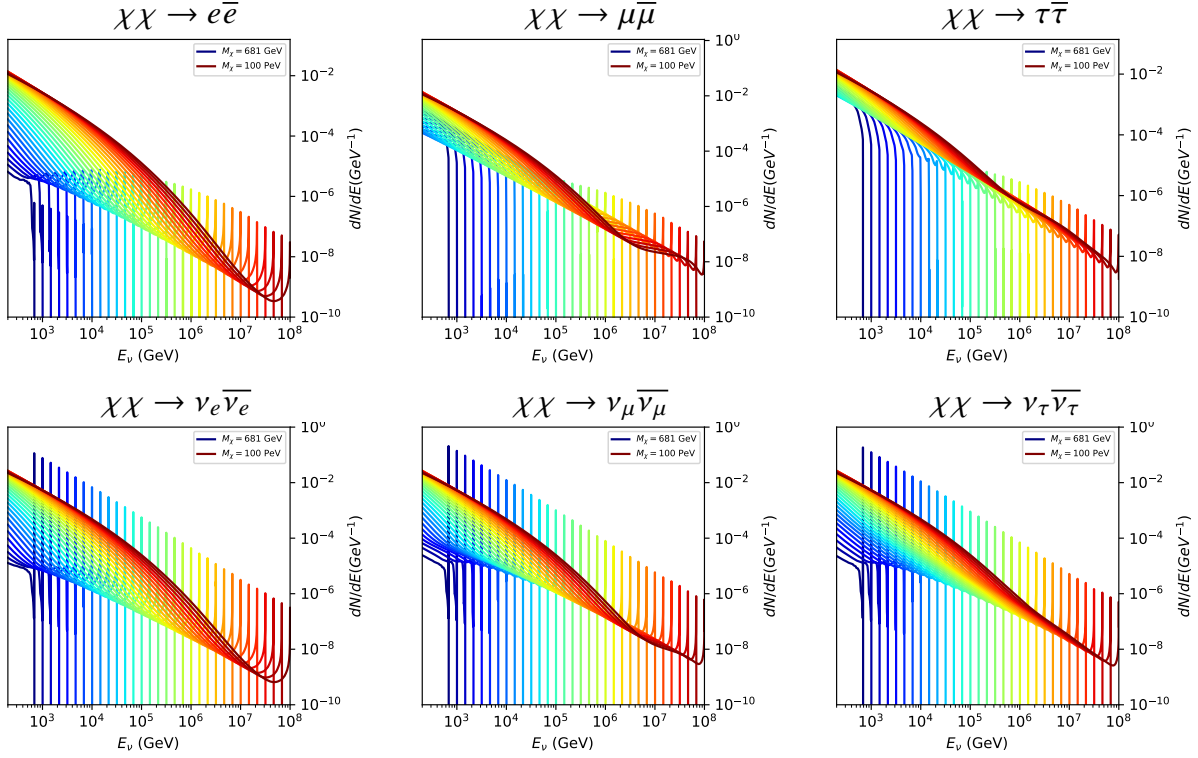


Figure 7.5 Summary of input spectral models that were smoothed with Gaussian kernel. Spectral models are for $\chi\chi \rightarrow e\bar{e}$, $\mu\bar{\mu}\tau\bar{\tau}$, $\nu_e\bar{\nu}_e$, $\nu_\mu\bar{\nu}_\mu$, and $\nu_\tau\bar{\nu}_\tau$. These spectra are the composite ($\nu_\mu + \nu_\tau$) of neutrino flavors. Every spectral model used for this analysis is featured as a colored solid line. Bluer lines are for lower DM mass spectral models. DM masses range from 681 GeV to 100 PeV. HDM [65], χ arov [71], and Photospline [75] are used to generate these spectra. Energy (x-axis) was chosen to roughly represent the energy sensitivity of NST.

1618 The ν_e spectra at Earth are not considered in this analysis, so no work was done to refine the
 1619 spline fits for this flavor. A Final inspection of the splines by eye to verify that the spline fitting did
 1620 not introduce spurious features into the distribution that would corrupt the likelihood fitting.

1621 7.3.1.3 Composite Neutrino Spectra

1622 With all of the previously mentioned pieces, we are ready to fully assemble a comprehensive
 1623 description of the particle physics term dN/dE in Eq. (7.1).

$$\frac{dN_\nu}{dE_{\nu_\oplus}} = \left(\frac{dN_{\nu_e}}{dE_{\nu_e}} + \frac{dN_{\nu_\mu}}{dE_{\nu_\mu}} + \frac{dN_{\nu_\tau}}{dE_{\nu_\tau}} \right)_{\text{src}} \cdot \mathbf{P}(\nu_\alpha \rightarrow \nu_\beta) \quad (7.5)$$

1624 Figure 7.5 shows the spectral models that required Gaussian smoothing, the leptonic annihilation
 1625 channels. The remaining models where the only processing was spline fitting are documented in
 1626 Section C.3. Notice that the different neutrino flavors are unique, especially in their low energy

1627 tails. Therefore, this analysis will be sensitive to DM annihilating to the distinct neutrino flavors.

1628 7.3.2 *J*- Astrophysical Component

1629 For this analysis, we re-adopt the \mathcal{GS} model used in Sec. 5 for dSph from [45]. These
1630 models are based on a modified Navarro-Frenk-White (NFW) profile where the indices of the NFW
1631 (traditionally 1,3,1) are allowed to float. The angular width of these sources is much smaller than
1632 the angular resolution of IceCube NST [74]. We therefore treat these sources as point sources in
1633 this analysis, and forgo generating maps. These sources and the \mathcal{GS} model have already been
1634 discussed at length in Section 5.3.2 and is not repeated here. IceCube uses identical sources to
1635 Tab. 5.1 except we analyze source with declinations above 0.0 degrees.

1636 7.3.3 Source Selection and Annihilation Channels

1637 We use all of the dSphs presented in IceCube’s previous dSph DM search [69]. IceCube’s
1638 sources for these simulation studies include Bootes I, Canes Venatici I, Canes Venatici II, Coma
1639 Berenices, Draco, Hercules, Leo I, Leo II, Leo V, Leo T, Segue 1, Segue 2, Ursa Major I, Ursa
1640 Major II, and Ursa Minor. A full description of all sources used is in Table 5.1. Sources with
1641 declinations less than 0.0 are excluded from this analysis.

1642 This analysis improves on the previous IceCube dSph paper [69] in the following ways. Pre-
1643 viously, the IceCube detector was not yet completed to the 86 string configuration. Many more
1644 dSphs will be observed, from 4 to 15. Previously, the particle physics model used for neutrino-ray
1645 spectra from DM annihilation did not have EW corrections where they are now included [65]. The
1646 spectral models also predict substantial differences between the neutrino flavors, so this analysis
1647 will be the first DM dwarf analysis to discriminate between primary neutrino flavors. The study
1648 performed here studies 10.4 years of data.

1649 The SM annihilation channels probed for this study include $\chi\chi \rightarrow$

1650 $b\bar{b}, t\bar{t}, u\bar{u}, d\bar{d}, e\bar{e}, \mu\bar{\mu}, \tau\bar{\tau}, ZZ, W^+W^-, \nu_e\bar{\nu}_e, \nu_\mu\bar{\nu}_\mu$, and $\nu_\tau\bar{\nu}_\tau$

1651 **7.4 Likelihood Methods**

1652 I use the Point-Source search likelihood which is widely used in IceCube analyses. The
1653 likelihood function is defined as the following:

$$L(n_s) = \prod_{i=1}^N \left[\frac{n_s}{N} S_i + \left(1 - \frac{n_s}{N}\right) B_i \right] \quad (7.6)$$

1654 where i is an event index, S and B are the signal PDF and background PDF respectively. For a joint
1655 analysis where the sources are stacked the likelihood is expanded in the simplified way:

$$L(n_s) = \prod_{i=1}^{N_{\text{sources}}} L_i(n_s) \quad (7.7)$$

1656 Where L_i is the likelihood from the i -th source in the stacked analysis. The Test Statistic (TS)
1657 definition remains the same as Eq. (5.7)

1658 **7.5 Background Simulation**

1659 Before we look at data, we must first analyze background and signal injection to validate our
1660 analysis. This is in part because the TS distributions are not expected to behave according to a
1661 chi-squared distribution with 1 degree of freedom. TS distributions can also vary significantly
1662 between DM mass and annihilation models. Therefor, Wilks' theorem may not be applicable to the
1663 analysis. Instead, a critical value is defined from a large number of background trials. We study the
1664 TS distributions first for each source, then for the stacked analysis. The following sections show
1665 the results of the likelihood fitting for a suite of background trials.

1666 I assume that TS values are physical: $\text{TS} \geq 0$. η denotes the fraction of positive TS values
1667 above the threshold and written in the legend of the TS distributions. $\epsilon[x]$ indicate the fraction of
1668 events where $\text{TS} < x$. For TS plots shown here, the decimal values of x are 1.0e-2 and 1.0e-3. Each
1669 subplot represents a simulation of 100,000 data-scrambled background trials. Section 7.5.1 show
1670 the background TS distributions obtained from Segue 1, a source with little Earth attenuation and
1671 large J -factor, and Ursa Major II, similarly large J -fator but significantly more Earth attenuation,
1672 assuming that dark matter annihilates into $b\bar{b}$, $\tau\bar{\tau}$, and $\nu_\mu\bar{\nu}_\mu$. I show the TS distributions of a
1673 stacked study of 15 sources for all DM annihilation channels.

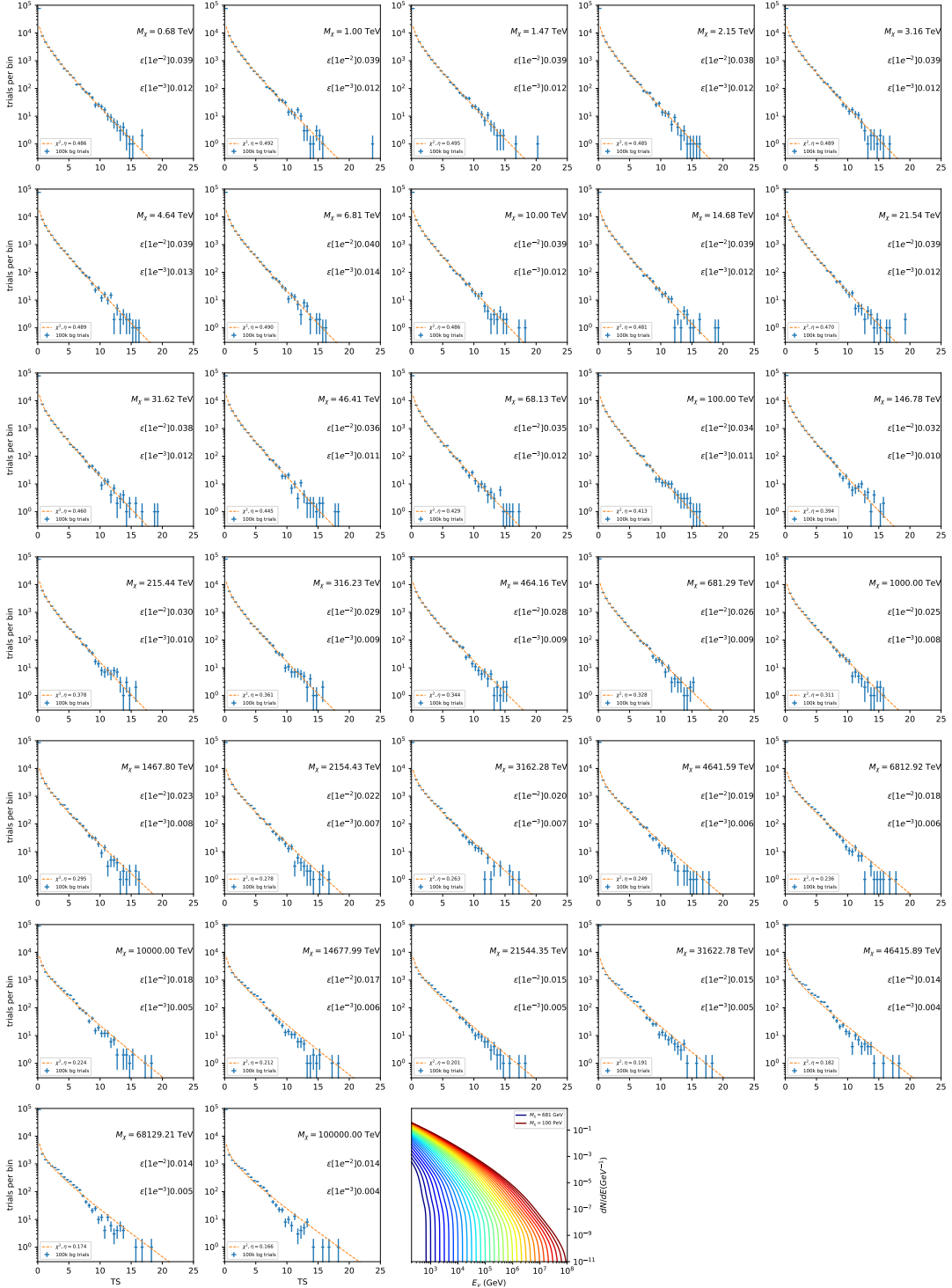


Figure 7.6 Test statistic (TS) distributions for Segue 1 and $\chi\chi \rightarrow b\bar{b}$. Each subplot, except the final, is the TS distribution for a specific DM mass listed in the subplot. Orange dashed lines are the traces for a χ^2 distribution with 1 degree of freedom. $\epsilon[\cdot]$ is the fraction of trials smaller than the bracketed value. The final subplot plots the all DM spectral models, similar to Fig. 7.5, used as input for the TS distributions.

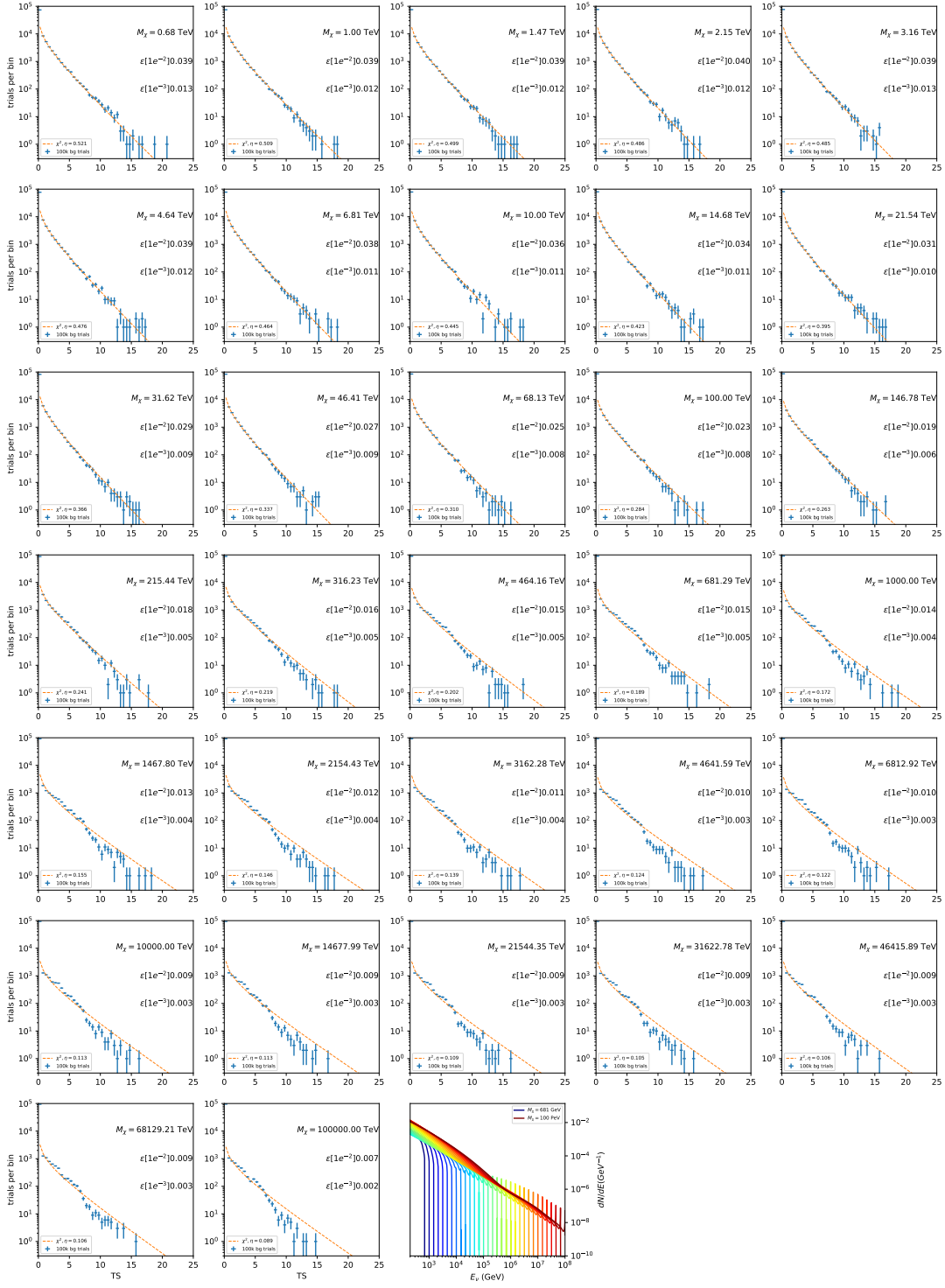


Figure 7.7 Same as Fig. 7.6 for Segue 1 $\chi\chi \rightarrow \tau\bar{\tau}$.

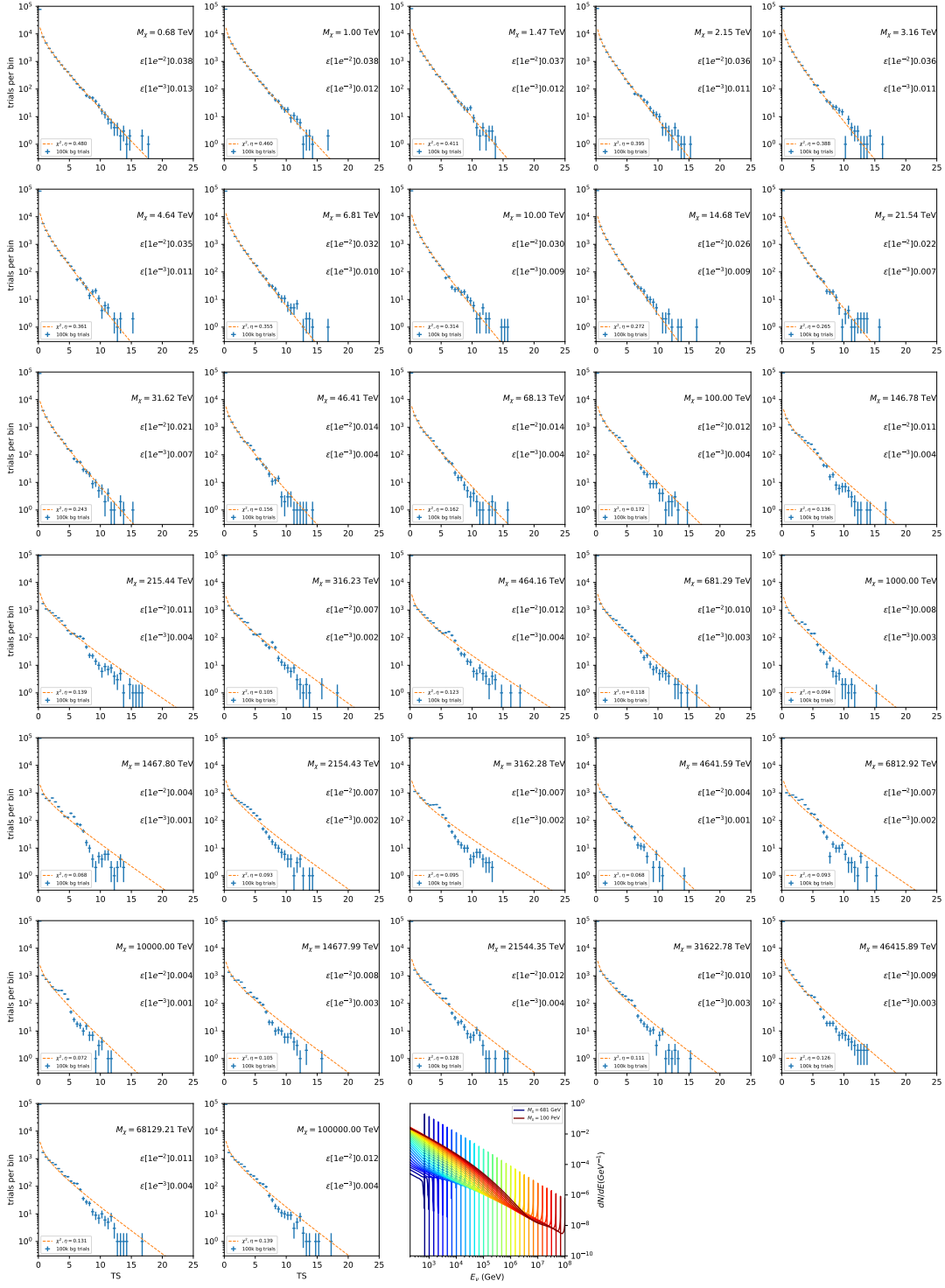


Figure 7.8 Same as Fig. 7.6 for Segue 1 $\chi\chi \rightarrow \nu_\mu\bar{\nu}_\mu$.

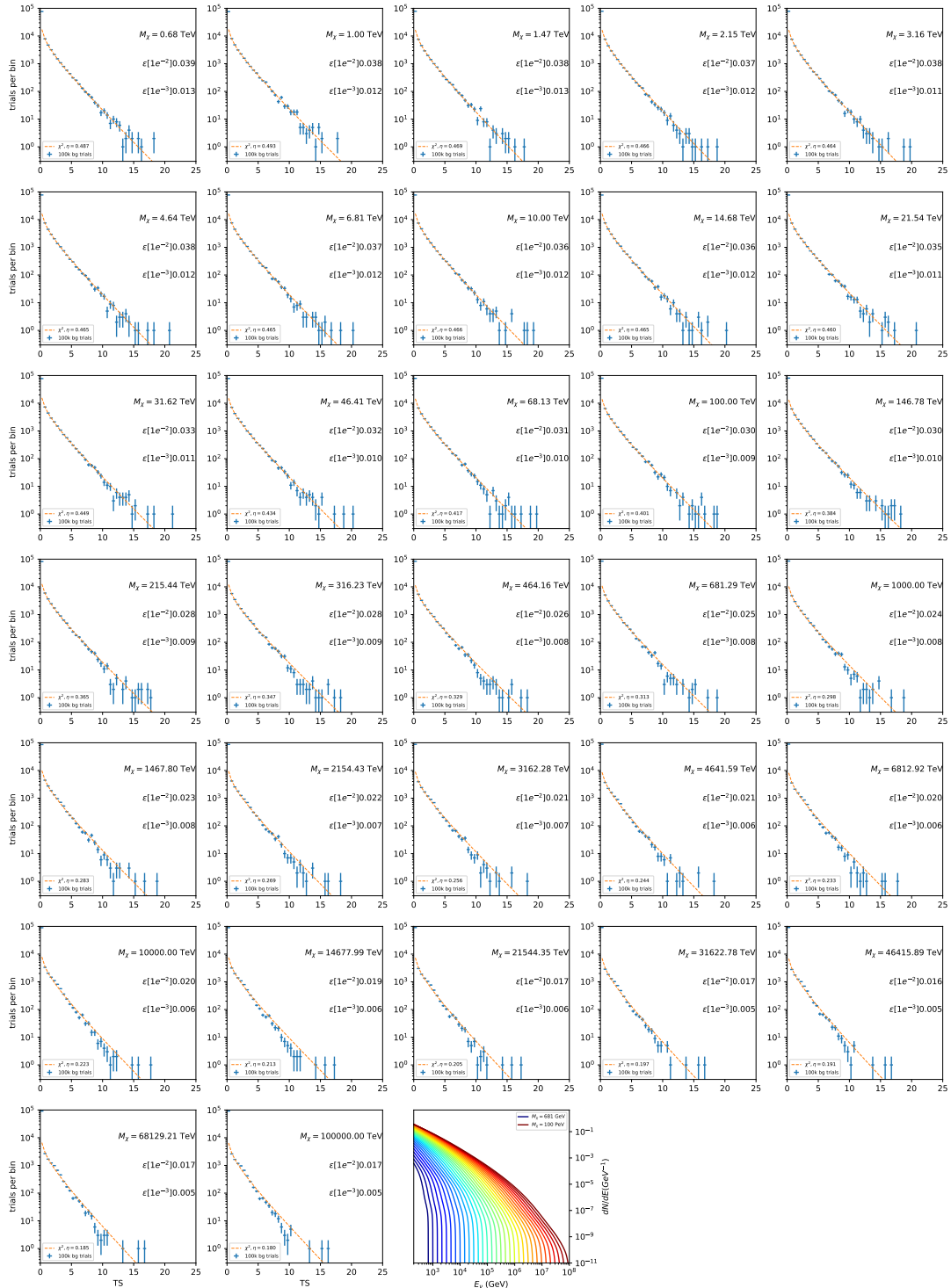


Figure 7.9 Same as Fig. 7.6 for Ursa Major II 1 $\chi\chi \rightarrow b\bar{b}$.

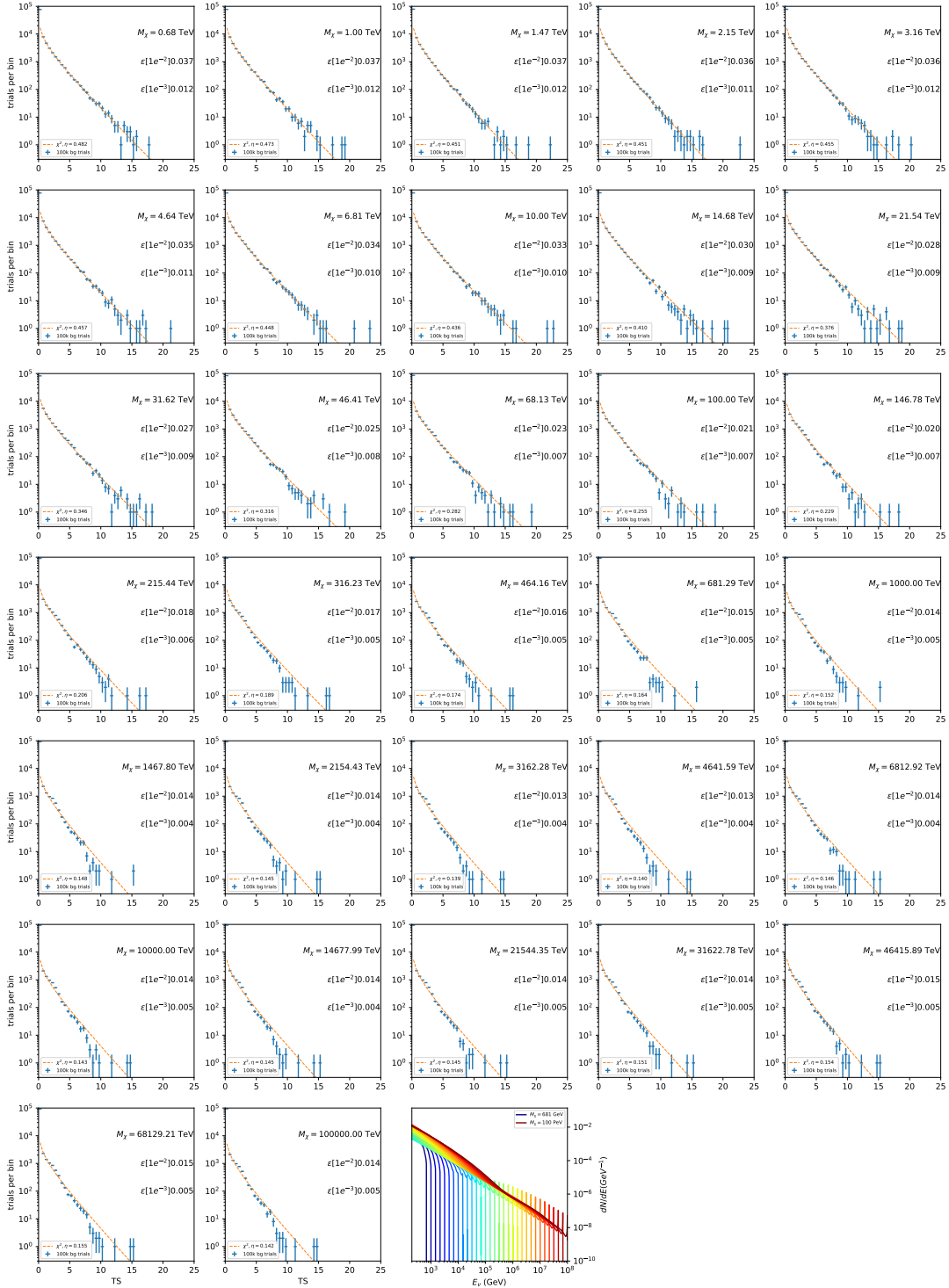


Figure 7.10 Same as Fig. 7.6 for Ursa Major II 1 $\chi\chi \rightarrow \tau\bar{\tau}$.

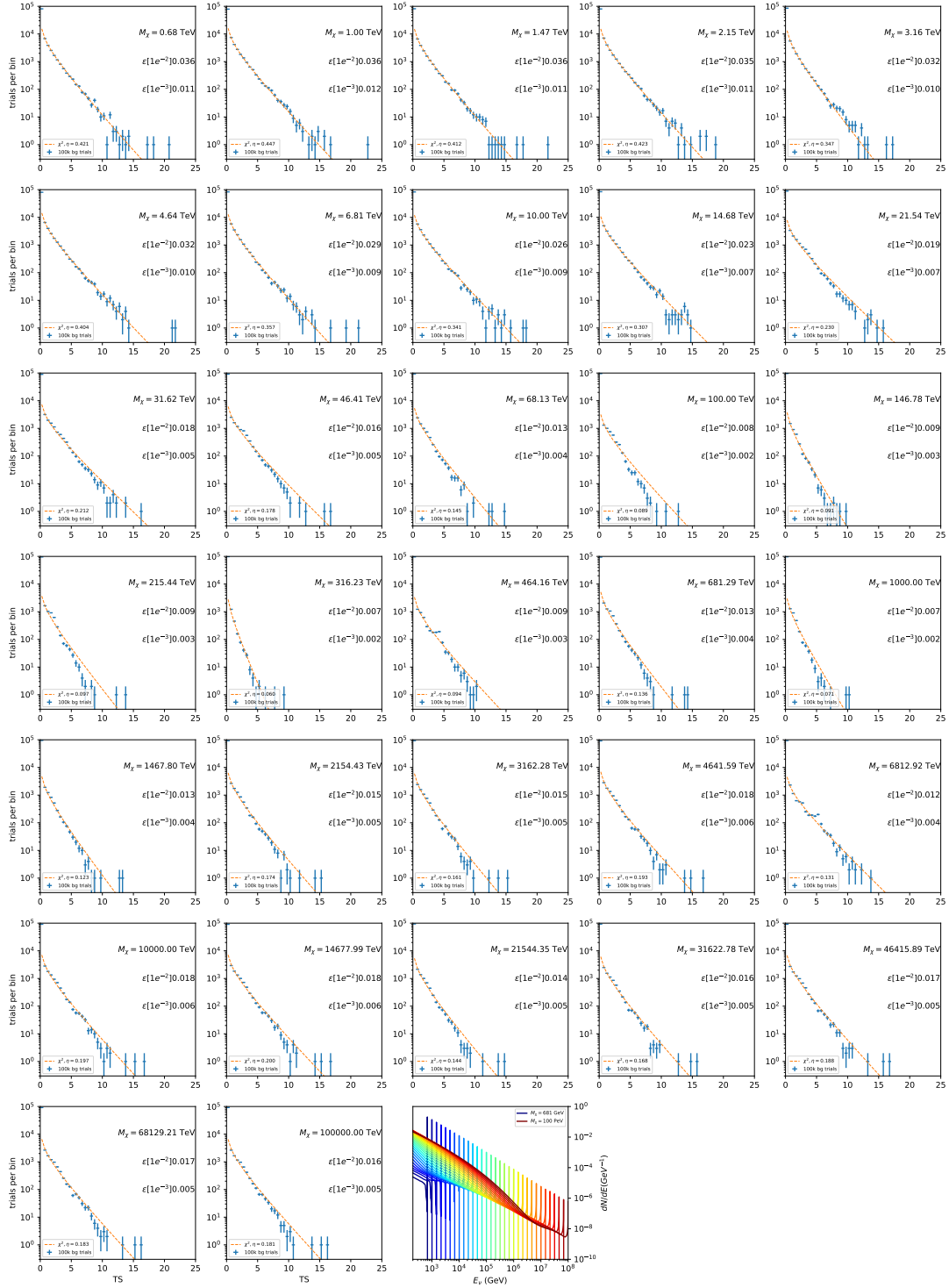


Figure 7.11 Same as Fig. 7.6 for Ursa Major II 1 $\chi\chi \rightarrow \nu_\mu \bar{\nu}_\mu$.

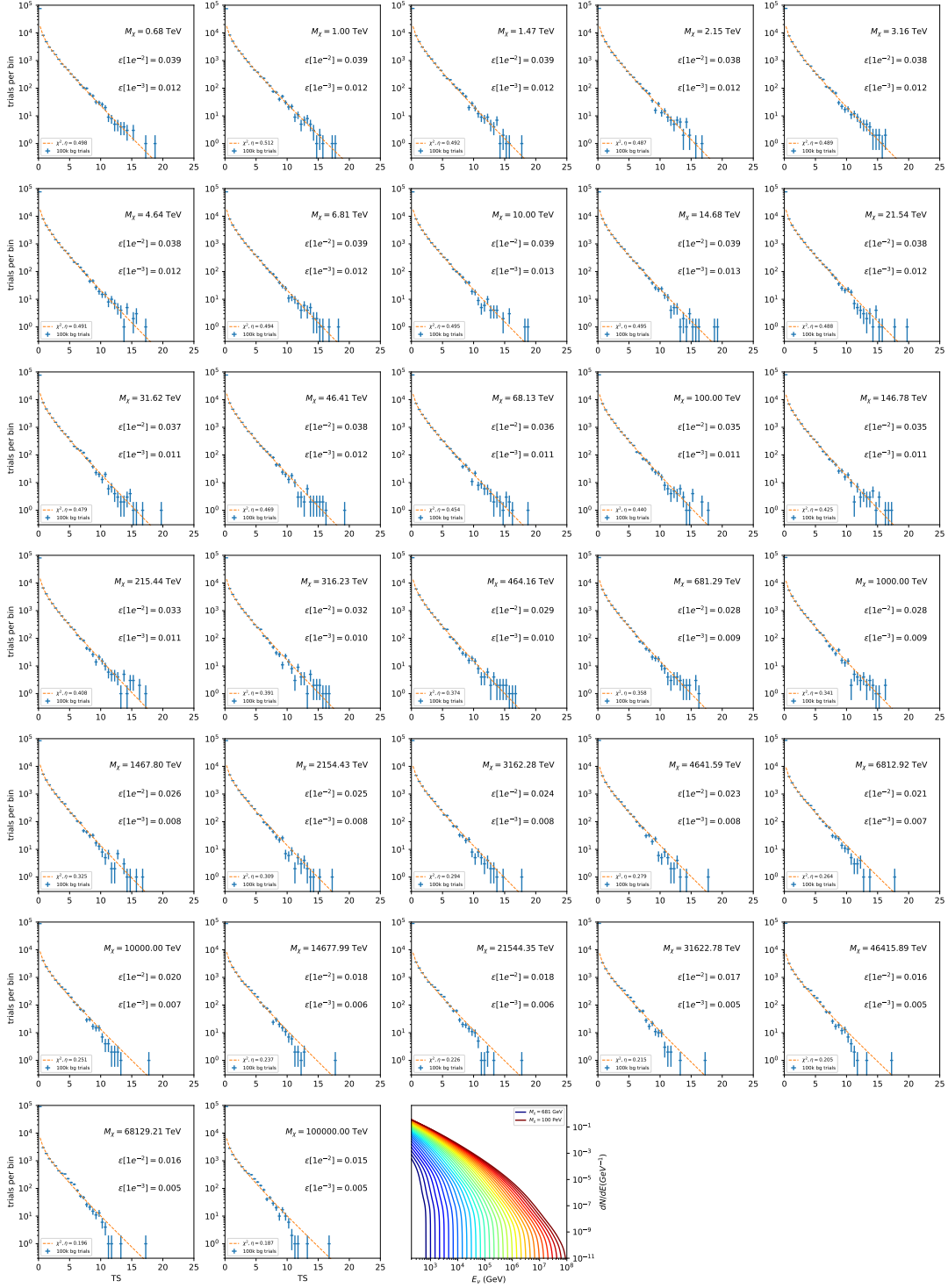


Figure 7.12 Same as Fig. 7.6 for 15, \mathcal{GS} J -factor, stacked sources and $\chi\chi \rightarrow b\bar{b}$.

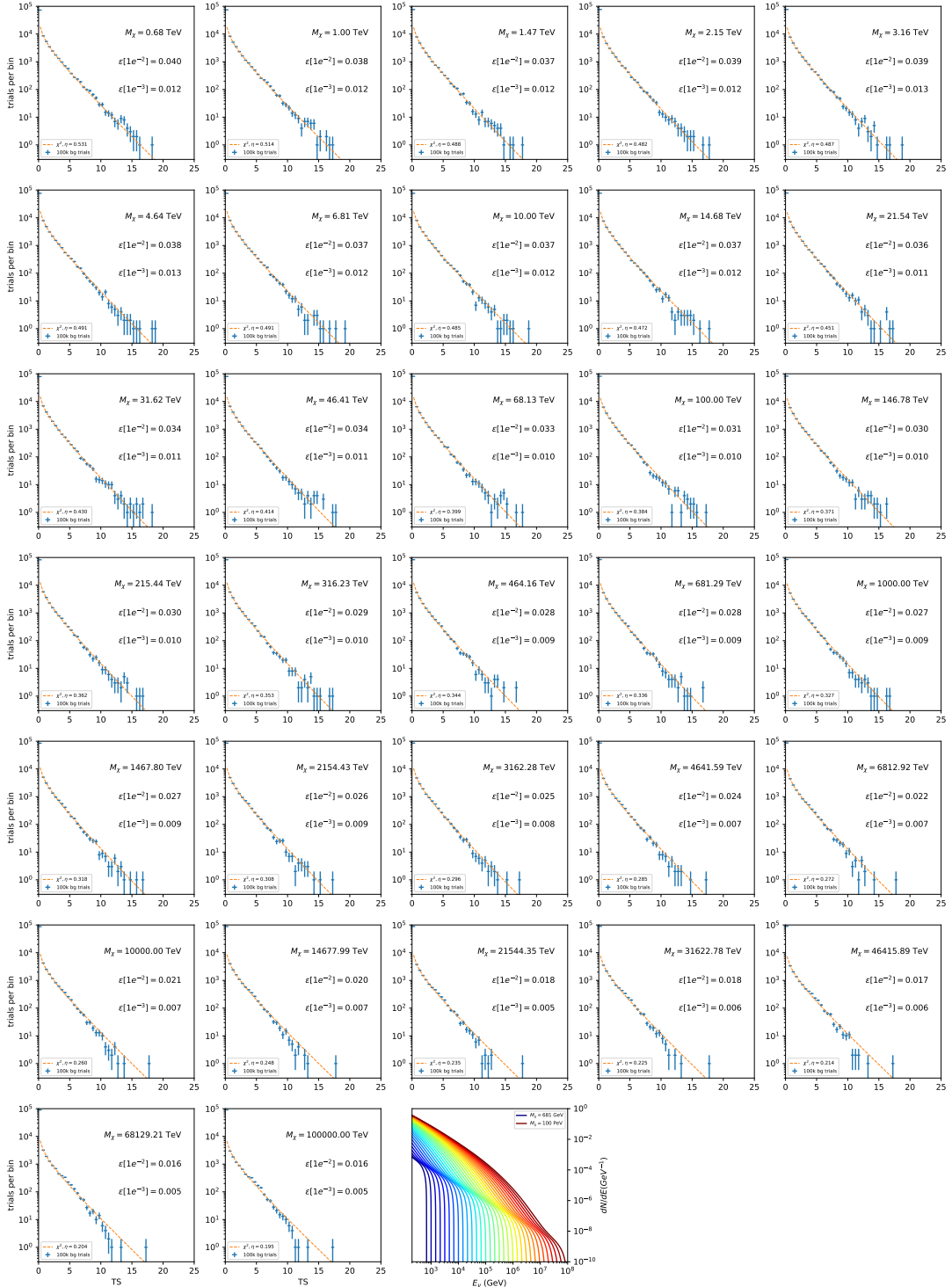


Figure 7.13 Same as Fig. 7.6 for 15, GS J-factor, stacked sources and $\chi\chi \rightarrow t\bar{t}$.

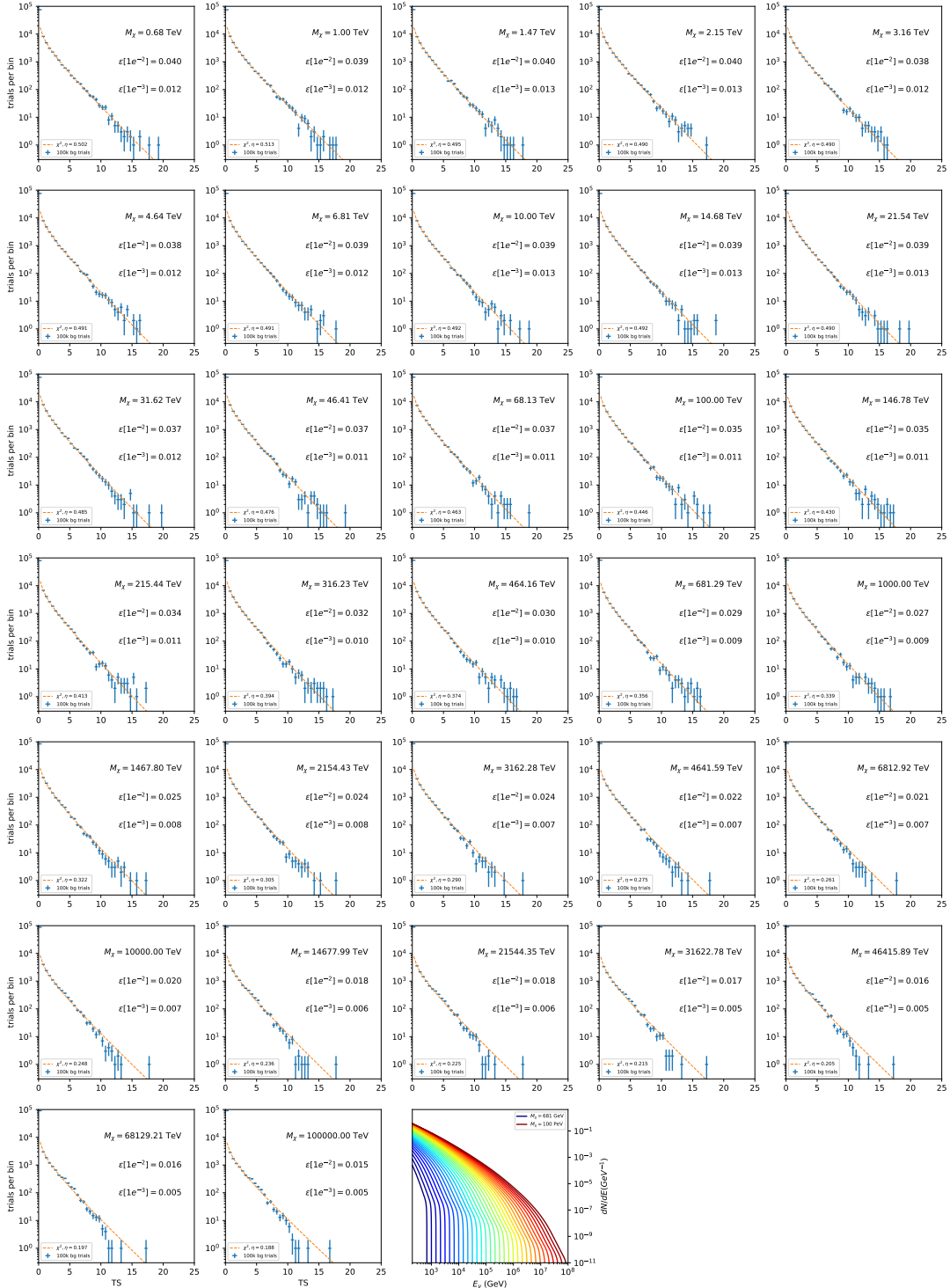


Figure 7.14 Same as Fig. 7.6 for 15, \mathcal{GS} J -factor, stacked sources and $\chi\chi \rightarrow u\bar{u}$.

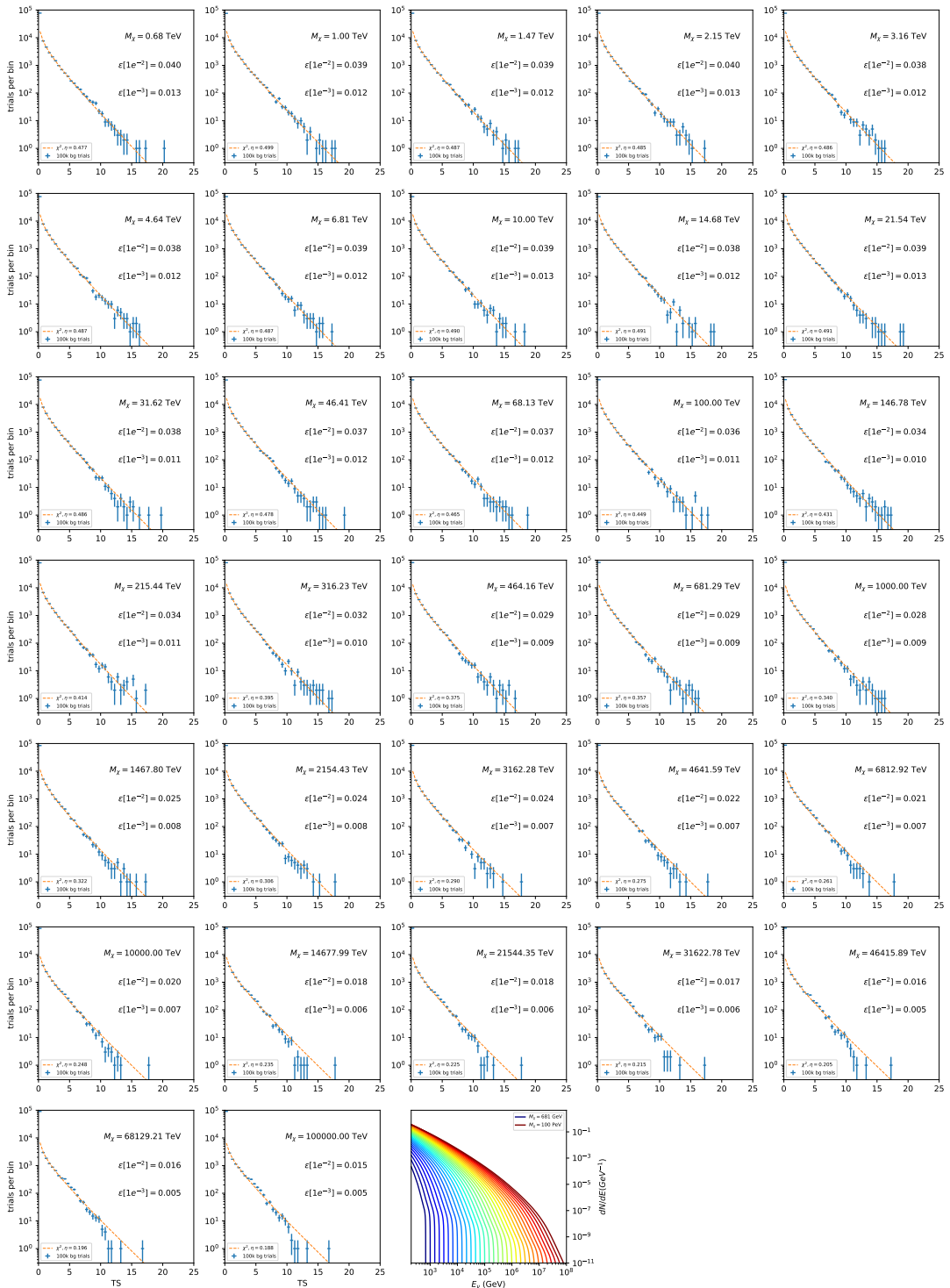


Figure 7.15 Same as Fig. 7.6 for 15, \mathcal{GS} J-factor, stacked sources and $\chi\chi \rightarrow d\bar{d}$.

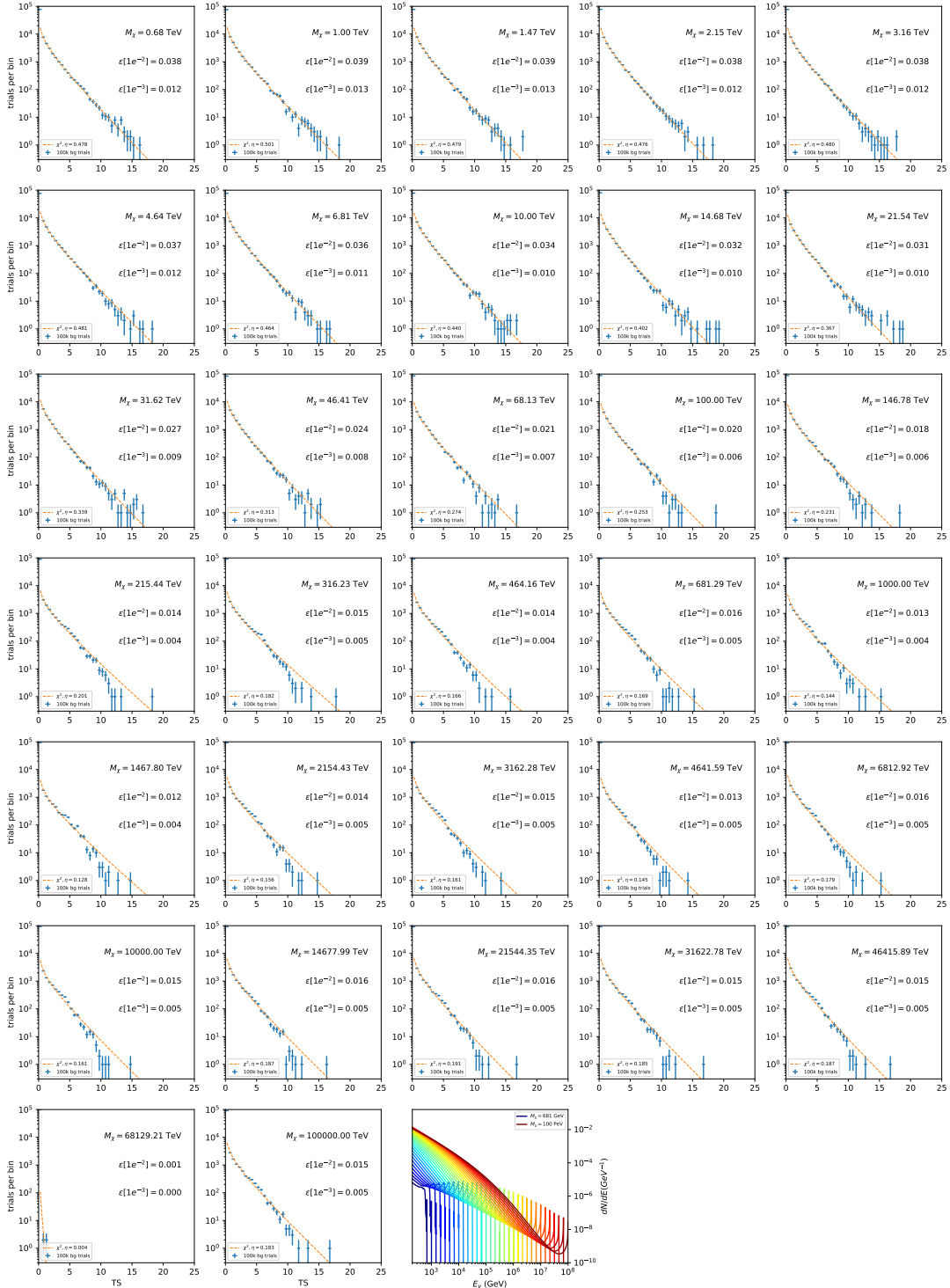


Figure 7.16 Same as Fig. 7.6 for 15, $\mathcal{G}\mathcal{S}$ J-factor, stacked sources and $\chi\chi \rightarrow e\bar{e}$.

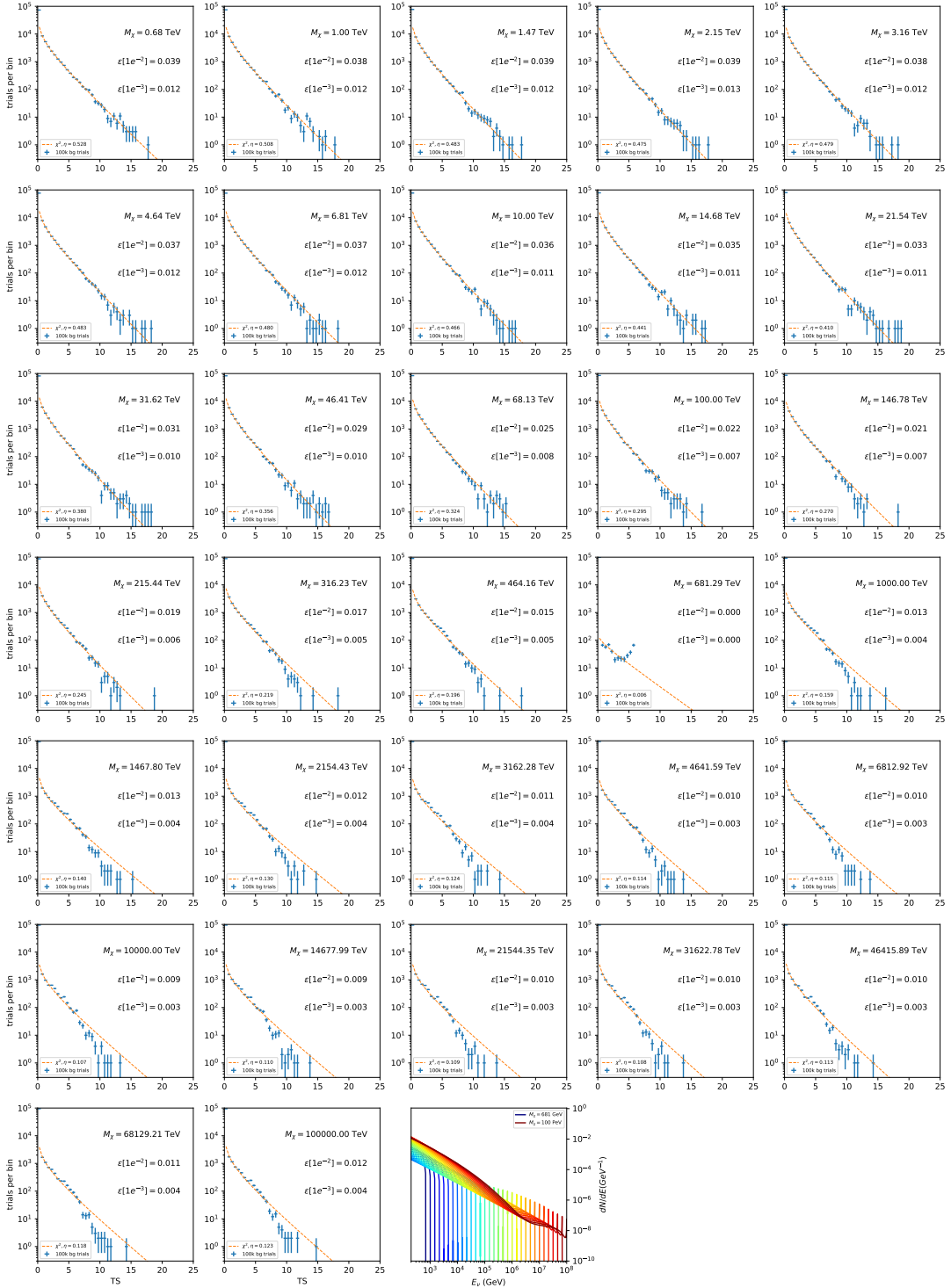


Figure 7.17 Same as Fig. 7.6 for 15, \mathcal{GS} J -factor, stacked sources and $\chi\chi \rightarrow \mu\bar{\mu}$.

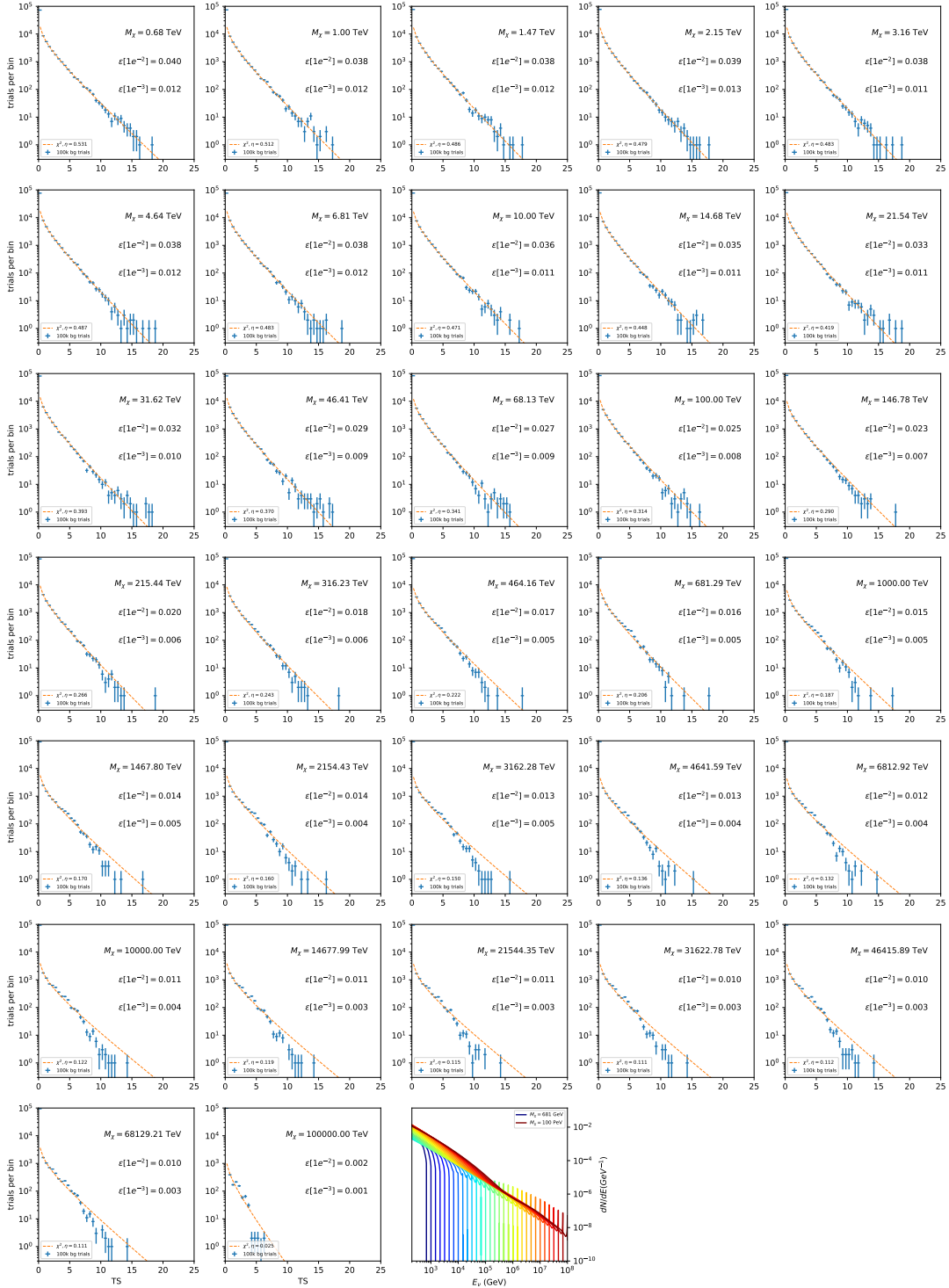


Figure 7.18 Same as Fig. 7.6 for 15, \mathcal{GS} J -factor, stacked sources and $\chi\chi \rightarrow \tau\bar{\tau}$.

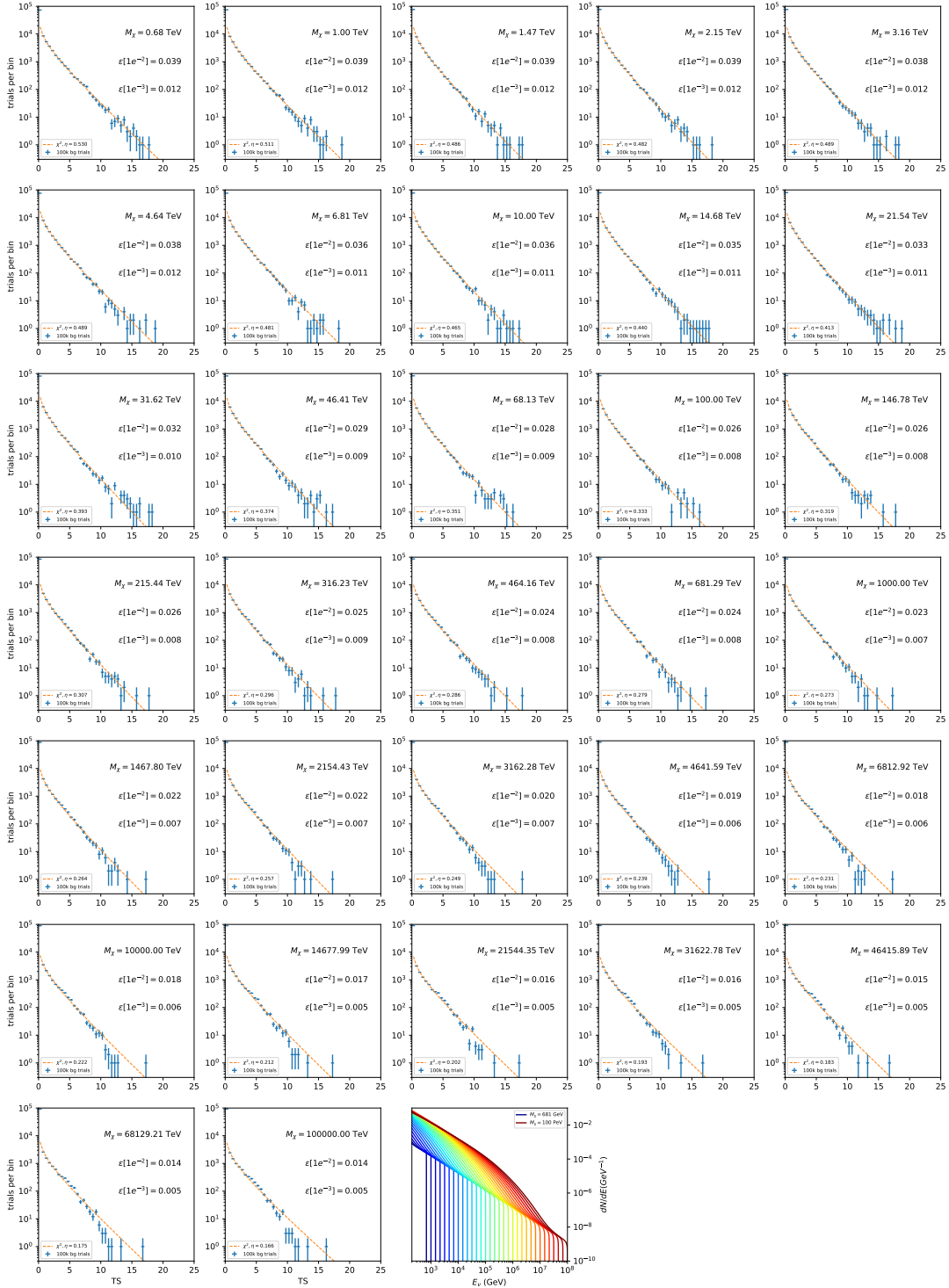


Figure 7.19 Same as Fig. 7.6 for 15, \mathcal{GS} J-factor, stacked sources and $\chi\chi \rightarrow W^+W^-$.

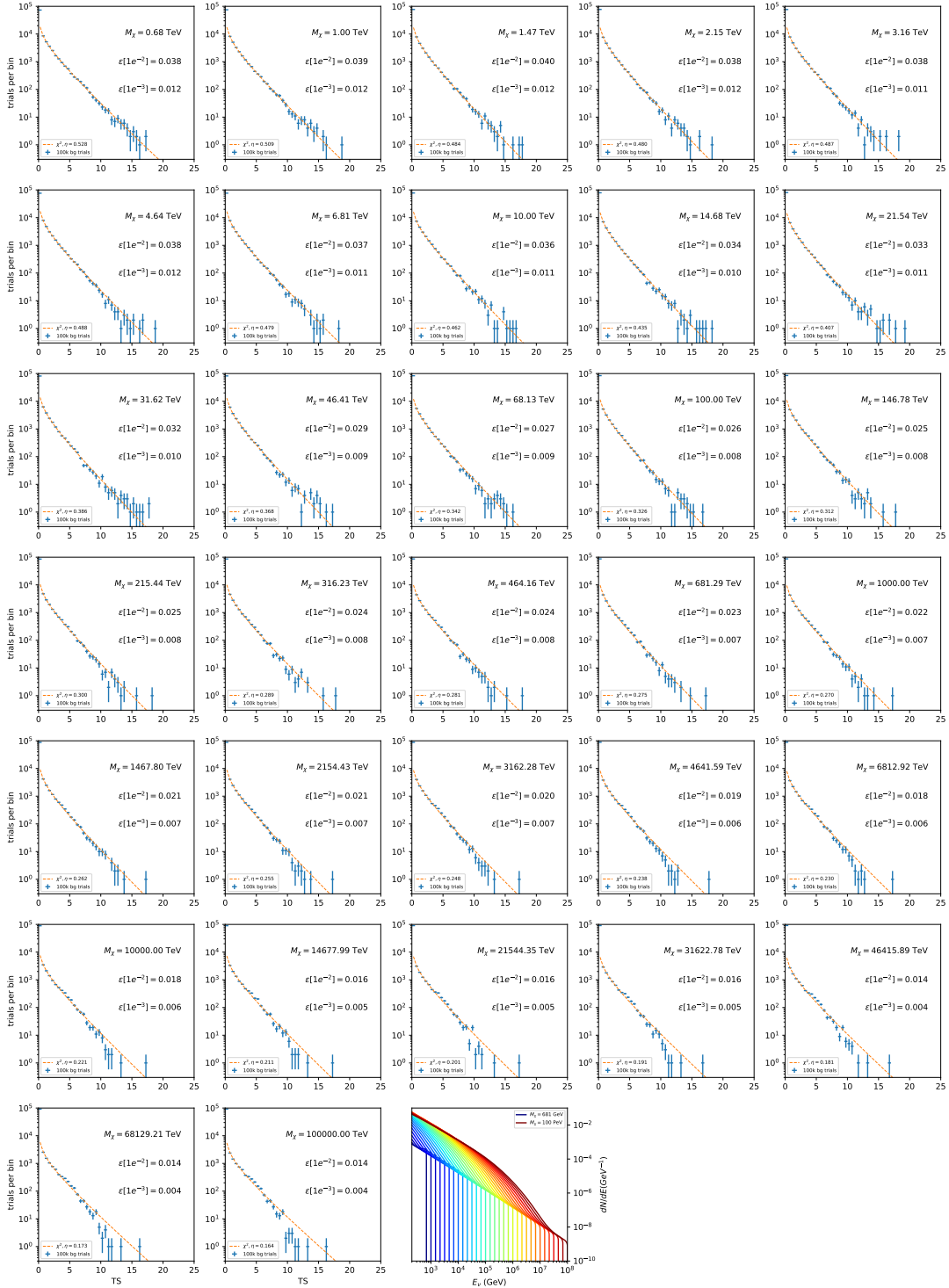


Figure 7.20 Same as Fig. 7.6 for 15, \mathcal{GS} J -factor, stacked sources and $\chi\chi \rightarrow ZZ$.

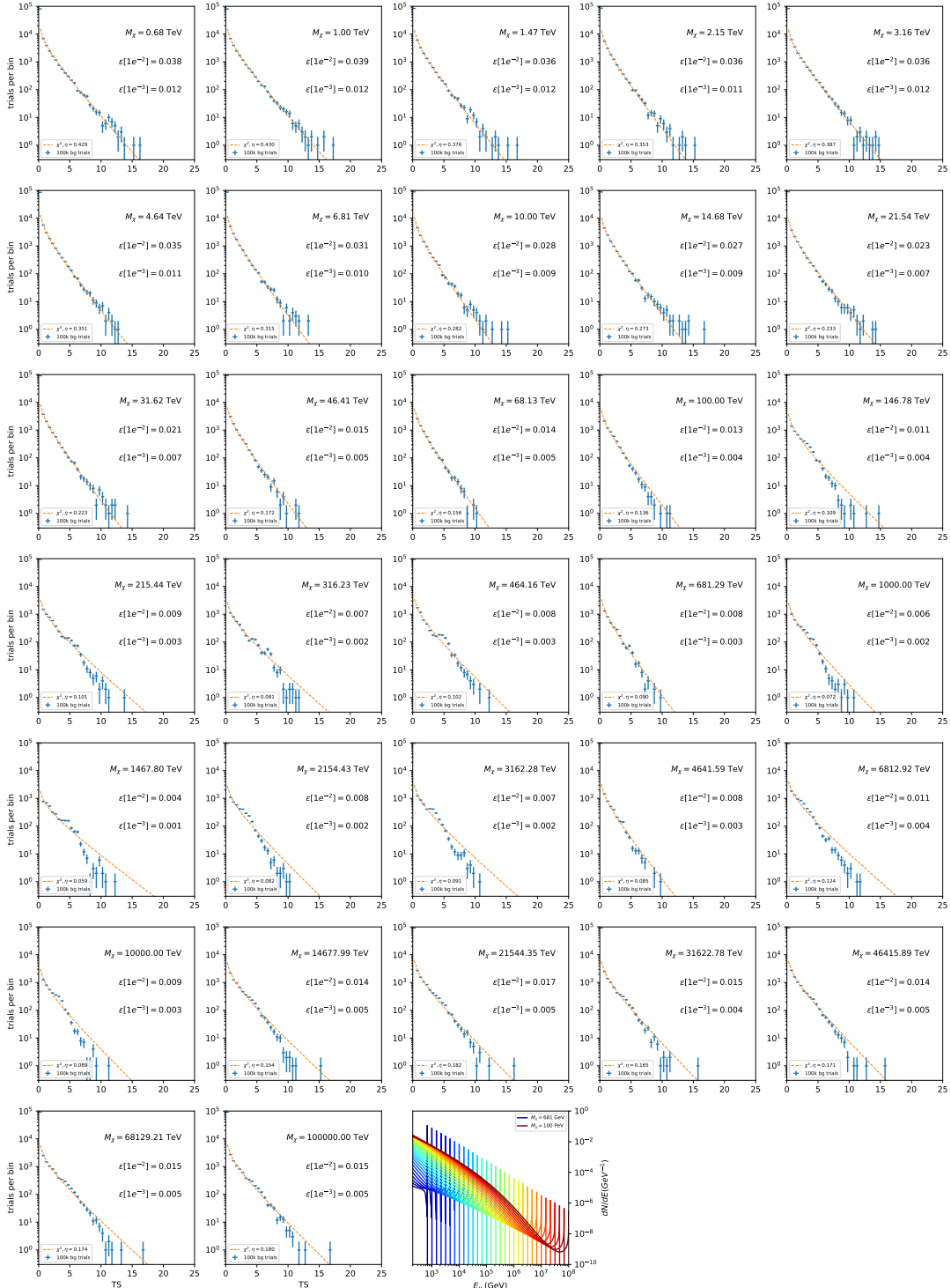


Figure 7.21 Same as Fig. 7.6 for 15, GS J-factor, stacked sources and $\chi\chi \rightarrow \nu_e \bar{\nu}_e$.

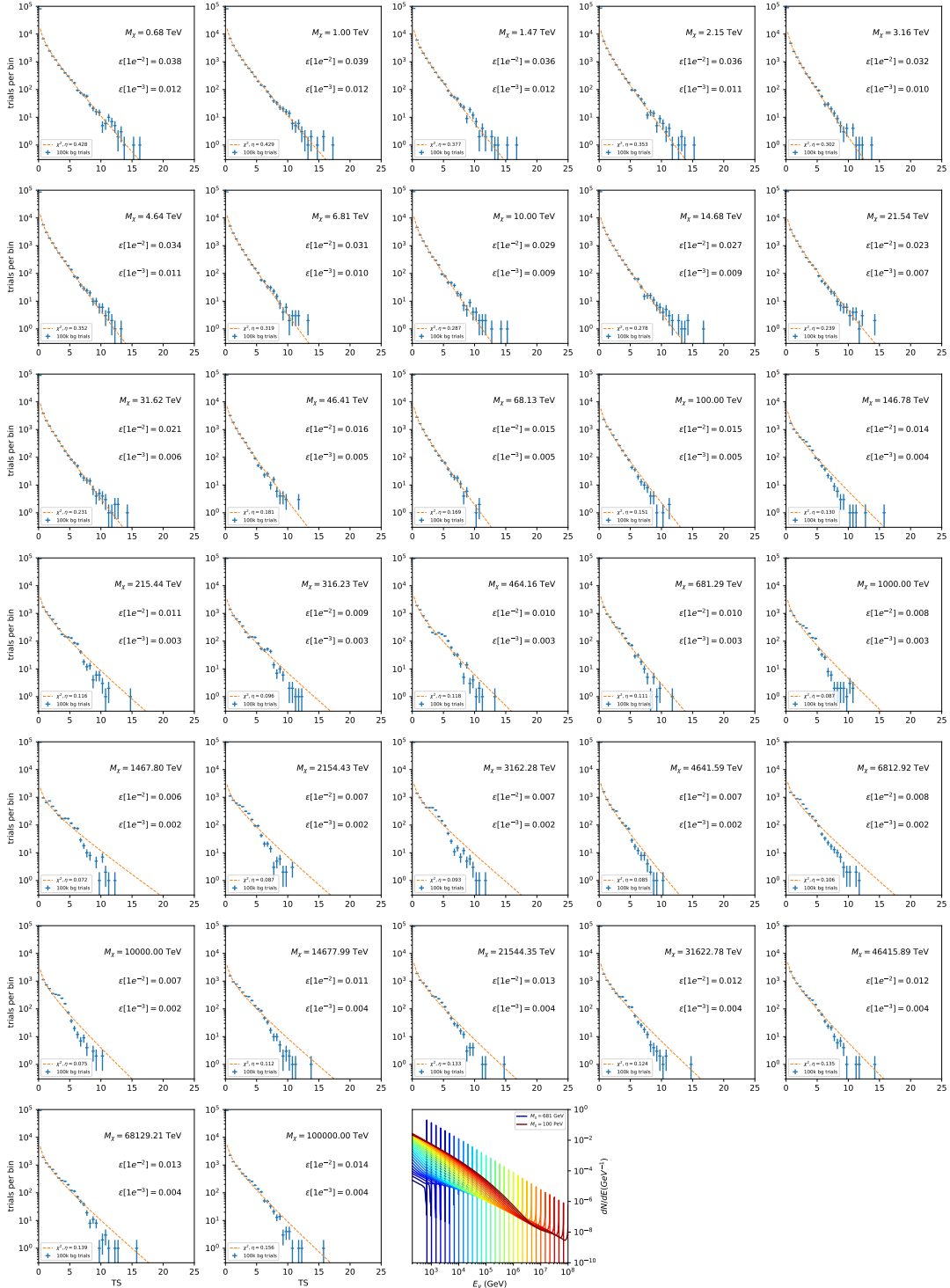


Figure 7.22 Same as Fig. 7.6 for 15, \mathcal{GS} J -factor, stacked sources and $\chi\chi \rightarrow \nu_\mu \bar{\nu}_\mu$.

1674 **7.5.1 TS per Source**

1675 Figure 7.6 to Figure 7.11 present the TS distributions for Segue 1 and Ursa Major II for 100,000
1676 trials. More studies for all annihilation channels and remaining 13 sources were also performed
1677 and are documented in IceCube’s internal wiki.

1678 Although it was not expected, almost every distribution produced follows a χ^2 distribution with
1679 1 degree of freedom. This is important for future assumptions made in Sec. 8 and may justify
1680 statistical calculations assuming Wilk’s theorem is valid.

1681 **7.5.2 Stacked TS**

1682 Figure 7.12 to Figure 7.22 present the TS distributions for a stacked study of 15 sources with
1683 \mathcal{GS} J -factors on 100,000 trials. The presentation of these plots are identical to the single source
1684 distributions in Section 7.5.1.

1685 Each subplot, except the final, is the TS distribution for a specific DM mass listed in the subplot.
1686 The final subplot plots the all DM spectral models used as input for the TS distribution calculations
1687 with bluer lines indicating lower DM mass and redder indicating higher DM mass.

1688 **7.6 Signal Recovery**

1689 We also wish to understand how well the analysis is able to reconstruct signal neutrinos. In
1690 order to test this, we inject neutrinos from our spectral models randomly then attempt to discern the
1691 number of signal neutrinos in the data. Figure 7.23 and Figure 7.24 show this study for $\chi\chi \rightarrow b\bar{b}$,
1692 $t\bar{t}$, and $\nu_\mu\bar{\nu}_\mu$ for a stacked analysis of 15 sources. We see that the analysis is conservative at smaller
1693 m_χ , yet improves at larger m_χ . We also see that the uncertainty around the reconstructed signal
1694 events shrinks for the neutrino annihilation spectra.

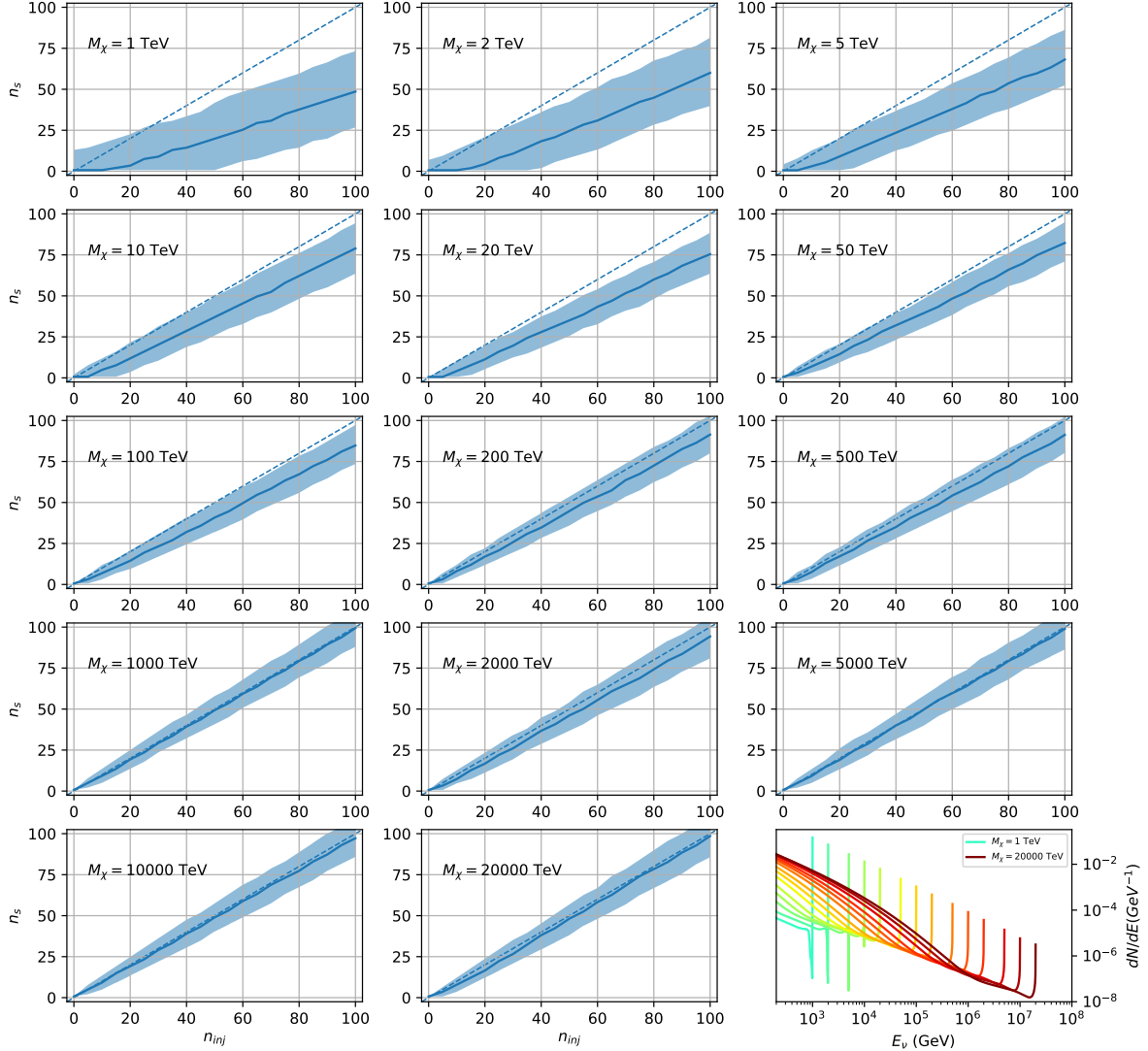


Figure 7.23 Signal Recovery study for an analysis with 15 stacked sources using the \mathcal{GS} J -factors [45]. Each panel block represents 14 studies for DM mass ranging between 1 TeV and 20 PeV and one annihilation channel. Panel block is for $\nu_\mu \bar{\nu}_\mu$. Each panel block features every spectral model used as input in the bottom-right subpanel. The remaining panels show n_{inj} as the number of signal events injected into background simulation. Whereas, n_s is the number of signal events recovered from analyzing the injected simulation. Blue line represents the median values of 100 simulations. Light blue bands show the 1σ statistical uncertainty around the median.

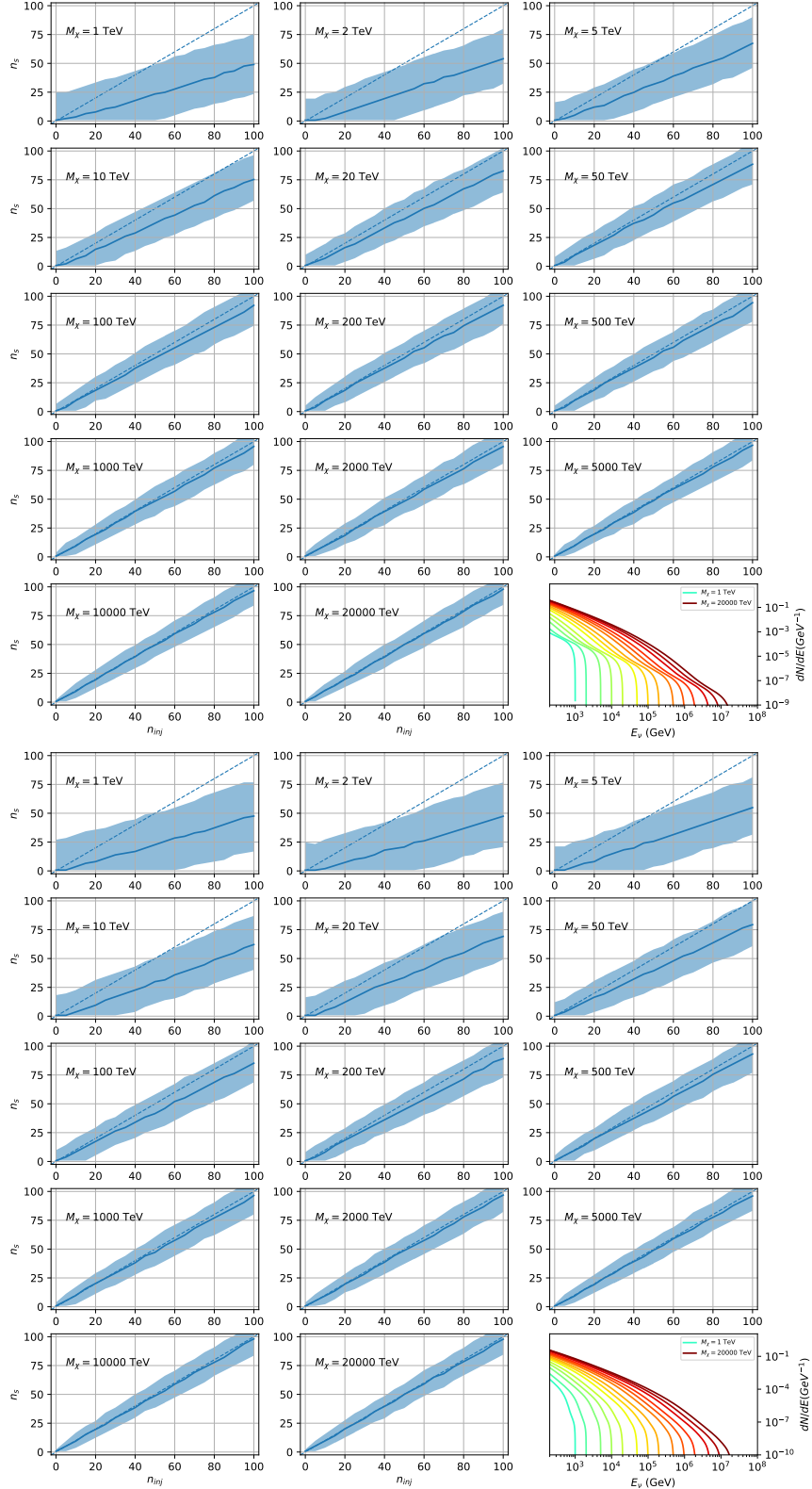


Figure 7.24 Same as Fig. 7.23 but for $\chi\chi \rightarrow t\bar{t}$ (top) and $b\bar{b}$ (bottom).

1695 **7.6.1 Sensitivities**

1696 In IceCube, we usually define the 90% confidence level (CL), as the minimum number of signal
1697 events (n_s) required to have a Type I error rate smaller than 0.5 and Type II error rate of 0.1. We
1698 compute n_s from the following equation

$$n_s = T_{\text{live}} \int_0^{\Delta\Omega} d\Omega \int_{E_{\min}}^{E_{\max}} dE_\nu A_{\text{eff}}(\hat{n}, E_\nu) \frac{d\Phi_\nu}{d\Omega dE_\nu}(\hat{n}, E_\nu), \quad (7.8)$$

1699 to extract the sensitivity on the dark matter annihilation cross-section. T_{live} is the detector livetime,
1700 A_{eff} is the effective area of the detector, and E_{\min} , E_{\max} are the minimum, maximum energies of
1701 the expected neutrinos, respectively.

1702 Sensitivities are calculated for each source individually as if they were the only source and as a
1703 stack over 1000 trials. From Eq. (7.8) and Eq. (7.1) we can compute the $\langle\sigma v\rangle$ at a 90% confidence
1704 level. Figure 7.25 and Fig. 7.26 show the sensitivities for some DM annihilation channels. Not
1705 all channels computed successfully in time for the writing of this dissertation. Among channels
1706 missing include two neutrino flavors: e and τ .

1707 **7.7 Systematics**

1708 Lol What Systematics. Beside signal recovery we don't have many additional studies for here.
1709 The current analysis plan is to compare these sensitivities to another J -factor catalog such as \mathcal{LS}
1710 [66]. Additionally, we set out to perform a standard suite of IceCube systematic studies which
1711 include: **TODO: THE BIG 4: ICE MODEL ETC** The following section enumerates the impact of
1712 the Earth on our hardest neutrino spectra.

1713 **7.7.1 Earth Effects**

1714 One systematic I check however is the impact of the Earth on our sensitivity to $\chi\chi \rightarrow \nu_\mu \bar{\nu}_\mu$.
1715 This channel is expected to be significantly impacted because it has a significant contribution at
1716 PeV energies for $m_\chi \geq 1\text{PeV}$. The Earth is expected to attenuate these higher energy neutrinos.
1717 However, these neutrino spectra have significant low energy contributions, so we do not expect to
1718 entirely loose our sensitivity. This motivated a study examining our $\langle\sigma v\rangle$ sensitivity over all DM
1719 masses sampled for a selection of declinations.

1720 For this systematic study, I sample 6 DM masses per decade from 1 TeV to 100 PeV. I select
1721 declinations that are shared with sources in the *GS* catalog: Bootes I, Canes Venatici II, Leo V,
1722 Ursa Major I, and Ursa Minor. I study a fake source who's *J*-factor is shared with Ursa Major II,
1723 but who's coordinates belong to the aformentioned list. The sensitivity studies performed for each
1724 source (Fig. 7.26 and Section C.5) provided n_s for 1000 trials which we extracted from Eq. (7.8).
1725 We derive $\langle \sigma v \rangle$ using $\log_{10} J = 19.42 \log_{10}(\text{GeV}^2\text{cm}^{-5})$ Figure 7.28 shows the results of these
1726 calculations.

1727 Figure 7.28 shows that we have significant but diminishing sensitivity to source at high decli-
1728 nation. We see in the worse case, the sensitivity at high declination is up to an order of magnitude
1729 worse than at low declination. However, for $m_\chi < 1 \text{ PeV}$, the sensitivities are very similar. Their
1730 similar sensitivities imply that a stacking analysis with IceCube is most powerful in the 1 TeV
1731 to 1 PeV region. Above 1 PeV, our limits and sensitivities are dominated by sources near the
1732 horizon. When we additionaly consider the *J*-factors, we expect Segue 1 to dominate contributions
1733 to sensitivity and limits where $m_\chi > 1 \text{ PeV}$.

1734 7.8 Conclusions

1735 We built many things for this analysis. We utilized advanced computing techniques like
1736 parrallel programming and spline fitting of particle physics Monte Carlo to greatly expand and
1737 refine IceCube's sensitivity to DM annihilation from dSphs. We imported updated astrophysical
1738 and particle physics models that better represent what we beleive neutrino signals from DM
1739 annihilation should look like. We, for the first time, build an analysis that is sensitvity to PeV DM
1740 annihilation.

1741 When we compare to previous IceCube publications of dSphs [69], we see an order of magnitude
1742 imrovement to our sensitivity. This analysis has been working group approved within IceCube and
1743 has begun the unblinding process. This processes did not complete in time for this dissertation.
1744 Therefor we do not show data for this thesis and is the clear next step.

1745 The test statistic distributions in this analysis also demonstrate more characteristic behaviour
1746 compared to previous DM analyses. With a 10 year dataset, we finally have enough statistics to

1747 almost trivially combine with other photon observatories, such as HAWC. The first ground work for

1748 a multi-messenger DM search is provided with concluding remarks in Sec. 8.

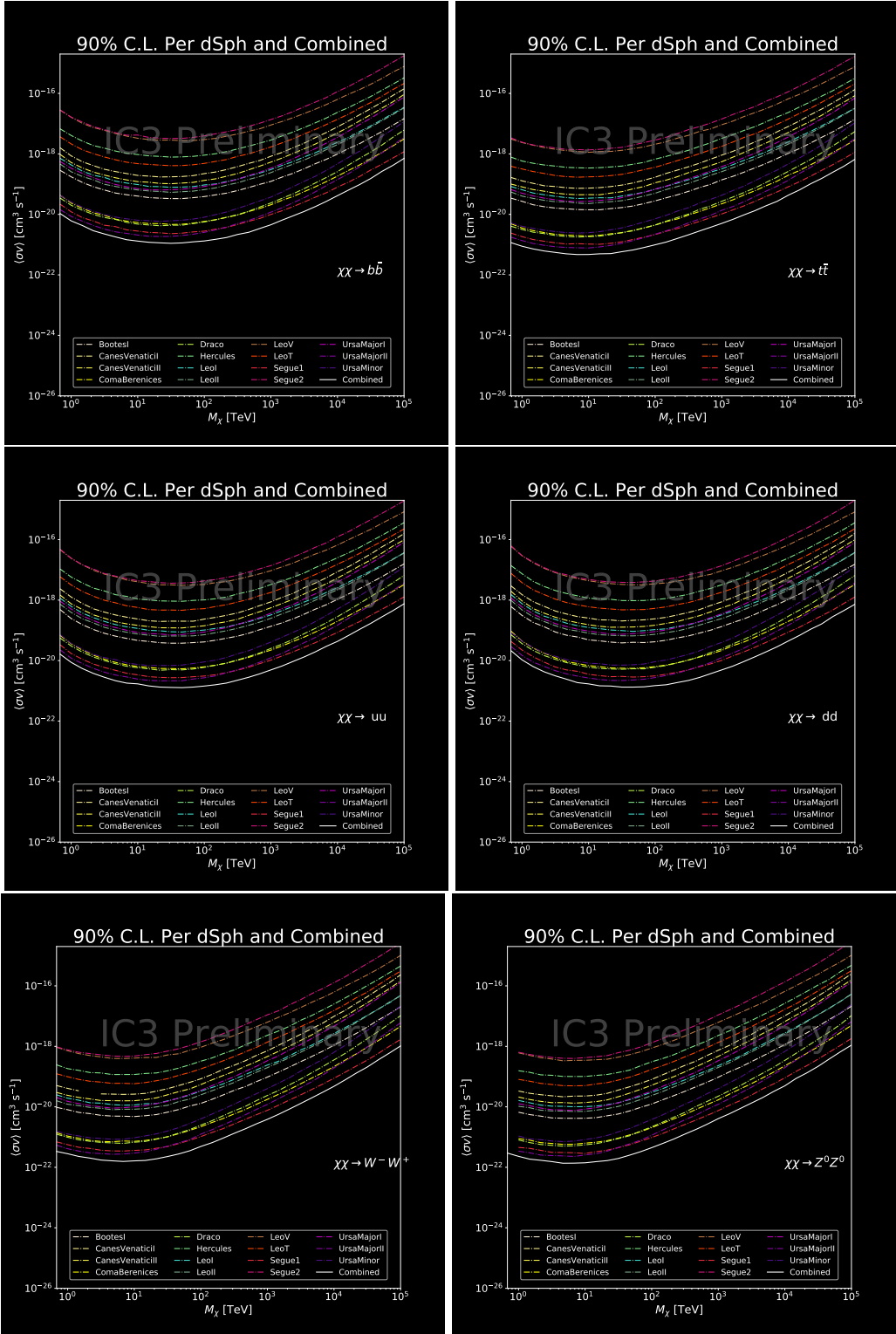


Figure 7.25 IceCube North Sky Track Sensitivities. Each panel shows sensitivity curves for a specific DM annihilation channel. Sensitivities are for the velocity-weighted cross-section $\langle\sigma v\rangle$ versus m_χ . Dotted, colored lines are sensitivities for individual sources. Solid white lines are for the combined sensitivity of all 15 \mathcal{GS} sources used in this study.

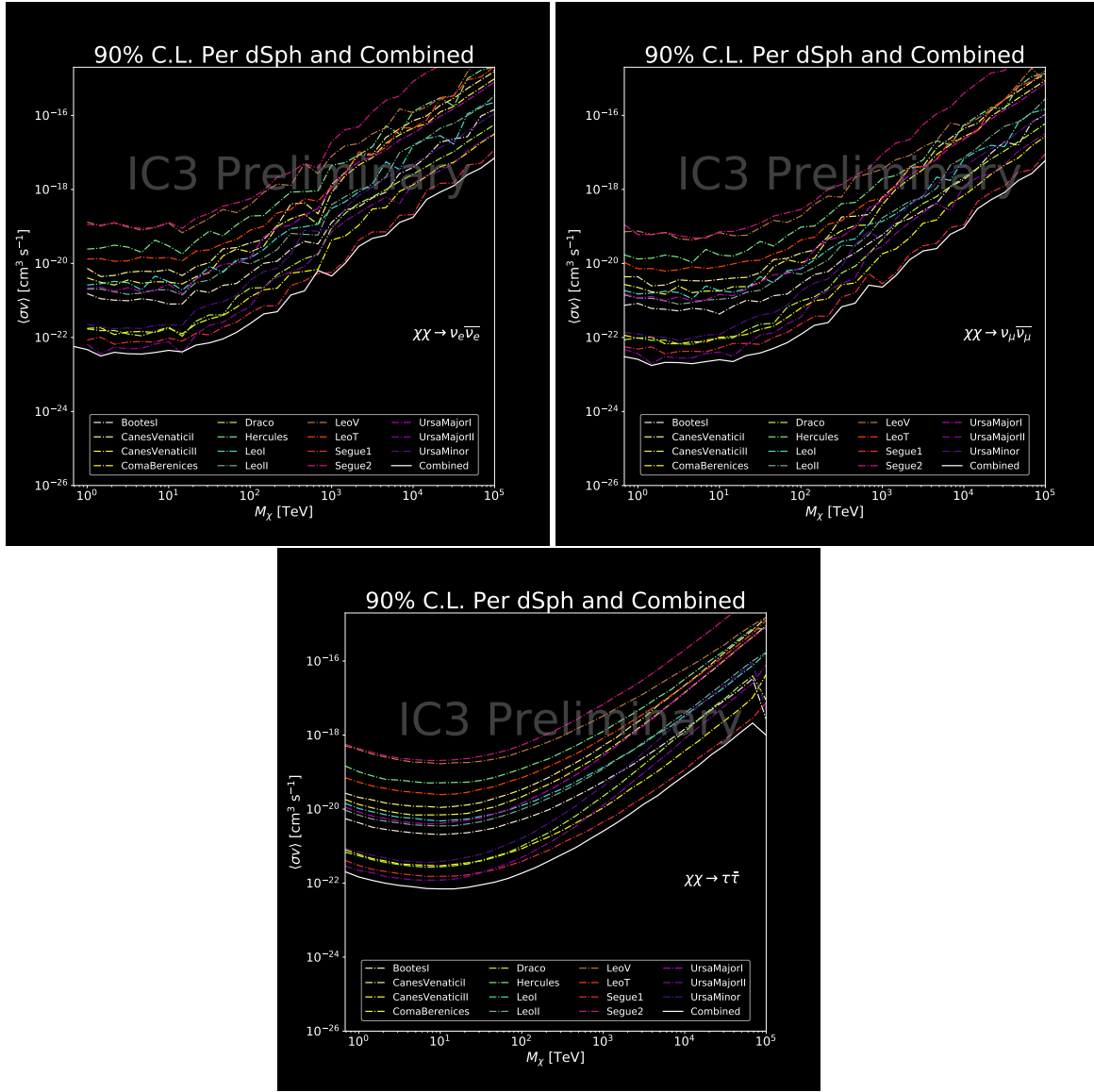


Figure 7.26 Same as Fig. 7.25 for three additional DM annihilation channels.

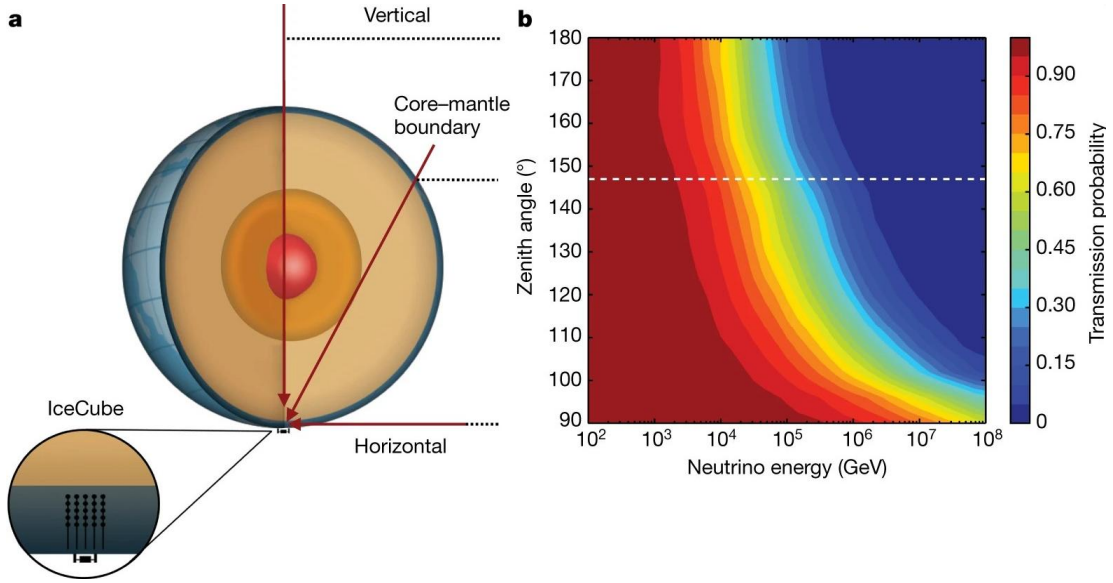


Figure 7.27 Panel A: Neutrino's from the Northern sky and incident on the IceCube detector will travel through the Earth. How much of the Earth these neutrinos travels is a function of zenith from the vertical axis. Panel B: SM precision of neutrino transmission probabilities for neutrinos arriving at 90° - 180° zenith and with 100 GeV to 100 PeV energies. High-energy neutrinos traversing the whole Earth are completely absorbed, whereas low-energy neutrinos pass through unimpeded. Neutrinos coming from above the horizon will arrive unimpeded for all neutrino energies. Figure pulled from [76].

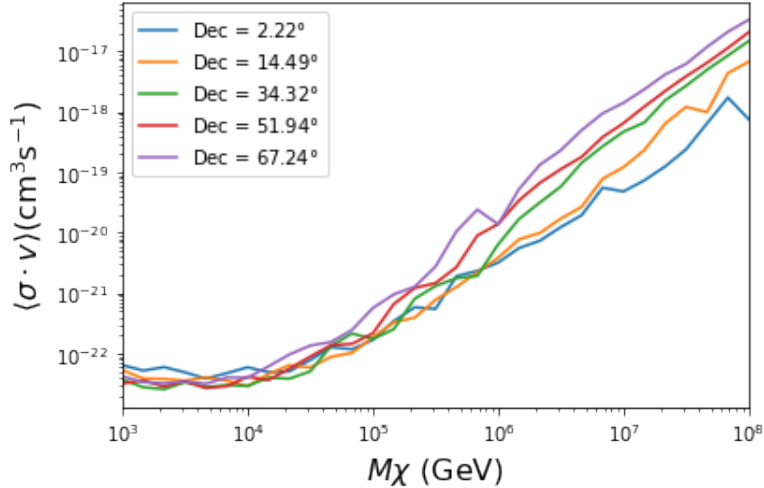


Figure 7.28 $\langle\sigma v\rangle$ sensitivities for 5 imaginary sources with $\log_{10} J = 19.42$ $\log_{10}(\text{GeV}^2 \text{cm}^{-5})$. Each imaginary source shares a declination with a source in Tab. 5.1

CHAPTER 8

NU DUCK

1749

MULTI-EXPERIMENT SUPPLEMENTARY FIGURES

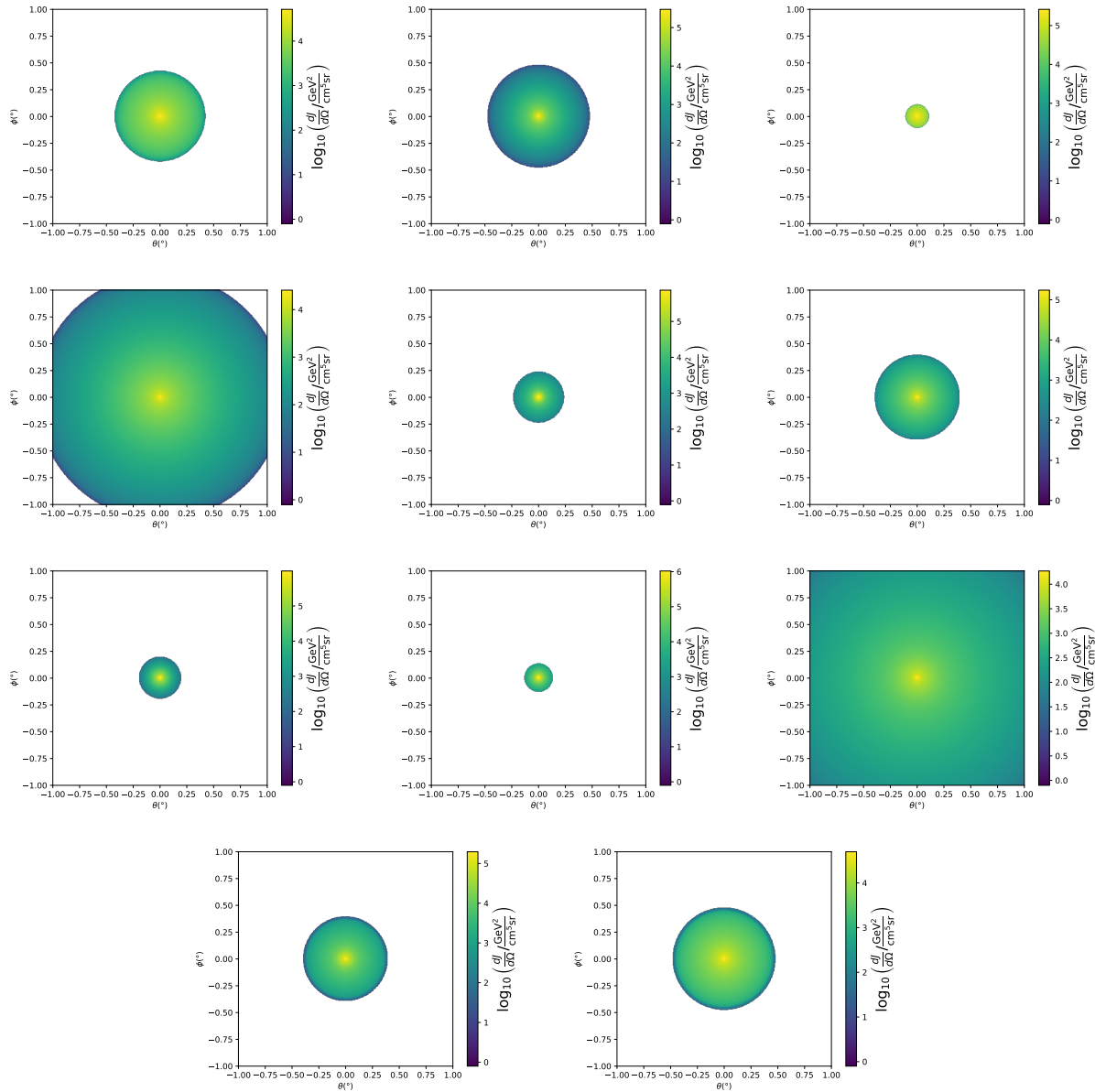


Figure A.1 Sister figure to Figure 5.3. Sources in the first row from left to right: Bootes I, Canes Venatici I, II. In second row: Draco, Hercules, Leo I. In the first row: Leo II, Leo IV, Sextans. In the final row: Ursa Major I, Ursa Major II.

APPENDIX B

1751 MULTITHREADING DARK MATTER ANALYSES SUPPLEMENTARY MATERIAL

1752 B.1 Remaining Spectral Models

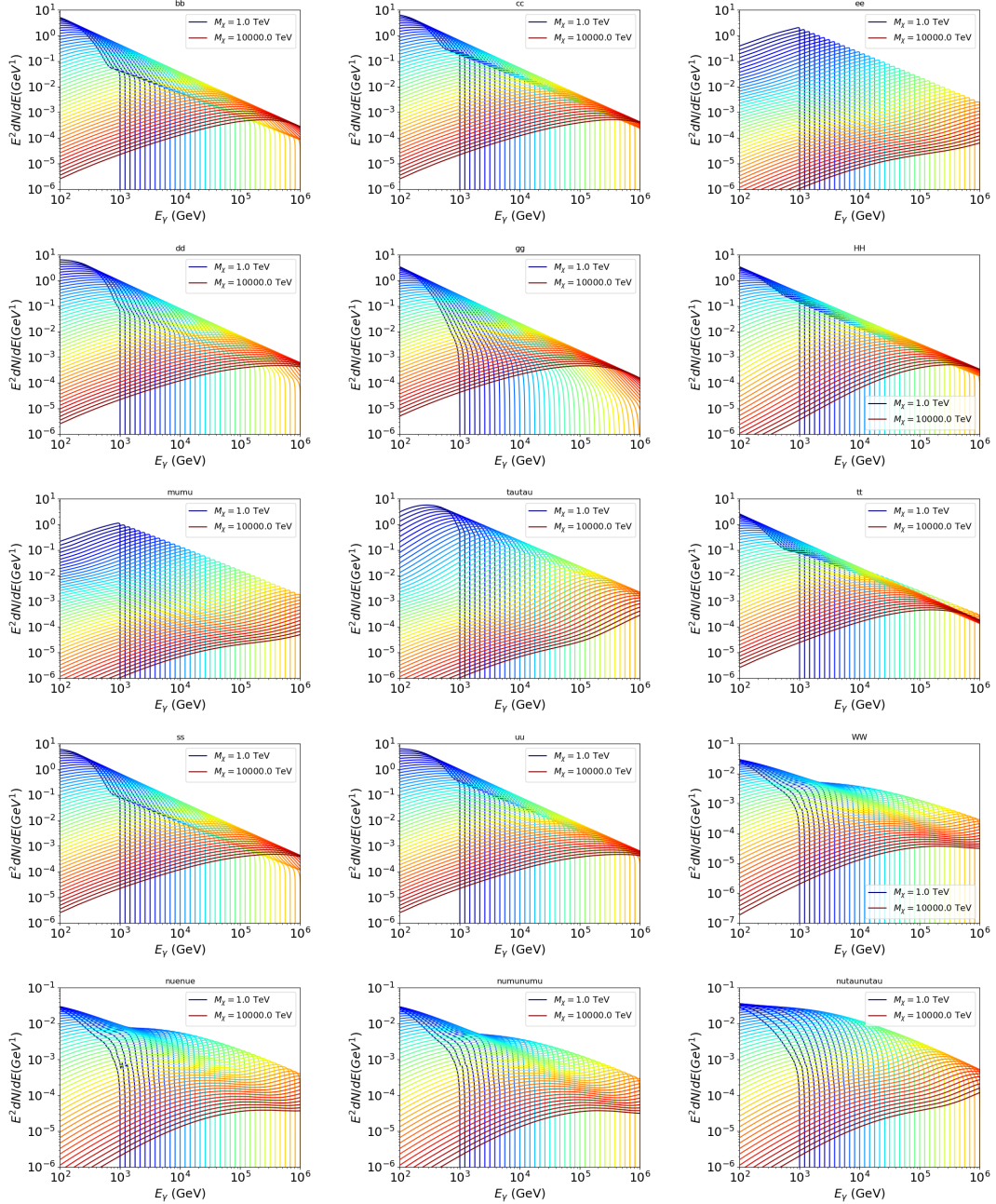


Figure B.1 Sister figure to Figure 6.2 for remaining SM primary annihilation channels studied for this thesis. These did not require any post generation smoothing and so are directly pulled from [65] with a binning scheme most helpful for a HAWC analysis.

1753 B.2 mpu_analysis.py

```
17541 import warnings
17552 with warnings.catch_warnings():
17563     warnings.simplefilter("ignore")
17574 # Python base libraries
17585 import os
17596 import sys
17607 import time
17618 # Import general libraries with namespace
17629 import matplotlib
17630 # Necessary for computing on cluster
17641 matplotlib.use("agg")
17652 import numpy as np
17663 import multiprocessing as mp
17674 # Import HAWC software
17685 sys.path.insert(1, os.path.join(os.environ['HOME'], 'hawc_software', 'threeML-
1769     analysis-scripts', 'fitModel'))
17706 from analysis_modules import *
17717 from threeML import *
17728 from hawc_hal import HAL, HealpixConeROI
17739 from threeML.minimizer.minimization import FitFailed
17740 # Import Dark Matter HAWC Libraries
17751 import analysis_utils as au
17762 import spectra as spec
17773 import sources as srcs
17784
17795 #* READ ONLY PATHS This block will change eventually
17806 MASS_LIST = './plotting/studies/nd/masses.txt'
17817 CHAN_LIST = './plotting/studies/nd/chans.txt'
17828
17839 #* WRITE PATHS, default location is to scratch
17840 OUT_PATH = os.path.join(os.environ["SCRATCH"], os.environ["USER"], 'New_duck')
```

```

17851 print('Our out path is going to be {}'.format(OUT_PATH))
17862
17873 # Define parallel Function. Can also be run serially
17884 def some_mass_fit(sigVs, datalist, shape, dSph, jfactor, mass_chan,
17895                 progress=None, log_file='', queue=None, i_job=0):
17906
17917     if progress is None:
17928         progress = [0]
17939     else: # Create log files for each thread
17940         log_file = log_file.replace('.log', '_ThreadNo_')
17951         log_file = log_file + str(i_job) + ".log"
17962         sys.stdout = open(log_file, "w")
17973
17984     fits = []
17995
18006     try:
18017         for m_c in mass_chan:
18028             print(f'Mass chan tuple: {m_c}')
18039             mass = int(m_c[0])
18040             ch = m_c[1]
18051             # Build path to output files
18062             outPath = os.path.join(OUT_PATH, ch, dSph)
18073             au.ut.ensure_dir(outPath)
18084
18095             if progress[i_job] < 0:
18106                 # If the master gets a Keyboard interrupt, commit suicide.
18117                     break
18128
18139                 ### Start Model Building for DM mass and SM channel #####
18140                 spectrum = spec.DM_models.HDMSpectra()
18151                 spectrum.set_channel(ch)
18162
18173                 myDwarf = ExtendedSource(dSph, spatial_shape=shape,

```

```

18184                     spectral_shape=spectrum)
18195
18206             spectrum.J = jfactor * u.GeV**2 / u.cm**5
18217             spectrum.sigmav = 1e-24 * u.cm**3 / u.s
18228             spectrum.set_dm_mass(mass * u.GeV)
18239
18240             spectrum.sigmav.bounds = (1e-30, 1e-12)
18251             model = Model(myDwarf)
18262             ##### End model Building #####
18273
18284             jl = JointLikelihood(model, datalist, verbose=False)
18295
18306             try:
18317                 result, lhdf = jl.fit(compute_covariance=False)
18328                 ts = -2.* (jl.minus_log_like_profile(1e-30) - jl.
1833 _current_minimum)
18349                 # Also profile the LLH vs sv
18350                 ll = jl.get_contours(spectrum.sigmav, sigVs[0],
18361                               sigVs[-1], len(sigVs),
18372                               progress=False, log=['False'])
18383
18394                 sigv_ll = au.ut.calc_95_from_profile(ll[0], ll[2])
18405                 # Write results to file
18416                 outFileLL = outPath+f"/LL_{dSph}_{ch}_mass{int(mass)}_GD.txt"
18427                 np.savetxt(outFileLL, (sigVs, ll[2]),
18438                               delimiter='\t', header='sigV\tLL\n')
18449
18450                 with open(outPath+f"/results_{dSph}_{ch}_mass{int(mass)}_GD.
1846 txt", "w") as results_file:
18471                     results_file.write("mDM [GeV]\tsigV_95\tsigV_B.F.\n")
18482
18493                     results_file.write("%i\t%.5E\t%.5E\t%.5E"%(mass, sigv_ll,
18504                                         ts, result.value[0]))

```

```

18515         # End write to file
18516
18517     except FitFailed: # Don't kill all threads if a fit fails
18518         print("Fit failed. Go back and calculate this spectral model
18519             later")
18520
18521         fits.append((ch, mass, -1, -1))
18522
18523         with open(log_file+'.fail', 'w') as f_file:
18524             f_file.write(f'{ch}, {mass}\n')
18525
18526
18527         progress[i_job] += 1
18528
18529         matplotlib.pyplot.close() # Prevent leaky memory
18530
18531
18532         fits.append((ch, mass, result.value[0], ts))
18533
18534         progress[i_job] += 1
18535
18536         matplotlib.pyplot.close()
18537
18538     except KeyboardInterrupt:
18539
18540         progress[i_job] = -1
18541
18542
18543         fits = np.array(fits)
18544
18545         if queue is None:
18546
18547             return fits
18548
18549         else:
18550
18551             queue.put((i_job, fits))
18552
18553
18554 def main(args):
18555
18556     masses = np.loadtxt(MASS_LIST, dtype=int)
18557
18558     chans = np.loadtxt(CHAN_LIST, delimiter=',', dtype=str)
18559
18560     mass_chan = au.ut.permute_lists(chans, masses)
18561
18562
18563     print(f"DM masses for this study are: {masses}")
18564
18565     print(f"SM Channels for this study are XX -> {chans}")
18566
18567     print(mass_chan)
18568
18569
18570     # extract information from input argument

```

```

18847 dSph = args.dSph
18858 data_mngr = au.ut.Data_Selector('P5_NN_2D')
18869 dm_profile = srcts.Spatial_DM(args.catalog, dSph, args.sigma, args.decay)
18870
18881     ### Extract Source Information ####
18892 if dm_profile.get_dec() < -22.0 or dm_profile.get_dec() > 62.0:
18903     raise ValueError("HAWC can't see this source D: Exitting now...")
18914
18925 print(f'{dSph} information')
18936 print(f'jfac: {dm_profile.get_factor()}\tRA: {dm_profile.get_ra()}\tDec: {dm_profile.get_dec()}\n')
18957
18968 shape = SpatialTemplate_2D(fits_file=dm_profile.get_src_fits())
18979     ### Finish Extract Source Information ####
18980
18991     ### LOAD HAWC DATA ####
19002 roi = HealpixConeROI(data_radius=2.0, model_radius=8.0,
19013                         ra=dm_profile.get_ra(), dec=dm_profile.get_dec())
19024 bins = choose_bins.analysis_bins(args, dec=dm_profile.get_dec())
19035
19046 hawc = HAL(dSph, data_mngr.get_datmap(), data_mngr.get_detres(), roi)
19057 hawc.set_active_measurements(bin_list=bins)
19068 datalist = DataList(hawc)
19079     ### FINISH LOAD HAWC DATA ####
19080
19091 # set up SigV sampling. This sample is somewhat standardized
19102 sigVs = np.logspace(-28,-18, 1001, endpoint=True) # NOTE This will change
1911 with HDM
19123
19134 if args.n_threads == 1:
19145     # No need to start || programming just iterate over the masses
19156     kw_arg = dict(sigVs=sigVs, datalist=datalist, shape=shape, dSph=dSph,
19167                     jfactor=dm_profile.get_factor(), mass_chan=mass_chan,

```

```

19178         log_file=args.log)
19189     some_mass_fit(**kw_arg)
19190 else:
19201     # I Really want to suppress TQMD output
19212     from tqdm import tqdm
19223     from functools import partialmethod
19234     tqdm.__init__ = partialmethod(tqdm.__init__, disable=True)
19245
19256     x = np.array_split(mass_chan, args.n_threads)
19267     n_jobs = len(x)
19278
19289     print("Thread jobs summary by mass and SM channel")
19290     for xi in x:
19301         print(f'{xi}')
19312
19323     queue = mp.Queue()
19334     progress = mp.Array('i', np.zeros(n_jobs, dtype=int))
19345
19356     # Define task pool that will be split amongsts threads
19367     kw_args = [dict(sigVs=sigVs, datalist=datalist, shape=shape,
19378                     dSph=dSph, jfactor=dm_profile.get_factor(),
19389                     mass_chan=mass_chan, progress=progress,
19390                     queue=queue, i_job=i, log_file=args.log)
19401             for i, mass_chan in enumerate(x)]
19412
19423     # Define each process
19434     procs = [mp.Process(target=some_mass_fit, kwargs=kw_args[i]) \
19445                 for i in range(n_jobs)]
19456
19467     ### Start MASTER Thread only code block ###
19478     # Begin running all child threads
19489     for proc in procs: proc.start()
19490

```

```

19501     try:
19512         # In this case, the master does nothing except monitor progress of
1952         the threads
19533             # In an ideal world, the master thread also does some computation.
19544                 n_complete = np.sum(progress)
19555                     while_count = 0
19566
19577                         while n_complete < len(mass_chan):
19588
19599                             if np.any(np.asarray(progress) < 0):
19600                                 # This was no threads are stranded when killing the script
19611                                     raise KeyboardInterrupt()
19622                                         if while_count%1000 == 0:
19633                                             print(f"{np.sum(progress)} of {len(mass_chan)} finished")
19644
19655                                         n_complete = np.sum(progress)
19666                                             time.sleep(.25)
19677                                                 while_count += 1
19688
19699                                         except KeyboardInterrupt:
19700                                             # signal to jobs that it's time to stop
19711                                                 for i in range(n_jobs):
19722                                                     progress[i] = -2
19733                                                         print('\nKeyboardInterrupt: terminating early.')
19744                                         ### End MASTER Thread only code block ###
19755
19766                                         fitss = [queue.get() for proc in procs]
19777                                             print(fitss)
19788                                             print(f'Thread statuses: {progress[:]}')
19799
19800                                         # putting results in a file
19811
19822                                             print("QUACK! All Done!")

```

```

19833
19844
19855 if __name__ == '__main__':
19866     import argparse
19877
19888     p = argparse.ArgumentParser(description="Run a DM annihilation analysis on
1989      a dwarf spheroidal for a specific SM channel for DM masses [1 TeV to 10
1990      PeV]")
19919
19920     # Dwarf spatial modeling arguements
19931     p.add_argument("-ds", "--dSph", type=str,
19942             help="dwarf spheroidal galaxy to be studied", required=
1995 True)
19963     p.add_argument("-cat", "--catalog", type=str, choices=['GS15', 'LS20'],
19974             default='LS20', help="source catalog used")
19985     p.add_argument("-sig", "--sigma", type=int, choices=[-1, 0, 1], default=0,
19996             help="Spatial model uncertainty. 0 corresponds to the
2000 median. +/-1 correspond to the +/-1sigma uncertainty respectively.")
20017
20028     # Arguements for the energy estimators
20039     p.add_argument("-e", "--estimator", type=str,
20040             choices=['P5_NHIT', 'P5_NN_2D'],
20051             default="P5_NN_2D", required=False,
20062             help="The energy estimator choice. Options are: P5_NHIT,
2007 P5_NN_2D. GP not supported (yet).")
20083     p.add_argument("--use-bins", default=None, nargs="*",
20094             help="Bins to use for the analysis", dest="use_bins")
20105     p.add_argument('--select_bins_by_energy', default=None, nargs="*",
20116             help="Does nothing. May fill in later once better
2012 understood")
20137     p.add_argument('--select_bins_by_fhit', default=None, nargs="*",
20148             help="Also does nothing see above")
20159     p.add_argument( '-ex', '--exclude', default=None, nargs="*",

```

```

20160         help="Exclude Bins", dest="exclude")

20171

20182     # Computing and logging arguements.

20193     p.add_argument('-nt', '--n_threads', type=int, default=1,
20204             help='Maximum number of threads spawned by script. Default
2021      is 4')

20225     p.add_argument('-log', '--log', type=str, required=True,
20236             help='Name for log files. Especially needed for threads')

20247

20258     p.add_argument('--decay', action="store_true",
20269             help='Set spectral DM hypothesis to decay')

20270

20281     args = p.parse_args()
20292     print(args.decay)
20303     if args.exclude is None: # default exclude bins 0 and 1
20314         args.exclude = ['B0C0Ea', 'B0C0Eb', 'B0C0Ec', 'B0C0Ed', 'B0C0Ee']

20325

20336     if args.decay: OUT_PATH += '_dec'
20347     else: OUT_PATH += '_ann'

20358

20369     OUT_PATH = OUT_PATH + '_' + args.catalog
20370     if args.sigma != 0: OUT_PATH += f'_{args.sigma}sig'

20381

20392     main(args)

```

2040 **B.3 Comparison with Glory Duck**

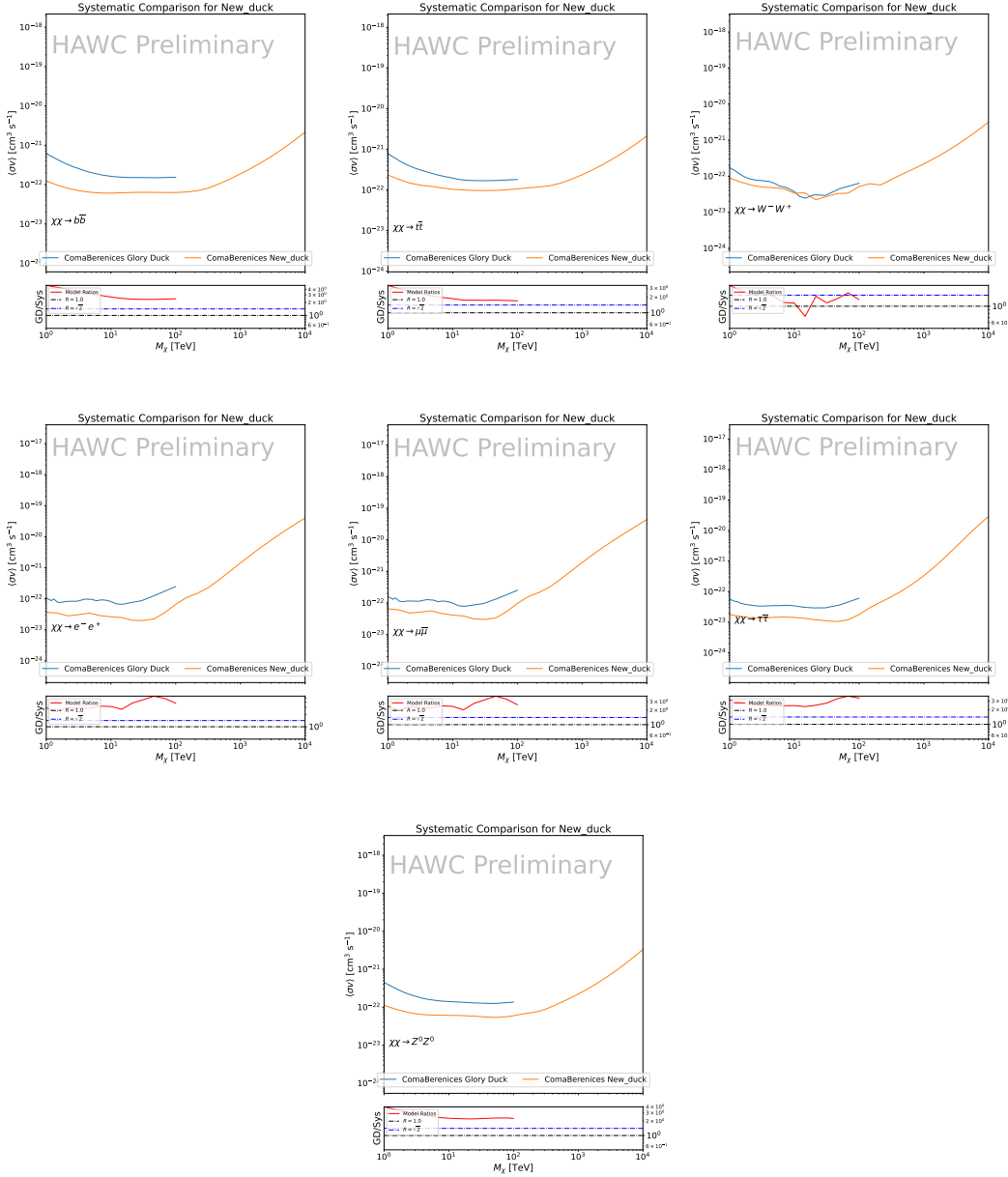


Figure B.2 Comparison of HAWC limits from this analysis to Glory Duck (Fig. 5.5) for Coma Berenices and 7 DM annihilation channels.

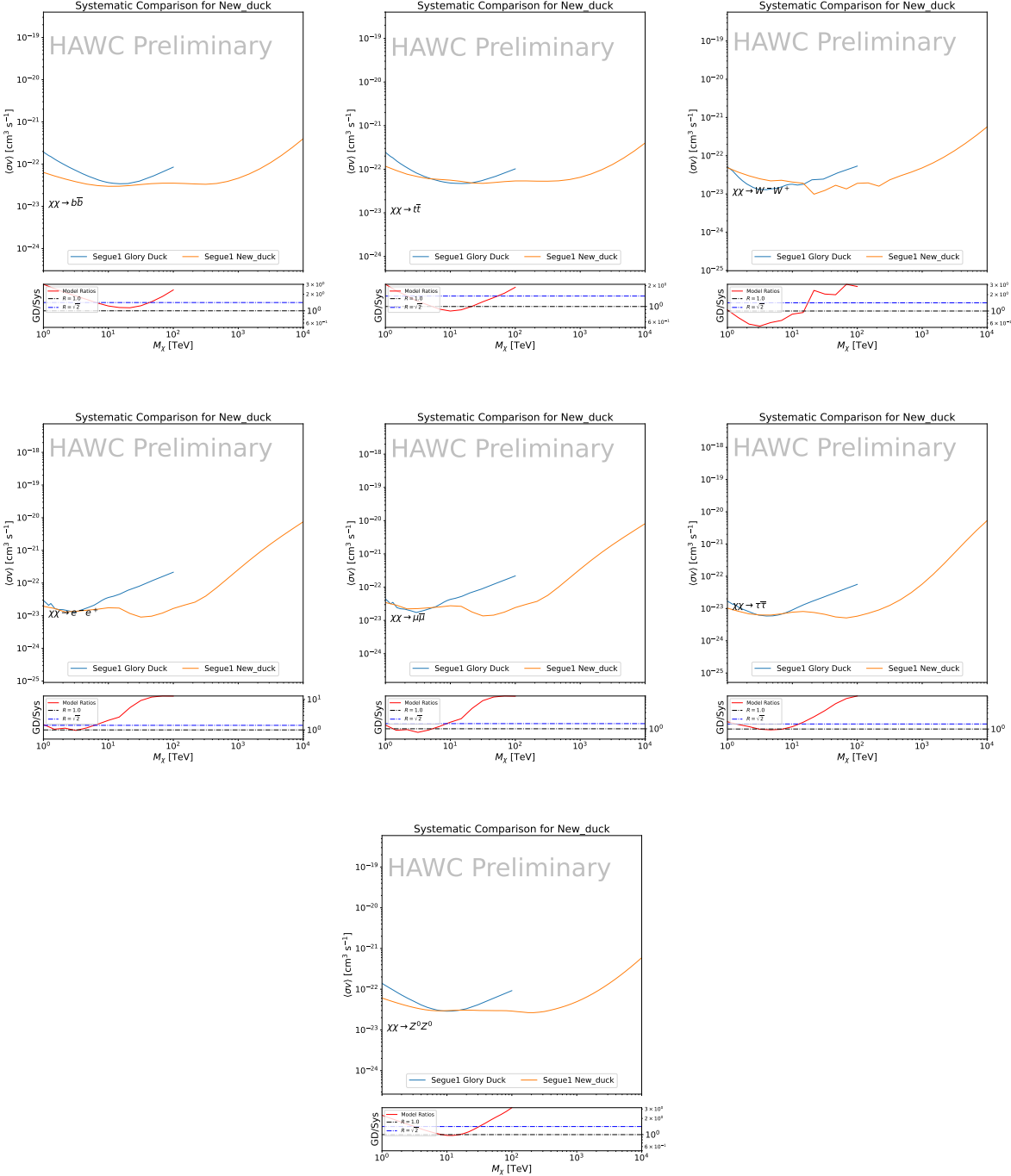


Figure B.3 Same as Fig. B.2 but for Segue 1.

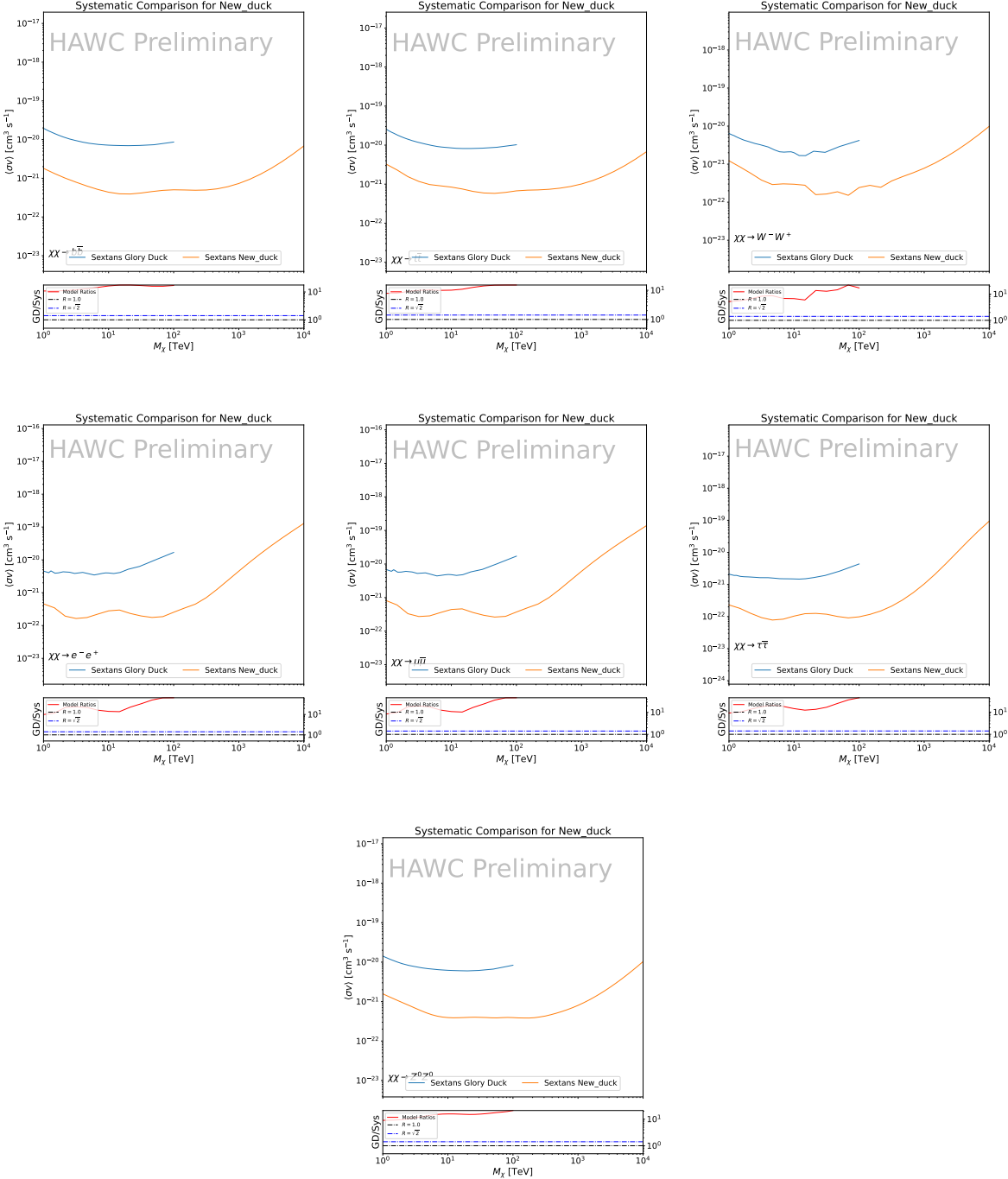


Figure B.4 Same as Fig. B.2 but for Sextans.

APPENDIX C

2041 ICECUBE HEAVY DARK MATTER ANALYSIS SUPPLEMENTARY MATERIAL

2042 C.1 Docker Image for Oscillating Neutrino Spectra

```
2043 1 FROM ubuntu:18.04
2044 2
2045 3 # Execute commands to install software packages
2046 4 RUN apt -y update
2047 5
2048 6     # Install utility programs
2049 7 RUN apt -y install vim wget git cmake
2050 8
2051 9 ARG DEBIAN_FRONTEND=noninteractive
2052 0
2053 1     # Install python
2054 2 RUN apt -y install python python-dev python-pip libjpeg-dev zlib1g-dev
2055 3
2056 4     # We need Python2 for installing Charon.
2057 5 RUN apt -y install python-numpy python-sympy python-matplotlib \
2058 6             python-sympy python-h5py python-astropy python-ipython
2059 7
2060 8     # Install dependencies of Charon : SQuIDS, NuSQuIDS
2061 9 RUN apt -y install libgsl-dev libgslcblas0 libgsl23 gsl-bin pkg-config
2062 0     # Install SQuIDS
2063 1 RUN mkdir /home/SQuIDS /home/SQuIDS_install
2064 2 WORKDIR /home/SQuIDS
2065 3 RUN git clone https://github.com/jsalvado/SQuIDS.git
2066 4 WORKDIR /home/SQuIDS/SQuIDS
2067 5 RUN git checkout 7ad9ba7c6ad06d1f0fa8418f937ebf1a403fef90
2068 6     # Before executing "make install" an environmental variable has to be set.
2069 7 ENV PKG_CONFIG_PATH=/home/SQuIDS/SQuIDS/lib
2070 8 RUN ./configure --prefix=../SQuIDS_install \
```

```

20719    && make
20720 RUN make install
20731
20742 # Set up an environmental variable that is required to install nuSQuIDS..
20753 ENV SQuIDS=/home/SQuIDS/SQuIDS
20764 ENV LD_LIBRARY_PATH=$SQuIDS/lib:$LD_LIBRARY_PATH
20785
20786 # Install NuSQuIDS
20797 RUN mkdir /home/nuSQuIDS
20808 WORKDIR /home/nuSQuIDS
20819 RUN git clone https://github.com/qrliu/nuSQuIDS.git
20820 WORKDIR /home/nuSQuIDS/nuSQuIDS
20831 RUN git checkout 072d8ef740e2fc7330f1fabaea94f0f4540c46f9
20842 RUN apt -y install libhdf5-dev hdf5-tools
20853 RUN apt -y install libboost1.65-all-dev
20864 RUN ./configure --with-squids=$SQuIDS --with-python-bindings --prefix=../
2087     nuSQuIDS_install \
20885     && make \
20896     && make install
20907
20918 # Set up an environmental variable for nuSQuIDS.
20929 ENV nuSQuIDS=/home/nuSQuIDS/nuSQuIDS
20930 ENV LD_LIBRARY_PATH=$nuSQuIDS/lib:$LD_LIBRARY_PATH
20941
20952 # Build the python bindings
20963 WORKDIR /home/nuSQuIDS/nuSQuIDS/resources/python/src
20974 RUN make
20985
20996 # Set up an environmental variable for the python bindings.
21007 ENV PYTHONPATH=$nuSQuIDS/resources/python/bindings/:$PYTHONPATH
21018
21029 # Install Charon in the /home/Charon/charon directory.
21030 RUN mkdir /home/Charon

```

```
21041 WORKDIR /home/Charon
21052 RUN git clone https://github.com/icecube/charon.git \
21063     && apt -y install unzip python-scipy
21074 WORKDIR charon
21085 RUN git checkout c531efe4e01dc364a60d1c83f950f04526ccd771
21096 RUN unzip ./charon/xsec/xsec.zip -d charon/xsec/ \
21107
21118 # Download neutrino spectra tables in the /home/Charon/charon/data directory
2112 .
21139 && mkdir ./charon/data
21140 WORKDIR ./charon/data
21151 RUN wget --no-check-certificate https://icecube.wisc.edu/~qliu/charon/
2116     SpectraEW.hdf5 \
21172 && wget --no-check-certificate https://icecube.wisc.edu/~qliu/charon/
2118     Spectra_PYTHIA.hdf5 \
21193 && wget --no-check-certificate https://icecube.wisc.edu/~qliu/charon/
2120     Spectra_noEW.hdf5
21214
21225 WORKDIR ../../
21236 RUN python setup.py install
21247 WORKDIR /home
```

2125 C.2 Spline Fitting Statuses

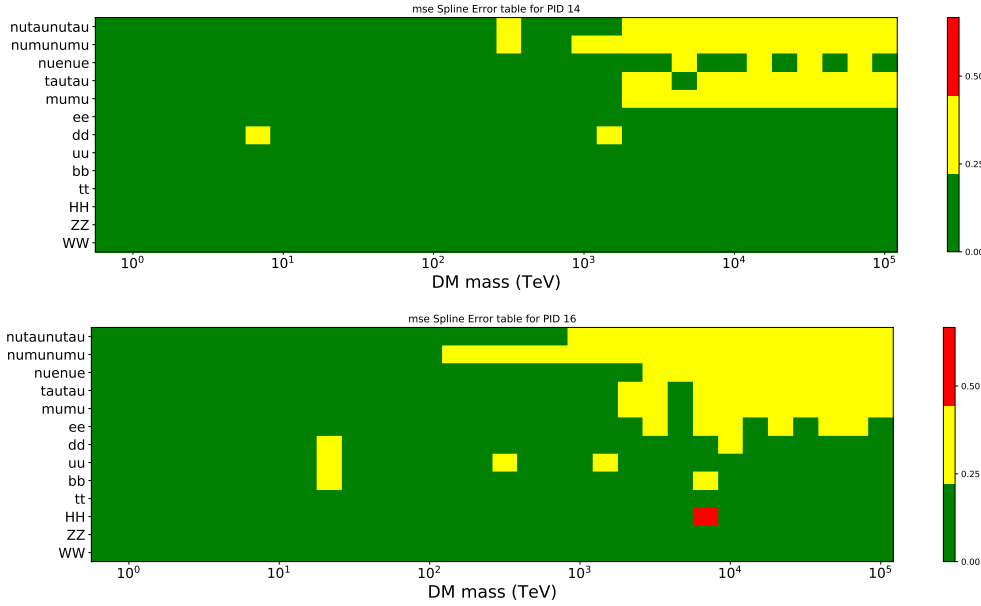


Figure C.1 Current status of spline tables according to constraints defined by Tab. 7.1. Green splines are splines that passed under the GOOD tolerance. Yellow are splines that are OK. Red are splines that FAIL. All yellow splines were inspected individually before running the analysis. Splines were made for the μ (PID 14; top panel) flavor and τ (PID 16; bottom panel) neutrino flavors.

2126 C.3 Neutrino Composite Spectra

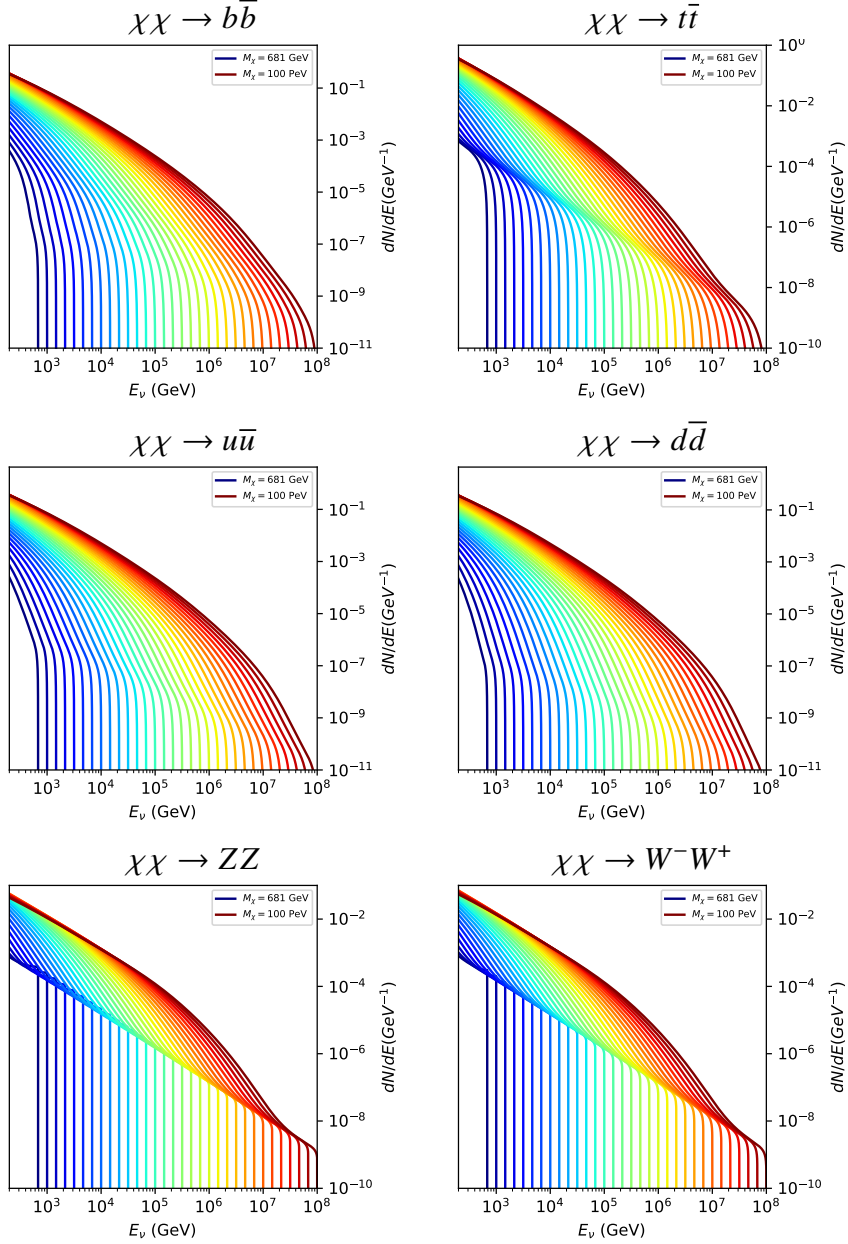


Figure C.2 Sister figure to Fig. 7.5 for annihilation channels that did not require kernel smoothing. These spectra are the composite ($\nu_\mu + \nu_\tau$) of neutrino flavors. Every spectral model used for this analysis is featured as a colored solid line. Bluer lines are for lower DM mass spectral models. DM masses range from 681 GeV to 100 PeV.

2127 C.4 Segue 1 And Ursa Major II Signal Recovery

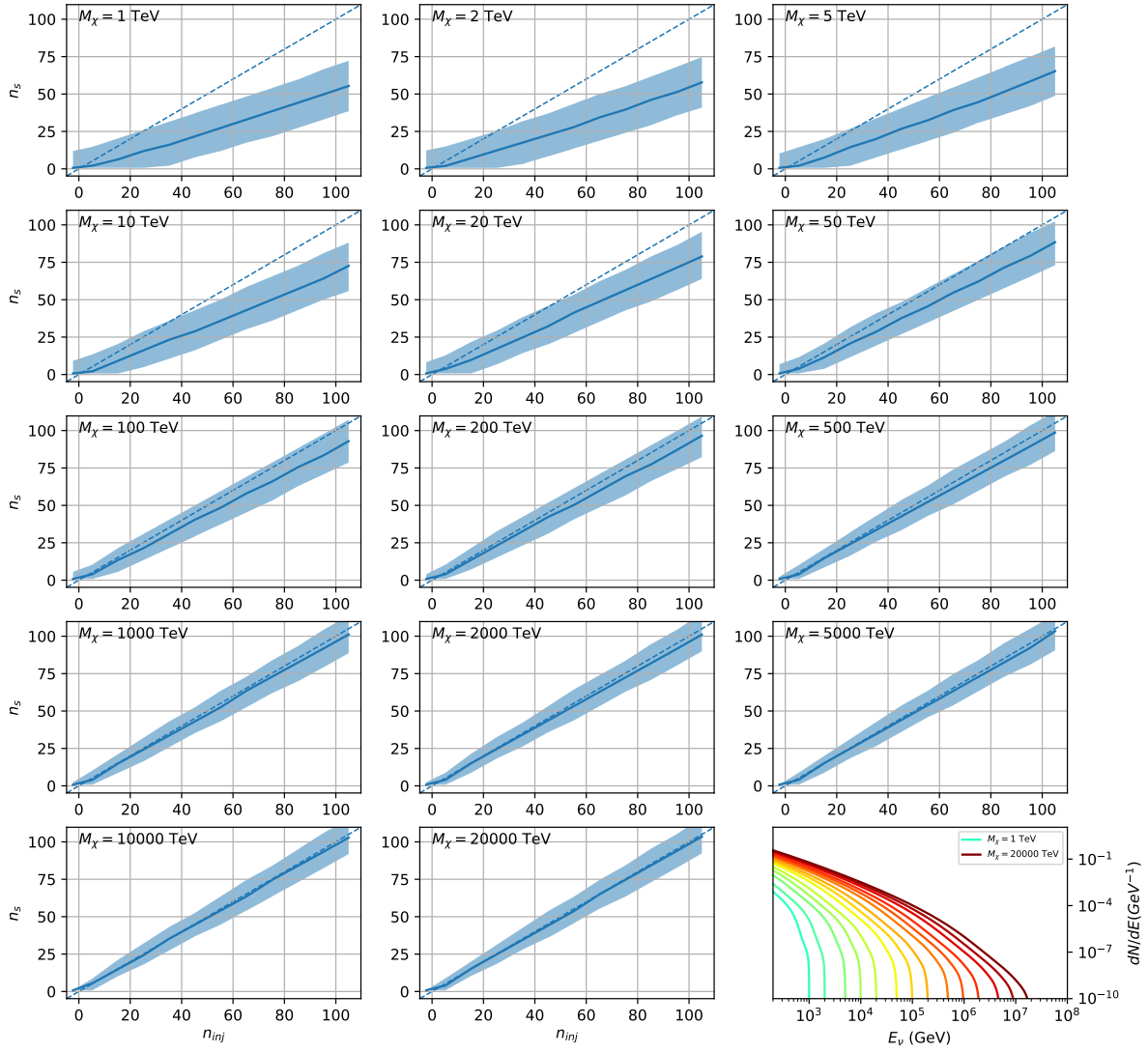


Figure C.3 Same as Fig. 7.23 but for Segue 1 and $\chi\chi \rightarrow b\bar{b}$.

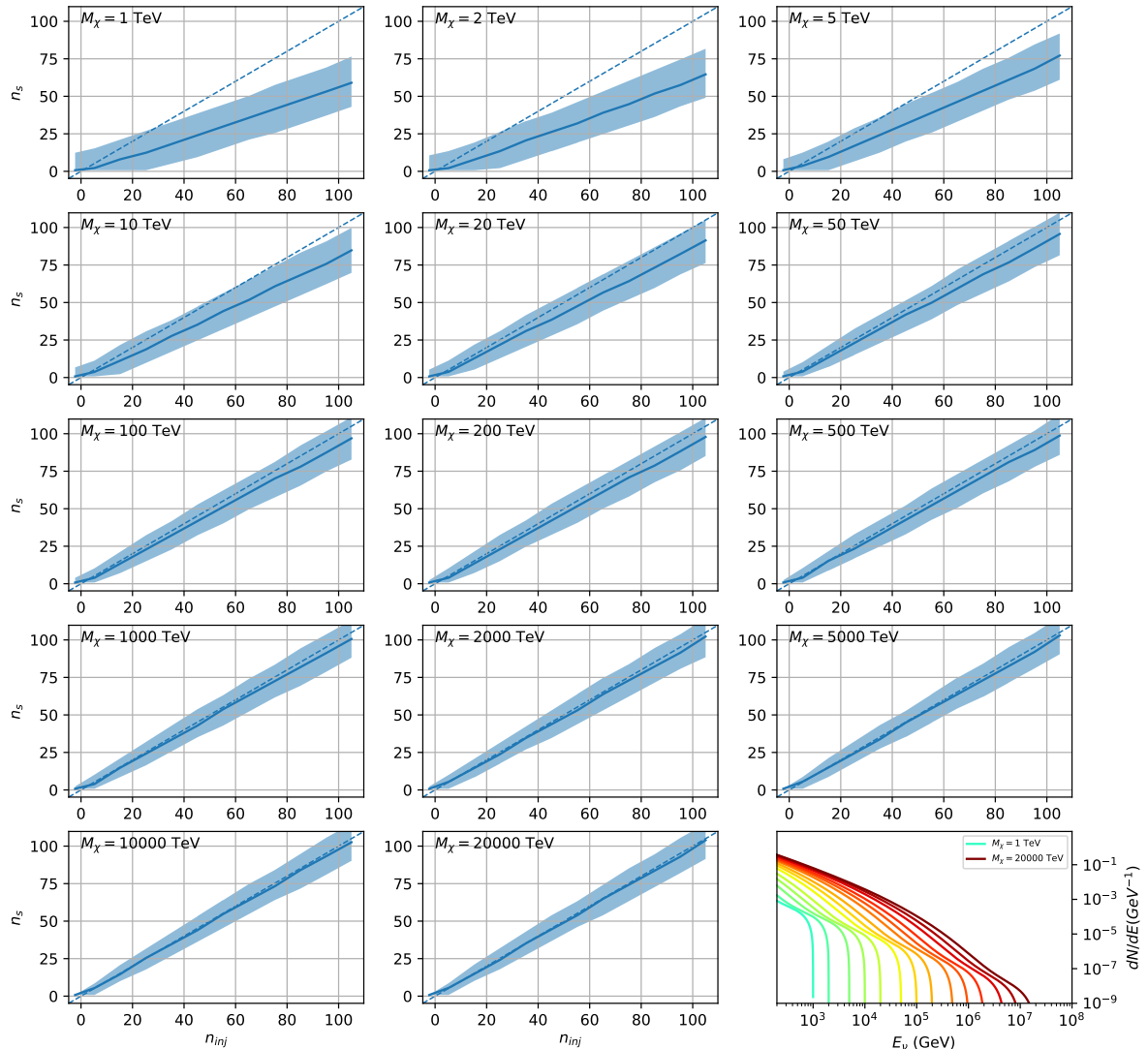


Figure C.4 Same as Fig. 7.23 but for Segue 1 and $\chi\chi \rightarrow t\bar{t}$.

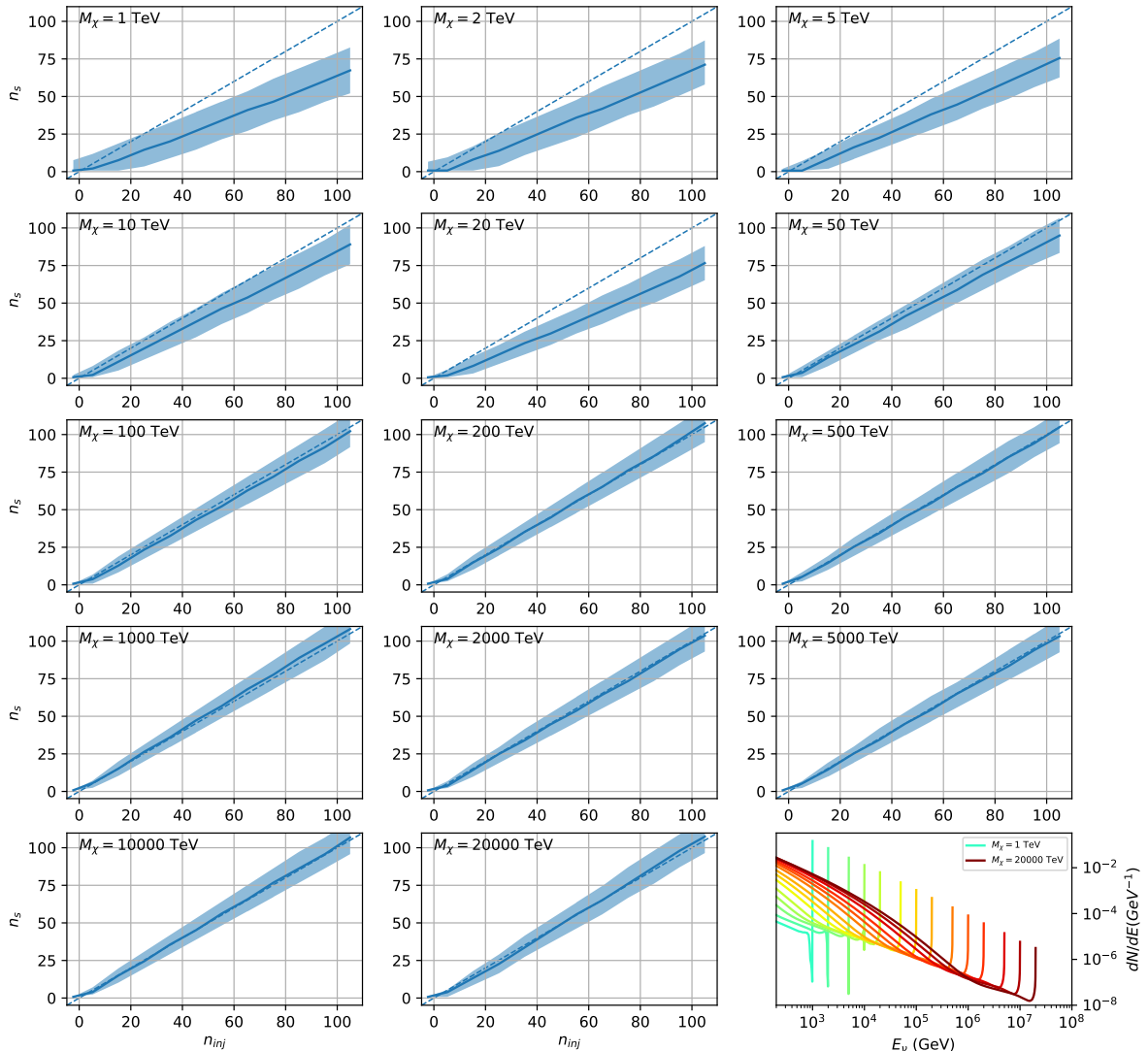


Figure C.5 Same as Fig. 7.23 but for Segue 1 and $\chi\chi \rightarrow \nu_\mu \bar{\nu}_\mu$.

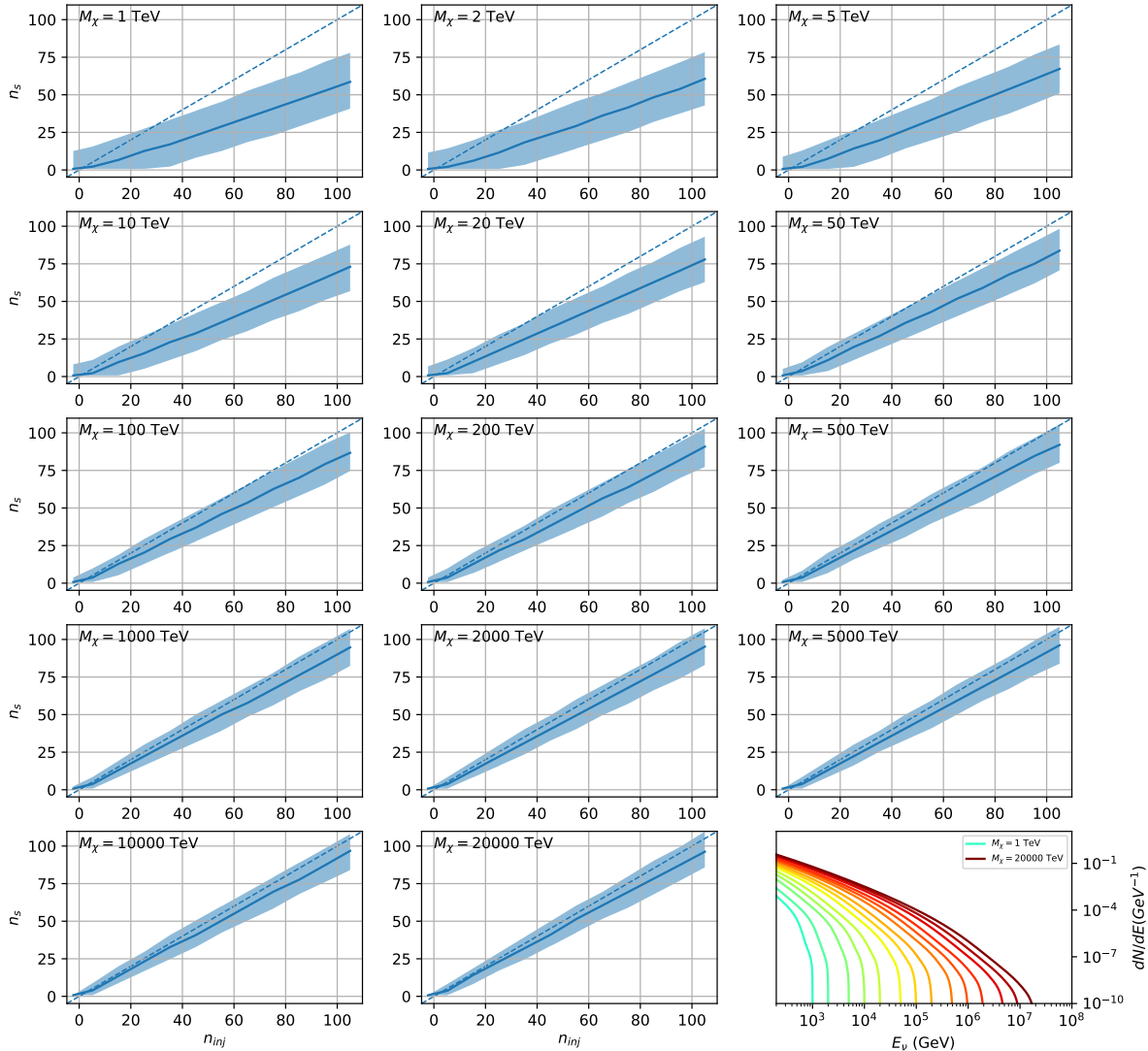


Figure C.6 Same as Fig. 7.23 but for Ursa Major II and $\chi\chi \rightarrow b\bar{b}$.

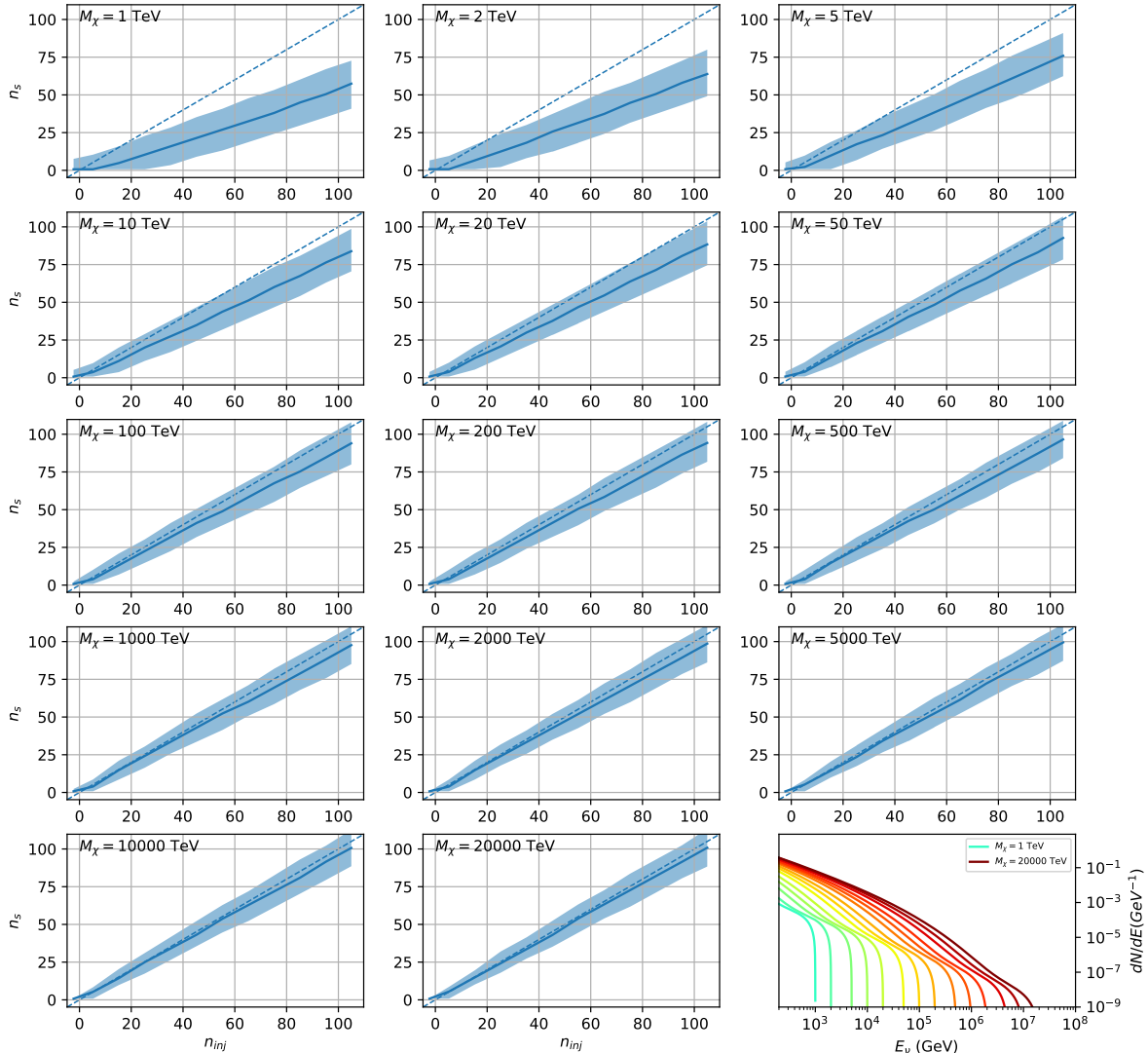


Figure C.7 Same as Fig. 7.23 but for Ursa Major II and $\chi\chi \rightarrow t\bar{t}$.

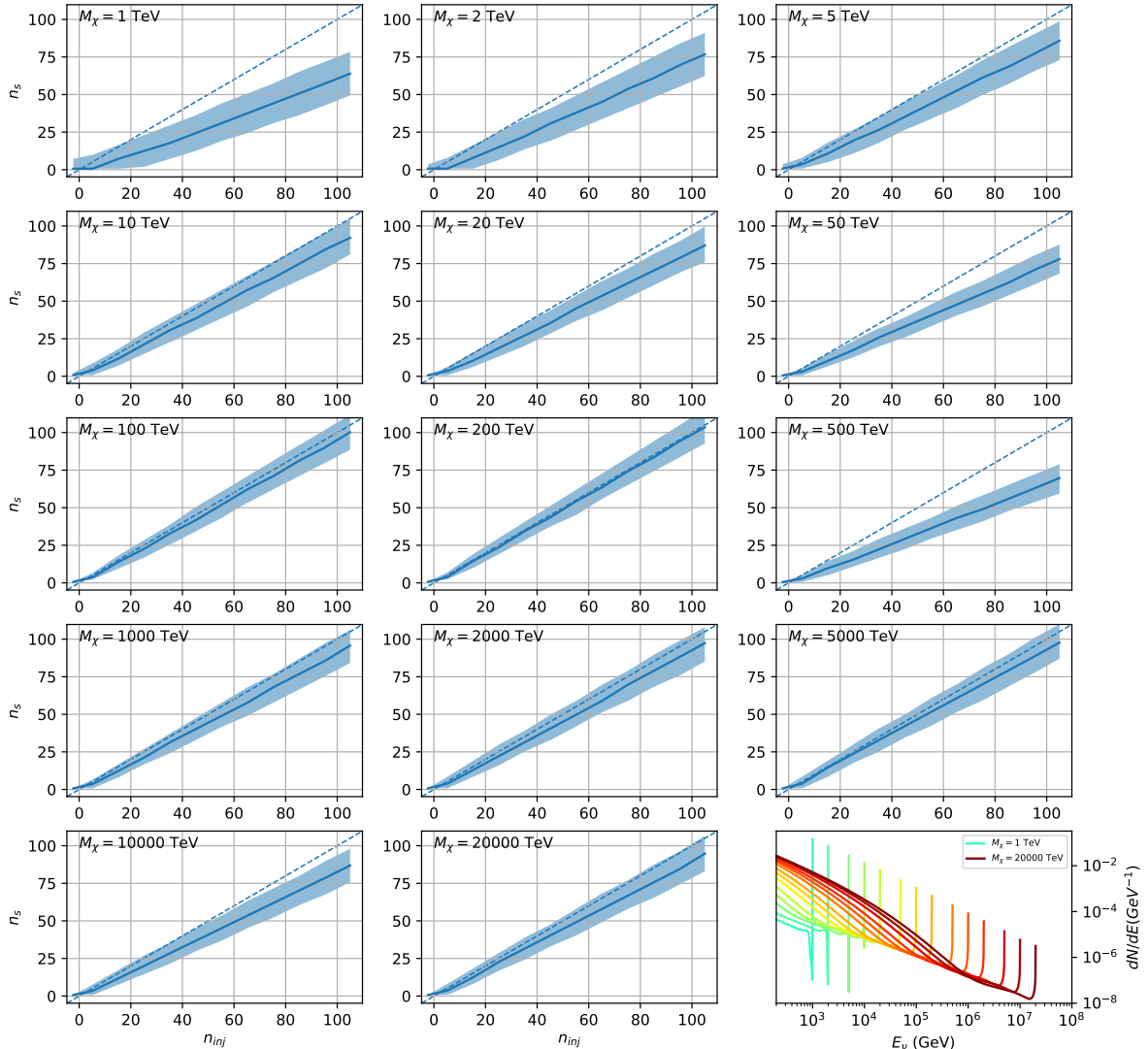


Figure C.8 Same as Fig. 7.23 but for Ursa Major II and $\chi\chi \rightarrow \nu_\mu \bar{\nu}_\mu$.

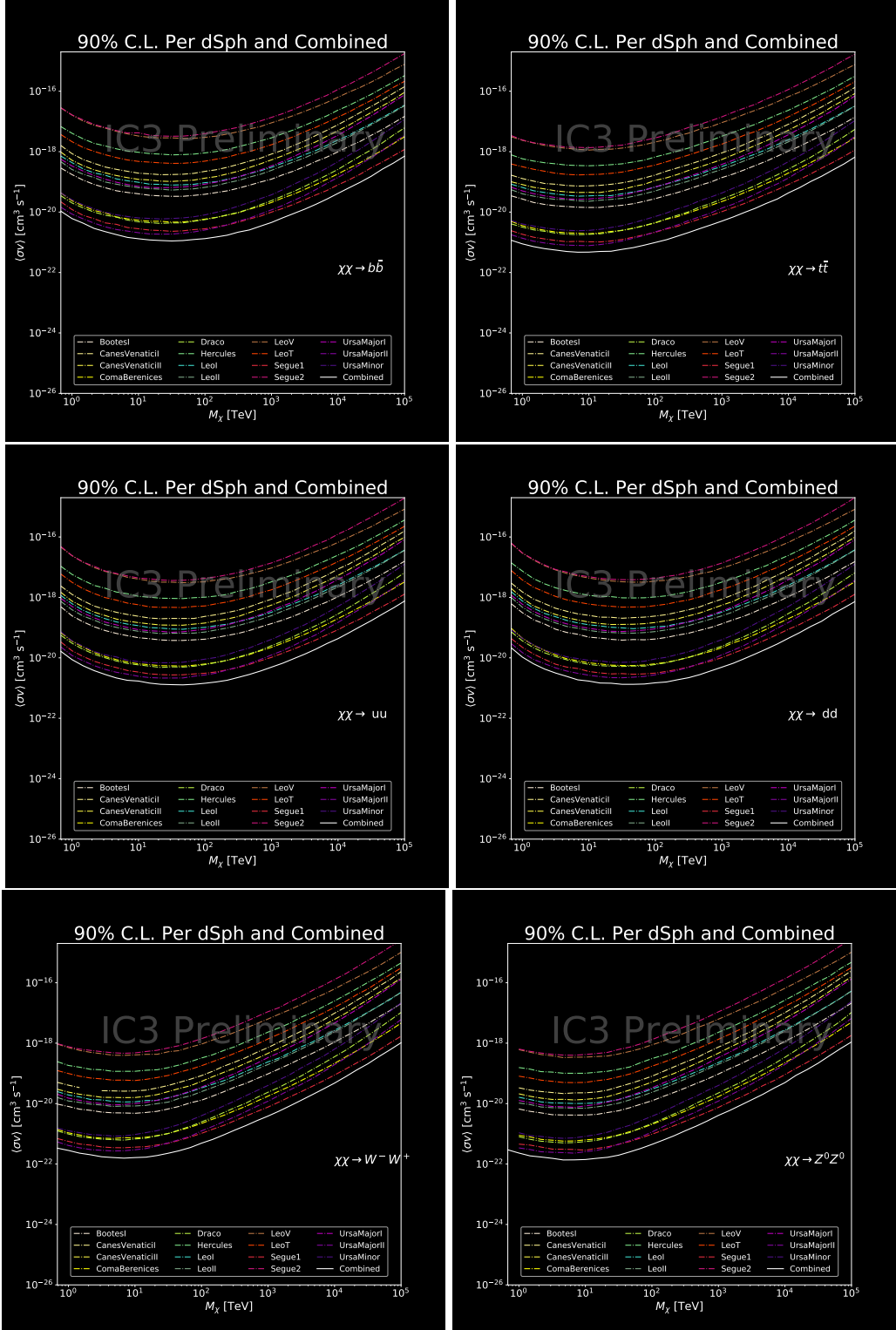


Figure C.9 IceCube North Sky Track Sensitivities for $n_s/\langle N \rangle$. n_s values are the counts fed into Eq. (7.8) to produce Fig. 7.25 and Fig. 7.26.

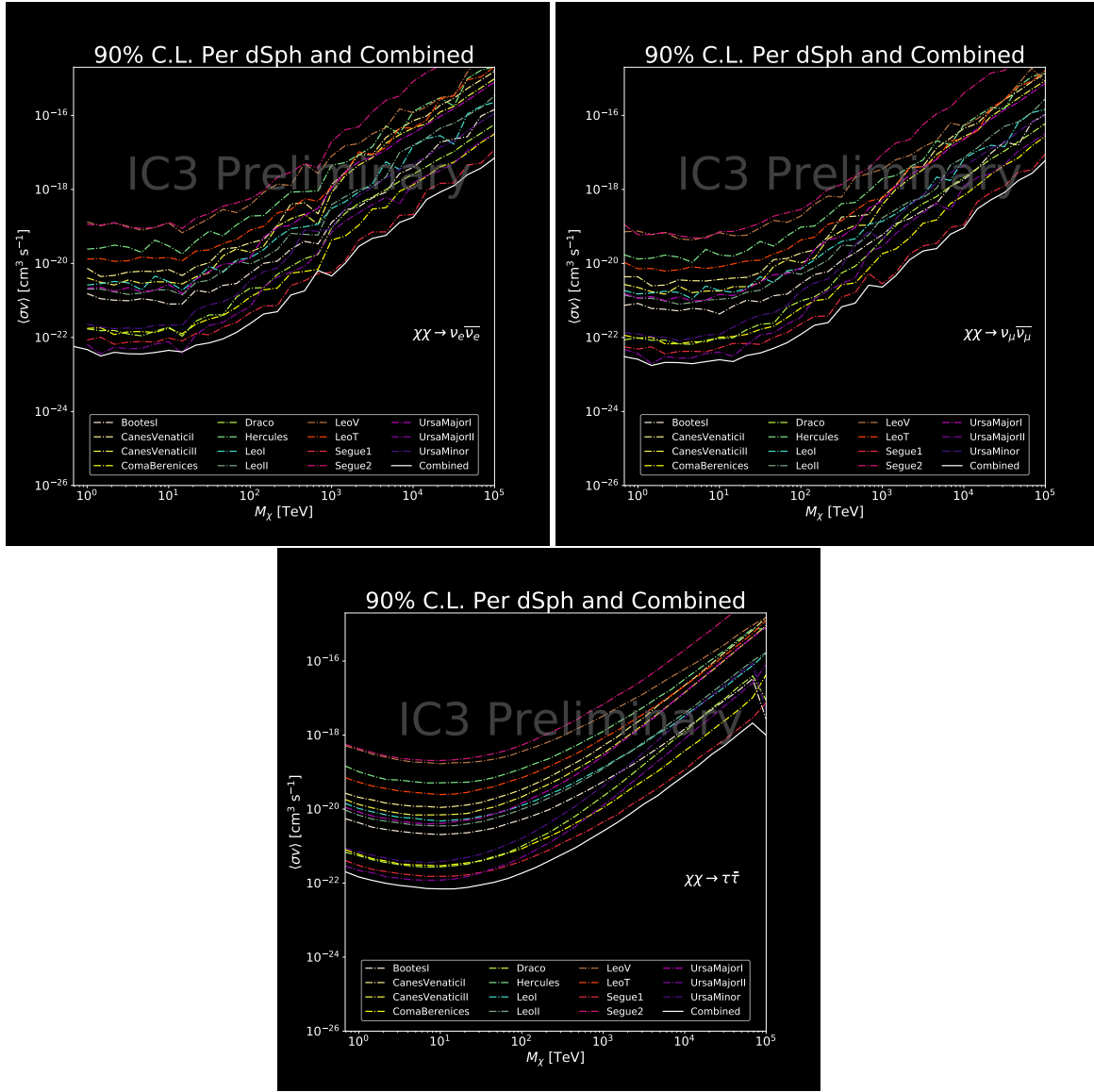


Figure C.10 Same as Fig. C.9 for three additional DM annihilation channels.

BIBLIOGRAPHY

- 2130 [1] Anne M. Green. “Dark matter in astrophysics/cosmology”. In: *SciPost Phys. Lect.*
 2131 *Notes* (2022), p. 37. doi: [10.21468/SciPostPhysLectNotes.37](https://doi.org/10.21468/SciPostPhysLectNotes.37). URL: <https://scipost.org/10.21468/SciPostPhysLectNotes.37>.
- 2133 [2] Bing-Lin Young. “A survey of dark matter and related topics in cosmology”. In: *Frontiers*
 2134 *of Physics* 12 (Oct. 2016). doi: <https://doi.org/10.1007/s11467-016-0583-4>.
 2135 URL: <https://doi.org/10.1007/s11467-016-0583-4>.
- 2136 [3] Gianfranco Bertone, Dan Hooper, and Joseph Silk. “Particle dark matter: evidence,
 2137 candidates and constraints”. In: *Physics Reports* 405.5 (2005), pp. 279–390. ISSN:
 2138 0370-1573. doi: <https://doi.org/10.1016/j.physrep.2004.08.031>. URL:
 2139 <https://www.sciencedirect.com/science/article/pii/S0370157304003515>.
- 2140 [4] Gianfranco Bertone and Dan Hooper. “History of dark matter”. In: *Rev. Mod. Phys.*
 2141 90 (4 Aug. 2018), p. 045002. doi: [10.1103/RevModPhys.90.045002](https://doi.org/10.1103/RevModPhys.90.045002). URL: <https://link.aps.org/doi/10.1103/RevModPhys.90.045002>.
- 2143 [5] Fritz Zwicky. “The Redshift of Extragalactic Nebulae”. In: *Helvetica Physica Acta* 6.
 2144 (1933), pp. 110–127. doi: [10.5169/seals-110267](https://doi.org/10.5169/seals-110267).
- 2145 [6] Vera C. Rubin and Jr. Ford W. Kent. “Rotation of the Andromeda Nebula from a
 2146 Spectroscopic Survey of Emission Regions”. In: *ApJ* 159 (Feb. 1970), p. 379. doi:
 2147 [10.1086/150317](https://doi.org/10.1086/150317).
- 2148 [7] K. G. Begeman, A. H. Broeils, and R. H. Sanders. “Extended rotation curves of spiral galax-
 2149 ies: dark haloes and modified dynamics”. In: *Monthly Notices of the Royal Astronomical So-*
 2150 *ciety* 249.3 (Apr. 1991), pp. 523–537. ISSN: 0035-8711. doi: [10.1093/mnras/249.3.523](https://doi.org/10.1093/mnras/249.3.523).
 2151 eprint: <https://academic.oup.com/mnras/article-pdf/249/3/523/18160929/mnras249-0523.pdf>. URL: <https://doi.org/10.1093/mnras/249.3.523>.
- 2153 [8] *Different types of gravitational lenses*. website. Feb. 2004. URL: <https://esahubble.org/images/heic0404b/>.
- 2155 [9] Douglas Clowe et al. “A Direct Empirical Proof of the Existence of Dark Matter”. In: *apjl*
 2156 648.2 (Sept. 2006), pp. L109–L113. doi: [10.1086/508162](https://doi.org/10.1086/508162). arXiv: [astro-ph/0608407](https://arxiv.org/abs/astro-ph/0608407)
 2157 [*astro-ph*].
- 2158 [10] Planck Collaboration and N. et. al. Aghanim. “Planck 2018 results I. Overview and the
 2159 cosmological legacy of Planck”. In: *A&A* 641 (2020). doi: [10.1051/0004-6361/201833880](https://doi.org/10.1051/0004-6361/201833880). URL: <https://doi.org/10.1051/0004-6361/201833880>.
- 2161 [11] Wayne Hu. *Matter Density Animation*. web. 2024. URL: <http://background.uchicago.edu/~whu/animbut/anim2.html>.

- 2163 [12] Wenlong Yuan et al. “A First Look at Cepheids in a Type Ia Supernova Host with JWST”. in:
2164 *The Astrophysical Journal Letters* 940.1 (Nov. 2022). doi: [10.3847/2041-8213/ac9b27](https://doi.org/10.3847/2041-8213/ac9b27).
2165 URL: <https://dx.doi.org/10.3847/2041-8213/ac9b27>.
- 2166 [13] Wendy L. Freedman. “Measurements of the Hubble Constant: Tensions in Perspective”. In:
2167 *The Astrophysical Journal* 919.1 (Sept. 2021), p. 16. doi: [10.3847/1538-4357/ac0e95](https://doi.org/10.3847/1538-4357/ac0e95).
2168 URL: <https://dx.doi.org/10.3847/1538-4357/ac0e95>.
- 2169 [14] Jodi Cooley. “Dark Matter direct detection of classical WIMPs”. In: *SciPost Phys. Lect.
2170 Notes* (2022), p. 55. doi: [10.21468/SciPostPhysLectNotes.55](https://doi.org/10.21468/SciPostPhysLectNotes.55). URL: <https://scipost.org/10.21468/SciPostPhysLectNotes.55>.
- 2172 [15] “Search for new phenomena in events with an energetic jet and missing transverse momentum
2173 in pp collisions at $\sqrt{s} = 13$ TeV with the ATLAS detector”. In: *Phys. Rev. D* 103
2174 (11 July 2021), p. 112006. doi: [10.1103/PhysRevD.103.112006](https://doi.org/10.1103/PhysRevD.103.112006). URL: <https://link.aps.org/doi/10.1103/PhysRevD.103.112006>.
- 2176 [16] *Jetting into the dark side: a precision search for dark matter*. website. July 2020. URL:
2177 <https://atlas.cern/updates/briefing/precision-search-dark-matter>.
- 2178 [17] Celine Armand et. al. “Combined dark matter searches towards dwarf spheroidal galaxies
2179 with Fermi-LAT, HAWC, H.E.S.S., MAGIC, and VERITAS”. in: *Proceedings of Science*.
2180 Vol. 395. Mar. 2022. doi: <https://doi.org/10.22323/1.395.0528>.
- 2181 [18] Tracy R. Slatyer. “Les Houches Lectures on Indirect Detection of Dark Matter”. In: *SciPost
2182 Phys. Lect. Notes* (2022), p. 53. doi: [10.21468/SciPostPhysLectNotes.53](https://doi.org/10.21468/SciPostPhysLectNotes.53). URL:
2183 <https://scipost.org/10.21468/SciPostPhysLectNotes.53>.
- 2184 [19] Christian W Bauer, Nicholas L. Rodd, and Bryan R. Webber. “Dark matter spectra from
2185 the electroweak to the Planck scale”. In: *Journal of High Energy Physics* 2021.1029-8479
2186 (June 2021). doi: [https://doi.org/10.1007/JHEP06\(2021\)121](https://doi.org/10.1007/JHEP06(2021)121).
- 2187 [20] Riccardo Catena and Piero Ullio. “A novel determination of the local dark matter density”.
2188 In: *Journal of Cosmology and Astroparticle Physics* 2010.08 (Aug. 2010), p. 004. doi:
2189 [10.1088/1475-7516/2010/08/004](https://doi.org/10.1088/1475-7516/2010/08/004). URL: <https://dx.doi.org/10.1088/1475-7516/2010/08/004>.
- 2191 [21] B. P. Abbott et al. “Observation of Gravitational Waves from a Binary Black Hole Merger”.
2192 In: *Phys. Rev. Lett.* 116 (6 Feb. 2016), p. 061102. doi: [10.1103/PhysRevLett.116.061102](https://doi.org/10.1103/PhysRevLett.116.061102). URL: <https://link.aps.org/doi/10.1103/PhysRevLett.116.061102>.
- 2194 [22] R. Abbasi et. al. “Observation of high-energy neutrinos from the Galactic plane”. In: *Science*
2195 380.6652 (June 2023), pp. 1338–1343.
- 2196 [23] NASA Goddard Space Flight Center. *Fermi’s 12-year view of the gamma-ray sky*. website.

- 2197 2022. URL: <https://svs.gsfc.nasa.gov/14090>.
- 2198 [24] Marco Cirelli et al. “PPPC 4 DM ID: a poor particle physicist cookbook for dark matter
2199 indirect detection”. In: *Journal of Cosmology and Astroparticle Physics* 2011.03 (Mar.
2200 2011), p. 051. doi: [10.1088/1475-7516/2011/03/051](https://doi.org/10.1088/1475-7516/2011/03/051). URL: <https://dx.doi.org/10.1088/1475-7516/2011/03/051>.
- 2202 [25] Javier Rico. “Gamma-Ray Dark Matter Searches in Milky Way Satellites—A Comparative
2203 Review of Data Analysis Methods and Current Results”. In: *Galaxies* 8.1 (Mar. 2020), p. 25.
2204 doi: [10.3390/galaxies8010025](https://doi.org/10.3390/galaxies8010025). arXiv: [2003.13482](https://arxiv.org/abs/2003.13482) [astro-ph.HE].
- 2205 [26] W. B. Atwood et al. “The Large Area Telescope on the Fermi Gamma-Ray Space Telescope
2206 Mission”. In: *apj* 697.2 (June 2009), pp. 1071–1102. doi: [10.1088/0004-637X/697/2/1071](https://doi.org/10.1088/0004-637X/697/2/1071). arXiv: [0902.1089](https://arxiv.org/abs/0902.1089) [astro-ph.IM].
- 2208 [27] M. Ackermann et al. “Searching for Dark Matter Annihilation from Milky Way Dwarf
2209 Spheroidal Galaxies with Six Years of Fermi Large Area Telescope Data”. In: *prl* 115.23,
2210 231301 (Dec. 2015), p. 231301. doi: [10.1103/PhysRevLett.115.231301](https://doi.org/10.1103/PhysRevLett.115.231301). arXiv:
2211 [1503.02641](https://arxiv.org/abs/1503.02641) [astro-ph.HE].
- 2212 [28] Mattia Di Mauro, Martin Stref, and Francesca Calore. “Investigating the effect of Milky
2213 Way dwarf spheroidal galaxies extension on dark matter searches with Fermi-LAT data”.
2214 In: *Phys. Rev. D* 106 (12 Dec. 2022), p. 123032. doi: [10.1103/PhysRevD.106.123032](https://doi.org/10.1103/PhysRevD.106.123032).
2215 URL: <https://link.aps.org/doi/10.1103/PhysRevD.106.123032>.
- 2216 [29] F. et al. Aharonian. “Observations of the Crab Nebula with H.E.S.S.”. In: *Astron. Astrophys.*
2217 457 (2006), pp. 899–915. doi: [10.1051/0004-6361:20065351](https://doi.org/10.1051/0004-6361:20065351). arXiv: [astro-ph/0607333](https://arxiv.org/abs/astro-ph/0607333).
- 2219 [30] J. Albert et al. “VHE γ -Ray Observation of the Crab Nebula and its Pulsar with the MAGIC
2220 Telescope”. In: *The Astrophysical Journal* 674.2 (Feb. 2008), p. 1037. doi: [10.1086/525270](https://doi.org/10.1086/525270). URL: <https://dx.doi.org/10.1086/525270>.
- 2222 [31] N. Park. “Performance of the VERITAS experiment”. In: *Proceedings, 34th International
2223 Cosmic Ray Conference (ICRC2015): The Hague, The Netherlands, July, 30th July - 6th
2224 August*. Vol. 34. 2015, p. 771. arXiv: [1508.07070](https://arxiv.org/abs/1508.07070) [astro-ph.IM].
- 2225 [32] A. Abramowski et al. “H.E.S.S. constraints on Dark Matter annihilations towards the Sculptor
2226 and Carina Dwarf Galaxies”. In: *Astropart. Phys.* 34 (2011), pp. 608–616. doi: [10.1016/j.astropartphys.2010.12.006](https://doi.org/10.1016/j.astropartphys.2010.12.006). arXiv: [1012.5602](https://arxiv.org/abs/1012.5602) [astro-ph.HE].
- 2228 [33] A. Abramowski et al. “Search for dark matter annihilation signatures in H.E.S.S. observations
2229 of Dwarf Spheroidal Galaxies”. In: *Phys. Rev. D* 90 (2014), p. 112012. doi: [10.1103/PhysRevD.90.112012](https://doi.org/10.1103/PhysRevD.90.112012). arXiv: [1410.2589](https://arxiv.org/abs/1410.2589) [astro-ph.HE].

- 2231 [34] H. Abdalla et al. “Searches for gamma-ray lines and ‘pure WIMP’ spectra from Dark
2232 Matter annihilations in dwarf galaxies with H.E.S.S”. in: *JCAP* 11 (2018), p. 037. doi:
2233 [10.1088/1475-7516/2018/11/037](https://doi.org/10.1088/1475-7516/2018/11/037). arXiv: [1810.00995 \[astro-ph.HE\]](https://arxiv.org/abs/1810.00995).
- 2234 [35] J. Aleksić et al. “Optimized dark matter searches in deep observations of Segue 1 with
2235 MAGIC”. in: *JCAP* 1402 (2014), p. 008. doi: [10.1088/1475-7516/2014/02/008](https://doi.org/10.1088/1475-7516/2014/02/008).
2236 arXiv: [1312.1535 \[hep-ph\]](https://arxiv.org/abs/1312.1535).
- 2237 [36] V.A. Acciari et al. “Combined searches for dark matter in dwarf spheroidal galaxies observed
2238 with the MAGIC telescopes, including new data from Coma Berenices and Draco”. In: *Physics of the Dark Universe* (2021), p. 100912. ISSN: 2212-6864. doi: <https://doi.org/10.1016/j.dark.2021.100912>. URL: <https://www.sciencedirect.com/science/article/pii/S2212686421001370>.
- 2242 [37] M. L. Ahnen et al. “Indirect dark matter searches in the dwarf satellite galaxy Ursa Major II
2243 with the MAGIC Telescopes”. In: *JCAP* 1803.03 (2018), p. 009. doi: [10.1088/1475-7516/2018/03/009](https://doi.org/10.1088/1475-7516/2018/03/009). arXiv: [1712.03095 \[astro-ph.HE\]](https://arxiv.org/abs/1712.03095).
- 2245 [38] S. et al. Archambault. “Dark matter constraints from a joint analysis of dwarf Spheroidal
2246 galaxy observations with VERITAS”. in: *prd* 95.8 (Apr. 2017). doi: [10.1103/PhysRevD.95.082001](https://doi.org/10.1103/PhysRevD.95.082001). arXiv: [1703.04937 \[astro-ph.HE\]](https://arxiv.org/abs/1703.04937).
- 2248 [39] Louise Oakes et al. “Combined Dark Matter searches towards dwarf spheroidal galaxies with
2249 Fermi-LAT, HAWC, HESS, MAGIC and VERITAS”. in: *Proceedings of Science*. 2019.
- 2250 [40] Celine Armand et al. on behalf of the Fermi-LAT, HAWC, HESS, MAGIC, VERITAS.
2251 “Combined Dark Matter searches towards dwarf spheroidal galaxies with Fermi-LAT,
2252 HAWC, HESS, MAGIC and VERITAS”. in: *Proceedings of Science*. 2021.
- 2253 [41] Daniel Kerszberg et al. on behalf of the Fermi-LAT, HAWC, HESS, MAGIC, and VER-
2254 TIAS collaborations. “Search for dark matter annihilation with a combined analysis of
2255 dwarf spheroidal galaxies from Fermi-LAT, HAWC, H.E.S.S., MAGIC and VERITAS”. in:
2256 *Proceedings of Science*. 2023.
- 2257 [42] A. U. Abeysekara et al. “Observation of the Crab Nebula with the HAWC Gamma-Ray
2258 Observatory”. In: *The Astrophysical Journal* 843.1 (June 2017), p. 39. doi: [10.3847/1538-4357/aa7555](https://doi.org/10.3847/1538-4357/aa7555). URL: <https://doi.org/10.3847/1538-4357/aa7555>.
- 2260 [43] Giacomo Vianello et al. *The Multi-Mission Maximum Likelihood framework (3ML)*. 2015.
2261 arXiv: [1507.08343 \[astro-ph.HE\]](https://arxiv.org/abs/1507.08343).
- 2262 [44] Marco Cirelli et al. “PPPC 4 DM ID: a poor particle physicist cookbook for dark matter
2263 indirect detection”. In: *Journal of Cosmology and Astroparticle Physics* 2011.03 (Mar.
2264 2011). ISSN: 1475-7516. doi: [10.1088/1475-7516/2011/03/051](https://doi.org/10.1088/1475-7516/2011/03/051). URL: <http://dx.doi.org/10.1088/1475-7516/2011/03/051>.

- 2266 [45] Alex Geringer-Sameth, Savvas M. Koushiappas, and Matthew Walker. “DWARF GALAXY
2267 ANNIHILATION AND DECAY EMISSION PROFILES FOR DARK MATTER EXPERI-
2268 MENTS”. In: *The Astrophysical Journal* 801.2 (Mar. 2015), p. 74. ISSN: 1538-4357. doi:
2269 [10.1088/0004-637x/801/2/74](https://doi.org/10.1088/0004-637x/801/2/74). URL: <http://dx.doi.org/10.1088/0004-637X/801/2/74>.
- 2271 [46] A. Albert et al. “Dark Matter Limits from Dwarf Spheroidal Galaxies with the HAWC
2272 Gamma-Ray Observatory”. In: *The Astrophysical Journal* 853.2 (Feb. 2018), p. 154. ISSN:
2273 1538-4357. doi: [10.3847/1538-4357/aaa6d8](https://doi.org/10.3847/1538-4357/aaa6d8). URL: <http://dx.doi.org/10.3847/1538-4357/aaa6d8>.
- 2275 [47] HongSheng Zhao. “Analytical models for galactic nuclei”. In: *Mon. Not. Roy. Astron. Soc.*
2276 278 (1996), pp. 488–496. doi: [10.1093/mnras/278.2.488](https://doi.org/10.1093/mnras/278.2.488). arXiv: [astro-ph/9509122](https://arxiv.org/abs/astro-ph/9509122)
2277 [[astro-ph](#)].
- 2278 [48] Julio F. Navarro, Carlos S. Frenk, and Simon D. M. White. “The Structure of Cold Dark
2279 Matter Halos”. In: *ApJ* 462 (May 1996), p. 563. doi: [10.1086/177173](https://doi.org/10.1086/177173). eprint:
2280 [astro-ph/9508025](https://arxiv.org/abs/astro-ph/9508025) ([astro-ph](#)).
- 2281 [49] V. Bonnivard et al. “Spherical Jeans analysis for dark matter indirect detection in dwarf
2282 spheroidal galaxies - Impact of physical parameters and triaxiality”. In: *Mon. Not. Roy.
2283 Astron. Soc.* 446 (2015), pp. 3002–3021. doi: [10.1093/mnras/stu2296](https://doi.org/10.1093/mnras/stu2296). arXiv:
2284 [1407.7822](https://arxiv.org/abs/1407.7822) [[astro-ph.HE](#)].
- 2285 [50] M. Ackermann et al. “Searching for Dark Matter Annihilation from Milky Way Dwarf
2286 Spheroidal Galaxies with Six Years of Fermi Large Area Telescope Data”. In: *prl* 115.23,
2287 231301 (Dec. 2015), p. 231301. doi: [10.1103/PhysRevLett.115.231301](https://doi.org/10.1103/PhysRevLett.115.231301). arXiv:
2288 [1503.02641](https://arxiv.org/abs/1503.02641) [[astro-ph.HE](#)].
- 2289 [51] M. L. Ahnen et al. “Limits to Dark Matter Annihilation Cross-Section from a Combined
2290 Analysis of MAGIC and Fermi-LAT Observations of Dwarf Satellite Galaxies”. In: *JCAP*
2291 1602.02 (2016), p. 039. doi: [10.1088/1475-7516/2016/02/039](https://doi.org/10.1088/1475-7516/2016/02/039). arXiv: [1601.06590](https://arxiv.org/abs/1601.06590)
2292 [[astro-ph.HE](#)].
- 2293 [52] Javier Rico et al. *gLike: numerical maximization of heterogeneous joint
2294 likelihood functions of a common free parameter plus nuisance parameters*.
2295 <https://doi.org/10.5281/zenodo.4601451>. Version v00.09.03. Mar. 2021. doi: [10.5281/zenodo.4601451](https://doi.org/10.5281/zenodo.4601451). URL: <https://doi.org/10.5281/zenodo.4601451>.
- 2297 [53] Tjark Miener and Daniel Nieto. *LklCom: Combining likelihoods from different experiments*.
2298 <https://doi.org/10.5281/zenodo.4597500>. Version v0.5.3. Mar. 2021. doi: [10.5281/zenodo.4597500](https://doi.org/10.5281/zenodo.4597500). URL: <https://doi.org/10.5281/zenodo.4597500>.
- 2300 [54] T. Miener et al. “Open-source Analysis Tools for Multi-instrument Dark Matter Searches”.
2301 In: *arXiv e-prints*, arXiv:2112.01818 (Dec. 2021), arXiv:2112.01818. arXiv: [2112.01818](https://arxiv.org/abs/2112.01818)

- 2302 [astro-ph.IM].
- 2303 [55] Alex Geringer-Sameth and Matthew Koushiappas Savvas M. and Walker. “Dwarf galaxy
2304 annihilation and decay emission profiles for dark matter experiments”. In: *Astrophys.*
2305 *J.* 801.2 (2015), p. 74. doi: [10.1088/0004-637X/801/2/74](https://doi.org/10.1088/0004-637X/801/2/74). arXiv: [1408.0002](https://arxiv.org/abs/1408.0002)
2306 [astro-ph.CO].
- 2307 [56] Gianfranco Bertone, Dan Hooper, and Joseph Silk. “Particle dark matter: evidence, can-
2308 didates and constraints”. In: *Physics Reports* 405.5-6 (Jan. 2005), pp. 279–390. ISSN:
2309 0370-1573. doi: [10.1016/j.physrep.2004.08.031](https://doi.org/10.1016/j.physrep.2004.08.031). URL: <http://dx.doi.org/10.1016/j.physrep.2004.08.031>.
- 2311 [57] V. Bonnivard et al. “Dark matter annihilation and decay in dwarf spheroidal galaxies: The
2312 classical and ultrafaint dSphs”. In: *Mon. Not. Roy. Astron. Soc.* 453.1 (2015), pp. 849–867.
2313 doi: [10.1093/mnras/stv1601](https://doi.org/10.1093/mnras/stv1601). arXiv: [1504.02048](https://arxiv.org/abs/1504.02048) [astro-ph.HE].
- 2314 [58] A. et al. Albert. “Searching for Dark Matter Annihilation in Recently Discovered Milky Way
2315 Satellites with Fermi-LAT”. in: *Astrophys. J.* 834.2 (2017), p. 110. doi: [10.3847/1538-4357/834/2/110](https://doi.org/10.3847/1538-4357/834/2/110). arXiv: [1611.03184](https://arxiv.org/abs/1611.03184) [astro-ph.HE].
- 2317 [59] Mattia Di Mauro and Martin Wolfgang Winkler. “Multimessenger constraints on the dark
2318 matter interpretation of the Fermi-LAT Galactic Center excess”. In: *prd* 103.12, 123005
2319 (June 2021), p. 123005. doi: [10.1103/PhysRevD.103.123005](https://doi.org/10.1103/PhysRevD.103.123005). arXiv: [2101.11027](https://arxiv.org/abs/2101.11027)
2320 [astro-ph.HE].
- 2321 [60] H. C. Plummer. “On the Problem of Distribution in Globular Star Clusters: (Plate 8.)”
2322 In: *Monthly Notices of the Royal Astronomical Society* 71.5 (Mar. 1911), pp. 460–470.
2323 ISSN: 0035-8711. doi: [10.1093/mnras/71.5.460](https://doi.org/10.1093/mnras/71.5.460). eprint: <https://academic.oup.com/mnras/article-pdf/71/5/460/2937497/mnras71-0460.pdf>. URL:
2325 <https://doi.org/10.1093/mnras/71.5.460>.
- 2326 [61] Daniel R. Hunter. “Derivation of the anisotropy profile, constraints on the local velocity
2327 dispersion, and implications for direct detection”. In: *JCAP* 02 (2014), p. 023. doi:
2328 [10.1088/1475-7516/2014/02/023](https://doi.org/10.1088/1475-7516/2014/02/023). arXiv: [1311.0256](https://arxiv.org/abs/1311.0256) [astro-ph.CO].
- 2329 [62] Barun Kumar Dhar and Liliya L. R. Williams. “Surface mass density of the Einasto family
2330 of dark matter haloes: are they Sersic-like?” In: *Mon. Not. Roy. Astron. Soc.* (2010). doi:
2331 [10.1111/j.1365-2966.2010.16446.x](https://doi.org/10.1111/j.1365-2966.2010.16446.x).
- 2332 [63] M. Baes and E. Van Hese. “Dynamical models with a general anisotropy profile”. In:
2333 *Astron. Astrophys.* 471 (2007), p. 419. doi: [10.1051/0004-6361:20077672](https://doi.org/10.1051/0004-6361:20077672). arXiv:
2334 [0705.4109](https://arxiv.org/abs/0705.4109) [astro-ph].
- 2335 [64] Matthew G. Walker, Edward W. Olszewski, and Mario Mateo. “Bayesian analysis of re-
2336 solved stellar spectra: application to MMT/Hectochelle observations of the Draco dwarf

- 2337 spheroidal”. In: *mnras* 448.3 (Apr. 2015), pp. 2717–2732. doi: [10.1093/mnras/stv099](https://doi.org/10.1093/mnras/stv099).
2338 arXiv: [1503.02589 \[astro-ph.GA\]](https://arxiv.org/abs/1503.02589).
- 2339 [65] Nicholas L. Rodd et al. “Dark matter spectra from the electroweak to the Planck scale”. In:
2340 *J. High Energy Physics* 121.10.1007 (June 2021).
- 2341 [66] Pace, Andrew B and Strigari, Louis E. “Scaling relations for dark matter annihilation and
2342 decay profiles in dwarf spheroidal galaxies”. In: *Monthly Notices of the Royal Astronomical
2343 Society* 482.3 (Oct. 2018), pp. 3480–3496. ISSN: 0035-8711. doi: [10.1093/mnras/sty2839](https://doi.org/10.1093/mnras/sty2839).
- 2345 [67] Albert, A. et al. “Search for gamma-ray spectral lines from dark matter annihilation in
2346 dwarf galaxies with the High-Altitude Water Cherenkov observatory”. In: *Phys. Rev. D* 101 (10 May 2020), p. 103001. doi: [10.1103/PhysRevD.101.103001](https://doi.org/10.1103/PhysRevD.101.103001). URL:
2347 <https://link.aps.org/doi/10.1103/PhysRevD.101.103001>.
- 2349 [68] Victor Eijkhout and Edmund Show and Robert van de Geijn. *The Science of Computing. The Art of High Performance Computing*. Vol. 3. Open Copy published under CC-BY 4.0
2350 license, 2023, pp. 63–66.
- 2352 [69] Aartsen, M. et al. “IceCube search for dark matter annihilation in nearby galaxies and galaxy
2353 clusters”. In: *Phys. Rev. D* 88 (12 Dec. 2013), p. 122001. doi: [10.1103/PhysRevD.88.122001](https://doi.org/10.1103/PhysRevD.88.122001). URL: <https://link.aps.org/doi/10.1103/PhysRevD.88.122001>.
- 2355 [70] Pearl Sandick et al. “Sensitivity of the IceCube neutrino detector to dark matter annihilating
2356 in dwarf galaxies”. In: *Phys. Rev. D* 81 (8 Apr. 2010), p. 083506. doi: [10.1103/PhysRevD.81.083506](https://doi.org/10.1103/PhysRevD.81.083506). URL: <https://link.aps.org/doi/10.1103/PhysRevD.81.083506>.
- 2358 [71] Qinrui Liu and Jeffrey Lazar and Carlos A. Argüelles and Ali Kheirandish. “ χ aro: a tool
2359 for neutrino flux generation from WIMPs”. In: *Journal of Cosmology and Astroparticle
2360 Physics* 2020.10 (Oct. 2020), p. 043. doi: [10.1088/1475-7516/2020/10/043](https://doi.org/10.1088/1475-7516/2020/10/043). URL:
2361 <https://dx.doi.org/10.1088/1475-7516/2020/10/043>.
- 2362 [72] Tessa Cerver. “Time Integrated searches for Astrophysical Neutrino Sources using the
2363 IceCube Detector and Gender in Physics studies for the Genera Project”. In: *UNIVERSITE
2364 DE GEN`EVE* (2019), pp. 57–64.
- 2365 [73] Minjin Jeong on behalf of the IceCube Collaboration. “Search for Dark Matter Decay in
2366 Nearby Galaxy Clusters and Galaxies with IceCube”. In: *Proceedings of Science* 444.38
2367 (2023).
- 2368 [74] IceCube Collaboration. “Evidence for neutrino emission from the nearby active galaxy NGC
2369 1068”. In: *Science* 378.6619 (2022).
- 2370 [75] Nathan Whitehorn and Jakob van Santen. *Photospline*. IceCube: GitHub.

- 2371 [76] The IceCube Collaboration. “Measurement of the multi-TeV neutrino interaction cross-
2372 section with IceCube using Earth absorption”. In: *Nature* 551 (2017).